

Decoding the metabolic program of deregulated MYCN expression in neuroblastoma

vorgelegt von

M. Sc.

Birte Arlt

an der Fakultät III - Prozesswissenschaften
der Technischen Universität Berlin
zur Erlangung des akademischen Grades

Doktorin der Naturwissenschaften

- Dr. rer. nat. -

genehmigte Dissertation

Promotionsausschuss:

Vorsitzender: Prof. Dr. Jens Kurreck

Gutachter: Prof. Dr. Roland Lauster

Gutachterin: PD Dr. Hedwig Deubzer

Gutachter: Prof. Dr. Juri Rappsilber

Gutachterin: Prof. Dr. Angelika Eggert

Tag der wissenschaftlichen Aussprache: 10. März 2020

Berlin 2020

Diese Arbeit wurde von August 2015 bis Januar 2020 an der Charité Universitätsmedizin Berlin und dem Max-Delbrück Center für Molekulare Medizin unter Leitung von PD Dr. Hedwig E. Deubzer und Dr. Stefan Kempa angefertigt.

Acknowledgment

I am deeply thankful to all the wonderful colleagues, friends and family members who went this inspiring and challenging, but also exhaustive journey together with me.

During my PhD I had the pleasure to be part of two labs. I would like to acknowledge my two supervisors PD Dr. Hedwig Deubzer and Dr. Stefan Kempa for the opportunity to work in their labs, for their guidance throughout the project, for their willingness to frequently travel between the two institutes and for constructive scientific discussions. They gave me the freedom to develop not only my project but also myself during the last four years.

A huge thank you goes to my former and present lab members for all your support, encouraging words, inspiration and for sharing tears of laughter and frustration.

To the former and present lab members from Hedi's group: Jasmin, Sebastian, Marco, Sabine, Daniela, Rasmus, Maddalena, Annika and Constantin. Thank you for being such a fantastic team to work and travel with. Legendary will remain our hilarious conversations, weird songs and nerdy games in the office. I would especially like to thank Jasmin Wünschel for her endless experimental support, for great talks at the cell culture bench while preparing incredibly high numbers of culture plates and for generating the most beautiful western blots.

To the former and present lab members from Stefan's group: Guido, Christin, Martin, Nadine, Jenny, Julia, Fardad, Safak, Henning, Tobias and Ela. Thank you for providing an exceptional working atmosphere combining scientific passion with cooking and good drinks. Special thanks go to Christin for introducing me to the field of data analysis, supporting me with ideas for neat-looking figures and sharing her scientific expertise. Furthermore I would like to thank Guido for introducing me to the world of nucleotides and proteins and supporting me with Italian coffee.

I would like to thank Prof. Angelika Eggert for contributing with experimental advice and introducing me to the scientific community. I thank Dr. Kathy Astrahantseff for her scientific input and support in writing scientific essays. Special thanks go to every group member from the pediatric oncology department - it was a great pleasure to work

with you! I further like to thank Annika for introducing me to CRISPR and her help in generating the knockout clones.

Furthermore I would like to acknowledge my cooperation partners Dr. Jana Wolf and Dr. Dennis Gürgen for carrying out the mice experiments and Dr. Anja Kühl for her expertise and support on the immunohistochemistry stainings. I would also like to thank all patients and their families for making precious neuroblastoma samples available for research purposes.

I would like to acknowledge Prof. Roland Lauster for his scientific support as well as Prof. Juri Rappsilber and Prof. Jens Kurreck for being part of the scientific commission.

Furthermore, I would like to thank my diligent thesis readers: Christin, Martin, Guido, Annika, Jasmin and Kerstin.

Ich danke von Herzen meiner Familie und meinen Freunden. Liebe Familie, ihr seid immer für mich da, unterstützt mich in jeder Lebenslage und habt mich stets ermutigt meine Interessen und Ziele zu verfolgen. Dafür bin ich euch unendlich dankbar! Tobi, du hast mich immer wieder aufgemuntert, mir Kraft gegeben und unerschütterliches Verständnis gezeigt. Danke, dass es dich gibt! Liebe Freunde, vielen Dank für eure vielfältige Unterstützung in all den unterschiedlichen Lebenslagen! Ihr seid die Besten!

Why do we do basic research?
To learn about ourselves.

Walter Gilbert

Summary

The oncogene *MYCN* is amplified in approximately 22% of all neuroblastomas and correlates with aggressive disease and unfavorable patient survival. Directly targeting *MYCN* remains a challenge due to its biochemical structure. We aimed for a deeper understanding of key metabolic pathways associated to amplified *MYCN* to discover druggable nodes that can be directly targeted for high-risk neuroblastoma therapy.

We performed GC-MS and LC-MS based methodologies for quantitative analysis of metabolites and proteins within the central carbon metabolism (CCM). Pulsed stable isotope-resolved metabolomics experiments (pSIRM) enabled the monitoring of glucose-derived carbons through the CCM. In order to decipher MYCN-dependent changes in the metabolic network, we quantified the proteome of a representative cohort of primary neuroblastoma biopsies and neuroblastoma cell lines by performing shotgun proteomics. High-level MYCN expression strongly correlated with the expression of proteins within the *de novo* serine synthesis pathway and the one-carbon metabolism.

We identified phosphoglycerate dehydrogenase (PHGDH), the rate-limiting enzyme in *de novo* serine synthesis, as a metabolic target of MYCN. High-level PHGDH expression correlated with amplified *MYCN* on transcriptional and translational level *in vitro*. We observed a recruitment of MYCN to two different regions within the *PHGDH* promoter site by applying ChIP qRT-PCR, indicating a MYCN-mediated transcriptional regulation of *PHGDH* in neuroblastoma cells. Further, we have shown by pSIRM experiments that glucose-derived carbon routing through *de novo* serine synthesis is enhanced in *MYCN*-amplified compared to *MYCN* non-amplified cells.

Serine and glycine starvation of *MYCN*-amplified cells did not affect proliferation and nucleotide pools, arguing for an independence of these cells to exogenous serine and glycine supply. This starvation induced PHGDH protein expression and enhanced *de novo* serine synthesis in *MYCN* non-amplified cells. However, proliferation was arrested and nucleotide pools were diminished in these cells.

We constructed *PHGDH* knockout clones by the CRISPR/Cas9 technology to genetically inhibit PHGDH expression *in vitro*. Proliferation of these clones was significantly decreased compared to the *MYCN*-amplified control cells. Pharmacological suppression of PHGDH activity with two small molecule inhibitors arrested proliferation in *MYCN*-amplified and *MYCN* non-amplified neuroblastoma cells *in vitro*. *In-vivo* PHGDH suppression in mice

carrying a patient-derived *MYCN*-amplified neuroblastoma xenograft hindered initial tumor growth which relapsed in later stages. A combination treatment of PHGDH inhibition with the chemotherapeutic drug cisplatin even induced an antagonizing effect on chemotherapy efficacy *in vivo*. In addition, we performed pSIRM experiments *in vitro* and observed a rerouting of glucose-derived carbons within the central carbon metabolism by PHGDH inhibition which will be further investigated. Moreover, we found evidence that glutamine starvation disrupted the *MYCN*-mediated regulation of PHGDH in neuroblastoma cells.

Antifolates targeting the one-carbon metabolism reduced proliferation more efficiently compared to PHGDH inhibitors *in vitro*. This observation was accompanied by a significant decrease in nucleotide levels in *MYCN*-amplified and *MYCN* non-amplified cells.

The herein presented thesis provides novel insights in the regulation of the *de novo* serine synthesis pathway and the one-carbon metabolism in neuroblastoma. We identified PHGDH as a promising target in dependency of *MYCN* expression. However, PHGDH inhibition did not induce lethal effects in neuroblastoma cells in *in vitro* and *in vivo* experiments. Thus additional research is needed to further exploit the application of small compounds targeting *de novo* serine synthesis and the one-carbon metabolism for the development of novel therapeutic strategies.

Zusammenfassung

Das Neuroblastom ist eine bösartige Krebserkrankung des sympathischen Nervensystems, die vor allem im frühen Kindesalter auftritt. In circa 22 Prozent aller Fälle liegt eine Amplifizierung des Onkogens *MYCN* vor, welche oft mit einer aggressiven Tumorbilogie und niedrigen Überlebensraten assoziiert ist. Die Anwendung von niedermolekularen Inhibitoren als Therapeutikum ist aufgrund der biochemischen Struktur des Onkogens wenig geeignet. Aus diesem Grund untersucht die vorliegende Arbeit *MYCN*-abhängige Stoffwechselwege mit dem Ziel direkte Angriffspunkte für neue Therapieformen zu identifizieren.

Die Anwendung von Massenspektrometrie-basierter Methoden (GC-MS / LC-MS) ermöglichte die Quantifizierung von Metaboliten und Proteinen des zentralen Kohlenstoffwechsels. Dieser ist ein wesentlicher Produzent notwendiger zellulärer Bausteine wie Aminosäuren und Nukleotide, die zur Erhaltung der energetischen Homöostase und damit zum Zellwachstum beitragen. Zusätzlich ermöglichten Markierungsexperimente unter Anwendung von stabilen Isotopen (pSIRM) die quantitative Betrachtung der Stoffwechselaktivität sowie deren Regulation. Ein Vergleich der Proteinexpressionen zwischen etablierten Zellkulturmodellen des Neuroblastoms und einer repräsentativen Kohorte primärer Biopsien von Neuroblastom-Patienten ergab eine direkte Korrelation zwischen *MYCN*-Status und der Expression der Enzyme der Serin-Synthese und des 'one-carbon'-Stoffwechsels. Basierend auf dieser Analyse identifizierten wir das Enzym Phosphoglyzeratdehydrogenase (PHGDH), welches den ersten Schritt der Serin-Synthese katalysiert, als metabolisches Target. In *in vitro* Experimenten zeigten wir, dass eine hohe Expression von PHGDH mit einer *MYCN* Amplifikation auf transkriptioneller und translationaler Ebene korreliert. Mittels ChIP qRT-PCR wiesen wir die Anwesenheit von *MYCN* in zwei Bereichen der PHGDH Promoterregion nach. Weiterhin konnten wir einen erhöhten Umsatz von Glukose in der *de novo* Synthese der Aminosäure Serin in *MYCN*-amplifizierten Neuroblastomzelllinien aufzeigen.

Die Wegnahme von Serin und Glycin, ein weiteres Substrat des Stoffwechselweges, im Zellkulturmedium zeigten keinen Effekt auf die Proliferation und Nukleotidlevel in *MYCN*-amplifizierten Zellen. Dagegen stellten wir in *MYCN* nicht-amplifizierten Zellen eine signifikante Erhöhung der PHGDH-Expression, sowie der Stoffwechselaktivität des *de novo* Serin-Syntheseweges fest. Gleichzeitig waren das Zellwachstum und die Nukleotidsynthese stark beeinträchtigt.

In weiterführenden Analysen hemmten wir PHGDH mittels genetischer Modifikation und pharmakologischer Intervention. Zunächst erzeugten wir mittels der CRISPR/Cas9-Technologie *PHGDH* knockout Klone. Diese zeigten ein verlangsamtes Wachstum im Vergleich zu den MYCN-amplifizierten Kontrollzellen *in vitro*. Im nächsten Schritt inhibierten wir PHGDH mit niedermolekularen Inhibitoren in Neuroblastom-Zelllinien und beobachteten einen Rückgang der Proliferation. Die PHGDH Inhibitorbehandlung von Mäusen mit Neuroblastom-Xenotransplantaten verlangsamte das initiale Tumorwachstum, welches jedoch über die Dauer der Behandlung wieder zunahm. Weiterführende *in vivo* Kombinationsbehandlungen der PHGDH Inhibitoren mit dem Zytostatikum Cisplatin zeigten sogar einen antagonistischen Effekt auf die Cisplatin-Effizienz. *In vitro* durchgeführte pSIRM Experimente gaben uns Hinweise auf eine veränderte Glukose-Verstoffwechselung im zentralen Kohlenstoffwechsel unter PHGDH Inhibition. Diese Beobachtung wird in weiterführenden Analysen eruiert. Darüber hinaus beobachteten wir, dass Glutaminmangel in die MYCN-abhängige Regulation von PHGDH in Neuroblastom-Zellen intervenierte.

Wir behandelten Neuroblastom-Zellen mit Antifolaten, die Enzyme des 'one-carbon'-Stoffwechsels inhibieren. Im Vergleich zur Behandlung mit PHGDH Inhibitoren zeigten diese einen verstärkten inhibitorischen Effekt auf das Wachstum und eine Verringerung der Nukleotidlevel in *MYCN*-amplifizierten und *MYCN* nicht-amplifizierten Zellen *in vitro*.

Zusammenfassend konnten wir zeigen, dass die *de novo* Serin-Synthese und der 'one-carbon'-Stoffwechsel eine signifikante Relevanz für *MYCN*-amplifizierte Neuroblastom-Zellen hat. Unsere Erkenntnisse ermöglichten neue Einblicke in die Regulation der *de novo* Serin-Synthese im Neuroblastom und identifizierten PHGDH als vielversprechendes Target dieses Stoffwechselweges. Jedoch induzierte eine PHGDH Inhibition keine letalen Effekte in Neuroblastom-Zellen. Weiterführende Forschung ist daher unabdingbar um die Bedeutung der *de novo* Serin-Synthese und des 'one-carbon'-Stoffwechsels für therapeutische Zwecke zu nutzen.

Contents

List of Figures	vi
List of Tables	vii
List of Abbreviations	ix
1. Introduction	1
1.1. Neuroblastoma	1
1.1.1. Clinical phenotype	1
1.1.2. Diagnostics	1
1.1.3. Tumor biology	2
1.1.4. Risk stratification and treatment	3
1.2. Metabolism in tumor cells	7
1.2.1. Glucose metabolism	7
1.2.2. Glutamine metabolism	10
1.2.3. <i>De novo</i> serine & glycine synthesis	10
1.2.3.1. Regulation of <i>de novo</i> serine and glycine synthesis in cancer	11
1.2.4. One-carbon metabolism	12
1.2.4.1. Folate cycle	13
1.2.4.2. Regulation of the folate cycle in cancer	15
1.2.4.3. Branching pathways	16
1.2.5. Time-resolved analysis of cancer cell metabolism	18
1.3. MYCN and its role in neuroblastoma metabolism	21
1.3.1. MYCN and glucose metabolism	21
1.3.2. MYCN and glutamine metabolism	22
1.3.3. MYCN and one-carbon metabolism	22
2. Aim of the Thesis	25
3. Materials and Methods	27
3.1. Patient samples for shotgun proteomics	27

3.2.	Cell culture	28
3.2.1.	Cell lines	28
3.2.2.	Monitoring cell growth	30
3.2.3.	Cell cycle analysis	31
3.2.4.	Generating <i>PHGDH</i> knockout clones	31
3.2.5.	siRNA-mediated knockdown	32
3.2.6.	Serine and glutamine starvation experiments	32
3.3.	Molecular Biology Methods	33
3.3.1.	Nucleic acid quantification	33
3.3.2.	DNA extraction	33
3.3.3.	RNA extraction	33
3.3.4.	Reverse-transcription PCR	34
3.3.5.	Quantitative real-time RT-PCR	34
3.3.6.	Chromatin immunoprecipitation qPCR	35
3.3.7.	CRISPR-Cas9 gene editing	36
3.4.	Biochemical Methods	39
3.4.1.	Preparation of protein lysates	39
3.4.2.	Protein quantification	39
3.4.3.	SDS-PAGE	39
3.4.4.	Western blot	39
3.4.5.	Immunohistochemistry	40
3.5.	Metabolomics	42
3.5.1.	Cell harvest	42
3.5.2.	Extraction of polar metabolites	42
3.5.3.	Measurement of intracellular metabolites	43
3.5.4.	Measurement of intracellular nucleotides	44
3.6.	Proteomics	46
3.6.1.	Sample preparation	46
3.6.2.	Protein quantification	46
3.6.3.	Protein digestion	46
3.6.4.	Liquid chromatography - mass spectrometry measurement	47
3.6.5.	Data analysis	47
3.7.	Patient-derived xenograft	49
3.8.	Statistics	50
4.	Results	51
4.1.	Identification of MYCN-dependent metabolic targets	51
4.1.1.	Synthetic MYCN expression in neuroblastoma cells	51
4.1.2.	Unbiased proteomics approach	55

4.2.	<i>In vitro</i> and <i>in vivo</i> characterization of PHGDH in neuroblastoma	62
4.2.1.	MYCN transcriptionally activates <i>PHGDH</i>	62
4.2.2.	ATF4-mediated regulation of PHGDH	63
4.2.3.	Effects of PHGDH on <i>de novo</i> serine synthesis	64
4.2.4.	Subcellular localization of PHGDH	67
4.2.5.	Clinical relevance	67
4.3.	Influence of serine and glycine starvation on PHGDH regulation	69
4.3.1.	MYCN-amplified cells are independent of exogenous serine and glycine supply	69
4.3.2.	ATF4-mediated regulation of PHGDH under serine and glycine starvation	72
4.3.3.	Metabolic effects triggered by serine and glycine starvation	73
4.4.	Genetic inhibition of <i>PHGDH</i> expression	79
4.4.1.	siRNA-mediated knockdown of <i>PHGDH</i>	79
4.4.2.	CRISPR-Cas9-mediated knockout of <i>PHGDH</i>	80
4.5.	Pharmacological inhibition of PHGDH activity	82
4.5.1.	PHGDH inhibition reduces cell growth <i>in vitro</i>	82
4.5.2.	PHGDH inhibitor treatment of mice carrying a patient-derived neuroblastoma xenograft	85
4.5.3.	Metabolic effects of PHGDH inhibitors	87
4.6.	Targeting the folate-mediated one-carbon metabolism	90
4.6.1.	Proliferation and nucleotide levels are decreased by antifolate treatment	90
4.7.	Response of neuroblastoma cell lines to glutamine starvation	93
4.7.1.	Glutamine starvation decreases proliferation in neuroblastoma cells	93
4.7.2.	ATF4-mediated regulation of apoptotic proteins under glutamine starvation	95
4.7.3.	Effects of glutamine starvation on <i>de novo</i> serine synthesis	97
5.	Discussion	99
5.1.	PHGDH as a metabolic target of MYCN in neuroblastoma	99
5.1.1.	Inhibition of PHGDH impairs cell growth and reduces <i>de novo</i> serine synthesis	101
5.1.2.	Strategies to compensate for inhibited PHGDH activity	102
5.1.3.	Inhibition of PHGDH in mice carrying a patient-derived neuroblastoma xenograft	103
5.1.4.	Secondary effects induced by PHGDH inhibition	105
5.1.5.	PHGDH inhibition in PHGDH-low expressing SH-EP cells	107
5.1.6.	Summary	107

5.2. Cellular response to serine and glycine starvation	108
5.2.1. The role of extracellular serine and glycine on cell growth	108
5.2.2. Mechanisms to escape external serine and glycine dependency	109
5.2.3. The importance of serine-glycine biosynthesis	111
5.2.4. Summary	111
5.3. Disruption of the folate cycle by antifolates	113
5.3.1. Antifolates disrupt nucleotide levels and impair proliferation	113
5.3.2. Bottlenecks of antifolate treatment	114
5.3.3. Summary	115
5.4. Cellular response to glutamine starvation	116
5.4.1. The role of extracellular glutamine on cell growth	116
5.4.2. Glutamine starvation triggers ATF4-dependent cell death	117
5.4.3. Glutamine starvation uncouples MYCN-mediated PHGDH regulation	118
5.4.4. Glutamine starvation induces deregulation of central metabolic path- ways	118
5.4.5. Summary	119
6. Outlook	121
7. Bibliography	123
Appendix	I
A. Supplementary: Materials and Methods	I
B. Supplementary: Results	XII

List of Figures

1.1. Scheme of glycolysis and TCA cycle	9
1.2. Scheme of <i>de novo</i> serine and glycine synthesis.	11
1.3. Scheme of folate cycle.	14
1.4. Scheme of <i>de novo</i> nucleotide biosynthesis.	17
1.5. Regulation between omics levels.	19
4.1. MYCN expression in SH-EP-Tet21/N and SH-SY5Y ^{MYCN}	52
4.2. Proliferation of SH-EP-Tet21/N and SH-SY5Y ^{MYCN}	53
4.3. Effect of MYCN induction on metabolite quantities.	54
4.4. Effects of MYCN induction on carbon-13 incorporation.	55
4.5. Spearman correlation analysis displaying known MYCN target genes. . . .	56
4.6. Spearman correlation analysis displaying proteins within the central carbon metabolism.	57
4.7. Spearman correlation analysis displaying proteins within the one-carbon metabolism.	60
4.8. Effect of MYCN on PHGDH expression.	62
4.9. Effect of ATF4 on PHGDH expression.	63
4.10. Absolute quantification of metabolites.	64
4.11. Timescale of glucose-derived carbon-13 incorporation into intermediates of the central carbon metabolism.	66
4.12. Immunohistochemical staining of neuroblastoma tissue.	67
4.13. <i>PHGDH</i> mRNA expression in neuroblastoma patients.	68
4.14. Effects of serine and glycine starvation on proliferation.	70
4.15. Effects of serine and glycine starvation on protein expression.	71
4.16. Effects of serine and glycine starvation on stress-response signaling.	72
4.17. Effects of ATF4 on PHGDH expression upon serine and glycine starvation. .	73
4.18. Effects of serine and glycine starvation on nucleotides.	74
4.19. Effects of serine and glycine starvation on central carbon metabolism. . . .	76
4.20. Effects of serine and glycine starvation on u- ¹³ C-glucose incorporation. . . .	77
4.21. Transient knockdown of <i>PHGDH</i>	80

4.22. Establishment of <i>PHGDH</i> knockout clones.	81
4.23. Effects of PHGDH inhibitors on proliferation.	83
4.24. Patient-derived neuroblastoma xenograft models.	85
4.25. Effects of PHGDH inhibitors on tumor volume.	86
4.26. Effects of PHGDH inhibitors on <i>de novo</i> serine and glycine synthesis. . . .	87
4.27. Effects of PHGDH inhibitors on nucleotide levels.	88
4.28. Effects of PHGDH inhibitor on central carbon metabolism.	89
4.29. Effects of 5-FU and MTX on proliferation and nucleotide levels.	91
4.30. Effects of 5-FU and MTX treatment on PHGDH and MYCN expression. . .	92
4.31. Effects of glutamine starvation on proliferation.	94
4.32. Effects of glutamine starvation on the expression of apoptotic marker proteins.	96
4.33. Effects of glutamine starvation on <i>de novo</i> serine synthesis.	97
5.1. PHGDH inhibitors target <i>de novo</i> serine synthesis.	101
5.2. Extracellular serine and glycine starvation.	108
5.3. Antifolates target the folate-mediated one-carbon metabolism.	113
B.1. MYCN expression in SH-EP-Tet21/N and SH-SY5Y ^{MYCN}	XII
B.2. Spearman correlation displaying proteins within the central carbon metabolism of primary biopsies from patients with neuroblastoma.	XIII
B.3. Effects of serine and glycine starvation on absolute metabolite quantities. .	XIV
B.4. Effects on proliferation of PHGDH inhibitor application in combination with serine and glycine starvation.	XV
B.5. Effects of PHGDH inhibitors on bodyweight of treated mice.	XVI
B.6. Effects of glutamine starvation on the expression of apoptotic marker proteins.	XVII
B.7. Effects of glutamine starvation on central carbon metabolism intermediates.	XIX

List of Tables

3.1. <i>MYCN</i> status and INSS stage of primary neuroblastoma biopsies.	27
3.2. <i>MYCN</i> score of primary biopsies from patients with neuroblastoma.	27
3.3. <i>MYCN</i> score of neuroblastoma cell lines.	29
3.4. Reverse-transcription PCR mastermix.	34
3.5. qPCR mastermix.	34
3.6. qPCR cyclor program.	35
3.7. ChIP qPCR mastermix.	36
3.8. ChIP qPCR program.	36
3.9. Separation and collection gel for SDS PAGE.	40
3.10. <i>MYCN</i> status and INSS staging of neuroblastoma tumor sections.	41
3.11. GC-MS injection temperature program.	43
3.12. GC temperature program for sample separation.	44
4.1. Top 5 correlating proteins in primary neuroblastoma biopsies.	59
4.2. Top 5 correlating proteins in neuroblastoma cell lines.	59
A.1. Cell culture reagents and chemicals.	I
A.3. Consumables.	IV
A.4. Equipment.	V
A.5. Kits.	VI
A.6. Compounds.	VI
A.7. Enzymes.	VI
A.8. Antibodies.	VII
A.9. Primer sequences for qPCR.	VII
A.10. Primer sequences for ChIP-qPCR.	VII
A.11. GuideRNA sequences for CRISPR-Cas9-mediated <i>PHGDH</i> knockout. . . .	VIII
A.12. Small interfering RNAs.	VIII
A.13. Plasmid.	VIII
A.14. GC-MS masses used for absolute quantification.	VIII
A.15. GC-MS fragments used for determination of stable isotope incorporation. .	IX
A.16. Direct-infusion MS transitions.	X

A.17. Software.	XI
B.1. Literature research on MYCN target genes.	XII

List of Abbreviations

General abbreviations

1C	One-carbon
5-FU	5-Fluorouracile
APS	Ammonium persulfate
AUC	Area under the curve
BSA	Bovine serum albumin
CCM	Central carbon metabolism
cDNA	Complementary DNA
ChIP	Chromatin immunoprecipitation
CO ₂	Carbon dioxide
Ct	Threshold cycle
DMEM	Dulbeccos modified eagle medium
DMSO	Dimethyl sulfoxide
DNA	Deoxyribonucleic acid
DTT	Dithiothreitol
E-boxes	Enhancer boxes
EDTA	Ethylenediaminetetraacetic acid
ETC	Electron transport chain
FACS	Fluorescence activated cell sorting
FAD	Flavin adenine dinucleotide
FCS	Fetal calf serum
GC-MS	Gas chromatography - mass spectrometry
H3K9m3	H3 lysine 9 trimethylation
IgG	Immunglobulin G
IHC	Immunohistochemistry
LC-MS	Liquid chromatography - mass spectrometry
LFQ	Label-free quantification
MeOH	Methanol
MeOx	Methoxamine
mIBG	Metaiodobenzylguanidine
mRNA	Messenger RNA
MS	Mass spectrometry
MSTFA	N-Methyl-N-(trimethylsilyl) trifluoroacetamide
MTX	Methotrexate
NAD	Nicotinamide adenine dinucleotide

OXPHOS Oxidative phosphorylation
P2101 PKUMDL-WQ-2101
PBS Phosphate buffered saline
PCR Polymerase chain reaction
PDX Patient-derived xenograft
pSIRM Pulsed stable isotope-resolved metabolomics
PVDF Polyvinylidene difluoride
qPCR Quantitative real-time PCR
RNA Ribonucleic acid
ROS Reactive oxygen species
RT-PCR Reverse transcription PCR
SD Standard deviation
SDS Sodium dodecyl sulfate
SDS-PAGE SDS polyacrylamide gel electrophoresis
siRNA Small interfering RNA
TCA cycle Tricarboxylic acid cycle
Tet Tetracycline
ToF Time-of-flight
tRNA Transfer RNA
WB Western blot

Metabolites

1,3-BPG 1,3-Biphosphoglycerate
2-PGA 2-Phosphoglycerate
3-PGA 3-Phosphoglycerate
5,10-mTHF 5,10-methyl-tetrahydrofolate
5-mTHF 5-methyl-tetrahydrofolate
α KG α -ketoglutarate
Acetyl-CoA Acetyl coenzyme A
ADP Adenosine diphosphate
Ala Alanine
AMP Adenosine monophosphate
Asp Aspartate
ATP Adenosine 5-triphosphate
cAMP Cyclic adenosine monophosphate
CDP Cytidine diphosphate
Cit Citrate
CMP Cytidine monophosphate
CTP Cytidine triphosphate
dADP Deoxyadenosine diphosphate
dAMP Deoxyadenosine monophosphate
dATP Deoxyadenosine triphosphate
dCDP Deoxycytidine diphosphate
dCMP Deoxycytidine monophosphate
dCTP Deoxycytidine triphosphate
dGDP Deoxyguanosine diphosphate

dGMP Deoxyguanosine monophosphate
dGTP Deoxyguanosine triphosphate
DHAP Dihydroxyacetone phosphate
DHF Dihydrofolate
dTDP Deoxythymidine diphosphate
dTMP Deoxythymidine monophosphate
dTTP Deoxythymidine triphosphate
dUDP Deoxyuridine diphosphate
dUMP Deoxyuridine monophosphate
dUTP Deoxyuridine triphosphate
F6P Fructose-6-phosphate
FBP Fructose-1,6-bisphosphate
FdUMP Fluorodeoxyuridine monophosphate
FdUTP Fluorodeoxyuridine triphosphate
Fum Fumarate
FUTP Fluorouridine triphosphate
G3P Glyceraldehyde-3-phosphate
G6P Glucose-6-phosphate
GDP Guanosine diphosphate
Glc Glucose
Glu Glutamate
Gly Glycine
GMP Guanosine monophosphate
GTP Guanosine triphosphate
IMP Inosine monophosphate
Isocit Isocitrate
Lac Lactate
Leu Leucine
Mal Malate
OAA Oxaloacetate
PEP Phosphoenolpyruvate
pOH-Pyr 3-Phosphohydroxypyruvate
PRPP 5-Phosphoribosepyrophosphate
pSer 3-Phosphoserine
Pyr Pyruvate
Q Glutamine
R5P Ribose-5-phosphate
Ru5P Ribulose-5-phosphate
SAH S-adenosyl-homocysteine
SAM S-adenosyl-methionine
Ser Serine
Suc Succinate
Suc-CoA Succinyl-CoA
THF Tetrahydrofolate
UDP Uridine diphosphate
UMP Uridine monophosphate
UTP Uridine triphosphate

Enzymes

ACO Aconitate hydratase
ALDA Aldolase A
ALK Anaplastic lymphoma receptor tyrosine kinase
ASCT Alanine, serine, cysteine, threonine transporters
ATF4 Activating transcription factor 4
CS Citrate synthase
DHFR Dihydrofolate reductase
eIF2 α Eukaryotic translation initiation factor 2A
ENO Enolase
FH Fumarate hydratase
FPGS Folylpolyglutamate synthetase
GAPDH Glyceraldehyde-3-phosphate dehydrogenase
GCN2 General control nonderepressible 2
GLS Glutaminase
GPI Glucose-6-phosphate isomerase
GPT Glutamate pyruvate transaminase
HIF1 α Hypoxia-inducible factor 1
HK Hexokinase
IDH Isocitrate dehydrogenase
LDH Lactate dehydrogenase
MDH Malate dehydrogenase
MTHF Methylenetetrahydrofolate reductase
MTHFD Methylenetetrahydrofolate dehydrogenase
MTHFD1L Monofunctional tetrahydrofolate synthase
mTOR Mammalian target of rapamycin
mTORC1 Mammalian target of rapamycin complex 1
MTR Methionine synthase
OGDH 2-Oxoglutarate dehydrogenase
PC Pyruvate carboxylase
PFK Phosphofructokinase
PGAM Phosphoglycerate mutase
PGK Phosphoglycerate kinase
PHGDH Phosphoglycerate dehydrogenase
PK Pyruvate kinase
PKM Pyruvate kinase isoenzyme M
PSAT1 Phosphoserine aminotransferase 1
PSPH Phosphoserine phosphatase
RFC Reduced folate carrier
SDH Succinate dehydrogenase
SHMT Serine hydroxymethyl transferase
TERT Telomerase reverse transcriptase
TK Thymidine kinase
TPI Triosephosphate isomerase
TYMS Thymidylate synthase

1 Introduction

1.1. Neuroblastoma

1.1.1. Clinical phenotype

Neuroblastoma is the most common extracranial pediatric solid tumor that arises in the developing sympathetic nervous system. The median age of diagnosis is 18 months, and 90% of tumors arise in children less than ten years of age [London et al., 2005]. Primary tumors can emerge in the adrenal glands or the sympathetic chain; presenting lesions in the neck, chest, abdomen or pelvis. Metastases are found in approximately 50% of patients at diagnosis in the regional lymph nodes, bone marrow, bones, liver or skin. Age at diagnosis is prognostic for clinical outcome. Patients diagnosed under 18 months of age have a better overall survival compared to patients diagnosed greater than 18 months of age [London et al., 2005]. Altogether, less than 5% of all neuroblastoma cases occur in adolescents and adults [Cheung et al., 2012].

1.1.2. Diagnostics

Neuroblastoma tumor biology is elucidated by molecular diagnostics, imaging and histopathology. Laboratory diagnostics include the measurement of catecholamine levels in the urine. In 90% of neuroblastoma patients, increased levels of catecholamine metabolites including homovanillic acid and vanillylmandelic acid can be detected. Preganglionic neurons from the central nervous system connect directly to adrenal medulla cells and stimulate the release of catecholamines. High levels of vanillylmandelic acid is associated with favorable biological features whereas patients with normal homovanillic acid levels have a significant better outcome [Strenger et al., 2007]. Further laboratory diagnostics comprise the determination of complete blood and platelet counts, prothrombin times, electrolytes, creatinine and uric acid levels and liver function, as well as ferritin and lactate dehydrogenase levels [Matthay et al., 2016]. Diagnostic imaging includes ultrasonography, computed tomography scans or magnetic resonance imaging. About 90% of neuroblastoma tumors express the noradrenaline transporter that transfers metaiodobenzylguanidine (mIBG) into the cells. By applying radiolabelled mIBG, local and metastatic tissue and bone marrow is assessed [Matthay et al., 2016]. In histopathology, neuroblastoma cells present as

small round blue cells with varying signs of immaturity [Shimada et al., 2001]. Histological analysis of tumor biopsies are used to determine the content of stromal Schwannian cells, the grade of morphological differentiation of the tumor and the mitotic-karyorrhexis index [Matthay et al., 2016]. All three factors go into the Shimada histology-grading system that helps to stratify patients into risk-groups [Shimada et al., 2000].

1.1.3. Tumor biology

Even though the clinical course of neuroblastoma is very heterogeneous, ranging from high-risk disease to spontaneous regression, the mutational burden of tumors is rather low [Pugh et al., 2013]. The majority of high-risk neuroblastomas show genetic alterations in *MYCN*, *TERT* or *ATRX* [Hertwig et al., 2016].

The oncogene *MYCN*

MYCN amplification occurs in about 22% of all neuroblastoma cases and was first described in 1983 [Schwab et al., 1983]. Amplified *MYCN* is diagnosed by fluorescent *in situ* hybridization or quantitative real-time PCR. More than a fourfold increase in the *MYCN* signal relative to chromosome 2 or greater equal ten copies for diploid genomes is considered as an amplification of the *MYCN* oncogene [Ambros et al., 2009]. In case of a *MYCN* amplification, a large region from chromosome 2p24 becomes amplified and *MYCN* is found in double-minute chromatin bodies or as homogenously staining regions [Corvi et al., 1994; Schwab et al., 1984]. *MYCN* is a transcription factor controlling various cellular processes. Thiele and colleagues showed decreased *MYCN* expression upon retinoic acid induced differentiation resulting in cell-cycle changes and morphological differentiation *in vitro* [Thiele et al., 1985]. In the same year, Seeger and colleagues observed a close relation between *MYCN* amplification and neuroblastoma disease progression in 89 patients with untreated primary neuroblastoma [Seeger et al., 1985]. Subsequently *MYCN* became the first molecular marker used for risk stratification in neuroblastoma patients.

The chromatin remodeling gene *ATRX*

Point mutations and in-frame deletions in the chromatin remodeling gene *ATRX* are among the most common lesions in sporadic high-risk neuroblastomas [Pugh et al., 2013; Molenaar et al., 2012]. *ATRX* mutations and *MYCN* amplifications are mutually exclusive in neuroblastoma cell lines and tumors and are associated with the activation of the alternative lengthening of telomeres pathway [Zeineldin et al., 2018; Hertwig et al., 2016]. It is a telomerase-independent pathway to maintain telomeres, essential for genomic stability and sustained survival, in highly proliferating cells [Zhang et al., 2019].

The telomerase reverse transcriptase gene *TERT*

Peifer and colleagues discovered recurrent genomic rearrangements proximal to the telomerase reverse transcriptase gene (*TERT*) in those tumors harboring no *MYCN* amplifications and no *ATRX* mutations. These genomic rearrangements induce a transcriptional upregulation of the *TERT* gene resulting in telomere maintenance beneficial for tumor cell survival [Peifer et al., 2015].

The predisposition genes *ALK* and *PHOX2B*

In sporadic neuroblastoma, mutations of the anaplastic lymphoma receptor tyrosine kinase gene (*ALK*) are detected in about 7 - 8% of all cases and *ALK* gene amplifications are found in 3 - 4% [Carpenter and Mossé, 2012]. The most frequent *ALK* mutations include F1174L and R1275Q. They induce the autophosphorylation of the tyrosine kinase domain and the activation of the *ALK* receptor, which pushes neuroblastoma cells into a proliferative phenotype [Carpenter and Mossé, 2012; Matthay et al., 2012]. Heritable mutations in *ALK* and in the paired-like homeobox 2b gene (*PHOX2B*) are the only known mutations to date associated with familial neuroblastoma that accounts for less than 2% of all neuroblastoma [Maris et al., 2002]. Half of familial neuroblastoma cases are associated with germline mutations in *ALK* [Mossé et al., 2008]. *PHOX2B* was the first lost-of-function mutation identified in familial neuroblastoma. It encodes for a transcription factor that promotes cell cycle exit, neuronal differentiation and is involved in the development of neural crest-derived autonomic neurons [Trochet et al., 2005; Raabe et al., 2008; Stovroff et al., 1995].

Chromosomal aberrations

Flow cytometry and single-nucleotide polymorphism arrays were used to assess DNA copy-number aberrations of neuroblastoma tumors [Ambros et al., 2014]. Gains or losses of entire chromosomes, described as numerical chromosomal alterations, are associated with a favorable disease outcome [Cunsolo et al., 2000]. Segmental rearrangements including losses of chromosome arm 1p [Ambros et al., 1996] or 11q [Vandesompele et al., 2005] or gain of chromosome arm 17q [Bown et al., 1999] are markers of poor prognosis.

1.1.4. Risk stratification and treatment**Staging system**

The most widely used staging system for neuroblastoma is the International Neuroblastoma Staging System (INSS). It classifies neuroblastoma tumors into six different stages (stage 1, 2a, 2b, 3, 4 and 4s). The patients outcome is predicted based on the INSS staging, the age of the patient at diagnosis and the site of the primary tumor. The two-year disease free survival of patients with stage 1, 2, or 4s is 80 - 90%. In contrast, patients with stage 3 and 4 have a survival probability of 40 - 50%. Generally, the outcome

of infants less than one year of age is better compared to older patients with the same stage of the disease [Brodeur, 2003]. Patients with 4s staging might undergo spontaneous differentiation leading to regression of the disease without treatment. In order to compare clinical trials conducted by different groups internationally, homogenous pretreatment risk groups were defined. The INSS staging system is based on the extent of surgical resection at diagnosis and metastases and not suitable for pretreatment risk classification. Therefore, the International Neuroblastoma Risk Group (INRG) classification system was developed as a new clinical staging system to stage tumors ahead of any treatment to the stages L1, L2, M or MS [Monclair et al., 2009]. Neuroblastoma risk groups (low-risk, intermediate-risk, high-risk) are classified based on clinical and biological features, including *MYCN* copy numbers, tumor histopathology and ploidy, patient age and INSS staging.

Treatment

Treatment of neuroblastoma patients depends strongly on their risk stratification. In Germany, first line treatment guidelines for patients with neuroblastoma are published by the Society for Pediatric Oncology and Hematology [Simon et al., 2017].

Excellent treatment outcomes can be achieved by surgery alone in the low-risk tumors including patients with stage 1, stage 2, stage 4s neuroblastoma in infants less than one year of age without any molecular risk factors [Schilling et al., 2002]. In Germany, *MYCN* non-amplified stage 3 tumors are also stratified as low-risk [Hero et al., 2008]. Nevertheless, surgery alone is not sufficient in all low-risk tumor cases. In case children present or develop threatening symptoms, chemotherapy treatment is needed. To date, radiotherapy treatment is avoided in low-risk tumors [Tonini et al., 2012].

Intermediate-risk tumors include patients with stage 4 neuroblastoma below the age of 18 months and with stage 3 over the age of two years. All patients receive chemotherapy at reduced intensity [Tonini et al., 2012].

High-risk tumors include patients with *MYCN*-amplified neuroblastoma of all INSS stages or with metastatic stage 4 disease over the age of 18 months independent of the *MYCN* status. Treatment in high-risk tumors is divided into three treatment modules (induction, consolidation, maintenance) that encompass 1.5 - 2 years of total treatment time. A neoadjuvant polychemotherapy regimen including vincristine, vindesine, etoposide, cisplatin, dacarbazine, doxorubicin, ifosfamide is administered for the induction of remission (6 - 9 months). Induction therapy aims at reducing the initial tumor burden by shrinking the primary tumor and reducing the load of metastases followed by surgical resection of the primary tumor. Consolidation therapy includes myeloablative chemotherapy supported by autologous hematopoietic stem-cell transplantation. Maintenance therapy, to eradicate minimal residual disease, is based on an anti-GD2 monoclonal antibody and cytokine immunotherapy in addition to differentiating therapy with isotretinoin [Park et al., 2013]. GD2, an acidic glycolipid, is presented on the surfaces of neuroblastoma cells

with an estimated 5 - 10 million molecules/cell [Wu et al., 1986], providing a target for immunotherapeutic approaches.

Most high-risk neuroblastomas initially respond to the therapy regimen and patients achieve complete remission even though 50 - 60% of tumors eventually relapse [Maris, 2010]. Patients with relapsed neuroblastoma have a four-year overall survival rate of approximately 20% [London et al., 2017]. There have been improvements in achieving a second partial or complete remission by application of chemotherapy combinations, e.g. topotecan with cyclophosphamide, irinotecan with temozolomide or topotecan with temozolomide [Bagatell et al., 2011; London et al., 2010; Di Giannatale et al., 2014; Kushner et al., 2006]. Iodine-131 radiolabelled mIBG therapy has a 27% response rate in refractory and relapsed neuroblastoma [Zhou et al., 2015]. Chemotherapy combined with molecular targeted therapy is also under investigation. The ALK inhibitor crizotinib is currently tested in clinical trials with high-risk neuroblastoma [Trigg and Turner, 2018]. Second and third generation ALK inhibitors are also evaluated for their safety and efficacy alone or in combination with chemotherapy in patients with neuroblastoma and other ALK-driven cancers [Trigg and Turner, 2018]. Aurora-A kinase forms a complex with MYCN and thereby protects MYCN from proteasomal degradation [Brockmann et al., 2013]. Aurora-A-selective inhibitors, such as alisertib, induce a conformation change of Aurora-A which is not compatible with the binding of MYCN and resulting in destabilized MYCN protein [Richards et al., 2016]. However, a clinical phase II study in pediatric patients with refractory or recurrent solid tumors or acute leukemia showed response rates to alisertib of less than 5% [Mosse et al., 2019]. Inhibition of MYCN with an extra-terminal motif (BET) bromodomain inhibitor (BMS-986158) is currently tested in a clinical trial with relapsed or refractory solid tumors and lymphoma in pediatric patients [ClinicalTrials.gov Identifier: NCT03936465]. T-cells engineered to express chimeric antigen receptors targeting GD2 and L1-CAM (CD171) are under investigation in clinical trials for relapsed or refractory neuroblastoma [Richards et al., 2018].

Treatment related long-term effects

Nearly all high-risk neuroblastoma patients experience treatment-associated acute toxicity, including severe transient myelosuppression, chemotherapy-induced renal dysfunction and poor weight gain [Matthay et al., 2016]. Studies of long-term survivors report a high prevalence for secondary malignancies [Applebaum et al., 2015], and late effects including growth hormone deficiency, dental problems, osteochondromas, hearing deficiencies, diabetes, hypothyroidism, ovarian insufficiency in women and azoospermia or oligospermia in men [Hobbie et al., 2008; Cohen et al., 2014].

Even though a lot of improvements in patient care and treatment have been achieved over the last years through the introduction of myeloablative chemotherapy with autologous haematopoietic stem-cell transplantation and GD2 antibody treatment for maintenance

therapy, we still face the urgent need for new therapeutic drug approaches for high-risk neuroblastomas. Elucidating the underlying metabolic network of neuroblastoma might enable us to identify pathways that can be exploited for therapeutic use in patients suffering from high-risk disease.

1.2. Metabolism in tumor cells

Tumor cells encompass a high level of complexity, which was specified by Hanahan and Weinberg in 2000. They defined six biological features acquired by human cells to transform from a normal cell into a cancer cell. These hallmarks of cancer include sustained angiogenesis, resistance to apoptosis, insensitivity to anti-growth signals, activation of invasion and metastasis, replicative immortality, and sustained proliferative signaling [Hanahan and Weinberg, 2000]. In 2011, Hanahan and Weinberg further expanded the hallmarks of cancer by two enabling characteristics, genome instability and mutation and tumor-promoting inflammation, as well as by two features, avoiding immune destruction and major reprogramming of energy metabolism [Hanahan and Weinberg, 2011]. Metabolic reprogramming is required by tumor cells to sustain accelerated cell growth and proliferation. One of the most frequent metabolic rewiring observed in cancer cells is the prevalence of aerobic glycolysis over oxidative phosphorylation, known as the Warburg effect [Warburg, 1924; Warburg et al., 1927]. Aerobic glycolysis is an inefficient way to produce energy carriers like adenosine 5-triphosphate (ATP), as two ATPs per molecule of glucose are produced through aerobic glycolysis and up to 36 ATPs per molecule glucose by oxidative phosphorylation [Lehninger et al., 1993]. Nonproliferative and differentiated cells meet their energetic demands via the production of ATP to maintain cellular processes [Vander Heiden et al., 2009]. Proliferative cells require additionally the construction of building blocks for cellular components, including proteins, lipids and nucleotides, and the maintenance of cellular redox balance and epigenetic status [Locasale, 2013]. Glucose and glutamine are two major metabolites used by cancer cells to meet their metabolic requirements.

1.2.1. Glucose metabolism

The metabolism of glucose is the primary source of energy generation within mammalian cells. One molecule of glucose is converted into two molecules of pyruvate, two molecules of ATP and two molecules of NADH in an oxygen-independent manner in a ten step reaction process, termed glycolysis (figure 1.1). As summarized in [Alberts et al., 2004], glucose is phosphorylated by hexokinase into glucose-6-phosphate under the consumption of one ATP molecule. The phosphorylation is irreversible and keeps glucose-6-phosphate within the cell. Glucose-6-phosphate is converted into ribose-5-phosphate that fuels the pentose phosphate pathway and is a precursor for nucleotide synthesis. Glucose-6-phosphate is also converted by isomerization into fructose-6-phosphate. The phosphofructokinase converts fructose-6-phosphate in an irreversible reaction into fructose-1,6-bisphosphate, thereby consuming one molecule of ATP. Fructose-1,6-bisphosphate is cleaved into two three-carbon molecules: Glyceraldehyde 3-phosphate and dihydroxyacetone phosphate, the latter one is also isomerized into glyceraldehyde 3-phosphate. The conversion of glyceraldehyde 3-phosphate into 3-phosphoglycerate (3-PGA) generates two molecules of

NADH and two molecules of ATP per invested molecule of glucose. 3-PGA can either enter the serine synthesis pathway via phosphoglycerate dehydrogenase (PHGDH) or remains in glycolysis as a precursor for phosphoenolpyruvate generation. In the last step of glycolysis, phosphoenolpyruvate is converted into pyruvate under ATP production [Alberts et al., 2004]. Pyruvate is either reduced to lactate, converted into alanine in the cytosol or it enters the mitochondria and is oxidized. Reduction of pyruvate into lactate and NAD is catalyzed by the lactate dehydrogenase A. Lactate is transported to the extracellular space and NAD is used to replenish the glycolysis [Alberts et al., 2004]. Under hypoxic conditions, lactate is imported through monocarboxylate transporters and converted into pyruvate by lactate dehydrogenase B. The pyruvate carboxylase converts pyruvate into oxaloacetate, an intermediate of the TCA cycle [Corbet and Feron, 2017]. Pyruvate further supports anaplerosis through decarboxylation by the pyruvate dehydrogenase complex into acetyl coenzyme A (acetyl-CoA), NADH and CO_2 . Acetyl-CoA, providing two carbon groups, binds to oxaloacetate, providing four carbon groups, to generate citrate. The six carbon atoms of citrate are sequentially oxidized yielding three molecules of NADH, two molecules CO_2 , one molecule GTP and one molecule FADH_2 . The eight enzymatic reactions within the TCA cycle further produce and consume isocitrate, α -ketoglutarate, succinate, fumarate and malate. At the end, oxaloacetate is generated, which binds to a new molecule of acetyl-CoA. The reduced electron carriers NADH and FADH_2 are oxidized by the electron transport chain, which spans through the inner-mitochondrial membrane. The electrons are transferred by four complexes of the ETC from electron donors to electron acceptors and thereby generate a proton potential that drives the phosphorylation of ADP with anorganic phosphate to produce ATP. In this process, called oxidative phosphorylation, one molecule of glucose is generated to 36 molecules of ATP [Alberts et al., 2004]. Thus, converting glucose in the TCA cycle coupled to oxidative phosphorylation is highly efficient to generate energy.

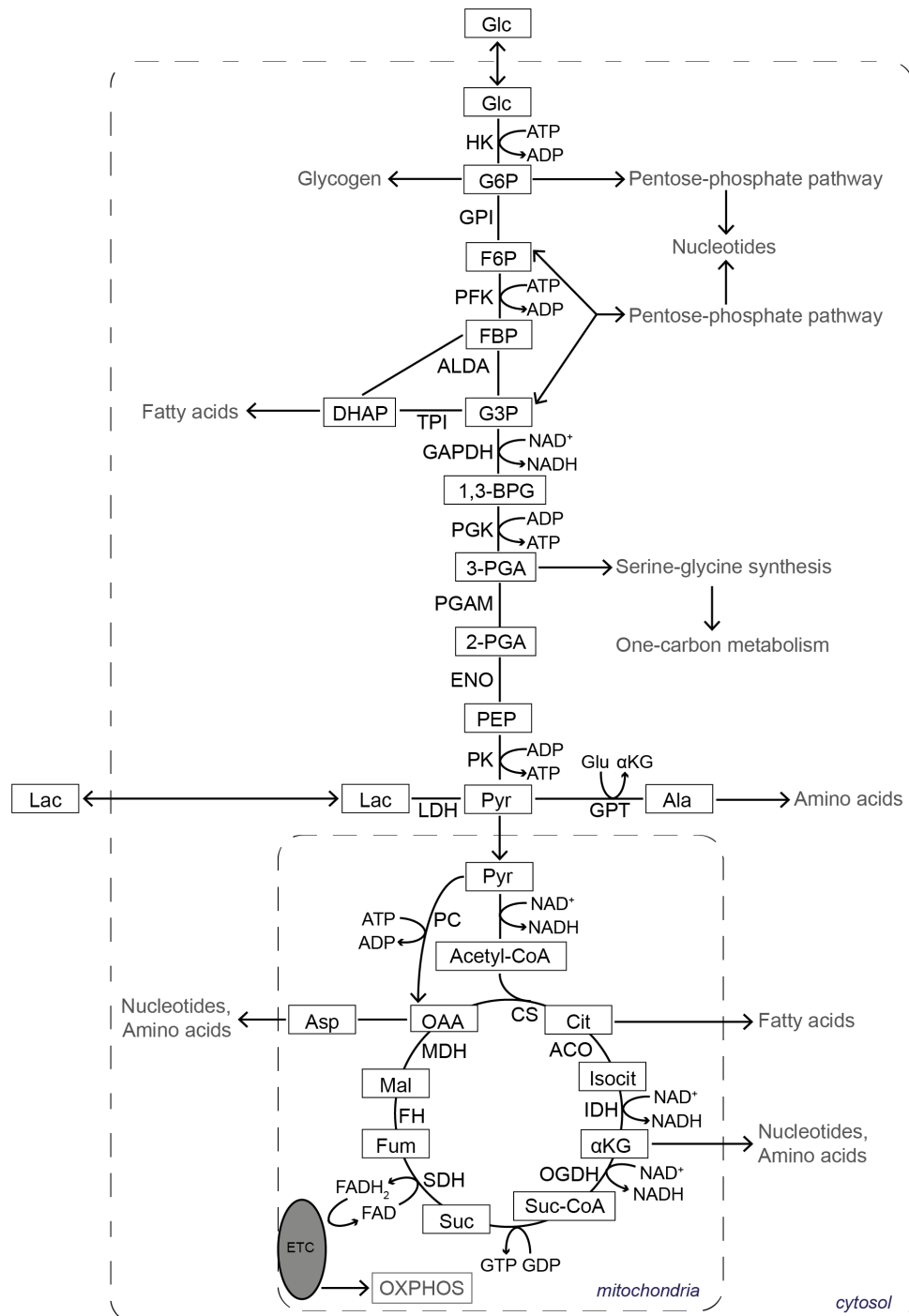


Figure 1.1.: Glycolysis and TCA cycle within the central carbon metabolism. The central carbon metabolism converts glucose and glutamine into metabolic precursors to generate building blocks (nucleotides, lipids, amino acids) for cellular components. Abbreviations: 1,3-BPG - 1,3-Bisphosphoglycerate, 2-PGA - 2-Phosphoglycerate, 3-PGA - 3-Phosphoglycerate, α KG - α -ketoglutarate, Ala - Alanine, Asp - Aspartate, Cit - Citrate, DHAP - Dihydroxyacetone phosphate, F6P - Fructose-6-phosphate, FBP - Fructose-1,6-bisphosphate, Fum - Fumarate, G3P - Glyceraldehyde 3-phosphate, G6P - Glucose-6-phosphate, Glc - Glucose, Glu - Glutamate, HK - Hexokinase, Isocit - Isocitrate, Lac - Lactate, Mal - Malate, OAA - Oxaloacetate, PEP - Phosphoenolpyruvate, Pyr - Pyruvate, Suc - Succinate, Suc-CoA - Succinyl-CoA, ACO - Aconitase, ALDA - Aldolase, CS - Citrate synthase, ENO - Enolase, FH - Fumarate hydratase, GAPDH - Glyceraldehyde-3-phosphate dehydrogenase, GPI - Glucose-6-phosphate isomerase, GPT - Glutamate pyruvate transaminase, IDH - Isocitrate dehydrogenase, LDH - Lactate dehydrogenase, MDH - Malate dehydrogenase, OGDH - 2-Oxoglutarate dehydrogenase, PC - Pyruvate carboxylase, PFK - Phosphofructokinase, PGAM - Phosphoglycerate mutase, PGK - Phosphoglycerate kinase, PK - Pyruvate kinase, SDH - Succinate dehydrogenase, TPI - Triosephosphate isomerase, ETC - electron transport chain, OXPHOS - oxidative phosphorylation. Figure based on [Alberts et al., 2004] with modifications.

1.2.2. Glutamine metabolism

Glutamine is a highly abundant non-essential amino acid. The majority of glutamine is absorbed from digested foods through the small intestine. Many transporters including the solute carrier family 1 member 5 (ASCT2) are transporting glutamine into the cell. Skeletal muscle, lung and adipose tissue can synthesize glutamine *de novo*. Glutamine is a carbon and nitrogen donor in mammalian cells. The nitrogen contributes to nucleotide and amino acid biosynthesis and the carbon backbone of glutamine fuels the TCA cycle. Both, nitrogen and carbon groups, contribute to glutathione biosynthesis and maintenance of redox homeostasis. Transaminases convert glutamine into glutamate. Glutamate can further be converted into proline and functions as a nitrogen donor in the generation of alanine, aspartate and serine [Altman et al., 2016]. Serine is processed into glycine as part of the one-carbon metabolism that is frequently deregulated in cancer cells [Ducker and Rabinowitz, 2016]. The generation of amino acids and precursors, which contribute to the majority of biomass accumulation [Hosios et al., 2016], triggers a glutamine dependency in a broad range of cancer cells [Amoêdo et al., 2013]. The carbon backbone of glutamine enters the TCA cycle via α -ketoglutarate that is converted from glutamate. Oxidation of the carbon groups generates bioenergetic NADH and FADH₂ equivalents that can either be used for redox balance maintenance or for ATP production in the electron transport chain. Glutamine-derived α -ketoglutarate can be converted into citrate via reductive carboxylation. Citrate is exported to the cytosol and converted into acetyl-CoA, a precursor for fatty acid and cholesterol biosynthesis [Zhang et al., 2017]. Additional biosynthetic precursors, generated in the TCA cycle and exported into the cytoplasm, include oxaloacetate and malate. Oxaloacetate is converted into aspartate supporting nucleotide synthesis. Malate is used as a precursor for pyruvate and NADPH generation [Altman et al., 2016]. The TCA cycle is supported by several anaplerotic reactions in order to meet the high demand of energy production and biosynthetic precursor generation. The oxidation of fatty acids into acetyl-CoA and reducing equivalents fuels the TCA cycle and supports oxidative phosphorylation. Glutamine and aspartate enter the TCA cycle through α -ketoglutarate and oxaloacetate, respectively [Corbet and Feron, 2017].

1.2.3. *De novo* serine & glycine synthesis

Serine is one of the major donors of one-carbon units in mammalian cells making serine availability crucial [Yang and Vousden, 2016]. It is also a precursor for the amino acids glycine and cysteine, necessary for the production of sphingolipids and furthermore serves as a headgroup or headgroup precursor for phospholipids [Mattaini et al., 2016]. Serine can either be imported by amino acid transporters from the extracellular space into the cell or is synthesized *de novo* (figure 1.2). The serine-glycine pathway is essential to convert the non-essential amino acids serine and glycine from glucose. PHGDH catalyzes

3-PGA into 3-phosphohydroxypyruvate (pOH-Pyr), a precursor of *de novo* serine synthesis. The subsequent enzymes phosphoserine aminotransferase (PSAT1) and phosphoserine phosphatase (PSPH) convert pOH-Pyr into serine by transamination and phosphate ester hydrolysis, respectively [Locasale, 2013]. PSAT1 also uses pOH-Pyr as a substrate to convert glutamate into α -ketoglutarate, an intermediate of the TCA cycle. Serine can be catabolized directly into pyruvate or via 3-hydroxypyruvate into glycerate thereby converting pyruvate into alanine [Mattaini et al., 2016]. Serine hydroxymethyl transferases (SHMT) convert serine into glycine. Glycine can be incorporated into purine nucleotide bases and glutathione and serves as a precursor for porphyrines [Mattaini et al., 2016]. It is also incorporated as an amino acid into protein synthesis and supports the methylation of DNA and histones [Amelio et al., 2014]. Glycine can be cleaved in the mitochondria by the glycine cleavage system. The oxidative cleavage of glycine produces CO_2 , ammonium, and a methylene group. The latter is used to form 5,10-mTHF which fuels into the folate cycle [Kikuchi et al., 2008].

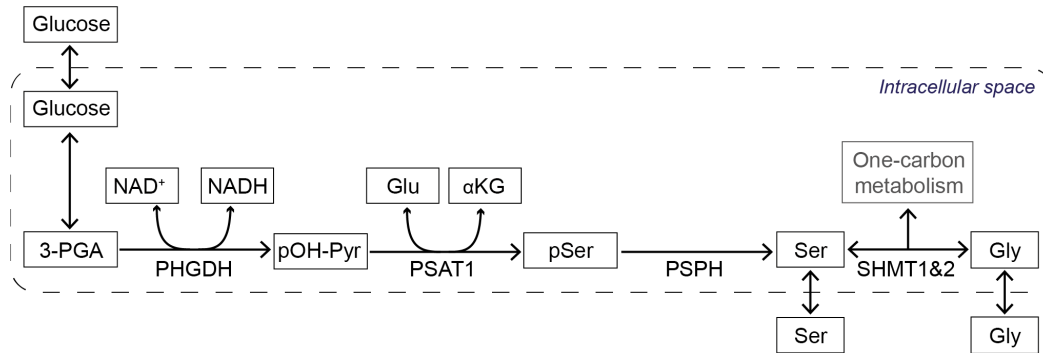


Figure 1.2.: Scheme of the *de novo* serine and glycine synthesis and linkage to one-carbon metabolism. Cells can either transport serine and glycine by transporters to the intracellular space or they produce serine and glycine *de novo*. *De novo* serine production derives from the glycolytic intermediate 3-Phosphoglycerate. Serine is converted into glycine by serine hydroxymethyltransferases in the cytosol and the mitochondria and provides one-carbon units to fuel the folate cycle. Abbreviations: 3-PGA - 3-Phosphoglycerate, Gly - Glycine, Ser - Serine, pOH-Pyr - 3-Phosphohydroxypyruvate, pSer - 3-Phosphoserine, PHGDH - Phosphoglycerate dehydrogenase, PSAT1 - Phosphoserine aminotransferase 1, PSPH - Phosphoserine phosphatase, SHMT1&2 - Serine hydroxymethyl transferase. Figure adapted from [Yang and Vousden, 2016].

1.2.3.1. Regulation of *de novo* serine and glycine synthesis in cancer

Several factors regulate the expression of serine synthesis genes and proteins in cancer cells. c-MYC, a major oncogene, transcriptionally activates the expression of *PHGDH*, *PSAT1* and *PSPH* in hepatocellular carcinoma cells *in vitro* [Sun et al., 2015]. The receptor tyrosine kinase HER2 activates *PHGDH* gene expression in breast epithelial cells [Bollig-Fischer et al., 2011]. The transcription factors Specificity Protein 1 and Nuclear Transcription Factor Y positively regulate the promoter activity of *PHGDH* [Jun et al., 2008]. Activating transcription factor 4 (ATF4)-mediated nuclear factor erythroid 2-related

factor 2 regulation of *PHGDH*, *PSAT1* and *SHMT2* expression supports glutathione and nucleotide production in non-small cell lung cancer [DeNicola et al., 2015]. Under serine starvation, ATF4 promotes the expression of serine synthesis genes by the histone lysine-specific demethylase 4C [Zhao et al., 2016] and the E3 ubiquitin ligase MDM2 [Riscal et al., 2016]. *PHGDH*, *PSAT1*, *PSPH* and *SHMT2* are further regulated by the histone H3 lysine methyltransferase G9A in response to serine deprivation [Ding et al., 2013]. The *de novo* serine synthesis pathway and glycolysis closely interact to maintain sufficient intracellular serine levels. Pyruvate kinase M2 (PKM2) is one of the four existing isoforms of the pyruvate kinase in mammalian cells. It catalyzes the final step of glycolysis, converting phosphoenolpyruvate to pyruvate and one molecule of ATP and is frequently overexpressed in cancer cells [Chaneton et al., 2012]. Under low intracellular serine levels, PKM2 activity is decreased resulting in an accumulation of glycolytic intermediates used to fuel the serine synthesis pathway. At the same time, low intracellular serine levels activate general control nonderepressible 2 (GCN2) kinase leading to subsequently enhanced ATF4 translation and increased expression of serine synthesis genes [Chaneton et al., 2012]. The serine synthesis pathway contributes to the mammalian target of rapamycin complex 1 (mTORC1) activity, enabling stable PKM2-expressing human lung carcinoma cells to proliferate in serine depleted conditions [Ye et al., 2012]. Small molecules inhibiting *PHGDH* activity have shown anti-tumoral effects *in vitro* and *in vivo*. The non-competitive *PHGDH* inhibitor CBR5884 blocks *de novo* serine synthesis and cell growth *in vitro* [Mullarky et al., 2016]. The small molecule inhibitor NCT503 reduces glucose-derived serine pools in breast cancer cells and suppresses cell growth of various cancer cell lines and in mice carrying a breast cancer xenograft [Pacold et al., 2016]. The allosteric inhibitor P2101 inhibits *de novo* serine synthesis in ovarian cancer cells and reduces cell growth of breast cancer cells *in vitro* and *in vivo* [Wang et al., 2017]. To date, none of the *PHGDH* inhibitors has entered clinical trials.

1.2.4. One-carbon metabolism

Cancer growth and proliferation is highly supported by changes in one-carbon metabolism [Ducker et al., 2017]. The one-carbon metabolism consists of the folate and the methionine cycles that are interconnected by 5-methyl-tetrahydrofolate [Reina-Campos et al., 2019]. Carbon units enter the one-carbon metabolism in the form of amino acids and are distributed by a series of chemical reactions, thereby supporting biosynthetic processes and the catabolism of nutrients [Locasale, 2013]. The one-carbon metabolism plays a central role in nucleic acid synthesis, amino acid homeostasis (serine, glycine, methionine, cysteine), epigenetic regulation and redox maintenance [Ducker and Rabinowitz, 2016].

1.2.4.1. Folate cycle

Humans require the dietary intake of folates to fuel the one-carbon metabolism. Folic acid, known as vitamin B9, is taken up as a food additive in western diets [Locasale, 2013]. Insufficient supply of folic acid can induce anemia. In the developing fetus it increases the incidence of neural tube defects resulting in failure of neural tube closure [Copp et al., 2015]. In order to enter the folate cycle, folic acid is sequentially reduced to dihydrofolate (DHF) and tetrahydrofolate (THF). THF can bind an one-carbon unit and interconvert it between different oxidation states including 5,10-methyl-tetrahydrofolate (5,10-mTHF), 5-methyl-tetrahydrofolate (5-mTHF), 10-formyl-tetrahydrofolate (10-formyl-THF) and 5-formyl-tetrahydrofolate (5-formyl-THF). Each THF oxidation state supports distinct biosynthetic functions except for 5-formyl-THF that serves as a one-carbon unit reserve [Ducker and Rabinowitz, 2016].

Increased flow of serine through the folate cycle promotes nucleotides synthesis, increases NADH and ATP production and provides increased capacity for mitochondrial NADPH production to limit reactive oxygen species (ROS) in cancer cells [Yang and Vousden, 2016]. The folate metabolism is compartmentalized into the mitochondria and the cytosol, each expressing different isoenzymes (figure 1.3). THF is the only folate that can be actively transported across the cell membrane by anionic reduced folate transporters, including RFC encoded by *SLC19A1* [Ducker and Rabinowitz, 2016]. Impaired RFC transport provides a mechanism of resistance to the anti-folate drug methotrexate (MTX) in leukemic cells [Liani et al., 2003]. The folypolyglutamate synthase catalyzes the ATP-dependent addition of glutamate moieties to folate and folate derivatives. These polyglutamated folates reduce their affinity for the folate transporters and enhance their affinity for folate enzymes [Kim et al., 1996]. Folypolyglutamate synthase has therefore a central role in maintaining folate homeostasis essential for cell proliferation [NCBI FPGS(human) GeneID: 2356, 18.11.2019]. As polyglutamated folates cannot pass the intracellular membrane, THF and serine are synthesized into 5,10-mTHF and glycine in both compartments, the mitochondria via SHMT2 and the cytosol via SHMT1.

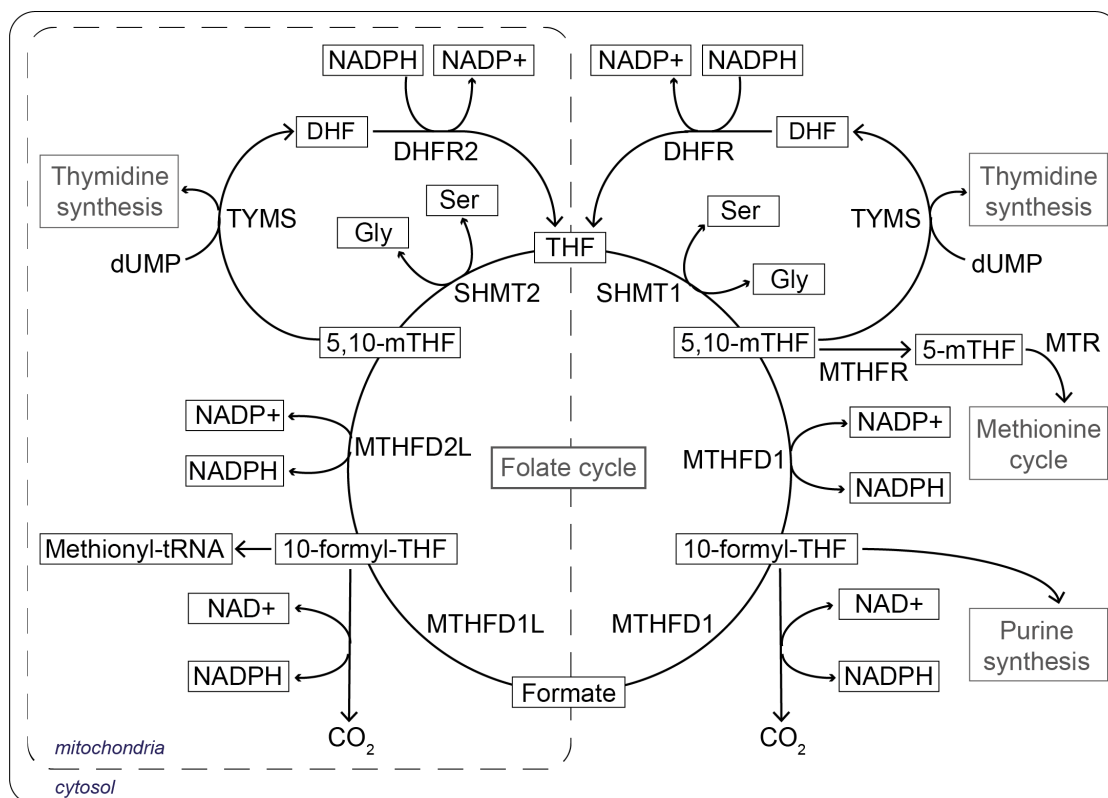


Figure 1.3.: Compartmentalization, inputs and outputs of folate metabolism. The folate cycle activates and transfers one-carbon units which are used as precursors for biosynthetic processes. The folate cycle is compartmentalized into the cytosol and the mitochondria. Tetrahydrofolate and formate can be actively transported through the mitochondrial membrane. Abbreviations: Gly - Glycine, Ser - Serine, THF - Tetrahydrofolate, DHFR - Dihydrofolate reductase, DHFR2 - Dihydrofolate reductase 2, MTHF - Methylene tetrahydrofolate reductase, MTHFD1 - Methylene tetrahydrofolate dehydrogenase 1, MTHFD1L - Monofunctional tetrahydrofolate synthase, MTHFD2L - Methylene tetrahydrofolate dehydrogenase 2, MTR - Methionine synthase, SHMT1&2 - Serine hydroxymethyltransferase, TYMS - Thymidylate synthetase. Figure adapted from [Ducker and Rabinowitz, 2016].

The THF-bound one-carbon pool is fueled by serine, formate and histidine in the cytosol and by serine, glycine, sarcosine and dimethylglycine in the mitochondria [Ducker and Rabinowitz, 2016]. Products generated within the folate cycle include methionine, thymidine, serine, glycine, purines, formate and CO_2 . Additionally, the majority of reactions within the folate metabolism produce and consume redox equivalents, including NADPH and NADP. 5,10-mTHF is a precursor for serine and thymidine synthesis and for remethylation of homocysteine into methionine (figure 1.3). The thymidylate synthase (TYMS) converts 5,10-mTHF and deoxyuridine monophosphate (dUMP) to DHF and deoxythymidine monophosphate (dTMP) required for thymidine production. DHF is reduced by the dihydrofolate reductase (DHFR) back into THF which binds one-carbon units. An average of one molecule of 5,10-mTHF is required for the production of four DNA bases. SHMT also uses 5,10-mTHF to convert glycine into serine and THF. This reaction is also reversible [Ducker and Rabinowitz, 2016]. 5,10-mTHF can be reduced to 5-mTHF by the methylene tetrahydrofolate reductase that is used by the methionine synthase

to convert homocysteine into methionine and THF. In mammals, methionine can also be produced using trimethylglycine from the choline degradation in a folate-independent manner [Ducker and Rabinowitz, 2016]. THF and formate are catalyzed by the formate-tetrahydrofolate ligase into 10-formyl-THF in an ATP-dependent reaction. 10-formyl-THF is essential for *de novo* purine synthesis. An average of one 10-formyl-THF molecule is required for the synthesis of one RNA or DNA base. The mitochondrial methionyl-tRNA formyltransferase uses 10-formyl-THF for formylation of methionyl tRNAs, essential for the translation of mitochondrial encoded proteins. In an ATP producing reaction, 10-formyl-THF is hydrolyzed to formate. Formate can be transferred between the cytosol and the mitochondria, thereby enabling the exchange of one carbon units between the compartments. Full oxidation of 10-formyl-THF bound one-carbon units results in terminal elimination and NADPH production [Ducker and Rabinowitz, 2016]. Altogether, folates are required for various cellular processes including the methionine cycle, nucleotide biosynthesis, redox balance maintenance, amino acid synthesis and protein translation.

1.2.4.2. Regulation of the folate cycle in cancer

In cancer, some enzymes of the one-carbon metabolism are consistently overexpressed, including DHFR, TYMS, SHMT2 and methylenetetrahydrofolate dehydrogenase 2 (MTHFD2) [Longley et al., 2003] [Jain et al., 2012] [Nilsson et al., 2014a]. MTHFD2 expression is transcriptionally regulated by mTORC1 via ATF4 and independent of eukaryotic initiation factor 2 α (eIF2 α) phosphorylation [Ben-Sahra et al., 2016]. High MTHFD2 expression is also associated with activating mutations in KRAS in non-small cell lung cancer [Moran et al., 2014]. AMP-activated protein kinase is a key sensor of metabolic stress and activates the PPAR γ co-activator 1 α and the oestrogen-related receptor α in breast cancer cells. Both negatively regulate the expression of methylenetetrahydrofolate dehydrogenase 1, monofunctional tetrahydrofolate synthase and MTHFD2 resulting in perturbed purine synthesis and an increased sensitivity to antifolate drugs [Audet-Walsh et al., 2016].

Folate analogs interact with a wide range of enzymes within the folate cycle resulting in decreased cell proliferation. The first antifolate, aminopterin, was discovered by Sydney Farber and colleagues in 1948. It induced temporary remission in children with acute lymphoblastic leukemia [Faber et al., 1948]. Subsequently, antifolate molecules including MTX, pemetrexed and pralatrexate were discovered, that target different enzymes within the folate cycle and disrupt the one-carbon metabolism. 5-Fluorouracil (5-FU) and gemcitabine are purine antimetabolites downstream of the one-carbon metabolism that are also described to disrupt nucleotide synthesis. 5-FU targets the enzyme TYMS and is incorporated into the RNA as it functions as an analog to the nucleobase uracil [Amelio et al., 2014; Ducker and Rabinowitz, 2016]. Gemcitabine is catalyzed to its active form gemcitabine-triphosphate which is incorporated into the DNA and RNA [Rizzuto et al., 2017]. Anti-folate therapy in cancers also causes toxicity in non-transformed cells. Most

frequent side-effects include gastric complications, fatigue, nausea, anemia, fever, cough and immune deficiency [Burchum and Rosenthal, 1990; Ducker and Rabinowitz, 2016]. Efforts have been made to minimize toxicity by introducing rescue therapies with 5-formyl-THF (leucovorin) or folates [Ducker and Rabinowitz, 2016]. However, not all cancer cells respond to folate inhibition. They can acquire resistance to anti-folate drugs by either overexpressing the enzymes TYMS or DHFR [Ducker and Rabinowitz, 2016] or by a loss of function in the folate transporters FPGS and RFC [Zhao and Goldman, 2003]. Drugs targeting molecules downstream of the one-carbon metabolism including methyltransferases of histones and DNA and enzymes of the polyamine metabolism was recently evaluated in clinical trials [Locasale, 2013]. The 2-difluoromethyl ornithine inhibitor targeting the ornithine decarboxylase in the polyamine metabolism is currently evaluated in high-risk neuroblastoma [ClinicalTrials ID NCT02395666].

1.2.4.3. Branching pathways

Methionine cycle

Methionine is an essential amino acid of the one-carbon metabolism. It can either be synthesized by remethylation of homocysteine under consumption of 5-mTHF in the methionine cycle or it can be recycled within the methionine salvage pathway. Methionine is catabolized into the universal methyl donor S-adenosyl-methionine (SAM) in an ATP consuming reaction [Sanderson et al., 2019]. Donation of its methyl group converts SAM into S-adenosyl-homocysteine (SAH). The most important SAM-dependent transmethylation reactions include the synthesis of creatine, phosphatidylcholine and sarcosine [Mudd et al., 2007]. Changes in the methionine concentration regulates SAM and SAH levels that drive specific histone methylation events, affecting the expression of various genes [Mentch et al., 2015]. Hydrolyzation of SAH by the adenosylhomocysteinase yields homocysteine that can be used as a substrate either for glutathione synthesis in the transsulfuration pathway or for remethylation reactions to produce methionine [Sanderson et al., 2019].

Glutathione biosynthesis

Glutathione is the most abundant oxidant [Meister, 1983] to tackle ROS, 2-oxoaldehydes and xenobiotics [Deponte, 2013]. It is composed of a tripeptide containing cysteine, glycine and glutamate [Amelio et al., 2014]. The active thiol group in the cysteine residue donates its electrons to reduce electrophilic compounds, hydroperoxides and disulfides [Deponte, 2013] thereby maintaining the intracellular redox balance [Shuvalov et al., 2017]. Oxidized glutathione forms a reactive dimer structure that is reduced by the glutathione reductase under NADPH consumption [Deponte, 2013]. Increased glutathione levels are frequently observed in many cancer entities [Shuvalov et al., 2017].

Nucleotide biosynthesis

Nucleotides are the building blocks for DNA and RNA. They are also energy carriers for intracellular processes (e.g. ATP and GTP), used as precursors for the formation of coenzymes (e.g. acetyl-CoA) and function as signaling molecules (e.g. cyclic adenosine monophosphate) [Alberts et al., 2004]. Nucleotides are constantly synthesized *de novo* or are rescued via salvage pathways in case the tumor microenvironment does not provide sufficient quantities to ensure proper cell growth and proliferation. Nucleotides are composed of a 5-carbon sugar, a nitrogen base and at least one phosphate group. Their synthesis requires one-carbon units from the one-carbon metabolism, ribose and non-essential amino acids, including aspartate and glutamine [Vander Heiden and DeBerardinis, 2017]. The central precursor for purine and pyrimidine synthesis is the activated 5-phosphoribosepyrophosphate (PRPP) derived from ribose-5-phosphate in the pentose-phosphate pathway [Lane and Fan, 2015].

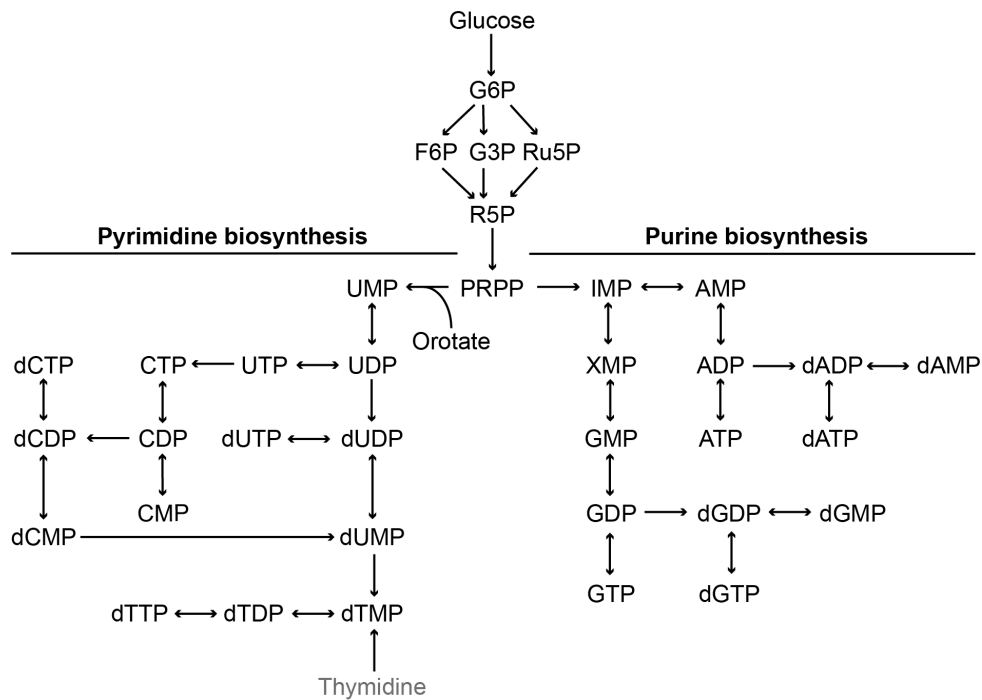


Figure 1.4.: Scheme of the *de novo* nucleotide biosynthesis. 5-phosphoribosepyrophosphate (PRPP), derived from ribose-5-phosphate (R5P), is the central precursor for purine and pyrimidine biosynthesis. Purine synthesis uses PRPP to generate the purine precursor molecule inosine monophosphate for adenosine- and guanosine triphosphate generation. Pyrimidine synthesis generates the pyrimidine derivate orotate which is fused to PRPP to generate uridine monophosphate and sequentially uridine-, cytidine- and thymidine triphosphates. dTTP can also be synthesized via the salvage pathway by phosphorylation of thymidine in a thymidine kinase-mediated reaction. Figure based on [Lane and Fan, 2015].

In pyrimidine synthesis, aspartate, glutamine, CO_2 and two molecules ATP are needed to produce dihydroorotate. Dihydroorotate is further synthesized into the pyrimidine derivate orotate by the orotate dehydrogenase in the mitochondria. All remaining steps

are carried out in the cytoplasm. The produced pyrimidine is fused with PRPP to generate uridine monophosphate (figure 1.4). Uridine monophosphate is phosphorylated into uridine diphosphate, a precursor for cytidine mono-, di- and triphosphates and uracil triphosphate. Deoxythymidine monophosphate (dTMP) is synthesized from deoxyuridine monophosphate (dUMP) by TYMS and the consumption of a one-carbon unit from 5,10-mTHF. dTMP is subsequently phosphorylated into deoxythymidine triphosphate (dTTP) [Lane and Fan, 2015]. dTTP can also be synthesized via the salvage pathway synthesis in which thymidine is phosphorylated into dTMP by the thymidine kinase and further processed into dTTP [Anderson et al., 2011].

Purine synthesis directly uses the activated PRPP to generate inosine monophosphate in a five step reaction that requires three nitrogen atoms derived from glutamate, glycine and aspartate, four molecules of ATP and five carbon atoms derived from glycine, 10-formyl-THF and CO₂. Inosine monophosphate is the common precursor of adenosine monophosphate and guanosine monophosphate. Nucleotide kinases catalyze the further conversion into adenosine and guanosine di- and triphosphates. Contrary to the pyrimidine synthesis, all reactions are carried out in the cytoplasm (figure 1.4) [Lane and Fan, 2015].

1.2.5. Time-resolved analysis of cancer cell metabolism

Glycolysis and TCA cycle are part of the central carbon metabolism (CCM) that further encompasses the amino acid metabolism and the pentose phosphate pathway [Zasada and Kempa, 2016b]. The central carbon metabolism delivers, through a series of enzymatic reactions, energy and biosynthetic precursor molecules which are essential for the generation of building blocks and maintenance of cell redox homeostasis and epigenetic status [Locasale, 2013].

The central dogma of molecular biology describes the conversion of genes into transcripts and sequentially into proteins [Crick, 1970]. Metabolites can interact, via various feedback loops, with DNA, RNA and proteins beyond this linear dogma (figure 1.5). They are the substrates and products of enzymatic reactions, precursor for DNA, RNA and protein synthesis and allosterically regulate transcription factors, protein folding and enzyme activity [Buescher and Driggers, 2016]. Thus, metabolic activity depends on the concentration levels of the metabolites themselves but also on the expression levels of enzymes. Further, metabolic activity may be influenced by allosteric regulation either by inhibition of transcription factors or by chromatin remodeling and by posttranslational modifications including ubiquitination, phosphorylation and acetylation [Pietzke et al., 2014].

DNA, RNA, proteins and metabolites act in different timescales. Mammalian cells generate 10 - 100 nucleotides within a second, and an entire gene is transcribed within 10 min. Translation takes around 1 min/protein (300 amino acids) and protein folding requires between 1 ms and 1 min. Proteins are the most stable building blocks with an

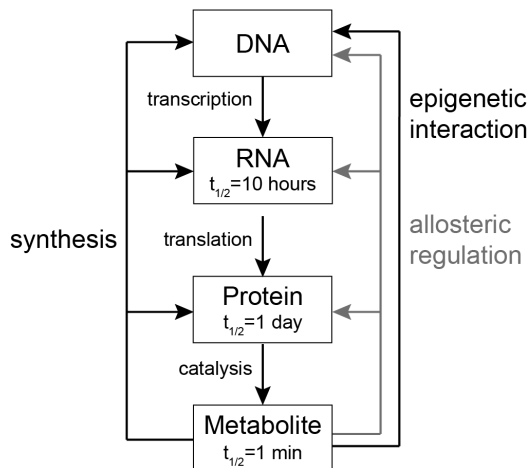


Figure 1.5.: Metabolites loop back into all omics levels. Metabolites are precursors for biosynthesis, allosterically regulate proteins, RNA molecules and transcription factors and maintain the epigenetic status of cells. Averaged half lives of mRNAs, proteins and metabolites are depicted by $t_{1/2}$. Figure adapted from [Buescher and Driggers, 2016] with modifications.

average half-life of one day. mRNAs have an average half-life of 10 hours before they are degraded. Metabolites have a half-life of only 1 min, making the metabolome the fastest responder to perturbations [Shamir et al., 2016].

Carbon routing through the CCM can be monitored by applying stable isotopes with subsequent mass spectrometry measurement [Pietzke et al., 2014]. However, long term application of stable isotopes might reflect a steady-state condition which does not account for the dynamic changes and regulation of the cellular system. Pietzke and colleagues developed a method, which enables the quantitative and time-resolved analysis of the metabolome in cell culture, taking into account a stable supply of essential nutrients to minimize metabolic stress and the measurement of stable isotope incorporation in an instationary manner. This method, called pulsed stable isotope-resolved metabolomics (pSIRM) enables the dynamic metabolic characterization at high resolution with subsequent gas chromatography coupled to mass spectrometry measurement (GC-MS) [Pietzke et al., 2014]. More specifically, cells are exposed to cell culture medium containing ^{13}C - or ^{15}N -labeled nutrients that can be traced throughout the CCM in a time- and atom-resolved manner.

Understanding the metabolic network requires knowledge of metabolites but also of proteins which catalyze the enzymatic reactions between metabolites. As reviewed in [Faria et al., 2017], proteins are identified in complex mixtures by liquid chromatography coupled to mass spectrometry (LC-MS) by a targeted- or a shotgun proteomics approach. Targeted proteomics yields for identifying a limited number of low-abundant proteins with high selectivity from complex samples [Zasada and Kempa, 2016a]. Therefore, it requires in-depth knowledge about the unique amino acid sequence of the protein of interest

[Faria et al., 2017]. The shotgun proteomics approach enables protein identification, quantification and the discrimination between isoforms in an unbiased manner of highly abundant proteins [Yates, 2013]. However, low abundant proteins such as transcription factors are rarely detectable by this approach. The identification of proteins is based on the comparison of *in silico* and experimentally derived proteolytic peptides [Zasada and Kempa, 2016a].

1.3. MYCN and its role in neuroblastoma metabolism

The MYC family includes three genes encoded in humans: *c-MYC* (*MYC*), *MCYL* and *MYCN* as reviewed in [Chi V. Dang, 2012]. They are transcription factors that build heterodimeric complexes with the transcription factor MAX to bind consensus DNA sites (E-boxes) with high affinity resulting in the regulation of gene expression. The retroviral *v-myc* oncogene enabled the discovery of *MYC* and *MYCN* as cellular homologues. *MYC* was the first human oncogene discovered within the MYC family and is one of the most frequently deregulated oncogenes in cancer [Stine et al., 2015]. *MYCN* was first described in neuroblastoma cell lines in 1983 and is the major oncogene in neuroblastoma until today [Schwab et al., 1983]. *MYCN* overexpression or amplification is also found in other tumors including retinoblastoma, Wilm's tumor, rhabdomyosarcoma, medulloblastoma, glioblastoma and small cell lung cancer [Westermarck et al., 2011]. Through its target genes, MYCN regulates fundamental cellular processes including proliferation, cell growth, protein synthesis, metabolism, apoptosis and differentiation. In normal cells, MYCN is only expressed in tissues of the developing embryo including the kidney, intestine, lung and heart [Westermarck et al., 2011]. MYC is expressed in all proliferating tissues in adults under tight transcriptional and post-transcriptional control [Stine et al., 2015]. Although, MYC and MYCN have different expression patterns, *MYCN* can functionally replace *MYC* in murine development, cell growth and differentiation [Malynn et al., 2000]. High-risk neuroblastoma tumors without *MYCN* amplification frequently harbor high level MYC expression [Westermann et al., 2008].

While MYC-derived metabolic reprogramming has been intensively studied in different cancer entities as reviewed by Stine and colleagues, far less is known about MYCN-regulated metabolic reprogramming [Stine et al., 2015]. MYC transformed cells increase glucose and glutamine utilization and expression of key glycolytic and glutaminolytic enzymes [Stine et al., 2015]. SHMT enzymes, which generate the carbon units required in the one-carbon metabolism, nucleotide and amino acid biosynthesis are directly regulated by MYC [Nikiforov et al., 2002]. Nucleotide biosynthesis is also under MYC control as the oncogene binds to and regulates many genes involved in purine and pyrimidine synthesis [Lane and Fan, 2015; Stine et al., 2015]. MYCN-induced metabolic remodeling in neuroblastoma cells also affects glycolysis, glutaminolysis and the one-carbon metabolism, which is described in detail in the following sections.

1.3.1. MYCN and glucose metabolism

Metabolic reprogramming is essential for cellular proliferation in cancer cells. Common changes include an increase in glycolysis with subsequent lactate formation [Zasada and Kempa, 2016b]. The hypoxia-inducible factor 1 α (HIF-1 α) and MYCN additively regulate the expression of glycolytic genes such as hexokinase 2 and lactate dehydrogenase A

[Qing et al., 2010]. High MYCN expression overrides HIF-1 α inhibition on cell cycle progression resulting in continued cell growth under hypoxic conditions [Qing et al., 2010]. Contrary, Dornenburg and colleagues reported that increased levels of lactate dehydrogenase A are independent of *MYCN* amplification and not essential for aerobic glycolysis in neuroblastoma cell lines [Dornenburg et al., 2018]. *Hexokinase 2* mRNA expression was also found by Oliynyk and colleagues to correlate with poor clinical outcome and elevated MYCN levels in neuroblastoma patients [Oliynyk et al., 2019].

1.3.2. MYCN and glutamine metabolism

Besides an increase of aerobic glycolysis, known as the Warburg effect, cancer cells rely on glutaminolysis for TCA cycle anaplerosis, energy production, biomass accumulation, glutathione synthesis and redox balance maintenance [Daye and Wellen, 2012]. Glutamine is transferred into the cell by transporters including ASCT2. Activation of ASCT2 is essential in *MYCN*-amplified neuroblastoma cells to maintain sufficient intracellular glutamine levels for TCA cycle anaplerosis. ASCT2 expression is co-regulated by ATF4 together with MYCN [Ren et al., 2015]. Glutamine starvation induces MYCN-dependent cell death mediated through ATF4 and GCN2 [Qing et al., 2012]. Glutaminase (GLS2) is the rate-limiting enzyme in glutaminolysis and converts glutamine into glutamate [Herranz, 2017]. MYCN is required to drive glutaminolysis in *MYCN*-amplified neuroblastoma cell lines and a *MYCN* amplification is associated with an enriched glutaminolysis gene signature in neuroblastoma tumors [Wang et al., 2018]. MYCN promotes the conversion of glutamine to glutamate by direct transcriptional activation of *GLS2* in *MYCN*-amplified neuroblastoma cells [Xiao et al., 2015]. Redox homeostasis maintenance, glutathione levels and TCA cycle anaplerosis by α -ketoglutarate are dependent on GLS2 in *MYCN*-amplified neuroblastoma cell lines [Xiao et al., 2015]. *MYCN* amplification is also associated with increased expression of glutathione biosynthesis- and glutathione-linked ROS detoxification enzymes in cells and tumors [Oliynyk et al., 2019]. By driving glutaminolysis, MYCN induces oxidative stress resulting in increased ROS levels which make neuroblastoma cells vulnerable to ROS-producing agents. Dimethyl fumarate, a drug inducing ROS, suppressed neuroblastoma cell proliferation and tumor growth as well as MYCN expression [Wang et al., 2018]. Enzymes catalyzing reactions within the TCA cycle (citrate synthase, isocitrate dehydrogenase 2, 2-oxoglutarate dehydrogenase-like) showed enhanced mRNA and protein expression in *MYCN* amplified neuroblastoma cell lines and patient samples [Oliynyk et al., 2019].

1.3.3. MYCN and one-carbon metabolism

The *de novo* serine synthesis pathway and the one-carbon metabolism provide one-carbon units required for the generation of building blocks (lipids, proteins, nucleotides), and for the

maintenance of the redox and epigenetic status in highly proliferating cancer cells [Locasale, 2013]. Increased expression of genes encoding for enzymes within the cholesterol and the serine-glycine synthesis pathways, mediated through sterol regulatory element binding factors and ATF4, are required for cell growth and tumorigenicity in human neuroblastoma cells with *MYCN* amplification [Liu et al., 2016]. *MYCN*-amplified neuroblastoma cells have an increased dependency on the serine-glycine-one-carbon metabolic pathways in order to provide glucose-derived carbons for the serine and glycine synthesis [Xia et al., 2019]. *MYCN* transcriptionally activates *ATF4* mRNA expression and ATF4 stabilizes the *MYCN* protein leading to increased transcription of the genes involved in the serine-glycine pathways and the one-carbon metabolism [Xia et al., 2019].

2 Aim of the Thesis

The transcription factor MYCN regulates several genes involved in fundamental cellular processes including proliferation and metabolism. In order to meet the high energy demands caused by rapid proliferation and invasion into surrounding tissue, cancer cells require metabolic reprogramming, thereby developing metabolic addictions to certain pathways. This dissertation describes recent efforts to identify and interfere with these pathways in order to develop novel and promising therapeutic interventions to tackle neuroblastoma.

In the first phase of the project, we aimed for the identification of metabolic targets of MYCN. We measured the metabolites of neuroblastoma cell lines in a time-resolved manner and the proteome of neuroblastoma cell lines and biopsies from patients with neuroblastoma by quantitative mass spectrometry methodologies.

In the second phase of the project, PHGDH - the rate-limiting enzyme in *de novo* serine synthesis - was validated as a target of MYCN. We investigated the cellular response to perturbations of *de novo* serine synthesis by depleting serine and glycine from the culture medium and by genetic and pharmacological inhibition of PHGDH. We constructed *PHGDH* knockout clones by CRISPR-Cas9 technology and monitored proliferation in comparison to the *MYCN*-amplified control cells *in vitro*. Pharmacological inhibition was performed by applying compounds targeting PHGDH activity in neuroblastoma cell lines *in vitro* and in mice carrying a patient-derived *MYCN*-amplified neuroblastoma xenograft *in vivo*.

In the third phase of the project, we applied antifolate drugs against enzyme activity of the folate-mediated one-carbon metabolism, downstream of *de novo* serine synthesis, in order to investigate cell proliferation and nucleotide abundances in neuroblastoma cells *in vitro*.

Further, we explored the role of external glutamine on neuroblastoma proliferation, survival and metabolism with special focus on *de novo* serine synthesis. The integration of the described methods aims for a new level of understanding metabolic regulation in MYCN-driven neuroblastoma.

3 Materials and Methods

All consumables, including chemicals, compounds, antibodies, small interfering RNAs (siRNA) and laboratory equipment are listed in the supplementary section.

3.1. Patient samples for shotgun proteomics

Tumor samples from 49 neuroblastoma patients, collected internationally between 1989 and 2015, were generously provided by the Cologne Tumorbank¹. The tumor sample cohort was representative for neuroblastoma as the majority was *MYCN* non-amplified (38 tumors) while eleven harbored a *MYCN* amplification (table 3.1). Within the 49 tumor samples, ten were stage 1, five were stage 2, two were stage 3, 23 were stage 4 and nine were stage 4s tumors based on the international neuroblastoma staging system (INSS) [Brodeur et al., 1993]. The tumor infiltration grade ranged between 55 and 90%.

Table 3.1.: *MYCN* status and INSS stage of primary biopsies from patients with neuroblastoma.

	Stage 1	Stage 2a	Stage 2b	Stage 3	Stage 4	Stage 4s
<i>MYCN</i> non-amplified	10	1	3	2	17	5
<i>MYCN</i> amplified	0	0	1	0	6	4

The *MYCN* expression levels of the tumor samples determined by fluorescence *in situ* hybridization (provided by the German Neuroblastoma Biobank) were transformed to a *MYCN* score in the range of 5 to -5 (table 3.2). A score of 5 was indicating the highest possible *MYCN* expression in the panel of tumor samples and a score of -5 was representing the *MYCN* non-amplified tumors. Proteins identified by the shotgun proteomics approach were correlated to the *MYCN* score.

Table 3.2.: *MYCN* score of primary biopsies from patients with neuroblastoma.

<i>MYCN</i> copy number	50	40	35	32	30	25	15	10	1.5	1
<i>MYCN</i> score	5	4	3	3	3	2	2	2	-4	-5

¹Biobank Embryonal Tumors, Reference Laboratory Neuroblastom, University Hospital in Cologne, Germany

3.2. Cell culture

3.2.1. Cell lines

The GI-ME-N, IMR-32, Kelly and SH-SY5Y cell lines were obtained from the German Collection of Microorganisms and Cell Cultures². CLB-GA, IMR5/75 and LAN-6 cell lines were kindly provided by M. Fischer³. The BE(2)-C cell line was purchased from the European Collection of Authenticated Cell Cultures⁴. The NB-1 cell line was kindly provided by O. Witt⁵. The SK-N-AS, SK-N-SH and SK-N-DZ cell lines were kindly provided by J. Schulte⁶. The CHP-134, NLF, NGP, LAN-1, SH-EP, SH-EP-Tet21/N [Lutz et al., 1996] and SH-SY5Y^{MYCN} cell lines were kindly provided by F. Westermann and M. Schwab⁷. Synthetic MYCN expression in SH-EP-Tet21/N and SH-SY5Y^{MYCN} cells is suppressed or promoted by the application of 1 $\mu\text{g/mL}$ tetracycline to the culture medium.

Cell lines were cultured in Dulbecco's modified Eagle Medium (DMEM) without glucose, glutamine, sodium pyruvate, phenol red, and supplemented with 10% fetal calf serum (FCS, v/v), 2.5 g/L glucose and 2 mM glutamine at 37°C, 5% CO₂, 21% O₂ and 85% humidity. The tetracycline-inducible SH-EP-Tet21/N cells were cultured with selection antibiotics G418 (0.2 $\mu\text{g/mL}$) and HygromycinB (0.1 $\mu\text{g/mL}$). The SH-SY5Y^{MYCN} cells were cultured with selection antibiotics G418 (0.2 $\mu\text{g/mL}$) and Blasticidin (7.5 $\mu\text{g/mL}$). Cell lines were starved for serine and glycine by using the DMEM without glucose, glutamine, serine, glycine, sodium pyruvate, phenol red, and supplemented with 10% FCS (v/v), 2.5 g/L glucose and 2 mM glutamine. In a first step, all cell lines were expanded for this work and controlled for mycoplasma contamination with the Mycoplasma detection kit 'PlasmoTest' (InvivoGen). Cell line authentication was confirmed by single-nucleotide polymorphism-based assay (Multiplexion) before aliquoting, freezing in cryovials and storage in liquid nitrogen. *PHGDH* knockout clones and respective control cells were cultured in DMEM supplemented with 10% fetal calf serum (v/v) and 1% nonessential amino acids at 37 °C, 5% CO₂ and 21% O₂.

Determination of the MYCN score

The MYCN expression levels in a panel of neuroblastoma cell lines were determined by relative quantification by western blotting and digital droplet PCR [Lodrini et al., 2017]. Those MYCN expression levels were transformed to MYCN scores in the range of 5 (highest MYCN expression in the panel of cell lines) to -5 (*MYCN* non-amplified cell lines). The order of the MYCN scores reflected the order of MYCN expression (table 3.3).

²DSMZ, Braunschweig, Germany

³Children's Hospital of the University of Cologne, Cologne, Germany

⁴ECACC, Salisbury, UK

⁵Department Pediatric Oncology, German Cancer Research Center, Heidelberg, Germany

⁶Department Pediatric Oncology and Hematology, Charité Universitätsmedizin Berlin, Germany

⁷Department of Neuroblastoma Genomics, German Cancer Research Center, Heidelberg, Germany

Proteins identified by the shotgun proteomics approach were correlated to the MYCN score.

Table 3.3.: MYCN score of neuroblastoma cell lines.

Cell line	MYCN score
BE(2)-C	5
Kelly	4.5
LAN1	3
NGP	3.2
SK-N-DZ	3
IMR-32	2.5
SH-EP-Tet21/N <i>MYCN</i> induced	2
SH-SY5Y ^{MYCN} <i>MYCN</i> induced	1.5
SH-EP-Tet21/N <i>MYCN</i> non-induced	-2
SH-SY5Y ^{MYCN} <i>MYCN</i> non-induced	-2
LAN6	-3
SH-SY5Y	-3
SH-EP	-5
SK-N-SH	-5
GI-ME-N	-5

Cell stock preparation

Cell freezing was performed with cell lines at a confluency of 75 - 85%. Cells were trypsinized as described in the paragraph 'Cell passaging'. Following cell counting and centrifugation, the cell pellet was resuspended in medium containing 10% dimethyl sulfoxide (DMSO) (v/v). One milliliter containing 3×10^6 cells were transferred into a cryotube. Immediately after aliquoting, cryovials were transferred into a freezing chamber (Mr. Frosty, Thermo Fisher Scientific) that ensures gentle freezing at $-1^\circ\text{C}/\text{min}$ at -80°C . The next day, cryovials were put into liquid nitrogen or remained in the -80°C freezer for short-term storage.

Cell thawing

Cryovials were taken from either the liquid nitrogen tank or the -80°C freezer and were immediately put in a 37°C waterbath. As soon as the cell suspension was thawed, cells were transferred into a falcon filled with pre-warmed culture medium. The cell suspension was centrifuged at $300 \times g$ at room temperature for 5 min. The supernatant was discarded, cells were resuspended in fresh culture medium and transferred into a new cell culture flask.

Cell passaging

When cells reached a confluency of 75-85%, they were passaged to avoid contact inhibition. Culture medium was discarded and cells were washed once with 1x phosphate buffered saline (PBS). Trypsin was added to detach the adherent cells. As soon as cells detached from the plate, fresh medium was added to quench trypsinization. The cell suspension was transferred into a falcon, a 10 μ L aliquot was taken for cell counting and the cell suspension was centrifuged at room temperature, 300 $\times g$, 5 min. Thereafter, the supernatant was discarded, and the pellet was resuspended in fresh medium. Dependent on the doubling time of the cell line and the size of the cell culture plate, an aliquot of the cell suspension was transferred into a new plate containing prewarmed fresh medium. Cells were checked once a week for mycoplasma contamination with the Mycoplasma Detection Kit "PlasmoTest" (InvivoGen) according to the manufacturers instructions. Cell cultivation was proceeded until a maximum of 30 passages.

Cell counting

Two different cell counting machines were used in the laboratory over time. Both technologies were based on the trypan blue exclusion method to quantify the total, viable and non-viable cell numbers [Strober, 2001]. Cells were trypsinized as described in the paragraph 'Cell passaging'. For semi-automated cell counting in the TC20 cell counter (BioRad), 10 μ L of the cell suspension were mixed with equal volumes of trypan blue, and a 10 μ L aliquot was transferred into the cell counting chamber. For automated cell counting in the Vi-Cell-XR (BeckmanCoulter), 500 μ L of cell suspension and 500 μ L trypan blue solution were automatically mixed in three mixing cycles and exposed to cell counting.

3.2.2. Monitoring cell growth**Proliferation assay**

Cells were trypsinized as described in the paragraph 'Cell passaging' and seeded into six-well plates. Total and viable cell count was measured 24, 48, 72 and 96 hours after seeding using trypan blue staining and automated cell counting (Vi-Cell-XR).

In starvation experiments, cells were directly seeded into six-well plates containing the appropriate culture medium. In compound-containing experiments, cells were seeded and compounds were applied as soon as cells were attached to the plate. Applied concentrations of the compounds are listed in the supplementary table A.6.

Colony formation assay

Seeding of the cells in six-well plates was performed according to paragraph 'Cell passaging'. A medium change was performed after five days. For cell harvest, medium was discarded and 1.5 mL ice-cold methanol/acetone (1:1) was added. After 5 min of incubation, the mixture was removed and cells were washed once with 2 mL PBS. One milliliter of

0.005% cristal violet solution (0.1% cristall violet in ethanol, dilution in ddH₂O) was added and incubated for 30 min. Cells were washed once with 2 mL ddH₂O. As soon as the cells were dry, plates were scanned with 1200 dpi, 24 bit and analyzed by the image processing software ImageJ (version 1.48) [Schneider et al., 2012].

In starvation experiments, cells were directly seeded into six-well plates containing the appropriate culture medium. In compound-containing experiments, cells were seeded and compounds were applied one day after seeding. Renewal of treatment was performed after five days. Applied concentrations of the compounds are listed in the supplementary table A.6.

3.2.3. Cell cycle analysis

Cells were trypsinized as described in paragraph 'Cell passaging'. Following centrifugation the cell pellet was washed in PBS, an aliquot of cells was counted by semi-automated cell counting with trypan blue staining and 2×10^6 cells were transferred into a tube suitable for fluorescence activated cell sorting (FACS) analysis. After centrifugation at 475 $\times g$ at 4°C for 5 min, supernatant was discarded and fixation of the cell pellet was realized by dropwise addition of 1 mL ice-cold 70% ethanol combined with gentle shaking. Cells were incubated at 4°C for at least 30 min, followed by centrifugation at 845 $\times g$ at 4°C for 5 min and another washing step with PBS. After centrifugation, supernatant was discarded and the pellet was treated with 50 μ L RNase A solution (Qiagen) and 400 μ L propidium iodide-staining solution (Thermo Fisher Scientific). After incubation at room temperature in the dark for 10 min, cellular DNA content was measured at the LSR Fortessa X-20 (BD Biosciences) and analyzed with the FACS Diva software (BD Biosciences, v.8.0.2). The forward scatter area and side scatter area (FSC-Area versus SSC-Area) were used to exclude cell debris. Cell doublets were excluded by the evaluation of the propidium iodide area (PI-A) versus propidium iodide width (PI-W) density plot. The distinct cell cycle phases were determined in a propidium iodide histogram. Further data analysis was performed with the FlowJo-X software (BD Biosciences, v10.0.7r2).

3.2.4. Generating *PHGDH* knockout clones

Cells were seeded in 10 cm² plates and transfected as soon as they reached a confluency of 75%. Medium volume was decreased per plate from 10 mL to 3 mL. OptiMEM (Thermo Fisher Scientific) and HiPerFect (Qiagen) were mixed together with the isolated plasmid DNAs. After incubation at room temperature for 7 min, 1 mL of the mixture was added dropwise onto the cells. Cells were gently shaken and incubated at standard cell culture conditions over night. After 24 hours, the medium was exchanged with medium supplemented with 2 μ g/mL puromycine for clone selection. Three days after puromycine addition, cells were trypsinized, counted and seeded in 96-well plates with one or one-half

clone per well. Single clones were expanded and monitored closely under the microscope (Axio Vert.A1, Carl Zeiss). As soon as clones reached a high population size, one third of the population was used for further cultivation, one third was frozen into cryostocks and one third was used for protein harvest in order to quantify PHGDH by western blotting.

3.2.5. siRNA-mediated knockdown

For knockdown of *ATF4* and *PHGDH*, siRNA pools (siTOOLS Biotech) were used (supplementary table A.12). Each siRNA pool consisted of 30 siRNAs specifically designed for the target gene. The negative control siRNA pool (Scramble) consisted of 30 siRNAs designed to not-target the gene of interest. siRNA-mediated knockdown experiments were performed in BE(2)-C and SH-EP cell lines.

Cell transfection

Cells were trypsinized as described in paragraph 'Cell passaging' and transfected as soon as they reached a confluency of 75%. Medium volume was decreased per plate from 10 mL to 3 mL. OptiMEM (Thermo Fisher Scientific) and HiPerFect (Qiagen) was mixed together with either the desired concentration of siRNA pool, Cy3 or scramble siRNA pool in a 15 mL falcon. A mixture containing solely OptiMEM or OptiMEM together with HiPerFect was used as additional transfection controls. After incubation at room temperature for 7 min, 1 mL of the mixtures were added dropwise onto the cells. Cells were gently shaken and incubated at standard cell culture conditions over night. After 24 hours, medium was exchanged to either standard culture medium, medium depleted for serine and glycine or medium depleted for glutamine. Protein lysates were harvested 72 or 96 hours after transfection (section 3.4.1). Cells transfected with Cy3 were visualized with the Olympus BX43 (Olympus) microscope coupled to a fluorescence light source (X-Cite 120 PCQ, Olympus) 24 hours after transfection to estimate the transfection efficacy.

3.2.6. Serine and glutamine starvation experiments

For glutamine starvation experiments, cells were washed once with PBS. Then, glutamine-depleted medium was readded to the cells. After 48 hours of glutamine starvation, cells were harvested for the different experimental procedures.

For serine and glycine starvation experiments, cells were washed once with PBS. Then serine and glycine-depleted medium was readded to the cells. In all experiments medium containing serine, glycine and glutamine was added to control cells.

3.3. Molecular Biology Methods

3.3.1. Nucleic acid quantification

Nucleic acid quantification was spectrophotometrically performed by measuring the absorbance at $\lambda=260$ nm in the Nanodrop (Thermo Fisher Scientific). Before measurement, the Nanodrop was calibrated with nuclease-free water. Samples containing extracted RNA or DNA were measured by adding 1 μ L onto the Nanodrop. Purity of the samples was determined by the ratio of $\lambda=260$ nm and $\lambda=280$ nm (pure DNA: 1.8, pure RNA: 2.0).

3.3.2. DNA extraction

Cells were trypsinized from the culture plate and centrifuged at 414 $\times g$ for 5 min at room temperature. After one washing step in PBS, cells were centrifuged again at the same speed and time. Supernatant was discarded, and the pellet was dissolved in 200 μ L PBS. DNA extraction was performed by using the QIAamp DNA Mini Kit (Qiagen) at room temperature. Shortly, 20 μ L of Proteinase K and 200 μ L of Buffer AL were mixed together in order to lyse the cells. Before pipetting onto the Qiagen column, 200 μ L of 100% ethanol were added. Columns were centrifuged at 6000 $\times g$ for 1 min. Membrane-bound DNA was washed by adding 500 μ L AW1 buffer followed by centrifugation at 6000 $\times g$ for 1 min and a second washing step with AW2 buffer and centrifugation. Incubation of 100 μ L DNase free water for 5 min on the column and subsequent centrifugation at 6000 $\times g$ for 1 min was eluting the bound DNA. Quantification of DNA was performed as described in section 3.3.1. Eluted DNA was stored at -20 °C.

3.3.3. RNA extraction

RNA extraction was performed using the RNeasy Mini Kit (Qiagen). Cell culture medium was discarded, and 350 μ L RLT-buffer containing 1% 14.3 M β -mercaptoethanol (v/v) was added. The cells were scratched from the plate and transferred into a new tube. Equivalent volumes of 70% ethanol (v/v) were added, and the cell suspension was immediately transferred onto the RNeasy Mini Kit column. Columns were centrifuged for 15 sec at maximal speed and flow-through was discarded. Columns were washed once with RW1 buffer followed by centrifugation for 15 sec at maximum speed. In order to remove all remaining DNA within the sample, a DNA digest was performed by adding 80 μ L of a 1:8 dilution of DNase in RDD buffer and incubation for 20 min. Membrane-bound RNA was washed twice with RPE buffer. RNA was eluted by adding 10 μ L of RNase-free water followed by centrifugation for 1 min at maximal speed. Quantification of RNA was performed as described in section 3.3.1. Eluted RNA was stored at -80 °C.

3.3.4. Reverse-transcription PCR

Single-stranded complementary DNA (cDNA) was synthesized from 1 μg extracted RNA using the First-Strand cDNA Synthesis Kit (Thermo Fisher Scientific). RNA was diluted in RNase-free water to end up with 10 μL . Random-hexamer primer of 1 μL was added to the sample and incubated at 65 °C for 5 min. The remaining components were mixed together according to table 3.4, and 9 μL were added to each sample followed by an incubation at 25 °C for 5 min and at 37 °C for 60 min. The synthesized cDNA was stored at -20 °C.

Table 3.4.: Reverse-transcription PCR mastermix.

Component	Concentration	Volume
5x reaction buffer		4 μL
RiboLock TM RNase Inhibitor	20 U/ μL	1 μL
dNTP Mix	10 mM	2 μL
M-MuLV Reverse Transcriptase	20 U/ μL	2 μL

3.3.5. Quantitative real-time RT-PCR

The relative expression of mRNA was measured by quantitative real-time RT-PCR (qPCR) in the StepOnePlus Real-Time PCR System (Applied Biosystems, version 2.3). RNA was extracted and transcribed as described in section 3.3.3 and 3.3.4. The cDNA was diluted 1:10 in RNase free water. A mastermix was pipetted according to table 3.5 with primers listed in the supplementary table A.9, and 20 μL of the mastermix were used per reaction together with 5 μL of diluted cDNA. A non-template control was included for each target to ensure contaminant-free measurement. Relative gene expression was normalized to averaged expression of *HPRT* and *SDHA*, whose expression levels are not associated with stage of disease or *MYCN* amplification status of neuroblastoma tumors [Fischer et al., 2005].

Table 3.5.: qPCR mastermix. Primers are listed in the supplementary table A.9

Component	Volume
2x Mastermix	12.5 μL
Primer forward	0.08 μL
Primer reverse	0.08 μL
SYBR Green	0.75 μL
RNase free water	6.6 μL

The qPCR thermal cycler program used to amplify each target is shown in table 3.6. The threshold cycle value (Ct) was determined for each target separately using the StepOne software (Applied Biosystems). Data was normalized by using the $\Delta\Delta\text{Ct}$ method [Livak and Schmittgen, 2001]. Shortly, housekeeping genes were averaged, and mRNA expression

for each target was determined by subtracting the housekeeper expression from the target expression. The fold change of the expression was calculated as $\Delta\Delta C_t = 2^{-\Delta C_t}$. Finally, biological replicates per condition and cell line were averaged and fold changes were calculated between treatment and control groups. In case of the neuroblastoma cell line panel, fold changes were calculated between the single cell line to the average of the entire panel.

Table 3.6.: qPCR cycler program.

	Holding Stage	Cycling Stage (40 cycles)		Melt Curve Stage		
	Step 1	Step 1	Step 2	Step 1	Step 2	Step 3
Ramp Rate	100%	100%	100%	100%	100%	
Temperature	95°C	95°C	60°C	95°C	60°C	95°C (+0.3°C)
Time	10 min	00:15 min	1 min	00:15 min	1 min	00:15 min

3.3.6. Chromatin immunoprecipitation qPCR

Hsu and colleagues [Hsu et al., 2016] published a dataset (GEO accession: GSE72640) containing predictive binding sites of MYCN across the genome of the *MYCN*-amplified neuroblastoma cell line SK-N-BE(2)-C after performing chromatin immunoprecipitation (ChIP) followed by sequencing. The sequencing data were used to identify two predictive binding sites of MYCN within the *PHGDH* promoter region. In order to verify this finding experimentally, ChIP followed by qPCR was performed with the *MYCN*-amplified BE(2)-C cell line.

Sheared, immunoprecipitated DNA fragments were already available in the laboratory and kindly provided by M. Lodrini⁸ for use in qPCR. The ChIP was performed with the ChIP Assay Kit (Millipore) according to the manufacturers instructions. Briefly, cell pellets were lysed in 50 mM Tris-HCl buffer (pH 8.1) and cross-linked to the proteins with 1% sodium dodecyl sulfate (SDS), 10 mM ethylenediaminetetraacetic acid (EDTA) and cOmplete protease inhibitor cocktail (Roche). Fragmentation of the chromatin-protein complex was performed by sonication. Immunoprecipitation was performed with the anti-MYCN antibody (B8.4B, sc-53993, Santa Cruz) and normal mouse immunoglobulin G (IgG) (sc-2025, Santa Cruz) as a negative control. Co-immunoprecipitated chromatin fragments were eluted in 10 mM dithiothreitol (DTT) in TE buffer for 30 min at 37°C. Eluates were diluted 1:20 in ChIP dilution buffer (Millipore) and used in second round of ChIP.

The qPCR was optimized with eight different primer pairs, all binding within the predictive binding sites of the *PHGDH* promoter region. In a first step, the primers (100 μ M) were tested in all combinations with different dilutions of the DNA fragments (1:10, 1:100, 1:1000, 1:10000) in order to find the most efficient qPCR conditions. A

⁸Department Pediatric Oncology and Hematology, Charité Universitätsmedizin Berlin, Germany

Table 3.7.: ChIP qPCR mastermix.

Component	Volume
2x PCR Mix	10.0 μ L
Primer forward	0.18 μ L
Primer reverse	0.18 μ L
H ₂ O	6.64 μ L

Table 3.8.: ChIP qPCR program.

Step	Time	Temperature
1: Hold	2 min	50°C
2: Hold	10 min	95°C
3: Denature	15 sec	95°C
4: Anneal / Extend	60 sec	60°C
Repeat Step 3-4 for 40 cycles		

mastermix was pipetted according to table 3.7 and 17 μ L of the mastermix were used per reaction together with 3 μ L of diluted DNA fragments. A non-template control was included for each primer pair to ensure contaminant-free measurement. Primer sequences are listed in the supplementary table A.10. All samples were measured in technical duplicates. The qPCR thermal cycler program used is shown in table 3.8. The Ct value was separately determined for each primer pair using the StepOnePlus software (Applied Biosystems, version 2.3). Data was normalized using the Δ Ct method. Input DNA values were averaged and mRNA expression for mouse IgG and MYCN was determined by subtracting the expression of Input DNA from the expression of mouse IgG and MYCN. Fold enrichment of MYCN to the *PHGDH* promoter sites was determined by the ratio of MYCN to mouse IgG.

3.3.7. CRISPR-Cas9 gene editing

CRISPR-Cas9 gene editing was used to construct *PHGDH* knockout clones originating from the BE(2)-C cell line, with help of A. Winkler and J. Wünschel⁹.

Design and cloning of guide RNAs

Guide RNAs were designed using the CRISPR design tool developed by F. Zheng¹⁰. In order to efficiently disrupt all coding exons in all isoforms of *PHGDH*, eight different guide RNAs were selected and ordered as DNA oligos (Eurofins Genomics) for cloning (supplementary table A.11). DNA oligos were dissolved in TE-buffer (0.001 M Tris-HCl pH 7.4, 0.1 mM EDTA pH 8) to reach a concentration of 50 μ M. Two microliter of each corresponding DNA oligo pair were mixed together and 496 μ L of TE-buffer were added.

⁹Department Pediatric Oncology and Hematology, Charité Universitätsmedizin Berlin, Germany

¹⁰<http://crispr.mit.edu/>

The DNA oligo's were annealed by incubation at 95°C for 5 min followed by 30 min incubation at room temperature. The plasmid px459 was digested with BbsI (R0539 S, New England Biolabs) at 37°C over night (5 μ g DNA with 20 units BbsI in 1x Buffer 2, New England Biolabs). The digested plasmid was loaded onto a 1% agarose gel and run at 100 V for 90 min. The linear DNA band was cut out and extracted from the gel using the QIAquick Gel Extraction Kit (Qiagen) according to the manufacturers instructions. Using 1 μ L of T4 DNA Ligase (New England Biolabs), 1 μ L of BbsI digested px459, 1 μ L oligo annealing mix, 2 μ L 10x T4-buffer and 15 μ L ddH₂O, the annealed oligo sequences were ligated into the px459 vector at 16°C over night. As a negative control, the mixture was depleted for the oligo annealing mix. The next day, all ligation mixes were transformed into freshly prepared chemically competent *E.coli* cells.

Preparation of chemically competent cells and transformation

To prepare chemically competent cells, XL10-Gold ultracompetent cells (Agilent Technologies, Santa Clara, USA) were cultured in 50 mL LB medium supplemented with 34 μ g/mL chloramphenicol and 10 mM MgCl₂ with gentle shaking over night at 37°C. From the starter culture, 0.5 mL were aliquoted in 300 mL LB medium, supplemented with chloramphenicol and MgCl₂ and shaken gently for 3 - 4 hours at 37°C. Subsequently, the bacteria suspension was measured in the Biophotometer (Eppendorf) at OD₆₀₀. As soon as cells reached an OD₆₀₀ of 0.5, they were harvested and stored on ice for 15 min, followed by a cold spin (4°C) at 590 xg 15 min. The supernatant was discarded, the pellet was resuspended in 1.5 mL LB medium, supplemented with 10 mM MgCl₂, 10 mM MgSO₄, 5% DMSO and incubated on ice for 30 min.

Following incubation, 200 μ L of the cell suspension were added to each ligation mix, containing the DNA oligos in px459 vector, mixed shortly and incubated on ice for 30 min. In order to perform a heatshock on the cells, the mix was incubated at 42°C for 90 sec followed by a 2 min incubation on ice. The reaction was quenched by addition of 800 μ L SOC medium and cells were left for recovery for 1 hour under gentle shaking at 37°C. In order to plate the cells onto LB plates, they were centrifuged at 2350 xg for 2 min, resuspended in leftover supernatant and plated onto LB-Ampicillin plates using glass beads for equal spreading. Agar plates were incubated at 37°C over night.

Plasmid isolation

Plasmid isolation was performed with the QIAprep Spin Miniprep Kit (Qiagen) and the NucleoBond Xtra Maxi Kit (Macherey-Nagel) with minor modifications on the manufacturers instructions. Mini-prep was performed in order to identify positive clones. The maxi-prep was used to set up big cultures of positive clones. Shortly, single colonies were picked from LB-Ampicillin plates, transferred into 4 mL LB medium supplemented with 100 μ g/mL Ampicillin and incubated under gentle shaking at 37°C over night. On the

next day, 1.5 mL of the cells were centrifuged at 2350 $\times g$ for 2 min. The supernatants were discarded and pellets were resuspended in 200 μL Buffer P1, supplemented with 100 $\mu\text{g}/\text{mL}$ RNase A. Cells were lysed using 200 μL Buffer P2 and inverting the tubes five times. The reaction was stopped by adding 200 μL Buffer P3. Cells were centrifuged at full speed at 4°C for 10 min, the supernatant was transferred into a fresh tube, and plasmids were precipitated by adding 800 μL isopropanol and inverting the tubes five times followed by centrifugation at 4°C for 30 min. The pellet was washed in 500 μL 70% ethanol, air dried and resuspended in 50 μL TE-buffer (0.001 M Tris-HCl pH 7.4, 0.1 mM EDTA pH 8). An aliquot of DNA was sent for sequencing together with 10 μM of the CRISPR sequencing primer (taaaatggactatcatatgcttacc). Sequencing results were confirmed by BLAST analysis, and positive clones were picked from a replica LB-agar plate for maxi-prep purification. Single colonies were transferred into 200 mL LB medium supplemented with 100 $\mu\text{g}/\text{mL}$ Ampicillin and incubated under gentle shaking at 37°C over night. Plasmid DNA was isolated with the NucleoBond Xtra Maxi Kit (Macherey-Nagel) according to the manufacturers instructions. DNA concentration of isolated clones was measured as described in section 3.3.1. Plasmids were sequenced and analyzed before they were used for transfection into BE(2)-C cells.

3.4. Biochemical Methods

3.4.1. Preparation of protein lysates

Cell lines were harvested to obtain protein lysates for western blot analysis. Depending on the experimental hypothesis, the conditioned medium was either included or discarded before harvest. In general, adherent cells were detached from the cell culture plates by adding 4.5 mL Versene. As soon as cells started floating, they were transferred into a falcon and centrifuged at 414 $\times g$, at 4°C for 5 min. Supernatant was discarded, the pellet was resuspended in urea lysis buffer (20 mM Tris-HCl, 7 M urea, 0.01% Triton X-100, 100 mM DTT, 40 mM MgCl₂, Complete protease inhibitor cocktail) and incubated on ice for 10 min. Protein lysates were stored at -80°C.

3.4.2. Protein quantification

Colorimetric protein quantification was carried out using the Bradford Assay (BioRad). In a 96-well plate, 0.5 μ L of protein lysate or quantification standard (0 - 8 μ g/mL in urea lysis buffer) was mixed together with 150 μ L ddH₂O and 30 μ L of Bradford reagent followed by incubation for 5 min at room temperature. The absorbance was measured at 595 nm in the EPOCH spectrophotometer (BioTek Instruments). Each sample was measured in technical duplicates.

3.4.3. SDS-PAGE

SDS-polyacrylamide gel electrophoresis (SDS-PAGE) was performed as described in [Laemmli, 1970]. Protein lysates were diluted in 2x SDS sampling buffer (1M Tris pH 8, 20% SDS (v/v), 20% glycerol (v/v), 10% β -mercaptoethanol (v/v), bromphenol-blue) and denaturated at 95°C for 5 min. Samples were spun down and put on ice until sample loading on SDS gel. SDS gels were poured with separation gel percentage suitable for the proteins of interest (table 3.9). The separation gel buffer contained 1.5 M Trizma Base (pH 8.8) and the collection gel buffer contained 1 M Trizma Base (pH 6.8). Gels were loaded with 12 μ L of sample and 3 μ L of prestained protein ladder (Thermo Fisher Scientific). Electrophoresis was run at 80 V for 30 min followed by 120 V for 60 min in the Mini-Protean Tetra Cell (BioRad) filled with SDS Running Buffer (0.3% Trizma Base (w/v), 1.44% glycine (v/v), 2% SDS (v/v) in ddH₂O).

3.4.4. Western blot

Semi-dry blot

After SDS-PAGE separation, proteins were transferred onto a polyvinylidene difluoride (PVDF) membrane at 25 V, 1.0 A for 30 min using the semi-dry blotting system Trans-Blot

Table 3.9.: Separation and collection gel for SDS PAGE.

Component	Separation Gel		Collection Gel
	Volume per 10% Gel	Volume per 12% Gel	Volume per Gel
Buffer	1.9 mL	1.9 mL	250 μ L
30% Polyacrylamide	2.5 mL	3 mL	335 μ L
20% SDS	37.5 μ L	37.5 μ L	10 μ L
TEMED	3 μ L	3 μ L	2 μ L
10% APS	75 μ L	75 μ L	20 μ L
ddH ₂ O	2.95 mL	2.45 mL	1.35 mL

Turbo Transfer system (BioRad). Before blotting, the PVDF membrane was activated in methanol and washed in blotting buffer (3% Trizma Base (w/v), 14.4% glycine (v/v), 20% methanol in ddH₂O). Filter paper and SDS-gel were also washed in blotting buffer.

Wet blot

In case proteins with high masses were analyzed, they were blotted by Wet blotting onto a PVDF membrane. Before blotting, all components including the sponges, Whatman paper, PVDF membrane and SDS gel were soaked in blotting buffer. Wet blotting was performed at 4°C under gentle stirring with a magnet stirrer at 300 mA for 90 min.

Blocking and antibody probing

After blotting, the membrane was blocked in either 5% milk or 5% BSA (w/v) in tris-buffered saline containing 10% Tween-20 (v/v) (TBS-T) at room temperature for 60 min. Proteins were probed with primary antibody at a dilution of 1:5000 at 4°C over night (supplementary table A.8). The membrane was then washed three-times in TBS-T each for 10 min. Dependent on the species of the primary antibody, the second antibody, coupled to horseradish peroxidase, was applied onto the membrane at room temperature for 60 min. After three additional washing steps in TBS-T, the membrane was exposed to Fusion-FX (Vilber Lourmat) using Western Lightning Plus-ECL solution (PerkinElmer). If several proteins were investigated, membranes were again washed three-times in TBS-T each for 10 min followed by a different antibody probing at 4°C over night. Membranes were then washed three-times in TBS-T followed by the secondary antibody probing at room temperature for 60 min. After three washing steps, the membrane was again exposed to the Fusion-FX.

3.4.5. Immunohistochemistry

Formalin-fixed, paraffin-embedded samples from 80 primary neuroblastomas were generously provided by the University Hospital in Cologne¹¹ and the Charité in Berlin¹². This

¹¹'Klinisches Studienzentrum Pädiatrie', 'Neuroblastomstudie', University Hospital in Cologne, Germany

¹²Department Pediatric Oncology and Hematology, Charité Universitätsmedizin Berlin, Germany

included 73 *MYCN* non-amplified and seven *MYCN* amplified tumors. The cohort was representative for the disease: eight tumors were graded as stage 1, 20 tumors as stage 2, eleven tumors as stage 3, 32 tumors as stage 4 and nine tumors as stage 4s (table 3.10).

Table 3.10.: *MYCN* status and INSS staging of neuroblastoma tumor sections.

	Stage 1	Stage 2	Stage 3	Stage 4	Stage 4s
<i>MYCN</i> amplified	0	0	3	4	0
<i>MYCN</i> non-amplified	8	20	8	28	9

Paraffin sections were dewaxed and subjected to an heat-induced epitope retrieval step prior to incubation with anti-PHGDH polyclonal rabbit antibody (Atlas Antibodies #HPA021241; dilution 1:100). For detection, EnVision+ System HRP-labelled polymer anti-rabbit antibody (Agilent) was used. HRP was visualized with diaminobenzidine (Agilent) as chromogen. Nuclei were counterstained with hematoxylin (Merck Millipore), and slides were coverslipped with glycerol gelatine (Merck). Negative controls were obtained by omitting the primary antibody. PHGDH-positive neuroblastoma cells and expression levels were determined in a semiquantitative manner using the AxioImager Z1 microscope (Carl Zeiss). Protocol establishment, all stainings and evaluations were performed in a blinded manner at the Core Unit 'Immunpathologie für Experimentelle Modelle' at the Charité Universitätsmedizin Berlin with support from Dr. A. Kühl.

3.5. Metabolomics

Pulsed stable isotope-resolved metabolomics (pSIRM) was applied to indirectly measure the metabolic flux within the central carbon metabolism and adjacent pathways [Pietzke et al., 2014]. Stable isotopes like $u\text{-}^{13}\text{C}$ -glucose were applied to the cells for short time periods followed by extraction of polar metabolites, derivatization and measurement in the gas chromatography coupled to mass spectrometry (GC-MS). The incorporation of stable isotopes within the central carbon metabolism intermediates combined with the quantification of metabolites are reflecting the metabolic pathway activity. Furthermore, nucleotide levels were measured by a method originally developed by P. Lorkiewicz and colleagues [Lorkiewicz et al., 2012] and adapted by N. Royla and G. Mastrobuoni [Dejure et al., 2017]. The method enables the measurement of nucleotides from the same sample as metabolites are identified and quantified.

3.5.1. Cell harvest

Adherent cells were seeded in 10 cm² plates with a defined cell number in order to ensure a confluency of 80% to the time point of harvest. Medium changes were performed 24 hours and 4 hours before harvest. In order to ensure proper comparison of cell lines, total and viable cell counts of three cell culture plates per cell line and condition were determined by semi-automated cell counting and trypan blue staining in the Vi-Cell-XR (BeckmanCoulter). In case stable isotopes were applied, an additional medium change was performed directly before harvest with medium supplemented with $u\text{-}^{13}\text{C}$ -glucose or $u\text{-}^{13}\text{C}$ -glutamine instead of the $u\text{-}^{12}\text{C}$ -glucose or $u\text{-}^{12}\text{C}$ -glutamine, respectively. Cell lines were incubated in the isotope labeled medium for experiment-defined time ranges reaching from 2, 5, 10 or 20 min for $u\text{-}^{13}\text{C}$ -glucose to 40 min for $u\text{-}^{13}\text{C}$ -glutamine application. Medium was discarded and cells were quickly washed with HEPES buffer (140 mM NaCl, 5 mM HEPES, pH 7.4 and supplemented with 2 mM glutamine and 2.5 g/L glucose) and quenched with 5 mL ice-cold 50% methanol (MeOH) containing 2 $\mu\text{g/mL}$ cinnamic acid as internal control for further sample preparation. Cells were scratched from the plate, transferred into falcons and stored at -20°C. Samples were transported on dry ice to the laboratory of Dr. S. Kempa¹³ for further sample preparation.

3.5.2. Extraction of polar metabolites

Polar metabolites were extracted by MeOH/chloroform/water extraction. One milliliter of chloroform was added to 5 mL of cell suspension in 50% MeOH. Samples were shaken at 4°C for one hour followed by centrifugation at 4°C with maximum speed for 10 min. After centrifugation, polar phases were split into two aliquots in order to ensure metabolite and

¹³Berlin Institute for Medical Systems Biology (BIMSB) at the Max-Delbrück Center for Molecular Medicine in the Helmholtz Association (MDC)

nucleotide measurement from the same sample. Polar phases were dried in the vacuum concentrator over night and stored for further preparation at -20°C.

3.5.3. Measurement of intracellular metabolites

Sample derivatization

Cell extracts, identification standards and quantification dilution series were put in the vacuum concentrator one hour ahead of derivatization in order to ensure proper evaporation of remaining liquid components. In all further steps, cell extracts and standards were treated in parallel. Derivatization was performed as described by [Kempa et al., 2009] with minor modifications. Briefly, 20 μ L of methoxyamine hydrochloride solution (40 mg/mL MeOx in 1 mL pyrimidine) were added to the samples followed by incubation in the thermomixer at 30°C, 1400 rpm for 90 min. In a second step, 80 μ L of N-methyl-N-[trimethylsilyl] trifluoroacetamide (MSTFA, containing a C17 alkane mixture) was added to the samples and shaken at 37°C for 60 min. The remaining MSTFA solution was transferred into a glass vial and used as a wash during GC-MS measurement. After incubation, samples were centrifuged at maximum speed for 10 min. Supernatants were split into three aliquots and transferred into glass vials for GC-MS measurement.

Gas chromatography - mass spectrometry measurement

Samples were subjected to gas chromatography coupled to a time-of-flight mass spectrometer (GC-ToF-MS, Pegasus IV-ToF-MS-System, LECO), complemented with an auto-sampler (MultiPurpose Sampler 2 XL, Gerstel). Injection of samples was done with a split mode of 1:5 (injection volume: 1 μ L) in a temperature-controlled injector (CAS4, Gerstel) with a baffled glass liner (Gerstel), running the temperature gradient as described in table 3.11.

Table 3.11.: GC-MS injection temperature program.

Step	Temperature	Time
Initial	80°C	30 sec
Ramp	12°C/min to 120 °C	
Ramp	7°C/min to 300 °C	
Hold	300°C	120 sec

Injected samples were separated by gas chromatography on an Agilent 78903 equipped with a VF-5 ms column (30 m length, 250 μ m inner diameter, 0.25 μ m film thickness) and helium as carrier gas (flow rate: 1.2 mL/min) running the temperature program as described in table 3.12.

Spectra were measured in a mass range of $m/z = 60$ to 600 mass units with 20 spectra/sec and a detector voltage of 1650 V.

Table 3.12.: GC temperature program for sample separation.

Step	Temperature	Time
Initial	70°C	120 sec
Ramp	5°C/min up to 120 °C	
Ramp	7°C/min up to 350 °C	
Hold	350°C	120 sec

Data analysis of GC-MS chromatograms

The data was initially analyzed in the ChromaTOF software (LECO, version 4.51.6.0). Retention times of alkanes, that were added to the samples during derivatization, were used to apply the Kovats retention index method. The method transforms retention times into the unit and system independent constant retention index (RI) [Kováts, 1958]. In a next step, the measured quantification dilution series consisting of eight quantification standards and the identification standards were used to identify the metabolites within the reference search of ChromaTOF. Mass spectra and mass isotopomer distributions were extracted from ChromaTOF by using the MetMax Software (MPIMP Golm, version 1.0.1.12) or the in-house developed software MAUI-VIA (version 1.0.5) [Kuich et al., 2015]. Sample preparation, data quality and machine performance were analyzed by using the in-house developed R-based script. Evaluation of the peak areas from the quantification dilution series enabled the quantification of identified metabolites within the cell lines. Quantification values were normalized to the internal standard cinnamic acid and cell count and calculated in pmol/1E+06 cells. Masses used for absolute quantification are listed in the supplementary table A.14. u-¹³C-glucose and u-¹³C-glutamine incorporation rates were corrected for natural abundance of isotopes by subtracting the mass isotope distribution of unlabeled metabolites from labeled metabolites. Mass isotopes used for calculating incorporation rates are listed in the supplementary section (supplementary table A.15).

3.5.4. Measurement of intracellular nucleotides

Sample preparation

Sample preparation for nucleotide measurement was performed with minor modifications as described by Lorkiewicz and colleagues [Lorkiewicz et al., 2012]. The dried cell extracts were resuspended in 5 mM buffer A (5 mM hexylamine, pH 6.3, adjusted with acetic acid) to end up with material corresponding to 3E+05 cells in 10 μ L. Samples and nucleotide calibration standards (10 μ M - 20 nM in buffer A) were centrifuged at 4°C, maximum speed for 5 min. Ten microliter of sample or calibration standard were transferred into a new tube on ice. Nucleotides were extracted, and samples were desalted by using ZipTips (Merck Millipore). Briefly, ZipTips were activated by aspirating and discarding 5 times 10 μ L of MeOH and equilibrated by aspirating and discarding 5 times 10 μ L of buffer A. Samples

and standards were loaded onto the solid phase by eight cycles of aspiration and dispensation followed by four washing cycles with buffer A. Nucleotides were eluted by aspirating and dispensing twelve times 10 μ L elution buffer (70% buffer A, 30% buffer B (90% MeOH, 10% ammonium acetate, pH 8.5, adjusted with ammonium hydroxide)). Eluted samples were mixed with 20 μ L MeOH and subjected to direct-infusion mass spectrometry.

Direct-infusion mass spectrometry measurement

Measurement of nucleotides was performed by direct-infusion mass spectrometry on a TSQ Quantiva triple quadrupole mass spectrometer (Thermo Scientific) coupled to a Triversa Nanomate nanoESI ion source (spray voltage: 1.5 kV, head gas pressure: 0.5 psi) and argon used as collision gas (pressure: 1.5 mTorr). FWHM Resolution for both Q1 and Q3 was set at 0.7. Data acquisition was run for 3 min per sample, using a cycle time of 3.3 sec and total acquisition of 55 SRM scans for each nucleotide. The sum of the two best transitions for each nucleotide were acquired in negative mode (supplementary table A.16).

Data analysis of direct-infusion mass spectrometry spectra

The software Xcalibur (Thermo Fisher Scientific, version 4.0.27.13) was used to manually check the quality of each measurement. Data was further processed with the OpenMS package, and machine performance was analyzed with an in-house written R-script. Calibration standards were used to control for a valid quantification range above the signal-to-noise threshold.

3.6. Proteomics

3.6.1. Sample preparation

Cell line harvest

In order to ensure proper integration of protein and metabolite data in later data analysis, protein lysates were harvested in the same experiment as polar metabolites (section 3.5.1). Briefly, cells were cultivated in 10 cm² plates, and medium was exchanged 24 and 4 hours before harvest. Adherent cells were directly harvested from the plate by discarding the medium followed by one washing step with PBS and adding 1.5 mL urea buffer (8 M urea in 100 mM Tris-HCl, pH 8.5). Cells were scratched from the plates, transferred into 15 mL falcons and immediately frozen at -20°C. For further sample preparation, falcons were transferred on dry ice to the lab of Dr. S. Kempa¹⁴.

Tissue disruption

Patient biopsies were cut on ice, and 4 - 13 mg of tissue were mixed with zirconia beads and 200 μ L urea buffer (8 M urea in 100 mM Tris-HCl, pH 8.5). Mechanical disruption was performed in the Precellys 24 homogeniser (Bertin Technologies) at 6500 min⁻¹ in two cycles each for 20 sec. After each cycle, samples were cooled down on ice. Following disruption of the tissue, samples were centrifuged at maximal speed at 4°C for 4 min. Supernatants were transferred into a new vial and stored at -20°C.

3.6.2. Protein quantification

Colorimetric protein quantification was carried out using the Pierce BCA Protein Assay (Thermo Fisher Scientific) according to the manufacturers protocol. Briefly, 2 μ L of cell lysate, bovine serum albumin (BSA) standard dilution series (50 - 10000 μ g/mL in PBS) or PBS were mixed together with 100 μ L working solution in a 96-well plate with subsequent incubation at room temperature for 30 min. The absorbance was measured at λ =562 nm in the Infinite200 (Tecan). Each sample was measured in technical duplicates. PBS was used as a blank control to correct for the background signal.

3.6.3. Protein digestion

Denaturation and alkylation of protein samples was achieved prior to digestion by adding 2 mM DTT and incubation at room temperature for 30 min followed by treatment with 11 mM iodoacetamide and incubation at room temperature in the dark for 15 min. In total, 100 μ g of protein extracted from cell lines and 50 μ g of protein extracted from tumor tissues were digested for the proteome analysis. Protein digestion was performed with

¹⁴Berlin Institute for Medical Systems Biology (BIMSB) at the Max-Delbrück Center for Molecular Medicine in the Helmholtz Association (MDC)

Lys-C (gentle shaking at 30°C over night) at a ratio of 1:40 (w/w) and 7-9 μL immobilized trypsin beads (gentle shaking at 30°C for 4 hours). Samples were diluted four times with 50 mM ammonium bicarbonate between Lys-C and trypsin treatment. Digestion was stopped through acidification after addition of 10 μL trifluoroacetic acid. Further sample processing was performed with 18 μg of protein digest. The remaining sample was frozen at -20°C. Digested proteins were desalted and purified on Stage Tips. Membranes within the Stage Tips were activated and equilibrated by addition of 50 μL 100% MeOH and 50 μL buffer A (0.5% acetic acid (v/v)) with subsequent centrifugation at 300 $\times g$ for 7 min, respectively. Peptide digest was loaded on the membranes and washed once with 50 μL 0.5% acetic acid (v/v). Elution of peptides was performed by adding 0.5% acetic acid (v/v) in 80% acetonitrile. Eluates were dried down in the vacuum concentrator, resuspended in 10 μL 0.5% acetic acid (v/v) and sonicated at 20°C for 5 min [Rappsilber et al., 2007].

3.6.4. Liquid chromatography - mass spectrometry measurement

Desalted and purified peptide mixtures were analyzed by liquid chromatography (NanoLC 400, Eksigent) coupled to tandem mass spectrometry (Q Exactive HF, Thermo Fisher Scientific) measurement (LC-MS/MS) in a shotgun proteomics approach [Yates, 2013]. Five microliter of sample were injected and each sample was measured in technical duplicates. The nanospray source was operated with a spray voltage differing in the range from 2.1 to 2.4 kV between experiments and ion transfer tube temperature of 260°C. Samples were loaded on the column with a flow rate of 450 nL/min. Elution was performed with a flow rate of 400 nL/min using a 240 min gradient ranging from 5% to 40% of buffer B (80% acetonitrile and 0.1% formic acid) in buffer A (5% acetonitrile in 0.1% formic acid). Chromatographic separation was performed on a 200 cm long MonoCap C18 HighResolution 2000 column (GL Sciences). The column was washed with 90% buffer B (80% acetonitrile and 0.1% formic acid) for 10 min and subsequent equilibration in buffer A (5% acetonitrile in 0.1% formic acid) in between runs. Data were acquired in data-dependent mode with one survey MS scan (resolution: $R=120,000$ at m/z 200) followed by a maximum of ten MS/MS scans (resolution: $R=30,000$ at m/z 200, intensity threshold: 5,000) of the most intense ions. Once ions were fragmented they were automatically excluded from further measurement for 45 sec to improve acquisition of low-abundant ions.

3.6.5. Data analysis

Raw data from LC-MS/MS measurements were analyzed by using the MaxQuant software (version 1.5.3.30) [Cox and Mann, 2008] and the build-in Andromeda search engine with the human Uniprot database (38,538 protein entries) and a common contaminants database (245 protein entries). MaxQuant identifies peptide sequences from mass spectra, assembles them into proteins and calculates label-free quantification (LFQ) intensities that are used

in further data analysis for protein quantification [Cox et al., 2014]. Carbamidomethylation of cysteines was chosen as a fixed modification, oxidation of methionine and acetylation of N-terminus were chosen as variable modifications. Two missed cleavage sites were allowed and peptide tolerance was set to 7 ppm. The search engine peptide assignments were filtered at 1% false-discovery rate at both the peptide and protein level. All other parameters were left as default. In order to keep the LFQ intensities calculation isoform specific, calculation was only performed on unique and unmodified peptides within the MaxQuant software. The minimum LFQ ratio count was set to two and a MS/MS spectrum was always required for LFQ comparison of the precursor ion intensities. Data quality was controlled with the in-house developed R-script PTXQC [Bielow et al., 2016]. Further data analysis was performed with the Perseus software (version 1.6.0.2) [Tyanova et al., 2016], [Cox and Mann, 2012].

3.7. Patient-derived xenograft

The efficacy of the PHGDH inhibitors NCT503 and P2101 was investigated in the *MYCN*-amplified neuroblastoma patient-derived xenograft #14647 in cooperation with the Experimental Pharmacology & Oncology company in Berlin, Germany. In addition to the monotherapy, a combination therapy with the chemotherapeutic drug cisplatin was tested on its anti-tumor activity in male NOG mice. Randomization of neuroblastoma engrafted NOG mice to treatment groups was realized with significant tumor growth three weeks after tumor fragment transplantation. Daily intraperitoneal treatment with NCT503 (40 mg/kg) and P2101 (20 mg/kg) started on day 20 post transplantation for 24 subsequent days. Cisplatin was applied intravenously once a week and started on day 20 post transplantation for 24 subsequent days with 2 mg/kg in the first week and adaptation to 1 mg/kg at the second week. Control mice were injected intraperitoneally with 0.2 mL of 10% DMSO and 0.1% Tween in PBS daily and intravenously with 0.1 mL of 0.9% sodium chlorid once a week. Body weight and tumor size measurements were performed every third day. Animals were euthanized when tumor size reached 1.5 cm³.

3.8. Statistics

GraphPad Prism Software (version 7) and R-Studio software (version 1.1.463) with R (version 3.5.1) were used for statistical analysis of the data. All data are presented as mean \pm standard deviation (SD). Except for patient-derived xenograft data and proliferation assays where area under the curve (AUC) values were used, statistical analysis was performed on single values. The two-tailed Student's t-test with Welch's correction was applied to test significance between cell lines and treatments. Significance levels were set as follows: * $0.01 < p \leq 0.05$; ** $0.001 < p \leq 0.01$; *** $p \leq 0.001$. Sample sizes differ between experiments and are indicated in the figure legends.

4 Results

4.1. Identification of MYCN-dependent metabolic targets

We aimed for identifying key metabolic pathways associated to high-level MYCN expression. In a first approach, the genetically engineered clones SH-EP-Tet21/N and SH-SY5Y^{MYCN} with adjustable MYCN levels were used to perform quantitative metabolomics in combination with the application of ¹³C-substrates. In a second approach, neuroblastoma cell lines and primary biopsies from patients with neuroblastoma were analyzed in a shotgun proteomics approach.

4.1.1. Synthetic MYCN expression in neuroblastoma cells

Two tetracycline-inducible models, SH-EP-Tet21/N [Lutz et al., 1996] and SH-SY5Y^{MYCN}, were used as clonal sublines that suppress or express MYCN, respectively. The SH-EP-Tet21/N cell line contains a tet-off system which represses the MYCN construct by addition of tetracycline in the culture medium. Contrary, the SH-SY5Y^{MYCN} cells contain a tet-on system which induces MYCN by adding tetracycline to the culture medium.

Before investigating the relationship between the oncogene *MYCN* and neuroblastoma metabolism, the tetracycline-inducible models were characterized. MYCN expression was monitored at 24, 48, 72 and 96 hours on both the mRNA and protein levels using qRT-PCR and western blotting. Cell cycle profiles were assessed at 72 and 96 hours using propidium iodide staining coupled with FACS analysis. Proliferation was assessed at 24, 48, 72 and 96 hours using trypan blue staining and semi-automated cell counting.

Stable high-level MYCN expression for up to 96 hours was achieved on mRNA and protein level by changing the growth medium every 24 and 48 hours in SH-EP-Tet21/N and SH-SY5Y^{MYCN} cultures, respectively (figure 4.1). Moreover, MYCN expression was also detected with minimal intensity when MYCN was not induced. Further analysis of this observation revealed a higher MYCN expression in the non-induced SH-EP-Tet21/N and SH-SY5Y^{MYCN} cells compared to the parental cell lines (supplementary figure B.1). We therefore concluded that SH-EP-Tet21/N and SH-SY5Y^{MYCN} cells harbor a leakiness in their MYCN constructs. This finding may be of high importance when studying MYCN-dependent effects as genes with high affinity to MYC are already bound by endogenous

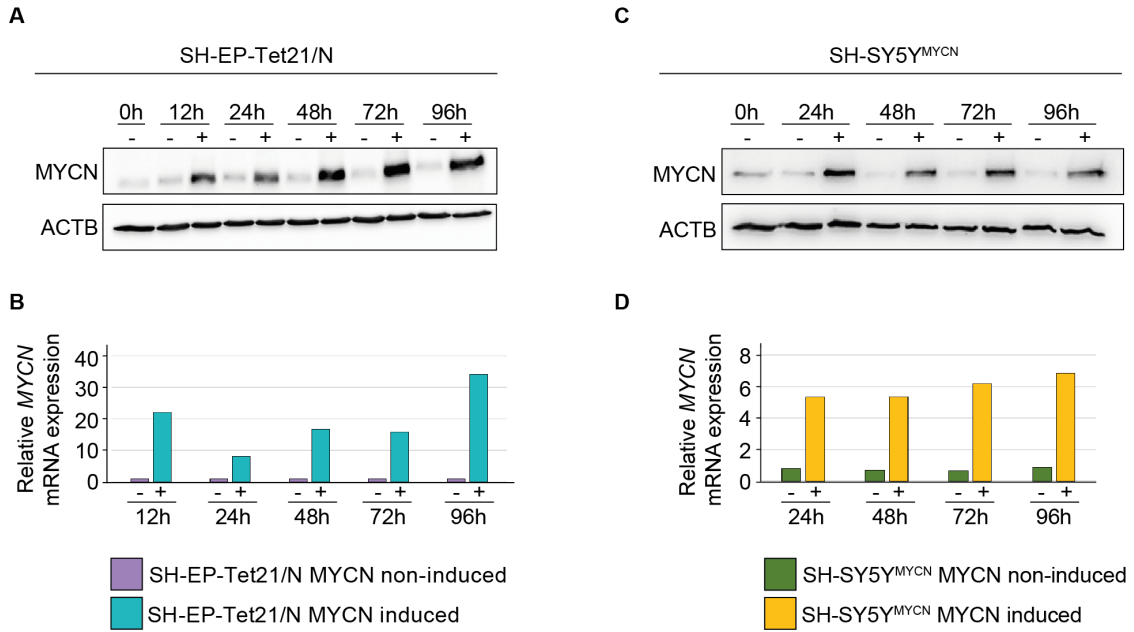


Figure 4.1.: MYCN expression in SH-EP-Tet21/N and SH-SY5Y^{MYCN}. Representative immunoblotting (A/C) and qRT-PCR data (B/D) showing non-induced (-) and induced (+) MYCN expression in SH-EP-Tet21/N (A/B) and SH-SY5Y^{MYCN} (C/D) cells monitored at 24, 48, 72 and 96 hours.

MYC levels and do not recruit additional MYC upon overexpression [Lorenzin et al., 2016].

Cell cycle analysis was performed with SH-EP-Tet21/N cells induced to express high-level MYCN. We observed an up to 1.7-fold enrichment of cells in S and a 1.2-fold enrichment of cells in G2/M as well as a 1.2-fold reduction in cells in G0/G1 after 96 hours compared to non-induced control cells (figure 4.2A). In line with the cell cycle analysis, proliferation of MYCN-overexpressing SH-EP-Tet21/N cells was increased by 1.5 and 1.9-fold at 72 and 96 hours, respectively compared to the parental SH-EP cell line or non-induced SH-EP-Tet21/N cells (figure 4.2B). Culturing SH-SY5Y^{MYCN} cells in the presence of tetracycline to enforce MYCN expression for 72 and 96 hours caused a 1.3 and 1.4-fold increase in proliferation compared to non-induced SH-SY5Y^{MYCN} cells or to the SH-SY5Y parental cell line (figure 4.2C). The parental cell lines SH-EP and SH-SY5Y were cultured in the presence of tetracycline to ensure that this antibiotic is not interfering with the proliferation behavior of cells harboring no tetracycline-inducible construct. Methanol was added to the culture medium as solvent control.

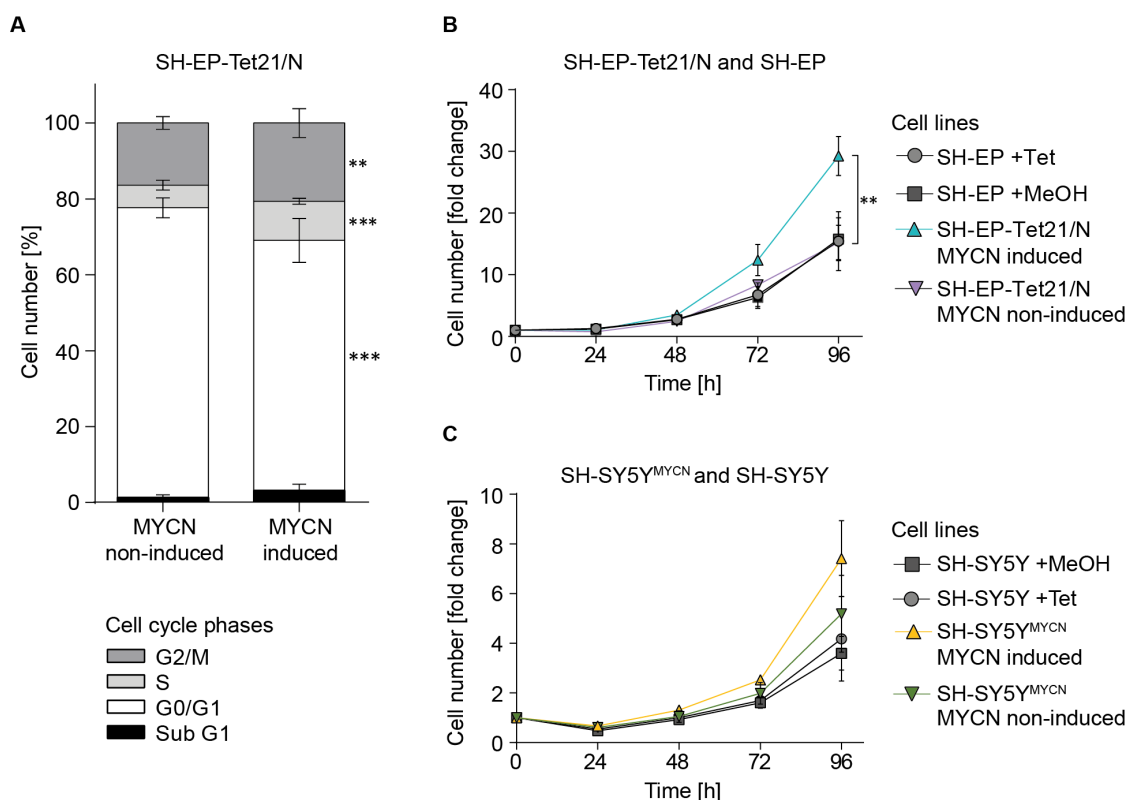


Figure 4.2.: Accelerated proliferation under MYCN overexpression. A: Cell cycle profiles were monitored after 96 hours in MYCN-induced and non-induced SH-EP-Tet21/N cells using propidium iodide staining coupled with fluorescence activated cell sorting (FACS) analysis. B: Proliferation assay of MYCN-induced and non-induced SH-EP-Tet21/N and SH-SY5Y^{MYCN} cells and the parental control cell lines SH-EP and SH-SY5Y. Results represent mean \pm SD, $n=3$ for SH-EP-Tet21/N and $n=2$ for SH-SY5Y^{MYCN}, each in three technical replicates. P-values were calculated with AUC values, using an unpaired Student's t -test (* $0.01 < p \leq 0.05$; ** $0.001 < p \leq 0.01$; *** $p \leq 0.001$). Abbreviations: MeOH - Methanol, Tet - Tetracycline.

Following the observation of a stable high MYCN expression, SH-EP-Tet21/N cells were used to examine MYCN-dependent changes of the metabolome. SH-EP-Tet21/N cells were induced for 96 hours to express high-level MYCN by removal of tetracycline from the culture medium. The parental SH-EP cells were also included in the analysis and served as control cells. In order to track the fate of carbon-13 among the intermediates of the CCM, cells were cultured in medium supplemented with u - ^{13}C -glucose for 20 min or u - ^{13}C -glutamine for 40 min. Additionally, cells were also harvested in medium containing non-labeled glucose and glutamine as reference. Polar metabolites were extracted from induced and non-induced SH-EP-Tet21/N cells as well as from SH-EP cells with solvent controls (1 $\mu\text{g}/\text{mL}$ tetracycline or methanol). Carbon-13 incorporation was determined by subsequent GC-MS measurement. Z-score transformed absolute metabolite quantities in SH-EP-Tet21/N and SH-EP cells are illustrated in figure 4.3. SH-EP cell lines with solvent control (tetracycline or methanol) were clustered together. Surprisingly, no obvious changes in metabolite concentrations were observed between MYCN-induced and MYCN

non-induced SH-EP-Tet21/N cells.

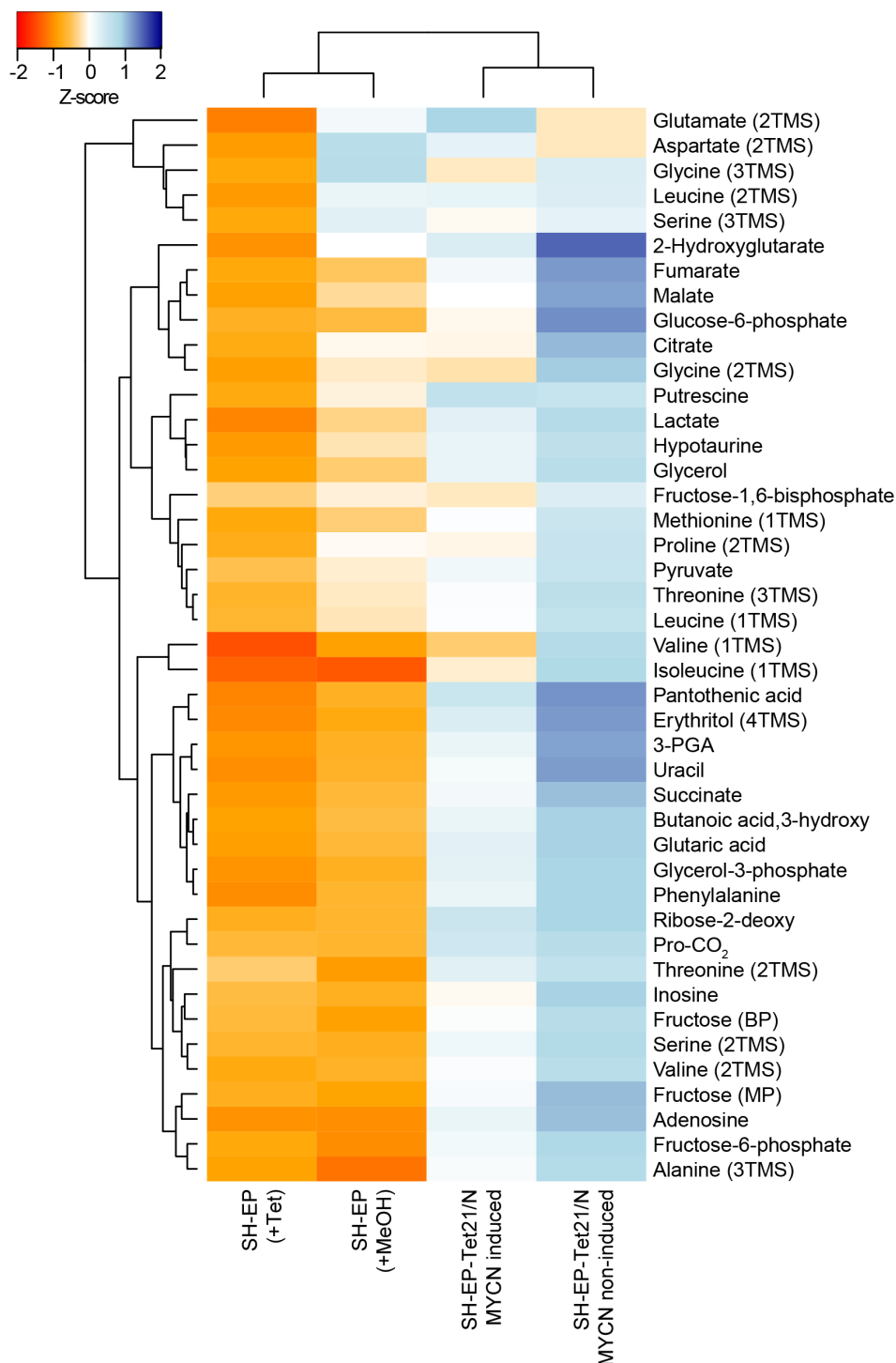


Figure 4.3.: Z-score transformed metabolite intensities in MYCN non-amplified SH-EP cells with solvent controls and SH-EP-Tet21/N cells with induced and non-induced MYCN expression. Results represent mean \pm SD, n=3. Abbreviations: Tet - Tetracycline, MeOH - Methanol.

In line with the metabolite quantities, the incorporation of glucose-derived carbon-13 showed no changes towards an accelerated glycolysis. The incorporation of carbon-13 derived from glutamine revealed no change on TCA cycle activity under MYCN induction. Two intermediates of the glycolysis, lactate and pyruvate, and two intermediates of the TCA cycle, malate and succinate, are illustrated in figure 4.4.

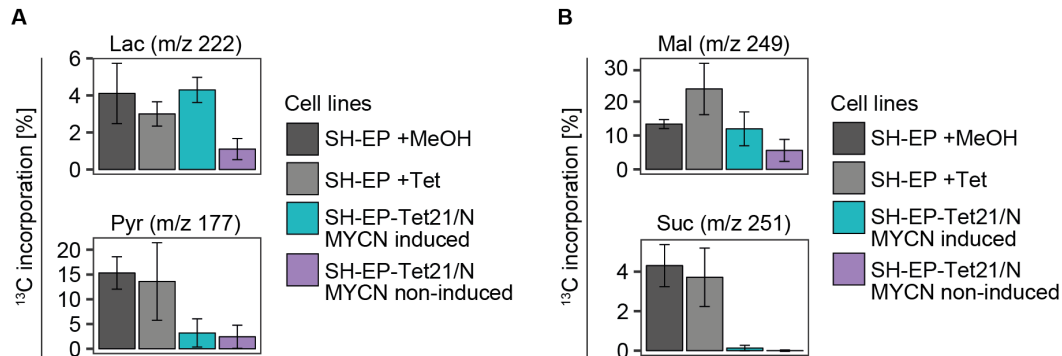


Figure 4.4.: Effects of MYCN induction on u-¹³C-substrate incorporation. SH-EP-Tet21/N were cultured for 96 hours with induced or non-induced MYCN expression. Before harvest, cell medium was changed to medium containing u-¹³C-glucose for 20 min (A) or u-¹³C-glutamine for 40 min (B). Polar metabolites were extracted, derivatized and subjected to GC-MS measurement. Results represent mean \pm SD, n=3. Abbreviations: Lac - Lactate, Mal - Malate, Pyr - Pyruvate, Suc - Succinate.

4.1.2. Unbiased proteomics approach

The proteome of primary biopsies from neuroblastoma patients (n=49) and a neuroblastoma cell line panel (n=15) including the MYCN-inducible models SH-EP-Tet21/N and SH-SY5Y^{MYCN} was analyzed in order to decipher expression changes in CCM proteins under deregulated MYCN expression. Primary biopsies and cell lines included were either *MYCN* non-amplified, had a gain or were *MYCN*-amplified. A MYCN score in the range of 5 to -5 was determined based on the MYCN levels (3.2 & table 3.3). Samples were digested, purified and measured by a shotgun proteomics approach with liquid chromatography coupled to mass spectrometry [Yates, 2013].

A total of 7,038 proteins was identified in the primary biopsies. In order to be quantified, a protein needed to be identified in at least 35% of all samples, resulting in a total of 2,319 quantified proteins. In the neuroblastoma cell line panel a total of 1,965 proteins was quantified out of 5,957 identified proteins. A spearman correlation analysis of protein expression and MYCN levels was performed using the LFQ's and the determined MYCN score, respectively. In a first approach, all proteins known to be targets of MYCN from literature research (supplementary table B.1) were used for correlation analysis. A direct correlation of all targets to the MYCN score was observed for those known to be upregulated by MYCN, and an inverse correlation of those known to be downregulated by MYCN. Nevertheless, the MYCN target hexokinase 2 (HK2) did not show the expected direct

correlation to MYCN (figure 4.5).

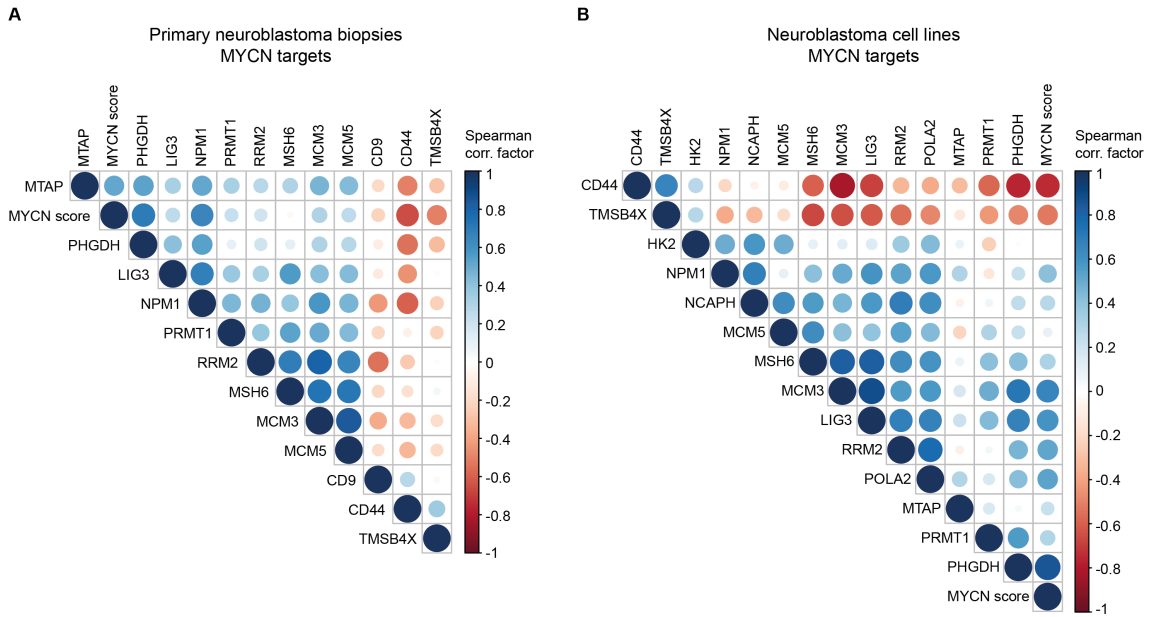


Figure 4.5.: Spearman correlation analysis with hierarchical clustering after shotgun proteomics displaying known MYCN target genes. Proteins identified with LC-MS with a least one unique peptide were correlated to the MYCN levels of neuroblastoma patient biopsies (A) and cell lines (B). Hierarchical clustering of Spearman correlation factor displayed a high correlation of proteins known to be MYCN targets from literature.

In a second step, we used the data from the cell line panel and subjected 47 proteins located within the CCM to the correlation analysis. We found 20 proteins to be directly correlated and 27 proteins to be inverse correlated to the MYCN score (figure 4.6).

Interestingly, a subcellular compartment-specific correlation was observed. The majority of directly correlated proteins (n=14) were localized in the mitochondria whereas the inverse correlated proteins were localized predominately in the cytosol (n=20). Moreover, an isoform-switch of some proteins from the cell line panel was observed, e.g. aconitate hydratase (ACO). The cytoplasmic ACO1 was inversely correlated and the mitochondrial ACO2 was directly correlated to the MYCN score (figure 4.6). ACO1 and ACO2 catalyze the isomerization of citrate to isocitrate via cis-aconitate in the cytoplasm and the mitochondria, respectively [UniprotKB, P21399 and Q99798]. We performed the same approach with the CCM proteins from the primary neuroblastoma biopsies without observing any of the above described effects, indicating a specific protein signature *in vivo* (supplementary figure B.2).

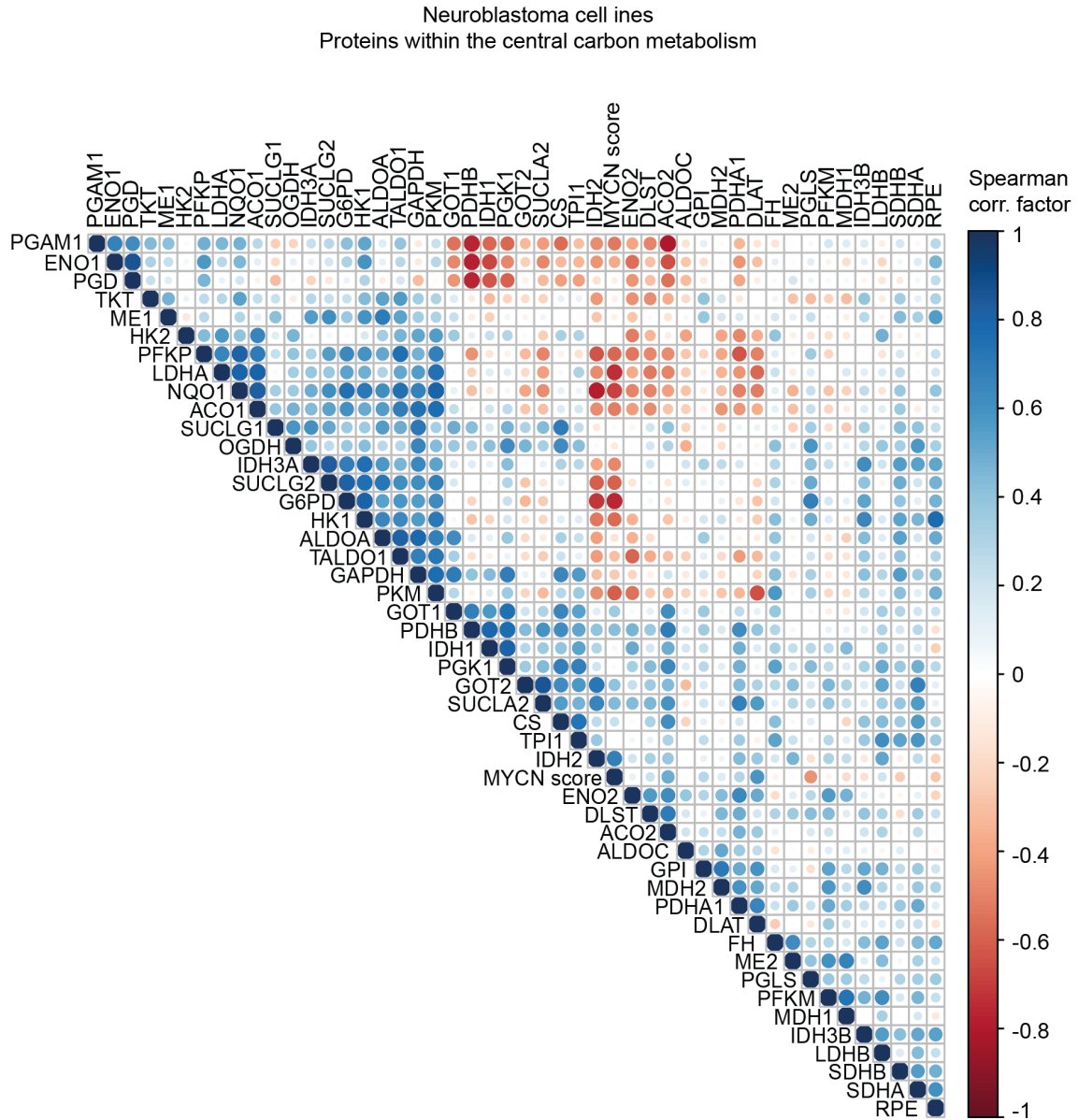


Figure 4.6.: Spearman correlation analysis with hierarchical clustering after shotgun proteomics displaying proteins within the central carbon metabolism. Proteins identified with LC-MS with a least one unique peptide were correlated to the MYCN levels of neuroblastoma cell lines. Hierarchical clustering of Spearman correlation factor of CCM proteins to the MYCN score.

In a next step, all quantified proteins of the primary neuroblastoma biopsy samples were sorted by their five most highest and lowest Spearman correlation factors ρ (table 4.1). The proteins with highest correlation factors to MYCN (descending order) were phosphoglycerate dehydrogenase (*PHGDH*), pyrroline-5-carboxylate synthase (*ALDH18A1*), nucleophosmin (*NPM1*), tubulin-tyrosine ligase-like protein 12 (*TTL12*), and UDP-glucose 6-dehydrogenase (*UGDH*). *PHGDH* catalyzes the reversible oxidation of 3-PGA to 3-phosphohydroxypyruvate (pOH-Pyr), which is the first step of the *de novo* serine biosynthesis pathway [Locasale, 2013]. High *PHGDH* levels are reported in various cancer entities including triple-negative breast cancer [Possemato et al., 2011], melanoma [Locasale et al., 2011], glioma [Liu et al., 2013], cervical cancer [Jing et al., 2013], and neuroblastoma [Liu et al., 2016]. Pyrroline-5-carboxylate synthase is a bifunctional enzyme that converts glutamate to glutamate-5-semialdehyde, an intermediate in the biosynthesis of proline, ornithine and arginine [UniProtKB, P54886]. Nucleophosmin binds to single-stranded nucleic acids and is involved in diverse cellular processes such as ribosome biogenesis, centrosome duplication, protein chaperoning, histone assembly, cell proliferation and TP53 and ARF regulation [UniProtKB, P06748]. The *NPM1* gene is also described in literature as a target gene of MYCN [Zeid et al., 2018]. Tubulin-tyrosine ligase-like protein 12 is a protein with ligase activity and binds ATP and nucleotides [UniProtKB, Q14166]. UDP-glucose 6-dehydrogenase is involved in the carbohydrate metabolism [UniProtKB, O60701].

The strongest inverse correlating proteins to MYCN in the tumor samples were syntaxin-12 (*STX12*), proton ATPase (*ATP6V1C1*), guanine nucleotide-binding protein (*GNAI1*), f-actin-capping protein (*CAPZA2*) and CD44. Syntaxin-12 regulates the protein transport between late endosome and the trans-Golgi network [UniProtKB, Q86Y82]. The proton ATPase is a subunit of the peripheral V1 complex of vacuolar ATPase, required for the assembly of the catalytic domain of the enzyme. Vacuolar ATPases are ATP-dependent proton pumps that acidify endocytic compartments in eukaryotic cells [UniProtKB, P21283]. The guanine nucleotide-binding protein functions as a transducer downstream of G protein-coupled receptors in numerous signaling cascades [UniProtKB, P63096]. The f-actin-capping protein binds to the fast growing ends of actin filaments [UniProtKB, P47755]. CD44 is cell-surface receptor which mediates cell-cell and cell-matrix interactions [UniProtKB, P47755]. The protein was already described in 1993 as a prognostic marker in neuroblastoma [Favrot et al., 1993].

Table 4.1.: Top 5 MYCN-correlating proteins in primary biopsies sorted by ascending and descending Spearman correlation factors (ρ).

Gene name	Correlation factor ρ	Biological process
<i>PHGDH</i>	0.71	Serine biosynthesis
<i>ALDH18A1</i>	0.66	Proline biosynthesis
<i>NPM1</i>	0.65	Host-virus interaction, chaperon, RNA-binding
<i>TTLL12</i>	0.65	ATP and nucleotide binding
<i>UGDH</i>	0.65	Carbohydrate metabolism
<i>STX12</i>	-0.71	Protein transport
<i>ATP6V1C1</i>	-0.69	Ion transport
<i>GNAI1</i>	-0.68	Cell cycle/division, transport
<i>CAPZA2</i>	-0.66	Actin cytoskeleton organization
<i>CD44</i>	-0.66	Cell adhesion

We next sorted all quantified proteins within the neuroblastoma cell line panel by their Spearman correlation factor ρ (table 4.2). Proteins with the strongest correlation to MYCN were phosphoglycerate dehydrogenase (*PHGDH*), RNA helicases DDX1 and DDX17, cytochrome c oxidase (*COX5A*) and acetyl-CoA acetyltransferase (*ACAT2*). DDX1 and DDX17 are ATP-dependent RNA helicases that unwind RNAs and alter RNA structures through ATP binding and hydrolysis [UniProtKB, Q92499 & Q92841]. The cytochrome c oxidase catalyzes reactions within the mitochondrial electron transport chain [UniProtKB, P10606]. Acetyl coenzyme A acetyltransferase is involved in lipid metabolic processes [UniProtKB, Q9BWD1].

Table 4.2.: Top 5 MYCN-correlating proteins in the neuroblastoma cell line panel sorted by ascending and descending Spearman correlation factors (ρ).

Gene name	Correlation factor ρ	Biological process
<i>PHGDH</i>	0.86	Serine biosynthesis
<i>DDX1</i>	0.82	Transcription regulation, nucleotide-binding
<i>DDX17</i>	0.82	Transcription regulation, nucleotide-binding
<i>COX5A</i>	0.81	Mitochondrial electron transport
<i>ACAT2</i>	0.78	Lipid metabolic processes
<i>PEA15</i>	-0.91	Apoptosis, sugar transport
<i>ITGB1</i>	-0.89	Cell adhesion
<i>ARHGAP1</i>	-0.89	GTPase activation
<i>VIM</i>	-0.86	Host-virus interaction
<i>PSME1</i>	-0.86	Immunoproteasome assembly

Proteins identified within the neuroblastoma cell line panel that show the highest inverse correlation to MYCN were astrocytic phosphoprotein PEA-15, integrin beta-1 (*ITGB1*), GTPase-activating protein (*ARHGAP1*), vimentin (*VIM*) and the proteasome activator complex (*PSME1*). The phosphoprotein PEA-15 blocks RAS-mediated inhibition of integrin activation and modulates the ERK MAP kinase cascade. It also mediates

apoptosis inhibition and regulates glucose transport by controlling the glucose transporters GLUT1 and GLUT4 [UniProtKB, Q15121]. Integrin-beta mediates cell adhesion processes [UniProtKB, P05556]. The GTPase-activating protein activates Rho, Rac and Cdc42 proteins [UniProtKB, Q07960]. Vimentin is attached laterally or terminally to the nucleus, the endoplasmic reticulum and the mitochondria [UniProtKB, P08670]. The proteasome activator complex subunit 1 is required for efficient antigen processing [UniProtKB, Q06323].

Overall, proteins directly correlating to high-level MYCN expression were notably involved in amino-acid biosynthesis, such as PHGDH and ALDH18A1. PHGDH was listed as the strongest direct correlating protein to high-level MYCN expression in the primary patient samples and in the cell line panel with Spearman correlation factors of 0.71 and 0.86, respectively (table 4.1 & 4.2). PHGDH is the rate-limiting enzyme in *de novo* serine synthesis and a precursor protein for the one-carbon metabolism. Subsequent spearman correlation analysis revealed a strong correlation of all proteins within the one-carbon metabolism to high-level MYCN expression (figure 4.7).

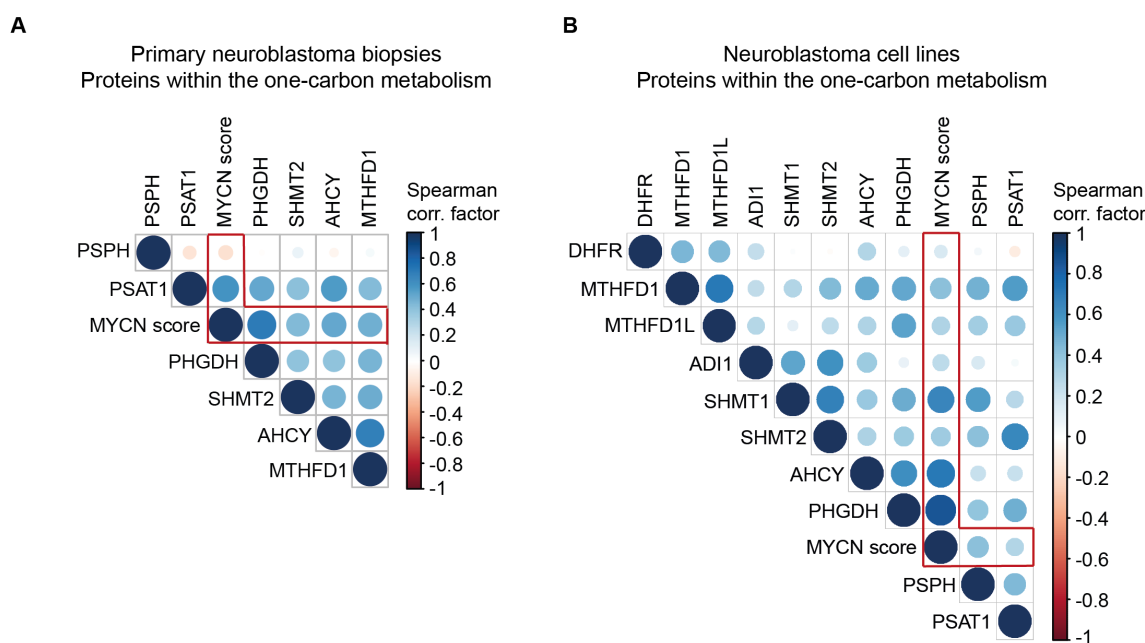


Figure 4.7.: Spearman correlation analysis with hierarchical clustering after shotgun proteomics displaying proteins within the one-carbon metabolism. Proteins identified with LC-MS with a least one unique peptide were correlated to the MYCN levels of neuroblastoma patient biopsies (A) and cell lines (B). Hierarchical clustering of Spearman correlation factor displayed a high correlation of proteins within the one-carbon metabolism pathway to MYCN.

In summary, we observed a stable high-level MYCN expression in the genetically engineered clones SH-EP-Tet21/N and SH-SY5Y^{MYCN}. However, we could not detect any MYCN-dependent changes in CCM intermediates. Spearman correlation analysis of proteins identified from primary neuroblastoma biopsies and cell lines revealed a strong

correlation between MYCN expression and the expression of proteins within the *de novo* serine synthesis pathway and the one-carbon metabolism. PHGDH was the highest correlating protein to MYCN in both panels.

4.2. *In vitro* and *in vivo* characterization of PHGDH in neuroblastoma

4.2.1. MYCN transcriptionally activates PHGDH

In order to verify the strong correlation between MYCN and PHGDH, RNA extracts and protein lysates of seven *MYCN*-amplified and five *MYCN* non-amplified neuroblastoma cell lines were used for qRT-PCR and western blotting analysis. All *MYCN*-amplified cell lines showed a higher PHGDH expression compared to the *MYCN* non-amplified cell lines on transcriptional (figure 4.8A) and translational (figure 4.8B) level.

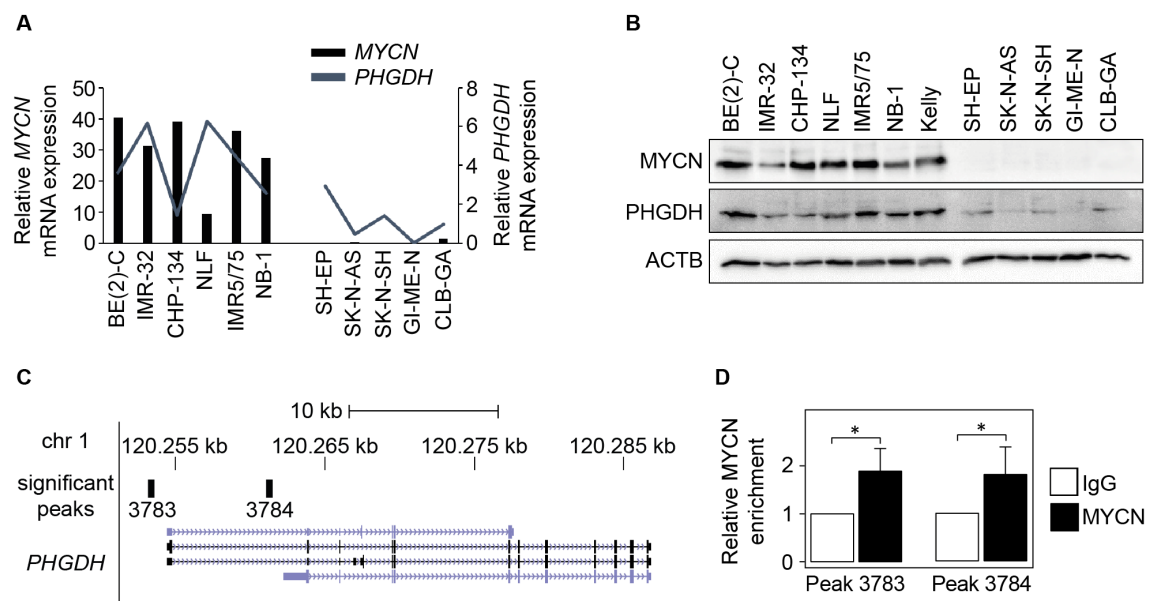


Figure 4.8.: MYCN-mediated transcriptional activation of PHGDH. qRT-PCR (A) and representative immunoblot (B) showed MYCN and PHGDH expression in seven *MYCN*-amplified and five *MYCN* non-amplified neuroblastoma cell lines. C: Open-access ChIP sequencing data from SK-N-BE(2)-C cell lysates revealed two enrichment locations (Peak 3783 and Peak 3784) of MYCN in the PHGDH promoter region (vertical lines). D: ChIP qRT-PCR analysis with BE(2)-C cell lysates immunoprecipitated with antibodies against MYCN or IgG (negative control) confirmed the recruitment of MYCN to PHGDH promoter sequences corresponding to peaks 3783 and 3784. Bars represent mean fold changes over the IgG control (\pm SD), p-values were calculated using an unpaired Student's t-test (* $0.01 < p \leq 0.05$; ** $0.001 < p \leq 0.01$; *** $p \leq 0.001$), $n=4$.

Open-access sequencing data of immunoprecipitated MYCN of SK-N-BE(2)-C cells (Hsu et al. Oncotarget, 2016; GEO accession: GSE72640) was used to analyze whether MYCN is recruited to the *PHGDH* promoter region. The predictive sequences were blasted in the genome data viewer (schematic model based on the GRCh37/hg19 UCSC genome browser) and revealed an enrichment of MYCN within chromosome 1 in the *PHGDH* promoter regions 120,253,334-120,253,470 (Peak 3783) and 120,261,235-120,261,331 (Peak 3784) (figure 4.8C). To validate the computational analysis, *MYCN*-amplified BE(2)-C

cells were harvested according to the ChIP protocol (section 3.3.6). The chromatin was fragmented by ultrasound, and immunoprecipitation was performed against MYCN and control IgG. After elution of co-immunoprecipitated chromatin fragments, qRT-PCR was performed with primers framing the two predicted binding sites within the promoter region of *PHGDH*. Both regions showed an enrichment by 2-fold over IgG control which argues for a recruitment of MYCN to the *PHGDH* promoter region (figure 4.8D).

4.2.2. ATF4-mediated regulation of PHGDH

Work from Liu and colleagues on mouse neuroblastoma sphere-forming cells showed an ATF4-mediated transcriptional activation of *PHGDH* [Liu et al., 2016]. Based on this data we performed an siRNA-mediated *ATF4* knockdown and quantified ATF4 and PHGDH protein expression by western blotting. Knockdown efficiency of ATF4 protein was higher in SH-EP cells with a decrease of 36% compared to BE(2)-C cells in which ATF4 protein expression was reduced by 14%. The siRNA-mediated *ATF4* knockdown resulted in a significant reduced PHGDH protein expression by 43% and 48% in BE(2)-C and SH-EP cells, respectively (figure 4.9).

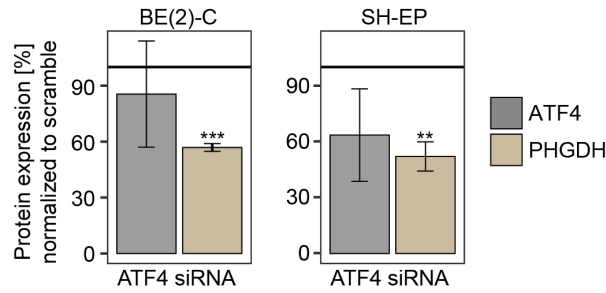


Figure 4.9.: *ATF4* knockdown downregulates *PHGDH* expression. BE(2)-C and SH-EP cells were subjected to an siRNA-mediated *ATF4* knockdown. ATF4 and PHGDH protein expression were quantified by immunoblotting. Results represent mean \pm SD, n=3. P-values were calculated using an unpaired Student's t-test (* $0.01 < p \leq 0.05$; ** $0.001 < p \leq 0.01$; *** $p \leq 0.001$).

4.2.3. Effects of PHGDH on *de novo* serine synthesis

PHGDH converts 3-PGA, derived from glucose in the glycolysis, into pOH-Pyr, a precursor of *de novo* serine synthesis. pOH-Pyr is further converted by transamination and phosphate ester hydrolysis into serine. Our previous results have shown that *MYCN*-amplified neuroblastoma cells harbor a high PHGDH expression level. In order to test whether enhanced PHGDH expression results in a higher *de novo* serine pathway usage, BE(2)-C (*MYCN*-amplified) and SH-EP (*MYCN* non-amplified) cells were exposed to culture medium containing fully labeled u-¹³C-glucose for 2, 5, 10 and 20 min before harvest. Subsequent GC-MS measurement enabled the measurement of metabolite abundances (figure 4.10) as well as the measurement of stable isotope incorporation, derived from carbon-13 (figure 4.11). 3-PGA, alanine and serine pools were significant lower in SH-EP compared to BE(2)-C cells. Lactate pools were significant higher in the SH-EP cells compared to BE(2)-C cells. Citrate and fumarate pool sizes remained at constant levels (figure 4.10).

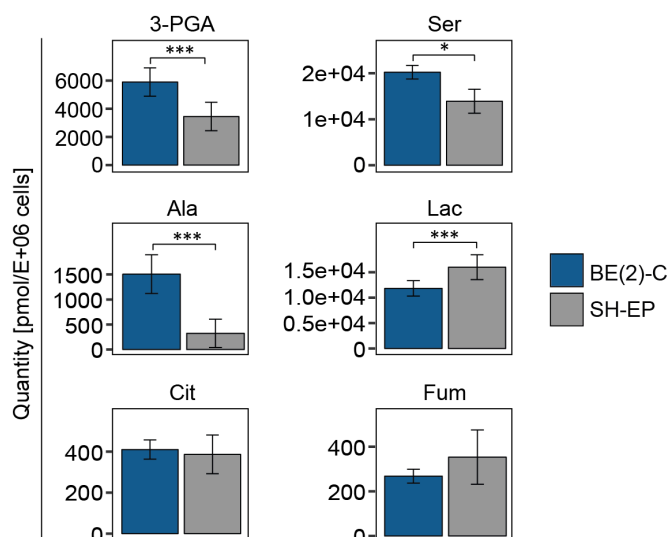
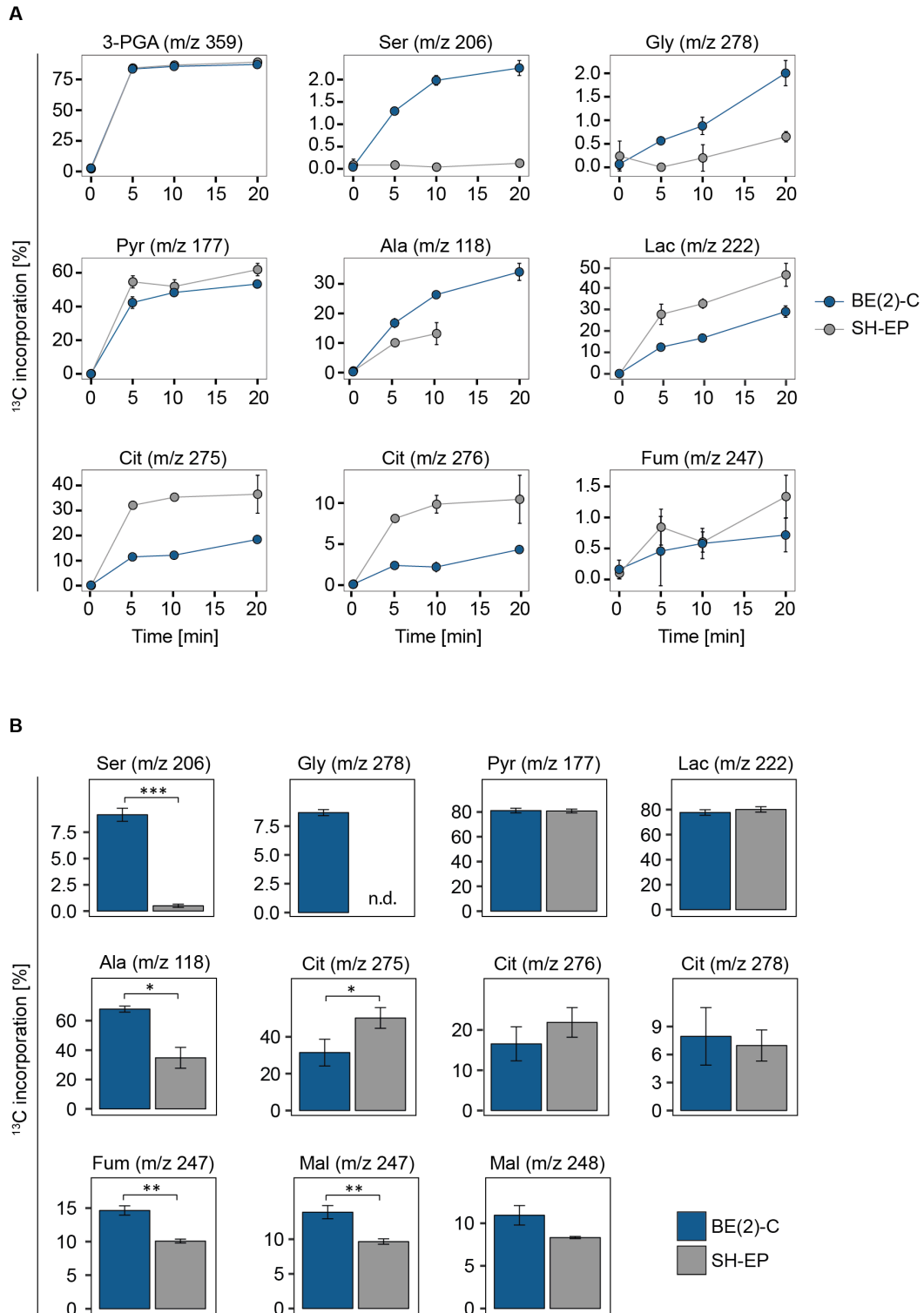


Figure 4.10.: Absolute quantification of metabolites after GC-MS measurement. Polar metabolites were extracted from BE(2)-C and SH-EP cells. Samples were subjected to GC-MS for metabolite measurement. Results represent mean \pm SD, n=3. P-values were calculated using an unpaired Student's t-test (* $0.01 < p \leq 0.05$; ** $0.001 < p \leq 0.01$; *** $p \leq 0.001$). Abbreviations: 3-PGA - 3-Phosphoglycerate, Ala - Alanine, Cit - Citrate, Lac - Lactate, Fum - Fumarate, Ser - Serine.

The incorporation of carbon-13 into intermediates of the central carbon metabolism increased in dependence of incubation time of the cells in the medium containing fully labeled glucose (figure 4.11A). As expected, glucose was directed into *de novo* serine and glycine synthesis pathway only in the *MYCN*-amplified BE(2)-C cells, which showed 2.5% carbon-13 incorporation into serine and a 2% label incorporation into glycine after 20 min labeling time. The percentage of u-¹³C-glucose incorporation into pyruvate did not differ between BE(2)-C and SH-EP cells. In SH-EP cells, glucose was predominately directed

into lactate and the TCA cycle intermediates citrate and fumarate, whereas in BE(2)-C cells glucose was predominately directed into serine and alanine.

In order to determine the maximal incorporation rate of u- ^{13}C -glucose into the intermediates of the CCM, BE(2)-C and SH-EP cells were exposed to medium containing u- ^{13}C -glucose for six hours. Polar metabolites were extracted, derivatized and measured by GC-MS. Incorporation of glucose-derived carbon-13 into serine and glycine reached 9% in BE(2)-C cells and was rarely detectable in SH-EP cells with 0.5% incorporation into serine. Glycine was not detectable in the SH-EP cells. Although, BE(2)-C cells showed a higher *de novo* serine synthesis compared to SH-EP cells, they still require around 91% of their serine from other sources. One possibility is the import of serine and glycine from the surrounding environment which is analyzed in section 4.3. Incorporation of u- ^{13}C -glucose into pyruvate and lactate did not differ between the cell lines. Incorporation into alanine was double in the BE(2)-C cells compared to the SH-EP cell line. Citrate, fumarate and malate were measured as representative metabolites of the TCA cycle. ^{13}C -glucose incorporation was detected in citrate m/z 275, m/z 276 and m/z 278 and malate m/z 248, indicating the routing of glucose-derived carbons through the citrate synthase as well as through the pyruvate carboxylase to enter the TCA cycle in both cell lines. Incorporation into fumarate and malate was higher in the BE(2)-C compared to the SH-EP cell line (figure 4.11B).



4.2.4. Subcellular localization of PHGDH

In order to define the subcellular localization of PHGDH, 80 primary tumor tissue slides were stained with hematoxylin/eosin and an anti-PHGDH antibody (Atlas Antibodies HPA021241). Hematoxylin stains all nuclei in blue, and eosin stains all mitochondria, plasma proteins, collagen and creatinin in red. PHGDH, stained in brownish colour, was predominately expressed in *MYCN*-amplified tumor tissues and was expressed homogeneously in the cytosol (figure 4.12).

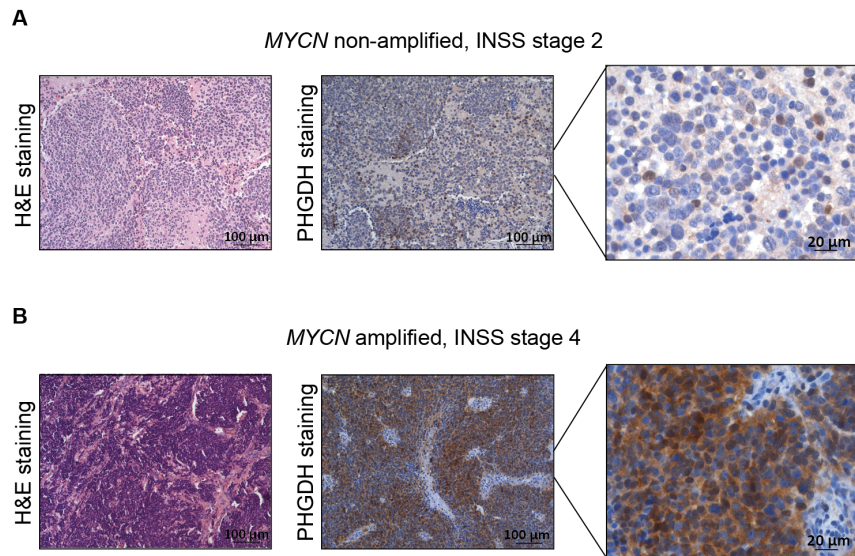


Figure 4.12.: Representative immunohistochemical staining of primary neuroblastoma tissue samples. PHGDH was localized homogenously in the cytosol. *MYCN*-amplified tumors showed a higher staining intensity of PHGDH compared to *MYCN* non-amplified tumors, n=80.

4.2.5. Clinical relevance

A computational genomics analysis of neuroblastoma gene expression profiles was performed to analyze the clinical relevance of *PHGDH* mRNA expression in neuroblastoma tumors for overall survival of patients. The R2 platform, developed by Jan Koster in the Academic Medical Center Amsterdam, Netherlands¹ was used to compare the *MYCN* and *PHGDH* expression levels of 643 neuroblastoma samples. *MYCN*-amplified tumors (n=93) correlated with a higher PHGDH expression compared to *MYCN* non-amplified tumors (n=550) (figure 4.13A). The Kaplan-Meyer curve indicated the unfavorable overall survival probability of patients harboring a high *PHGDH* expression compared to those with low *PHGDH* expression (figure 4.13B).

¹R2: Genomics Analysis and Visualization Platform (<http://r2.amc.nl>)

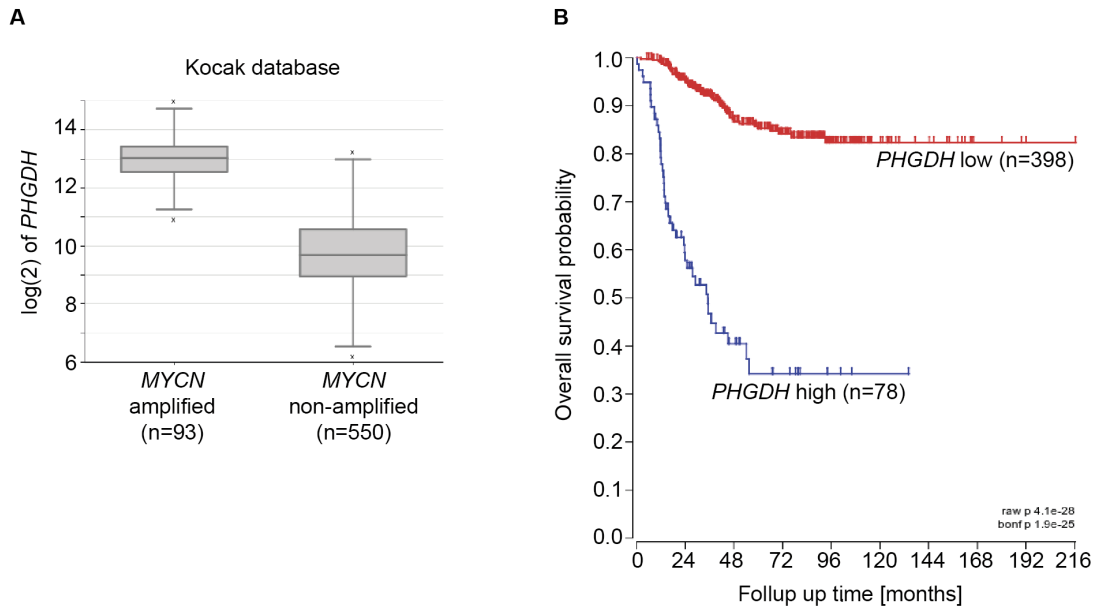


Figure 4.13.: *PHGDH* mRNA expression in neuroblastoma patients. A: Kocak database visualized via the R2 database by Jan Koster, Amsterdam, Netherlands revealed a correlation between *MYCN* amplification and high *PHGDH* expression in neuroblastoma tumors. B: Patients with high *PHGDH* mRNA expression had an unfavorable overall survival probability compared to those harboring a low *PHGDH* mRNA expression level.

4.3. Influence of serine and glycine starvation on PHGDH regulation

4.3.1. *MYCN*-amplified cells are independent of exogenous serine and glycine supply

We have identified a strong correlation between amplified *MYCN* and high-level PHGDH expression *in vitro* and *in vivo*. We further showed in *in vitro* experiments an enhanced *de novo* serine synthesis in *MYCN*-amplified cells compared to *MYCN* non-amplified cells. Besides *de novo* serine synthesis, cells can also import serine and glycine from the extracellular environment by transporters. In order to evaluate the effects of depleted serine and glycine pools in the culture medium on cell proliferation and *de novo* serine synthesis activity, BE(2)-C and Kelly (*MYCN*-amplified) as well as SH-EP and SK-N-AS neuroblastoma cell lines (*MYCN* non-amplified) were cultured in medium depleted for serine and glycine for 96 hours (figure 4.14A). Total and viable cell count was measured every 24 hours and used for calculating the fraction of non-viable cells between treatment and control (figure 4.14B). Semi-quantitative analysis of PHGDH expression was performed via western blotting (figure 4.15A) and proteins of the *de novo* serine synthesis pathway were measured by shotgun proteomics (figure 4.15B) after 48 hours of serine and glycine starvation in BE(2)-C and SH-EP.

The *MYCN* non-amplified cell lines SH-EP and SK-N-AS decreased their cell count by 3 and 2.4-fold, respectively under serine and glycine starvation for 96 hours. The *MYCN*-amplified cell lines BE(2)-C and Kelly revealed an accelerated proliferation under the same condition (figure 4.14A). The fraction of non-viable cells after 96 hours was not modified between cells cultured with serine and glycine or without, except for SK-N-AS (figure 4.14B).

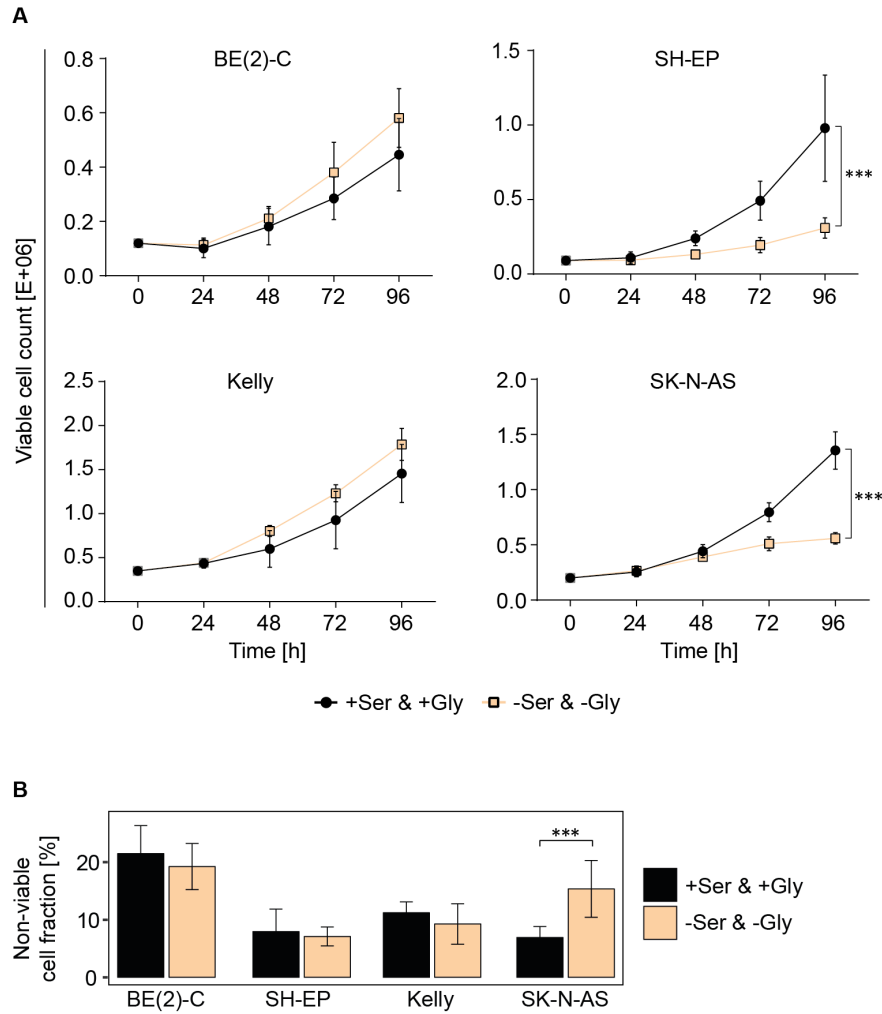


Figure 4.14.: Proliferation measurement of BE(2)-C, Kelly, SH-EP and SK-N-AS in control (+Ser & +Gly) and serine and glycine depleted condition (-Ser & -Gly). A: Proliferation rate was changing under serine and glycine starvation in dependence of the MYCN status. *MYCN*-amplified cell lines showed a slightly higher proliferation rate under serine and glycine starvation whereas the *MYCN* non-amplified cell lines arrested proliferation under serine and glycine starvation. Results represent mean \pm SD, $n=3$ each in three technical replicates. P-values were calculated with AUC values, using an unpaired Student's t-test (* $0.01 < p \leq 0.05$; ** $0.001 < p \leq 0.01$; *** $p \leq 0.001$). B: Fraction of non-viable cells was only increased in serine and glycine starved SK-N-AS cells. Results represent mean \pm SD, $n=3$, each in three technical replicates. P-values were calculated using an unpaired Student's t-test (* $0.01 < p \leq 0.05$; ** $0.001 < p \leq 0.01$; *** $p \leq 0.001$).

We observed an upregulation of PHGDH protein expression in the *MYCN* non-amplified SH-EP cells after 48 hours of serine and glycine starvation by western blotting (figure 4.15A). In contrast, the *MYCN*-amplified BE(2)-C cells did not alter its endogenous PHGDH expression levels. We identified a total of 5,613 proteins by shotgun proteomics of which 2,760 were quantified in BE(2)-C and SH-EP cells. The immunoblot result was verified as we observed increased expression levels of *de novo* serine synthesis proteins only in SH-EP cells under serine and glycine starvation (figure 4.15B). SHMT expressions were not changed in BE(2)-C cells but were antagonistically regulated in SH-EP cells with reduced SHMT1 and enhanced SHMT2 expression. The protein TYMS, which converts dUMP to dTMP by using a one-carbon unit from serine, was downregulated in BE(2)-C and SH-EP cells. We further observed a consistent expression in all other quantified proteins within the one-carbon metabolism.

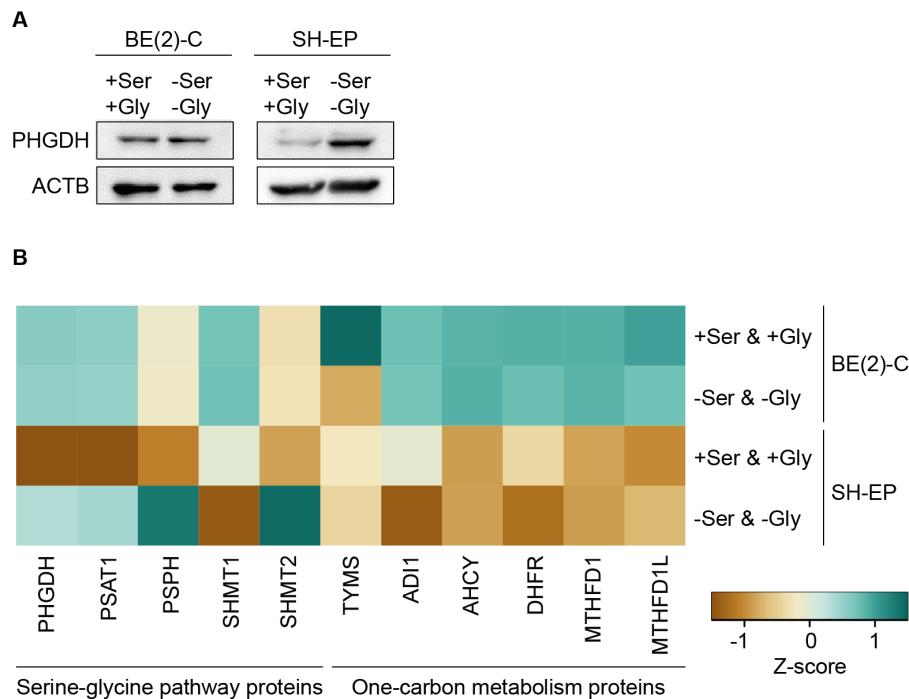


Figure 4.15.: Effects of serine and glycine starvation on the expression of proteins within the serine-glycine pathway and one-carbon metabolism. BE(2)-C and SH-EP cells were cultured in presence (+Ser & +Gly) and absence (-Ser & -Gly) of serine and glycine for 48 hours. A: Representative immunoblot showing no change in PHGDH expression in BE(2)-C cells, but enhanced PHGDH expression SH-EP cells under serine and glycine starvation. B: Shotgun-proteomics revealed no change in expression of proteins within the the serine and glycine pathway in BE(2)-C cells by serine and glycine starvation. A general upregulation of expression in all proteins within the *de novo* serine synthesis pathway was observed in the SH-EP cell line. Expression levels of one-carbon metabolism proteins were not altered in BE(2)-C and SH-EP cells by serine and glycine starvation. Results represent mean \pm SD, n=3.

4.3.2. ATF4-mediated regulation of PHGDH under serine and glycine starvation

GCN2, a serine-threonine kinase, binds to uncharged tRNAs and thereby senses intracellular amino acid depletion. It inactivates eIF2 α through phosphorylation at serine 51 resulting in inactivation of global protein synthesis but also in enhanced expression of selected mRNAs, such as *ATF4*. The transcription factor ATF4 is described by Xia and colleagues to induce *PHGDH* expression in a positive feedback loop together with MYCN in neuroblastoma [Xia et al., 2019]. In order to analyze whether neuroblastoma cells are following the described mechanistic cascade to upregulate PHGDH expression, BE(2)-C and SH-EP cells were starved for serine and glycine for 48 hours. Protein lysates were extracted and used for western blot analysis. This starvation induced no regulation of the observed proteins in BE(2)-C cells (Fig 4.16A). In SH-EP cells, GCN2 was upregulated, eIF2 α was phosphorylated and ATF4 expression was increased (Fig 4.16B).

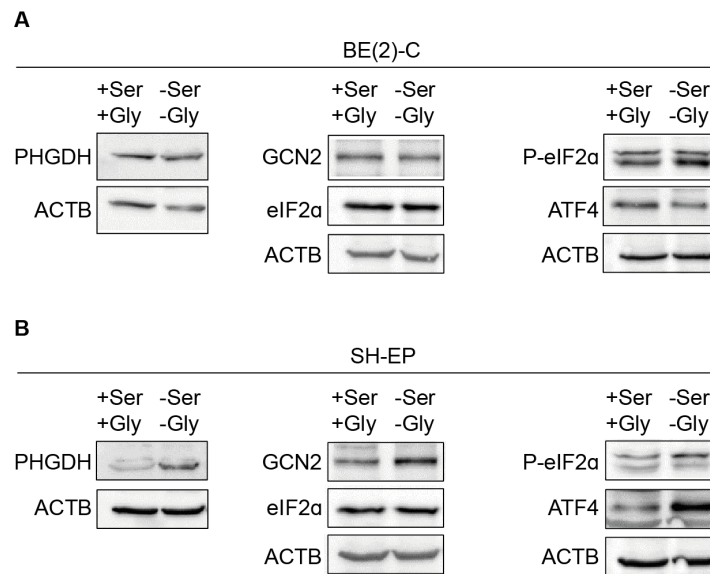


Figure 4.16.: Regulation of GCN2-eIF2 α kinase and ATF4 under serine and glycine starvation. BE(2)-C (A) and SH-EP cells (B) were cultured in the presence (+Ser & +Gly) and absence (-Ser & -Gly) of serine and glycine for 48 hours. Protein expression was measured by immunoblotting in four independent replicates (n=4) for P-eIF2 α , eIF2 α , PHGDH and MYCN, in three independent replicates (n=3) for GCN2 and in two independent replicates (n=2) for ATF4.

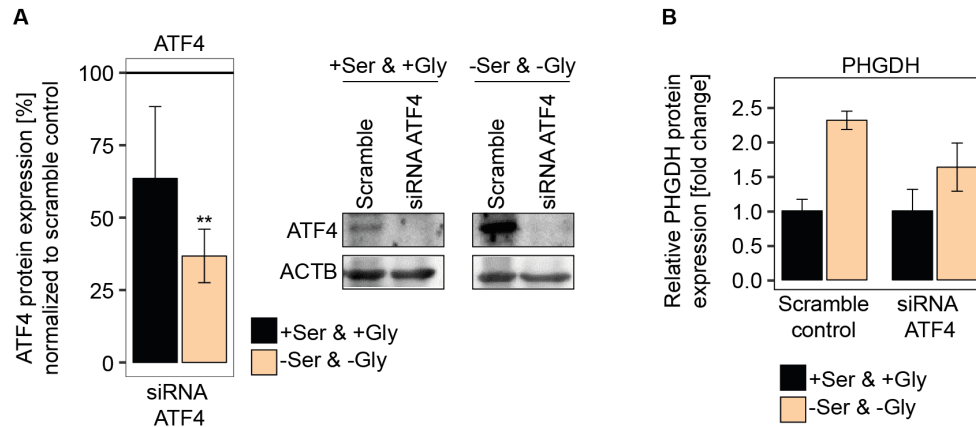


Figure 4.17.: Regulation of PHGDH expression by *ATF4* knockdown. SH-EP cells were transfected with siRNA-Pool targeting *ATF4* with subsequent cultivation in the presence (+Ser & +Gly) and absence (-Ser & -Gly) of serine and glycine for 72 hours. A: Quantification and representative immunoblot of ATF4 following siRNA treatment. B: Regulation of PHGDH following siRNA treatment in serine and glycine starved SH-EP cells. Results represent mean \pm SD, n=3. P-values were calculated using an unpaired Student's t-test (* $0.01 < p \leq 0.05$; ** $0.001 < p \leq 0.01$; *** $p \leq 0.001$), n=3.

We performed an siRNA-mediated knockdown of *ATF4* to investigate its role in PHGDH regulation in SH-EP cells under serine and glycine starvation. ATF4 protein expression was reduced to a higher extend in serine and glycine starved cells compared to non-starved cells due to enhanced ATF4 expression under starvation (figure 4.17A). Protein expression of PHGDH was decreased following *ATF4* knockdown in medium depleted for serine and glycine, indicating an ATF4-mediated regulation of PHGDH (figure 4.17B).

4.3.3. Metabolic effects triggered by serine and glycine starvation

Even though proteins within the *de novo* serine synthesis were upregulated, we have shown that SH-EP cells decreased proliferation under serine and glycine starvation. Contrary, BE(2)-C cells did not alter protein expression or proliferation. We therefore intended to investigate the metabolite and nucleotide levels in both cell lines. BE(2)-C and SH-EP cells were cultivated in the absence or presence of serine and glycine in the culture medium for 48 hours. Polar metabolites were extracted, and samples were measured by GC-MS and direkt-infusion MS for metabolite and nucleotide measurement, respectively.

Ribo- and deoxynucleotide abundances were not altered in serine and glycine starved BE(2)-C cells (figure 4.18A). However, a significant reduction in nucleotide levels was observed in starved SH-EP cells, except for all uridine-derived nucleotides, GTP, dAMP and dTMP (figure 4.18B). Whereas dUMP and dTMP levels were not altered, dTDP and dTTP levels decreased significantly.

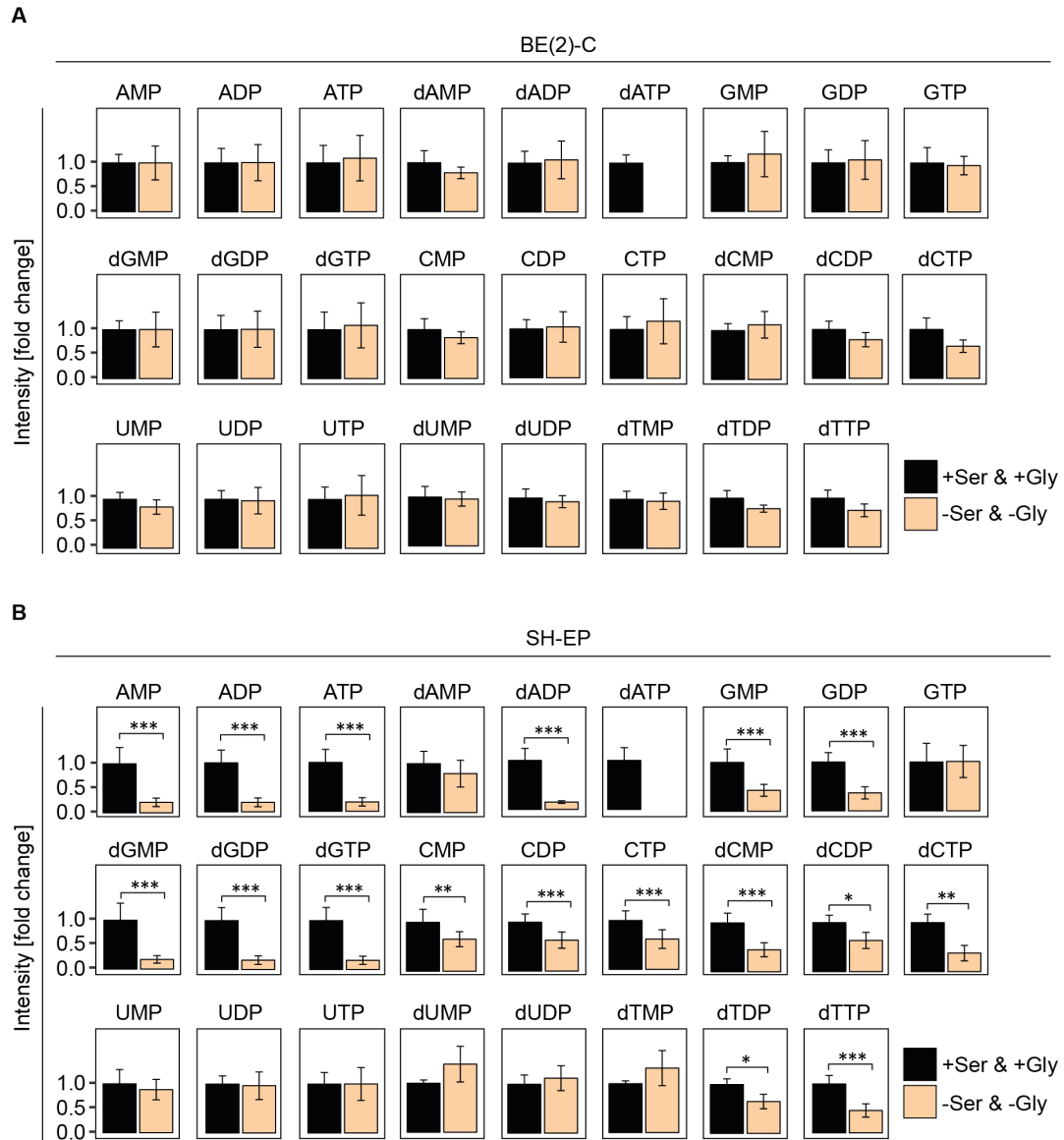


Figure 4.18.: Effects of serine and glycine starvation on nucleotide levels. BE(2)-C (A) and SH-EP cells (B) were cultivated in the presence (+Ser & +Gly) and absence (-Ser & -Gly) of serine and glycine for 48 hours. Results represent mean \pm SD, $n=3$. P-values were calculated using an unpaired Student's t-test (* $0.01 < p \leq 0.05$; ** $0.001 < p \leq 0.01$; *** $p \leq 0.001$).

Quantitative metabolomics analysis in combination with the application of $u\text{-}^{13}\text{C}$ -glucose revealed decreased routing of glucose into serine in BE(2)-C cells (figure 4.19A) and increased routing in SH-EP cells (figure 4.19B) by serine and glycine starvation. However, serine synthesis still remained 4-fold higher in BE(2)-C compared to SH-EP cells. Of note, serine synthesis was 90-fold higher in BE(2)-C compared to SH-EP cells in the presence of serine and glycine in the culture medium. In BE(2)-C cells, we further observed reduced pools of labeled 3-PGA, elevated pools of labeled lactate and fumarate and consistent levels of labeled alanine and citrate. In SH-EP cells, we determined a significant increase in labeled 3-PGA and alanine levels, decreased levels of labeled lactate and fumarate and no change in labeled citrate by serine and glycine starvation. The reduction in serine production in BE(2)-C cells by serine and glycine starvation might be due to an overestimation of the serine pool sizes in the control cells (supplementary figure B.3). Before cells were harvested, they were washed thoroughly with HEPES buffer. However, minimal serine and glycine residues from the culture medium might have remained in the culture plate. We therefore focused on the incorporation rates of $u\text{-}^{13}\text{C}$ -glucose and did not take into account the absolute pools of CCM intermediates.

Incorporation of $u\text{-}^{13}\text{C}$ -glucose into glycolytic intermediates, the *de novo* serine and glycine synthesis pathway and the TCA cycle in BE(2)-C and SH-EP cells is illustrated in figure 4.20. Around 77% of glucose-derived carbon-13 was incorporated into 3-PGA in the presence and absence of serine and glycine in BE(2)-C and SH-EP cells. Under serine and glycine starvation, $u\text{-}^{13}\text{C}$ -glucose incorporation into serine was significantly enhanced by 40-fold and 20-fold in BE(2)-C and SH-EP cells, respectively. Interestingly, the incorporation into glycine was not modulated in SH-EP cells. The starvation with another amino acid, glutamine, revealed no increased incorporation of glucose-derived carbons in serine (section 4.7.3). Incorporation of $u\text{-}^{13}\text{C}$ -glucose into TCA-cycle intermediates, such as citrate and fumarate remained at consistent levels in serine and glycine starved BE(2)-C and SH-EP cells. However, incorporation into lactate was significantly elevated in BE(2)-C cells and reduced in SH-EP cells. Incorporation into pyruvate was only decreased in SH-EP cells.

Long-term exposure of SH-EP cells to $u\text{-}^{13}\text{C}$ -glucose for six hours generally increased the incorporation in all investigated metabolites compared to 10 min of $u\text{-}^{13}\text{C}$ -glucose exposure (figure 4.20C). Six hours of $u\text{-}^{13}\text{C}$ -glucose exposure induced an elevated shuttling of $u\text{-}^{13}\text{C}$ -glucose into *de novo* serine synthesis (40-fold) in line with a decreased routing into lactate, alanine and pyruvate in serine and glycine starved SH-EP cells. Glycine was not detected in the measurement. No alterations in labeled citrate, fumarate and malate were detected in SH-EP cells cultured in medium containing serine and glycine compared to those without.

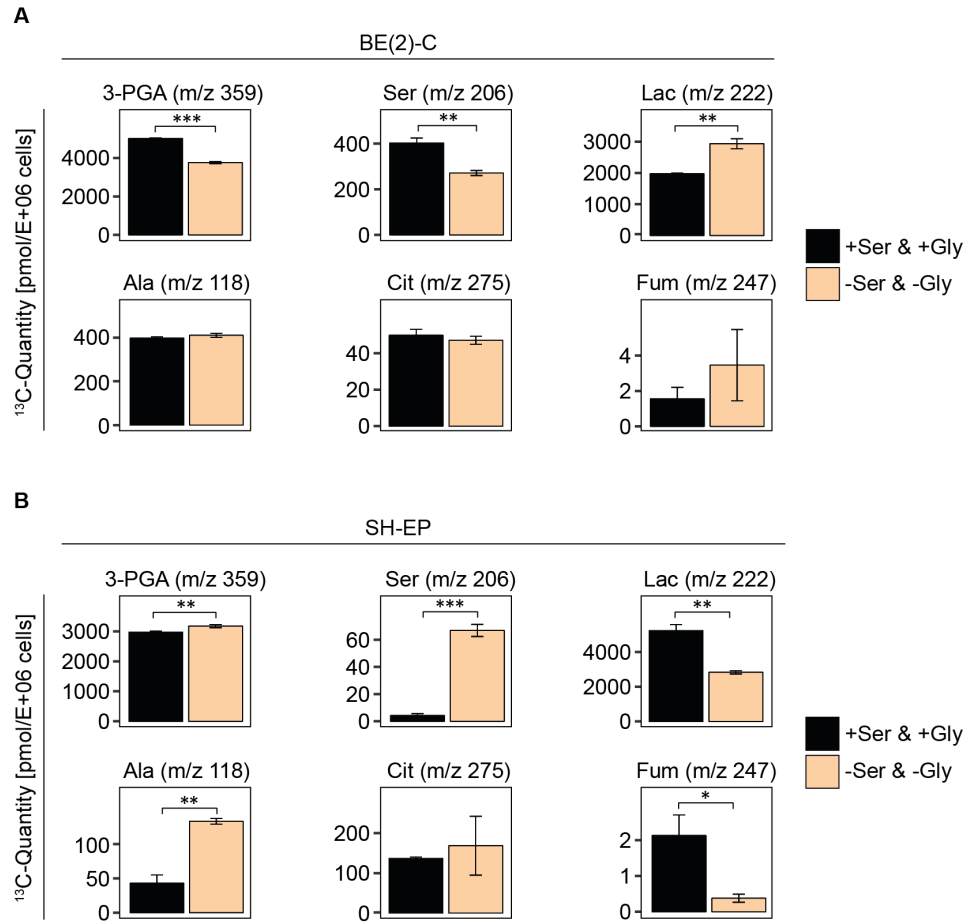


Figure 4.19.: Effects of serine and glycine starvation on u-¹³C-glucose quantities of CCM intermediates. BE(2)-C (A) and SH-EP cells (B) were cultivated in the presence (+Ser & +Gly) and absence (-Ser & -Gly) of serine and glycine for 48 hours with subsequent incubation in medium containing fully labeled ¹³C-glucose for 10 min before harvest. Results represent mean ± SD, n=3. P-values were calculated using an unpaired Student's t-test (* 0.01 < p ≤ 0.05; ** 0.001 < p ≤ 0.01; *** p ≤ 0.001). Abbreviations: 3-PGA - 3-Phosphoglycerate, Ala - Alanine, Cit - Citrate, Fum - Fumarate, Lac - Lactate, Ser - Serine.

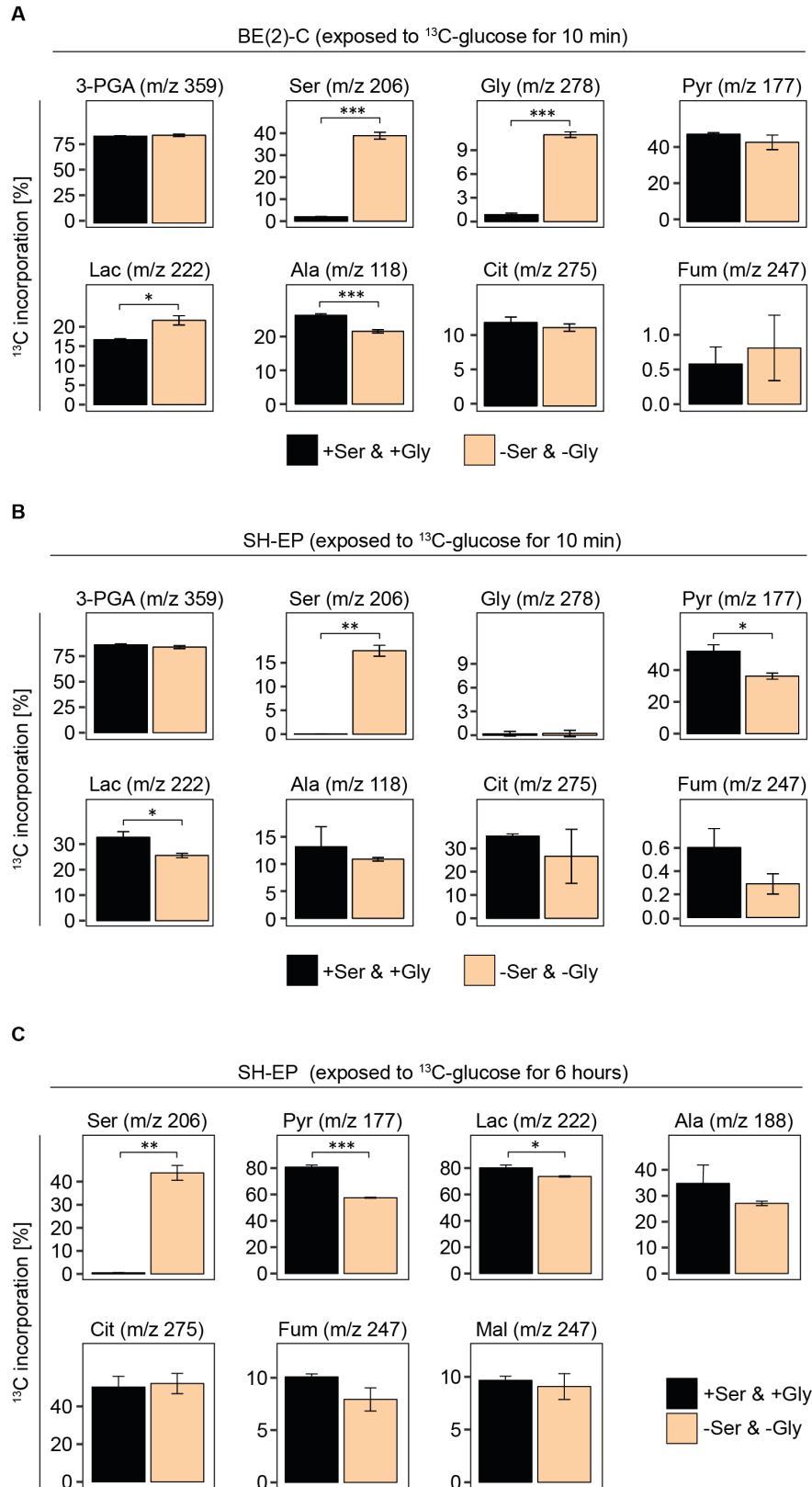


Figure 4.20.: Effects of serine and glycine starvation on u- ^{13}C -glucose incorporation. BE(2)-C (A) and SH-EP cells (B & C) were cultivated in the presence (+Ser & +Gly) and absence (-Ser & -Gly) of serine and glycine for 48 hours with subsequent incubation in medium containing fully labeled ^{13}C -glucose for 10 min (A & B) or six hours (C) before harvest. Results represent mean \pm SD, n=3. P-values were calculated using an unpaired Student's t-test (* $0.01 < p \leq 0.05$; ** $0.001 < p \leq 0.01$; *** $p \leq 0.001$). Abbreviations: 3-PGA - 3-Phosphoglycerate, Ala - Alanine, Cit - Citrate, Fum - Fumarate, Gly - Glycine, Lac - Lactate, Mal - Malate, Pyr - Pyruvate, Ser - Serine.

In summary, the *MYCN* non-amplified and low-level PHGDH-expressing SH-EP cell line is highly susceptible to serine and glycine starvation as shown by a significant decrease in proliferation and a depletion of nucleotide abundances. Compensatory mechanisms for serine and glycine starvation included an upregulation of *de novo* serine synthesis proteins including PHGDH, through mediation of ATF4, in line with a significant increase in *de novo* serine production. The *MYCN*-amplified and high-level PHGDH-expressing BE(2)-C cell line is independent of extracellular serine and glycine as shown by an unaltered proliferation, no change in the expression of *de novo* serine synthesis proteins and stable nucleotide levels under serine and glycine starvation. Routing of u-¹³C-glucose into serine increased in BE(2)-C cells and remained higher compared to SH-EP cells.

4.4. Genetic inhibition of *PHGDH* expression

4.4.1. siRNA-mediated knockdown of *PHGDH*

We have shown that *MYCN*-amplified neuroblastoma cells harboring high *PHGDH* expression maintain their proliferation rate and metabolic homeostasis independently of the provided serine and glycine in the environment. Besides the uptake of serine and glycine into the cells, both metabolites can be synthesized via the serine-glycine pathway where 3-PGA is converted via pOH-Pyr and pSer into serine and glycine. *PHGDH* is the rate-limiting enzyme in this pathway. We aimed for analyzing the role of *PHGDH* in neuroblastoma cells by its genetic and pharmacological inhibition. In this section we describe the transient *PHGDH* knockdown in BE(2)-C and SH-EP cells and the establishment of *PHGDH* knockout clones in BE(2)-C cells. The pharmacological inhibition of *PHGDH* is described in section 4.5.

In a first approach, we performed an siRNA-mediated knockdown of *PHGDH* in BE(2)-C and SH-EP cells. To determine the best conditions of transfection, BE(2)-C cells were transfected with either 1 nM or 3 nM siRNA-Pool and SH-EP cells were transfected with either 5 nM, 10 nM or 20 nM siRNA-Pool. Additionally one cell culture plate per cell line was transfected with the dye Cy3 to determine transfection efficacy. BE(2)-C cells were harvested 72 and 96 hours after transfection, SH-EP cells were harvested 96 hours after transfection. BE(2)-C and SH-EP cells showed intracellular Cy3 staining 24 hours after transfection, proving that the delivery of the siRNAs into the cells was efficient in both cell lines (figure 4.21A&B). In BE(2)-C cells, a successful *PHGDH* knockdown was achieved with 1 nM and 3 nM of the siRNA-Pool after 72 and 96 hours (figure 4.21C). In SH-EP cells, 5 nM siRNA-Pool were not sufficient to reduce *PHGDH* expression. A siRNA-Pool concentration of 10 nM downregulated *PHGDH* expression and was even stronger by applying 20 nM siRNA-Pool (figure 4.22D). For further experiments, a 96 hour time frame post-transfection and siRNA-Pool concentrations of 3 nM in BE(2)-C and 20 nM in SH-EP cells was chosen. But further experiments could not be conducted with this technology, as the siRNA-mediated knockdown of *PHGDH* could not be reproduced with a stable knockdown efficiency.

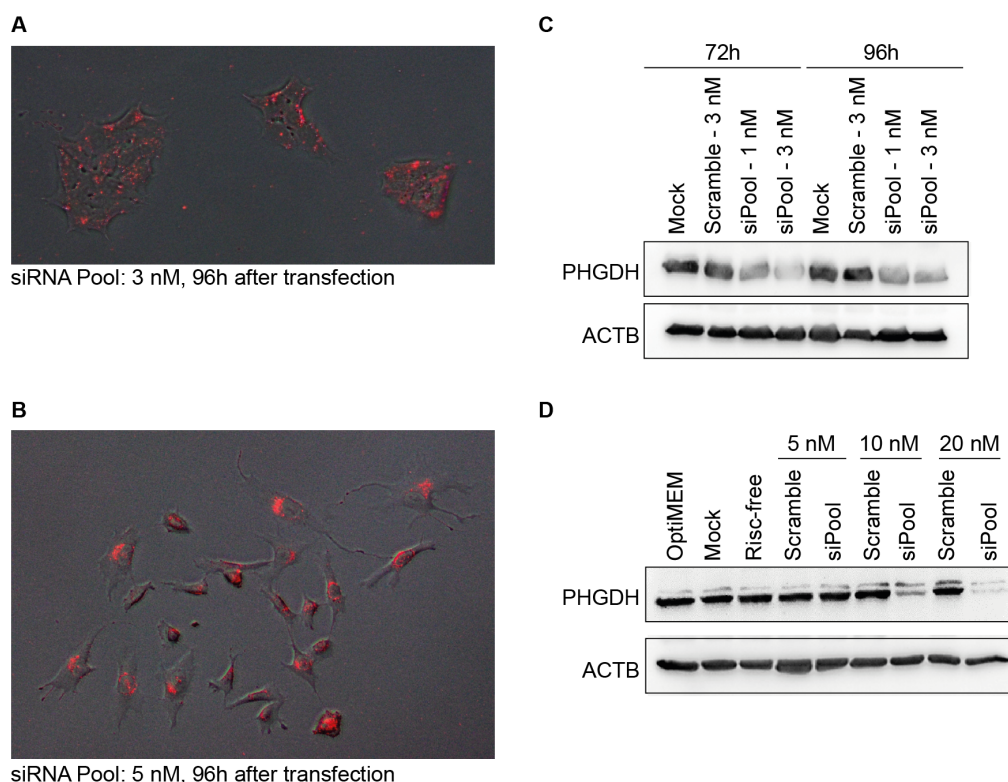


Figure 4.21.: Transient *PHGDH* knockdown in BE(2)-C (A&C) and SH-EP (B&D) cells. BE(2)-C and SH-EP cells were transfected with 1 or 3 nM and 5, 10 or 20 nM siRNA-Pool targeting *PHGDH*, respectively. BE(2)-C cells were harvested 72 or 96 hours after transfection, SH-EP cells were harvested 96 hours after transfection. Transfection was controlled by Cy3 staining (A&B) 24 hours after transfection and *PHGDH* expression was analyzed by immunoblotting (C&D).

4.4.2. CRISPR-Cas9-mediated knockout of *PHGDH*

In a second approach, *PHGDH* knockout clones were established in BE(2)-C cells. For the CRISPR-mediated *PHGDH* knockout, guide RNA sequences were designed using the Zhang lab CRISPR design tool² and the Broad Institute sgRNA designer³. The guide RNAs with high off-target potential were eliminated with predicting tools. Protein lysates were harvested from all potential knockout clones and used to determine those clones where *PHGDH* protein expression was absent. *PHGDH* expression was not detectable in any of the knockout clones by western blotting (figure 4.22A). Protein lysates of cells transfected with empty vector were used as reference. Further, proliferation of the *PHGDH* knockout cells was assessed for 96 hours with cell counting every 24 hours. Proliferation in all *PHGDH* knockout clones was significantly reduced compared to the control cells transfected with the empty vector (figure 4.22B).

²<http://www.genome-engineering.org/crispr/?page.id=41>

³<http://www.broadinstitute.org/rnai/public/analysis-tools/sgRNA-design>

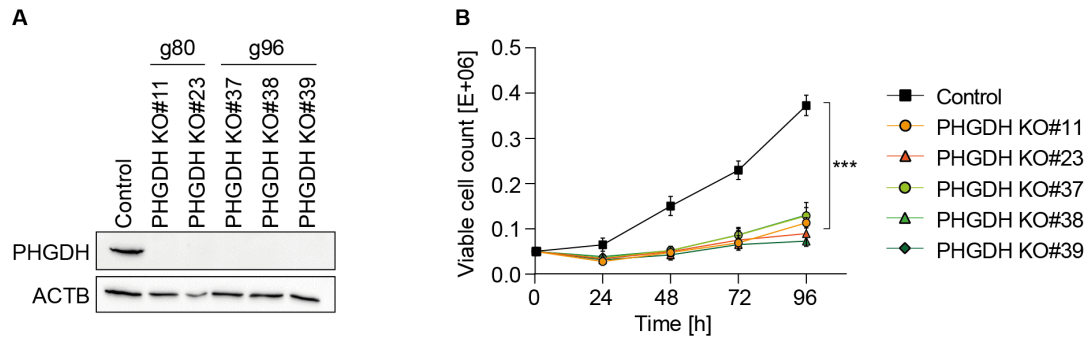


Figure 4.22.: CRISPR-mediated *PHGDH* knockout clones in BE(2)-C cells. BE(2)-C cells were transfected with guide RNAs g80 and g96. Knockout clones were selected by exposition to 2 $\mu\text{g}/\text{mL}$ puromycin for two days and seeded with 0.5 or 1 cells/well in a 96-well plate. Immunoblotting revealed an abolished PHGDH protein expression in all knockout clones (A). Viable cell count was measured every 24 hours. All knockout clones showed a significant decrease in proliferation compared to control cells. Results represent mean \pm SD, $n=3$. P-values were calculated with AUC values, using an unpaired Student's t-test (* $0.01 < p \leq 0.05$; ** $0.001 < p \leq 0.01$; *** $p \leq 0.001$).

In further experiments, we intend to investigate the metabolism of the *PHGDH* knockout cells in-depth. In a first step, cells will be exposed to $\text{u-}^{13}\text{C}$ -glucose in order to control if the *PHGDH* knockout blocks the routing of glucose-derived carbons into *de novo* serine synthesis. In a second step, we are going to quantify the metabolites within the CCM in a time-resolved manner and analyze if the observed metabolic changes by pharmacological inhibition of PHGDH can be reproduced in the *PHGDH* knockout cells.

4.5. Pharmacological inhibition of PHGDH activity

4.5.1. PHGDH inhibition reduces cell growth *in vitro*

In order to enhance the knowledge of PHGDH function in neuroblastoma, small molecules suppressing PHGDH activity were applied to neuroblastoma cell lines and to mice carrying a patient-derived neuroblastoma xenograft. We hypothesized that MYCN- and PHGDH-high expressing neuroblastoma cells are addicted to *de novo* serine synthesis to maintain proliferation. Consequently, perturbation within this pathway by PHGDH suppression might impair proliferation in these cells.

Two MYCN-amplified neuroblastoma cell lines, BE(2)-C and Kelly, as well as two MYCN non-amplified neuroblastoma cell lines, SH-EP and SK-N-AS, were cultivated in medium containing serine and glycine with addition of 10 μ M PHGDH inhibitors P2101 or NCT503. As a control, cells were treated either with DMSO or the inactive NCT503 compound. Total and viable cell count was measured every 24 hours. P2101 and NCT503 treatment significantly reduced the proliferation in all investigated cell lines (figure 4.23A&B). Microscopic observations did not reveal any floating cells in the culture medium and also the non-viable cell fraction did not differ between control and inhibitor treatment, except for NCT503-treated Kelly cells (figure 4.23C). Decrease in proliferation was not enhanced when serine and glycine were depleted from cell culture medium during treatment (supplementary figure B.4).

To study if the inhibitory effect of NCT503 and P2101 on colony formation prolonged for longer time periods, cells were treated for nine days with a refresh of culture medium and respective inhibitors or solvent controls on day five. Colony formation capacity of BE(2)-C (figure 4.23D) and Kelly cells (figure 4.23E) was significantly reduced.

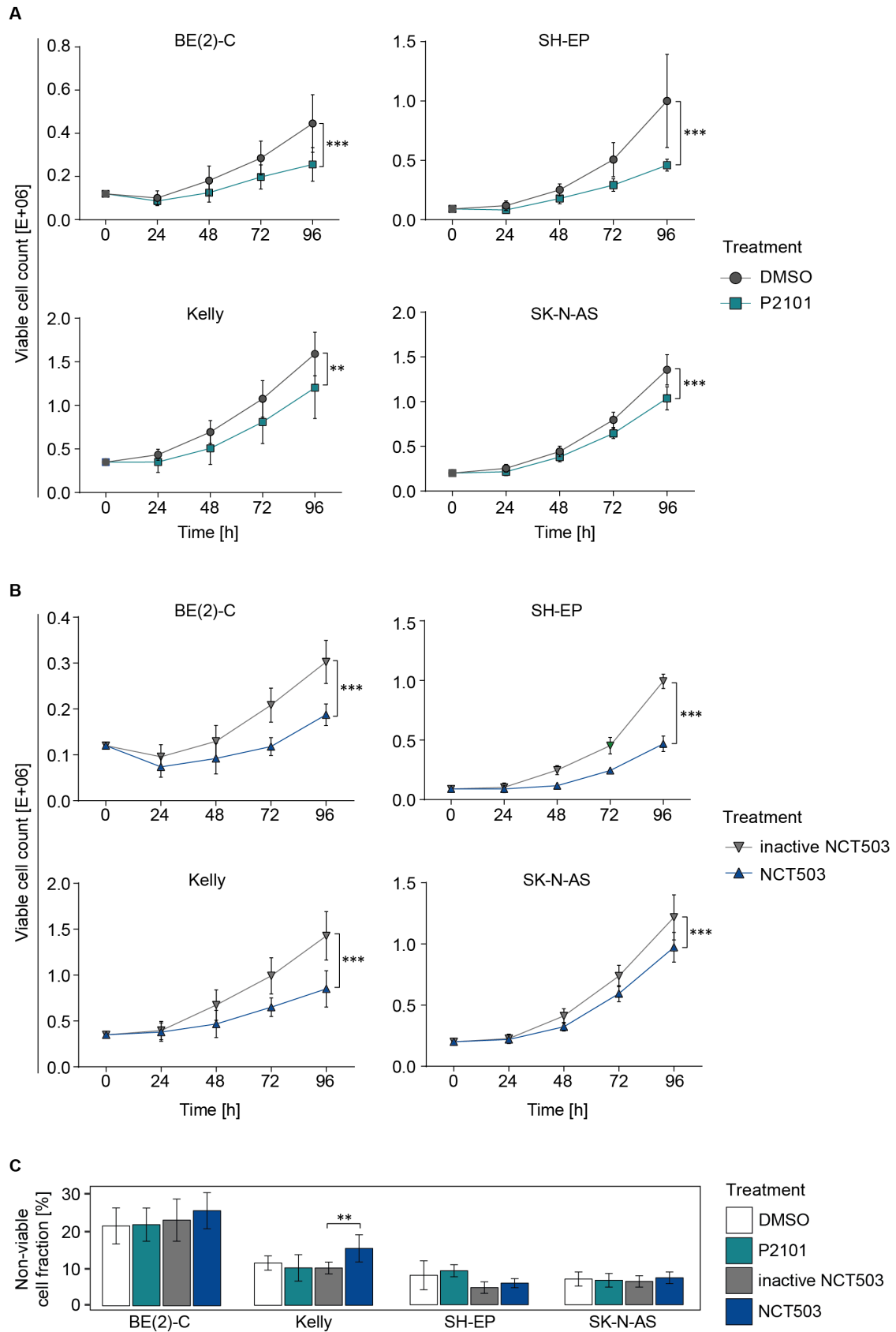


Figure 4.23.: Effects of PHGDH inhibitors on neuroblastoma cell proliferation *in vitro*. Continued on next page.

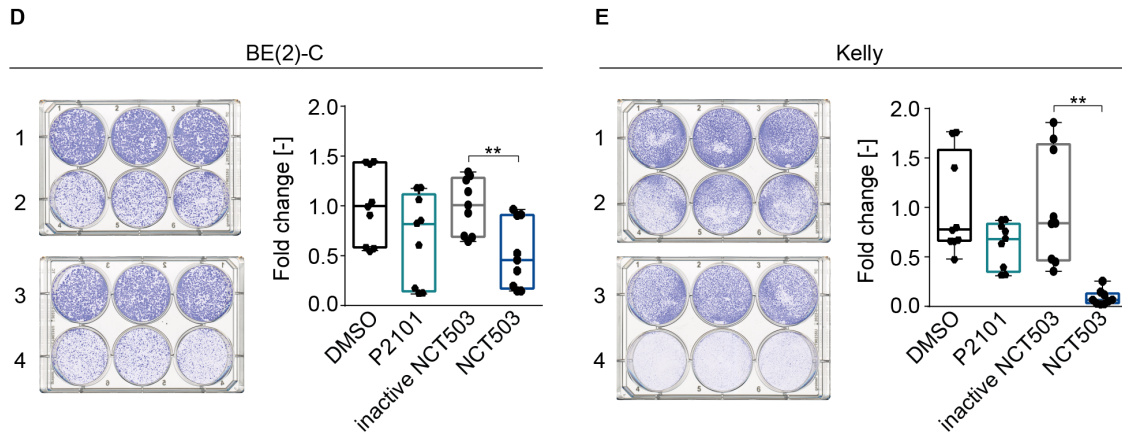


Figure 4.23.: Effects of PHGDH inhibitors on neuroblastoma cell proliferation *in vitro*. A-B: BE(2)-C, Kelly, SH-EP and SK-N-AS were treated on day 0 with PHGDH inhibitors (P2101 (A) or NCT503 (B)) and respective controls (DMSO or inactive NCT503). Viable cell count was measured every 24 hours. All cell lines showed a significant decrease in proliferation. Results represent mean \pm SD, $n=3$ each in three technical replicates. P-values were calculated with AUC values, using an unpaired Student's t-test (* $0.01 < p \leq 0.05$; ** $0.001 < p \leq 0.01$; *** $p \leq 0.001$). C: Fraction of non-viable cells [%] after 96 hours of PHGDH inhibitor treatment and respective controls. Results represent mean \pm SD, $n=3$, each in three technical replicates. P-values were calculated using an unpaired Student's t-test (* $0.01 < p \leq 0.05$; ** $0.001 < p \leq 0.01$; *** $p \leq 0.001$). D&E: Colony formation capacity was significantly decreased under P2101 and NCT503 treatment. BE(2)-C (D) and Kelly (E) were treated on day 0 with PHGDH inhibitors (2: P2101 or 4: NCT503) and respective controls (1: DMSO or 3: inactive NCT503). Cell culture medium and respective inhibitors or solvent controls were refreshed after five days of treatment. On day 9 cells were stained and colony formation was analyzed. NCT503 treatment decreased colony formation capacity in both cell lines significantly. P2101 was not able to inhibit colony formation to such a high extend. Results represent mean \pm SD, $n=3$, each in three technical replicates. P-values were calculated using an unpaired Student's t-test (* $0.01 < p \leq 0.05$; ** $0.001 < p \leq 0.01$; *** $p \leq 0.001$).

4.5.2. PHGDH inhibitor treatment of mice carrying a patient-derived neuroblastoma xenograft

We have shown that the PHGDH inhibitors NCT503 and P2101 significantly reduced cell proliferation *in vitro*. We therefore decided to apply both inhibitors to mice carrying a patient-derived neuroblastoma xenograft (PDX) with high PHGDH expression levels. Eight neuroblastoma PDX mouse models are available from the Department of Pediatric Oncology and Hematology (Charité Universitätsmedizin Berlin, Germany) in cooperation with the Experimental Pharmacology & Oncology company (Berlin, Germany). Immunoblotting of protein lysates from all PDX models confirmed the direct correlation of MYCN and PHGDH. PHGDH inhibitor testing was performed with the PDX model #14647 as it showed a high MYCN to PHGDH expression (figure 4.24).

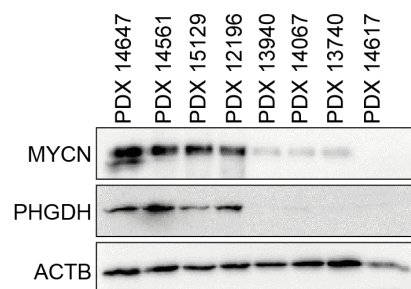


Figure 4.24.: Immunoblotting of MYCN and PHGDH of protein lysates from patient-derived neuroblastoma xenograft models.

Male NOG mice were subcutaneously transplanted with the patient-derived neuroblastoma xenograft PDX #14647. Three weeks post transplantation a significant tumor growth was achieved and the mice were treated in mono- or combination therapy with PHGDH inhibitors (NCT503, P2101) or cisplatin. NCT503 and P2101 applied as a monotherapy decreased tumor cell growth. In contrast, mice treated with the chemotherapeutic drug cisplatin in monotherapy showed a strong reduction in tumor growth compared to the control group. Interestingly, the combination therapy of either NCT503+cisplatin or P2101+cisplatin demonstrated an antagonistic effect on tumor growth compared to cisplatin monotherapy (figure 4.25A&C). At day 36 (figure 4.25B&D), tumor volume was significantly reduced after P2101 and cisplatin treatment in mono- and combination therapy. NCT503 did not reduce tumor volume significantly. Moreover combination therapy of cisplatin+NCT503 significantly increased tumor volume compared to cisplatin monotherapy. Animals from all treatment groups maintained a stable bodyweight throughout the experiment (supplementary figure B.5).

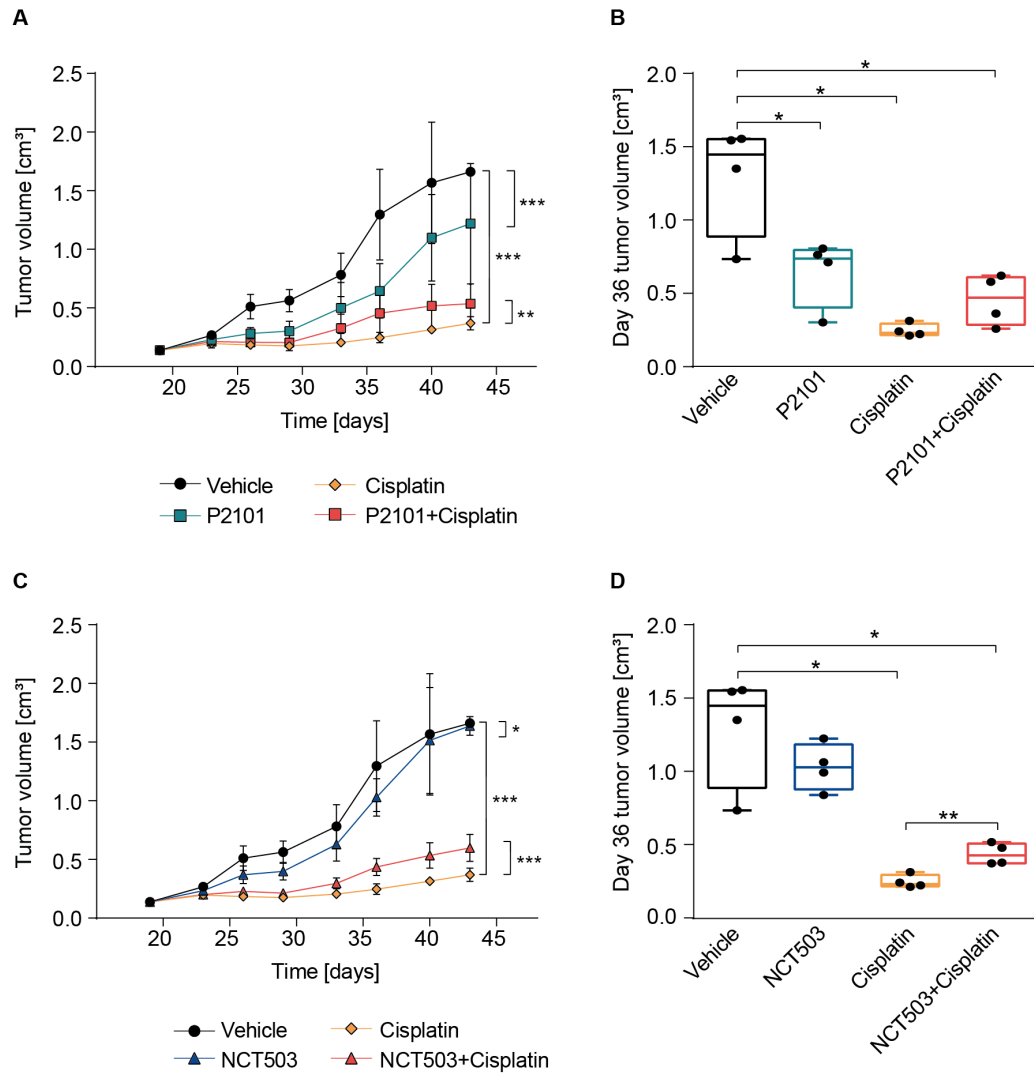


Figure 4.25.: Tumor volume of NOG mice transplanted with patient-derived neuroblastoma xenograft and treated in mono- or combination therapy with PHGDH inhibitors or cisplatin. Treatment was started three weeks post transplantation. NCT503 and P2101 were injected intraperitoneally daily with a concentration of 40 mg/kg and 20 mg/kg, respectively. Cisplatin was applied intravenously once a week with 2 mg/kg in the first week and 1 mg/kg in weeks 2-4. Tumor volume was analyzed with AUC calculation, n=4. P-values were calculated using an unpaired Student's t-test (* $0.01 < p \leq 0.05$; ** $0.001 < p \leq 0.01$; *** $p \leq 0.001$).

4.5.3. Metabolic effects of PHGDH inhibitors

Treatment of mice carrying a patient-derived PHGDH-high expressing neuroblastoma xenograft with PHGDH inhibitors did not reveal striking effects on tumor growth as expected. In order to further investigate the effect of NCT503 and P2101 on cell metabolism, BE(2)-C and SH-EP cells were treated for 48 hours with these inhibitors. Before harvesting, cells were cultivated in medium containing $u\text{-}^{13}\text{C}$ -glucose for 10 min. Polar metabolites were extracted, half of the samples were derivatized and measured with GC-MS. The other half was analyzed with direct-infusion mass spectrometry for nucleotide measurement. BE(2)-C cells treated with P2101 showed no decrease of carbon-13 incorporation into serine or glycine compared to control-treated cells (figure 4.26A). However, treatment with NCT503 decreased incorporation by 3-fold in serine and was not detectable in glycine, proving that NCT503 efficiently blocked the conversion of 3-PGA into serine, most likely by inhibiting PHGDH. The application of P2101 did not affect *de novo* serine synthesis. In SH-EP cells, glucose-derived carbon-13 incorporation into serine and glycine was less than 1% in all conditions. Total pool sizes of serine and glycine were not changed in the inhibitor-treated groups compared to the control groups in BE(2)-C cells. In SH-EP cells, P2101 treatment decreased serine but not glycine pools (figure 4.26B). Nucleotide levels were not altered upon PHGDH inhibitor treatment (figure 4.27).

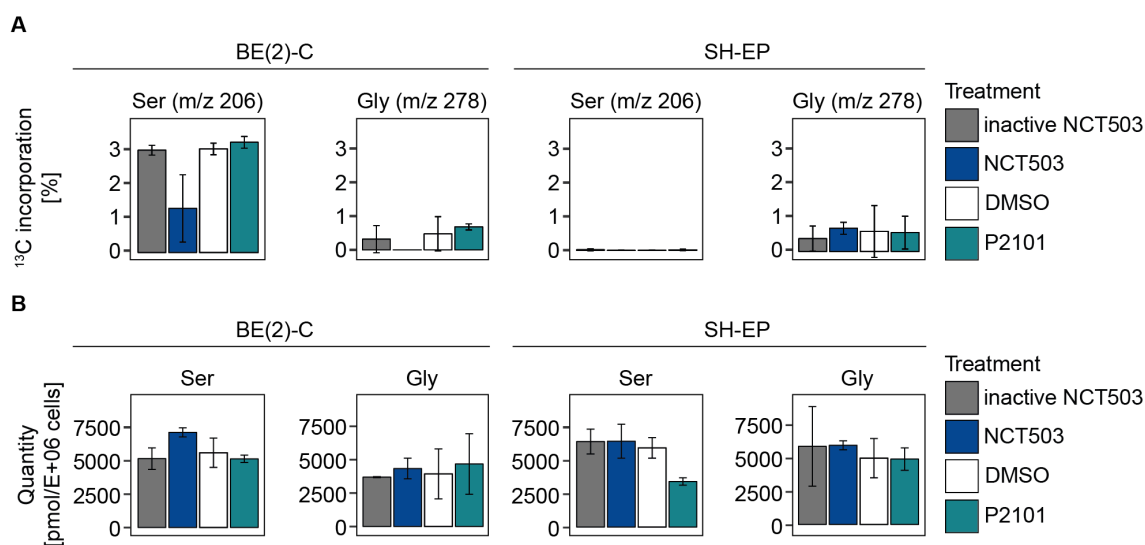


Figure 4.26.: Effects of PHGDH inhibitors on *de novo* serine and glycine synthesis. BE(2)-C and SH-EP cells were treated with PHGDH inhibitors P2101, NCT503 and the respective controls DMSO and inactive NCT503. Before harvest, cells were incubated in medium containing $u\text{-}^{13}\text{C}$ -glucose instead of the unlabeled glucose for 10 min. $u\text{-}^{13}\text{C}$ -glucose incorporation (A) and absolute quantities (B) were determined. Results represent mean \pm SD, $n=3$. P-values were calculated using an unpaired Student's t-test (* $0.01 < p \leq 0.05$; ** $0.001 < p \leq 0.01$; *** $p \leq 0.001$). Abbreviations: Gly - Glycine, Ser - Serine

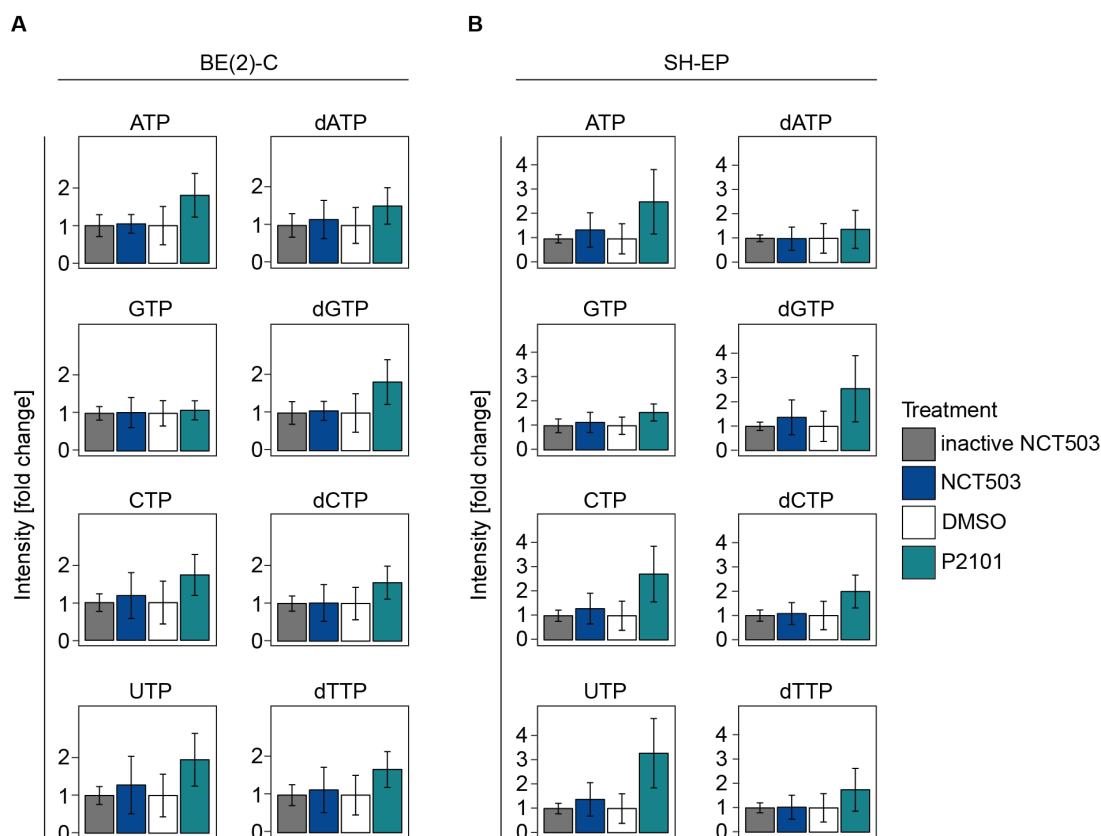


Figure 4.27.: Effects of PHGDH inhibitors on nucleotide levels. BE(2)-C and SH-EP cells were treated with PHGDH inhibitors P2101, NCT503 and the respective controls DMSO and inactive NCT503. Results represent mean \pm SD, $n=3$. P-values were calculated using an unpaired Student's t -test (* $0.01 < p \leq 0.05$; ** $0.001 < p \leq 0.01$; *** $p \leq 0.001$)

Additional metabolic effects of NCT503 treatment were observed in BE(2)-C and SH-EP cells such as an increase in labeled malate (m/z 248) and a significant decrease in labeled citrate quantities (m/z 275). Acetyl-CoA levels were increased in BE(2)-C cells. Based on the data we suppose an increased conversion of glucose-derived pyruvate by the pyruvate carboxylase in line with a decreased conversion by the citrate synthase under NCT503 treatment. Moreover, BE(2)-C cells increased their production of lactate and SH-EP cells increased their production of alanine (figure 4.28).

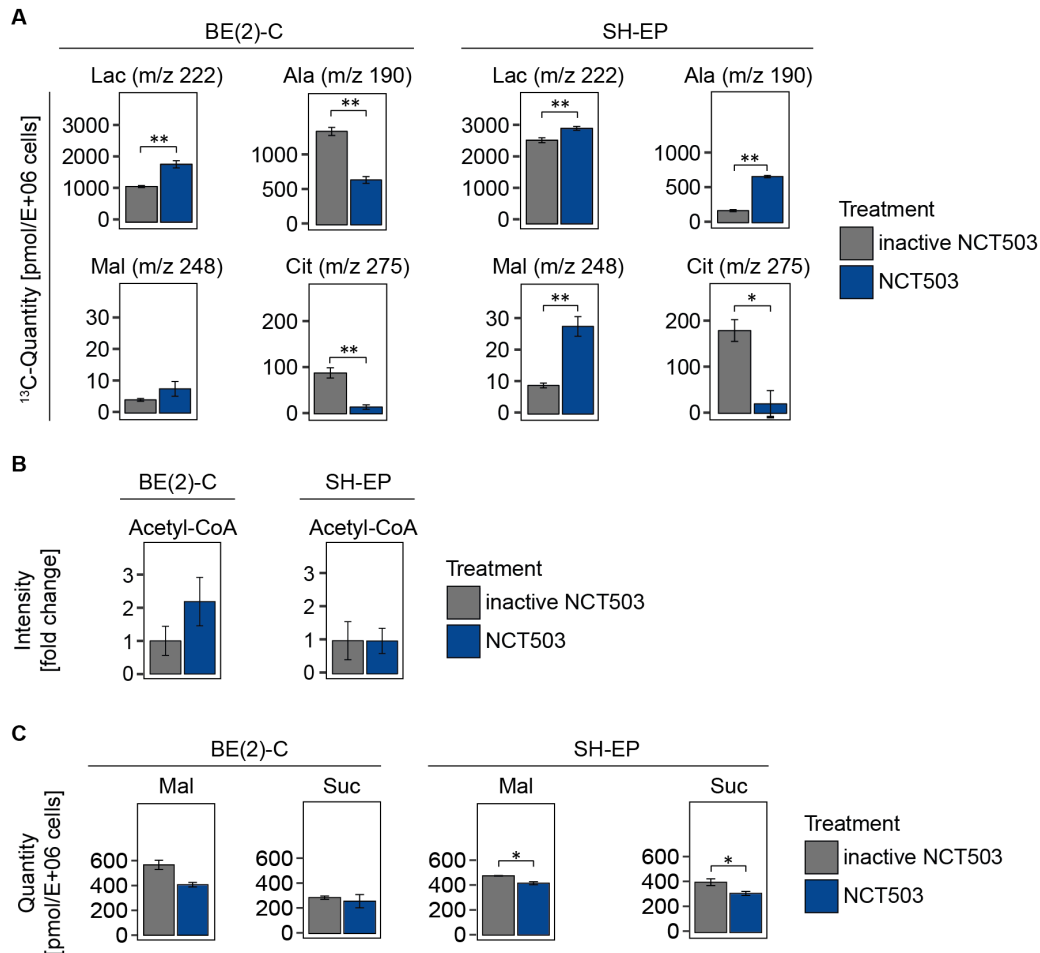


Figure 4.28.: Effects of PHGDH inhibitor on CCM intermediates. BE(2)-C and SH-EP were treated with PHGDH inhibitor NCT503 and its inactive compound. Before harvest, cells were incubated in medium containing $u\text{-}^{13}\text{C}$ -glucose instead of unlabeled glucose for 10 min. ^{13}C -labeled quantities (A) of CCM intermediates, relative intensities of acetyl-CoA (B) and absolute quantification of malate and succinate (C). Results represent mean \pm SD, $n=3$. P-values were calculated using an unpaired Student's t-test (* $0.01 < p \leq 0.05$; ** $0.001 < p \leq 0.01$; *** $p \leq 0.001$). Abbreviations: Acetyl-CoA - Acetyl coenzyme A, Ala - Alanine, Cit - Citrate, Lac - Lactate, Mal - Malate, Suc - Succinate.

In summary, application of PHGDH inhibitors NCT503 or P2101 significantly decreased proliferation in neuroblastoma cell lines, independent of their MYCN levels. Inhibition of PHGDH in mice carrying a patient-derived neuroblastoma xenograft reduced tumor growth. However, PHGDH inhibition in combination with cisplatin raised tumor growth compared to cisplatin monotherapy. NCT503 blocked the conversion of glucose-derived carbons into *de novo* serine synthesis but did not modify intracellular serine, glycine or nucleotide levels in BE(2)-C and SH-EP cells. Moreover, the data indicated an activation of the pyruvate carboxylase combined with a decrease in citrate synthase activity under NCT503 treatment.

4.6. Targeting the folate-mediated one-carbon metabolism

4.6.1. Proliferation and nucleotide levels are decreased by antifolate treatment

The Spearman correlation analysis of neuroblastoma cell lines and biopsies from patients with neuroblastoma revealed a strong correlation of high-level MYCN expression to the expression of proteins within the one-carbon metabolism. Antifolates such as MTX or 5-FU are approved as anticancer therapeutics and target enzymes within the folate-mediated one-carbon metabolism (figure 4.29A). We aimed for analyzing the effect of those drugs on the proliferation behavior of BE(2)-C and SH-EP cells. Both cell lines were cultured in medium containing 10 μ M 5-FU, 1 μ M MTX or DMSO as control. Total and viable cell counts were determined by automated cell counting with trypan blue staining every 24 hours.

Proliferation was arrested in both cell lines by 5-FU or MTX treatment (figure 4.29B). In BE(2)-C cells, the fraction of non-viable cells was not altered. However, this fraction was significantly increased in SH-EP cells after 5-FU and MTX treatment with the strongest effect after 5-FU treatment (figure 4.29C). In addition to the proliferation experiment, nucleotide levels were determined by direct-infusion MS measurement after 48 hours of 5-FU or MTX treatment (figure 4.29D&E). In BE(2)-C cells, levels of dUMP were significantly enhanced and levels of dTMP, dTDP, dTTP levels were sequentially reduced by 5-FU and MTX treatment. Other nucleotides including ATP, GTP, UTP, dATP, dGTP and CTP also decreased in abundance by both treatments, except for dATP which was only affected by MTX. Acetyl-CoA levels were not modified by any treatment. Contrary to the previous result in BE(2)-C cells, a decrease in dUMP levels was observed in SH-EP cells by 5-FU and MTX treatment. However, dTMP, dTDP levels were significantly decreased and dTTP level were even below the limit of detection. Overall, nucleotides were generally reduced to a stronger extend in SH-EP compared to BE(2)-C cells such as ATP, GTP, UTP, dATP, dGTP and CTP. In concordance with BE(2)-C cells, the acetyl-CoA levels were not affected by 5-FU or MTX treatment in SH-EP cells (figure 4.29).

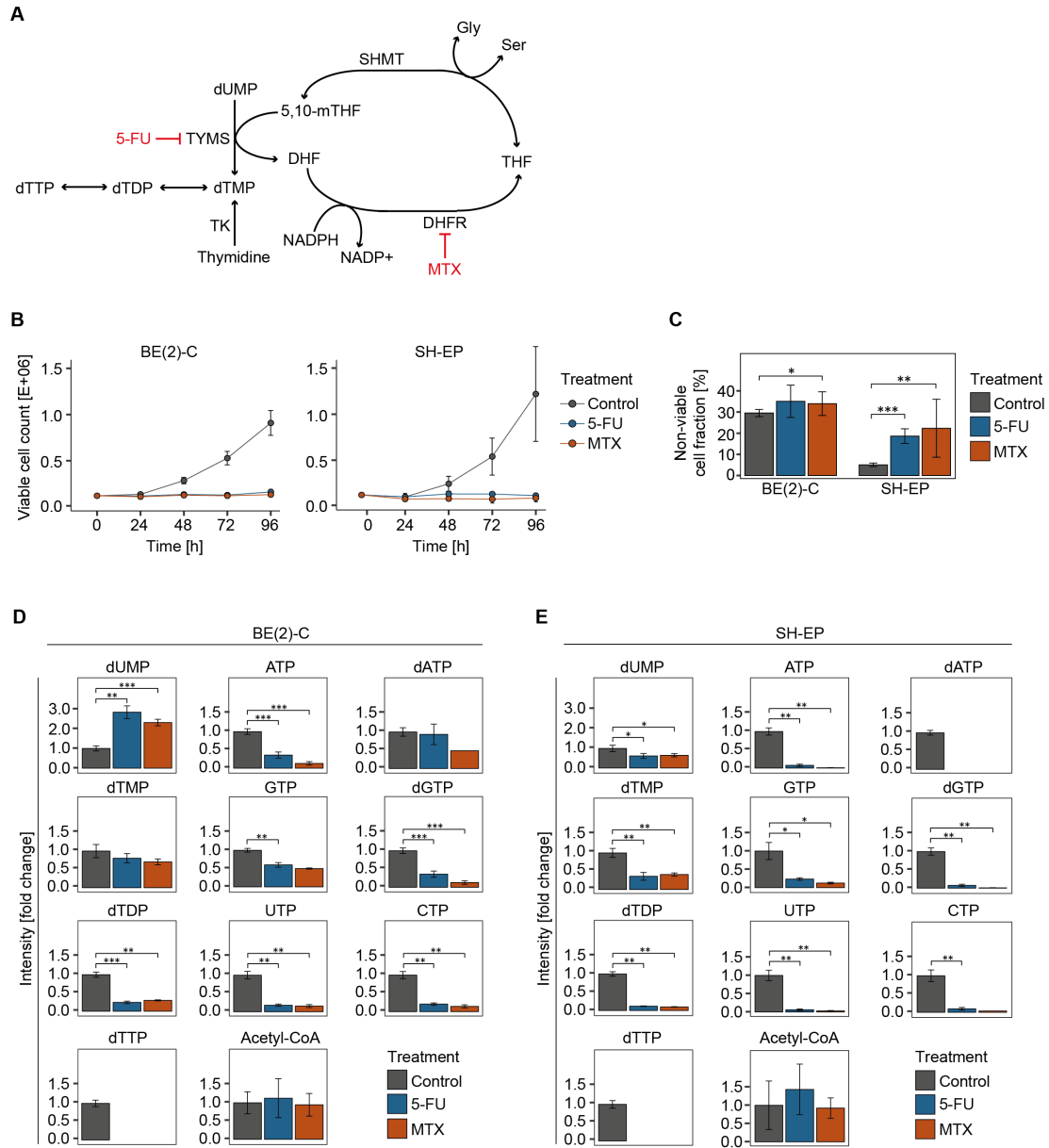


Figure 4.29.: Impact of 5-FU and MTX treatment on proliferation and nucleotide levels in BE(2)-C and SH-EP cells. A: Schematic overview of 5-FU and MTX targets within the folate-mediated one-carbon metabolism. B: Viable cell count in BE(2)-C and SH-EP cells decreased after 10 μ M 5-FU and 1 μ M MTX treatment. C: Fraction of non-viable cells significantly increased after 96 hours of treatment only in SH-EP cells. D-E: Deoxy- and ribonucleotide levels in BE(2)-C and SH-EP cells after 72 hours of 5-FU or MTX treatment. Results represent mean \pm SD, $n=3$, each in three technical replicates. P-values were calculated using an unpaired Student's t-test (* $0.01 < p \leq 0.05$; ** $0.001 < p \leq 0.01$; *** $p \leq 0.001$). Abbreviations: 5-FU - 5-Fluorouracile, MTX - Methotrexate.

As the folate-mediated one-carbon metabolism is interconnected with *de novo* serine synthesis, we aimed to analyze the PHGDH expression levels in BE(2)-C and SH-EP cells after perturbation with 5-FU and MTX. Further, MYCN expression levels were determined in both cell lines. BE(2)-C and SH-EP cells were treated with 10 μ M 5-FU or 1 μ M MTX for 72 hours. Protein lysates were harvested and subjected to western blotting. PHGDH expression was not altered in BE(2)-C cells after 5-FU or MTX treatment. In SH-EP cells, a decrease in PHGDH expression was measured, but due to alterations between the biological replicates no statistical significance was reached (figure 4.30A). As no proliferation was observed in BE(2)-C cells under 5-FU and MTX treatment, it was even more interesting to observe that MYCN was still highly expressed in these cells (figure 4.30B). MYCN expression was not detected in the *MYCN* non-amplified SH-EP cell line.

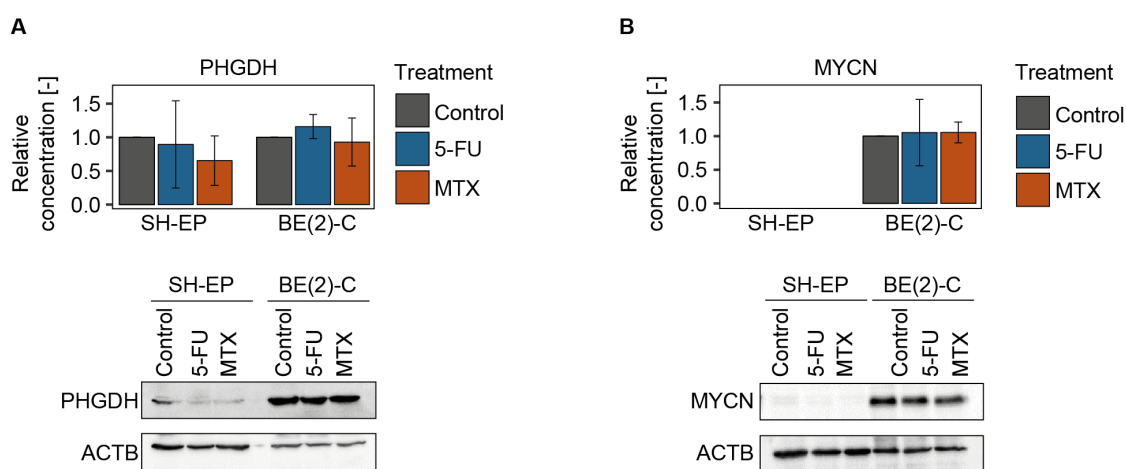


Figure 4.30.: Effect of 5-FU and MTX treatment on PHGDH and MYCN expression. Relative quantification and representative immunoblot showed PHGDH (A) and MYCN (B) expression after 72 hours of 5-FU or MTX treatment in BE(2)-C and SH-EP cells. Results represent mean \pm SD, n=3. Abbreviations: 5-FU - 5-Fluorouracile, MTX - Methothrexate.

In conclusion, nucleotide levels were significantly reduced and proliferation was arrested by 5-FU and MTX treatment in BE(2)-C and SH-EP cells. SH-EP cells reacted with enhanced sensitivity to the treatment as nucleotide levels were reduced to a higher extent compared to BE(2)-C cells. Levels of dUMP were raised in BE(2)-C and decreased in SH-EP cells. In both cell lines no regulatory feedback mechanism from the folate metabolism to PHGDH expression was observed. Moreover, BE(2)-C cells maintained their high MYCN expression levels even under proliferation arrest.

4.7. Response of neuroblastoma cell lines to glutamine starvation

4.7.1. Glutamine starvation decreases proliferation in neuroblastoma cells

As reviewed by Wise and Thompson, the oncogene *c-MYC* induces metabolic reprogramming that renders a variety of cancer cells to be addicted to glutamine [Wise and Thompson, 2011]. We aimed for analyzing the role of external glutamine supply on the proliferation of *MYCN*-amplified neuroblastoma cell lines. NLF, BE(2)-C, CHP-134, IMR-32 and Kelly cells were starved for glutamine for 48 hours. Cell count was measured by semi-automated cell counting with trypan blue staining, the fraction of cells in SubG1 was determined by propidium iodide staining with FACS analysis and nucleotide levels were determined by direct-infusion MS.

We observed a significantly reduced viable cell count in all neuroblastoma cell lines after glutamine starvation (figure 4.31A). However, the viable cell count was decreased to the highest extend in NLF and BE(2)-C cells. Kelly cells reacted less sensitive to glutamine starvation as their viable cell count was reduced by less than 30% compared to the non-starved control cells. We measured a significant enhanced apoptotic fraction in NLF and BE(2)-C cells under glutamine starvation compared to non-starved control cells (figure 4.31B&C). Glutamine starvation moderately raised the apoptotic fraction in IMR-32 cells and remained constant in Kelly and CHP-134 cells. Nucleotide levels were diminished in all cell lines after glutamine starvation. Non visible bars represent nucleotide intensities below the noise-threshold (figure 4.31D).

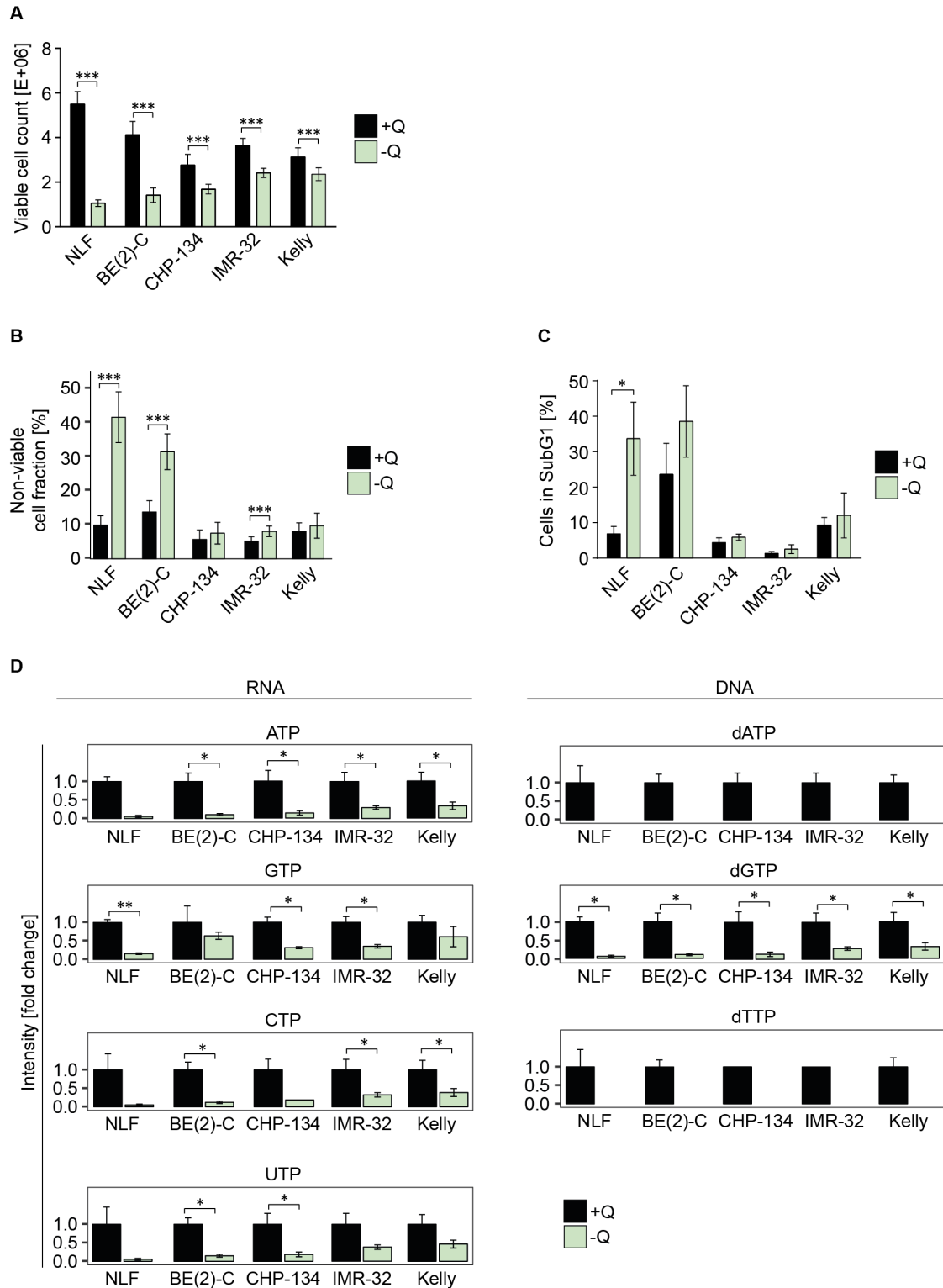


Figure 4.31: Effects of glutamine starvation on proliferation in *MYCN*-amplified neuroblastoma cell lines. NLF, BE(2)-C, CHP-134, IMR-32 and Kelly cells were cultured in the presence (+Q) or absence (-Q) of glutamine for 48 hours. A-B: Viable cell count and non-viable cell fraction was determined by semi-automated cell counting with trypan blue staining. C: SubG1 fraction of cells was determined after FACS measurement with PI staining D: Deoxy- and ribonucleotides were measured by direct-infusion MS. Bars represent mean \pm SD, $n=3$. P-values were calculated using a two-tailed Student's t-test with Welch's correction (* $0.01 < p \leq 0.05$; ** $0.001 < p \leq 0.01$; *** $p \leq 0.001$).

4.7.2. ATF4-mediated regulation of apoptotic proteins under glutamine starvation

Due to the observed increase of apoptosis in NLF, BE(2)-C and IMR-32 cells, we evaluated the expression of apoptotic marker proteins (PUMA and cleaved PARP) and ATF4, which can mediate apoptosis, in these cells. ATF4 protein expression was significantly enhanced in BE(2)-C and NLF cells (figure 4.32A). Total PARP protein decreased in all investigated cell lines, except for IMR-32. The expression of cleaved PARP protein, a marker protein for apoptosis, raised significantly in BE(2)-C and NLF cells. IMR-32 moderately increased cleaved PARP expression. PUMA expression was upregulated only in BE(2)-C cells whereas NLF and IMR-32 maintained consistent levels of PUMA expression.

We transfected BE(2)-C cells with siRNA pool targeting *ATF4* to analyze whether apoptosis is ATF4-mediated under glutamine starvation. Protein lysates were harvested 96 hours post transfection. ATF4 protein expression was reduced to a higher extend in glutamine starved BE(2)-C cells compared to non-starved cells due to enhanced ATF4 expression under starvation (figure 4.32B). Protein expression of cleaved PARP and PUMA were reduced following *ATF4* knockdown in glutamine-starved BE(2)-C cells (figure 4.32C). Moreover, PHGDH expression was reduced by *ATF4* knockdown in glutamine-starved BE(2)-C cells, revealing the ATF4-mediated regulation of PHGDH also under glutamine starvation.

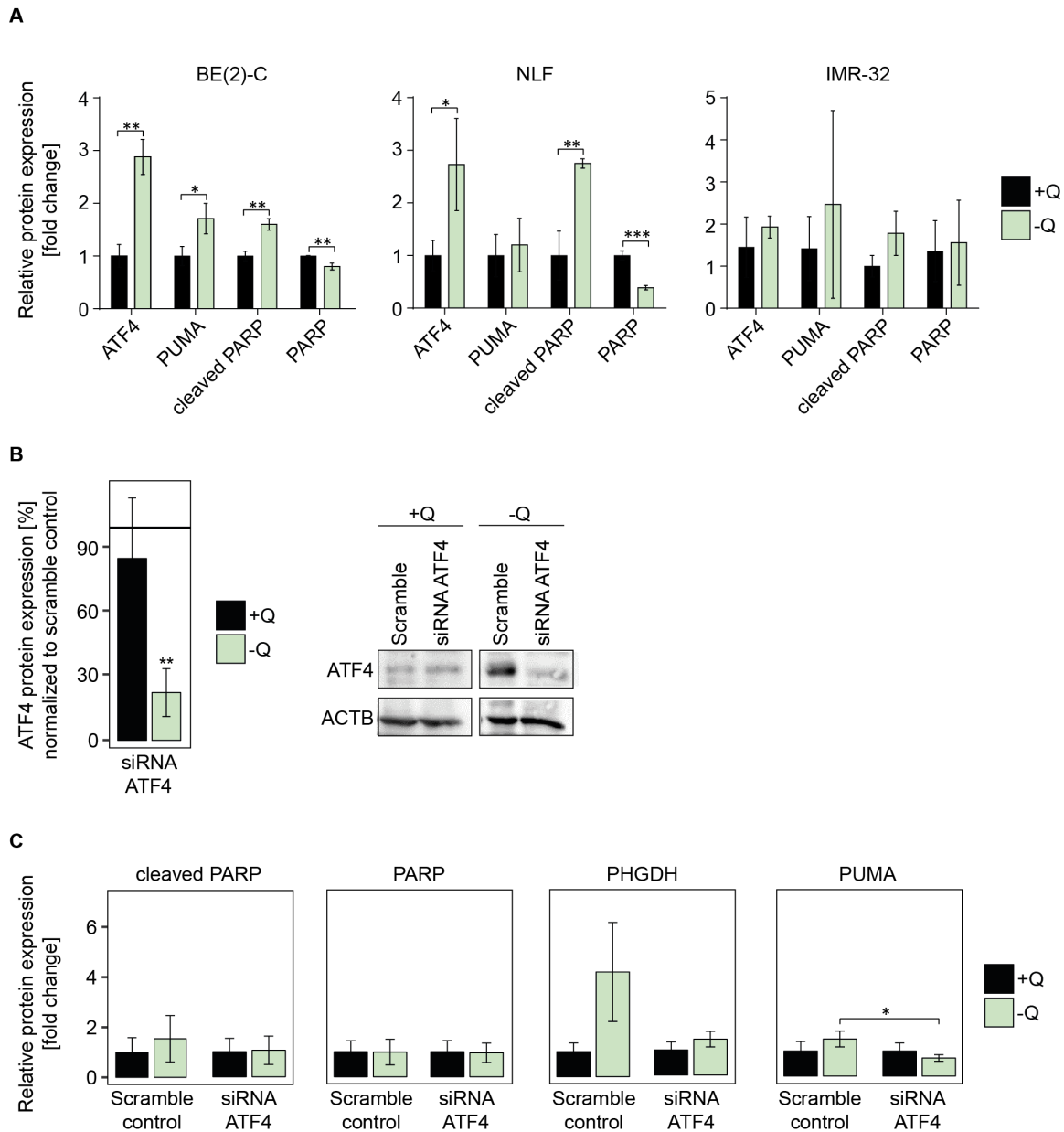


Figure 4.32.: Effects of glutamine starvation on the expression of apoptotic marker proteins. A: Relative protein expression of the apoptotic marker proteins PARP, cleaved PARP and PUMA, as well as ATF4 in BE(2)-C, NLF and IMR-32 cells cultured in the presence (+Q) or absence (-Q) of glutamine for 48 hours. B-C: BE(2)-C cells were transfected with siRNA Pool targeting *ATF4* with subsequent starvation for glutamine (-Q) for 96 hours. Representative immunoblot and relative quantification revealed the downregulation of ATF4 expression and the regulation of apoptotic marker proteins. Results represent mean \pm SD, n=3. P-values were calculated using an unpaired Student's t-test (* $0.01 < p \leq 0.05$; ** $0.001 < p \leq 0.01$; *** $p \leq 0.001$), n=3.

4.7.3. Effects of glutamine starvation on *de novo* serine synthesis

We aimed for analyzing the effect of glutamine starvation on PHGDH expression and *de novo* serine synthesis in neuroblastoma cells. *MYCN*-amplified and *MYCN* non-amplified neuroblastoma cell lines were starved for glutamine for 48 hours and *MYCN* and PHGDH protein expression was determined by western blotting. Independent of the *MYCN* status, PHGDH protein expression was upregulated in all neuroblastoma cell lines when cultivated in glutamine-depleted medium (figure 4.33A). Except for CHP-134, all *MYCN*-amplified cell lines decreased *MYCN* protein expression in response to glutamine starvation. Our data indicates that the strong correlation of *MYCN* to PHGDH was disrupted when glutamine is absent in the culture medium.

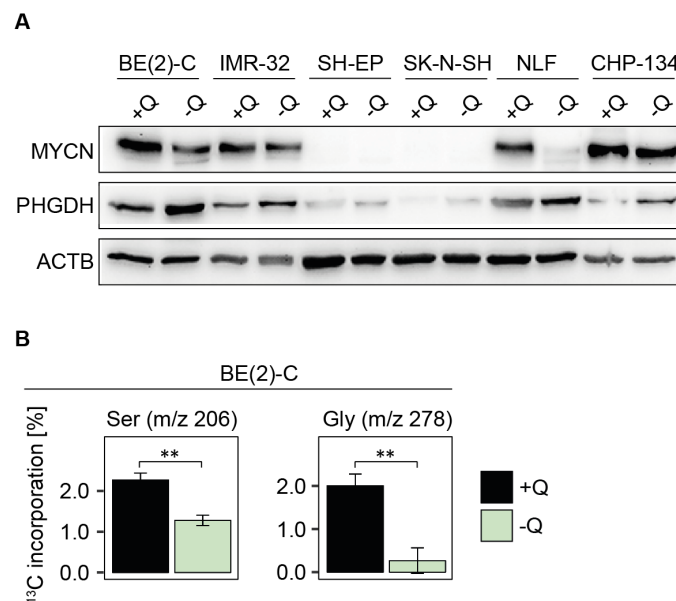


Figure 4.33.: Glutamine starvation increases PHGDH expression but not *de novo* serine synthesis A: Immunoblotting showing MYCN and PHGDH expression in neuroblastoma cell lines after 48 hours of glutamine starvation. B: BE(2)-C cells were cultivated in the presence (+Q) and absence (-Q) of glutamine for 48 hours with subsequent incubation in medium containing fully labeled ^{13}C -glucose for 20 min before harvest. Results represent mean \pm SD, $n=3$. P-values were calculated using an unpaired Student's t-test (* $0.01 < p \leq 0.05$; ** $0.001 < p \leq 0.01$; *** $p \leq 0.001$). Abbreviations: Gly - Glycine, Ser - Serine.

To analyze whether enhanced PHGDH protein expression results in an increase of glucose-derived carbons into *de novo* serine synthesis, BE(2)-C cells were starved for glutamine for 48 hours with subsequent labeling with $u\text{-}^{13}\text{C}$ -glucose for 20 min. This starvation decreased the incorporation of glucose-derived carbon-13 into serine and glycine (figure 4.33B). Thus, enhanced PHGDH protein expression was not accompanied by an increase in *de novo* serine synthesis. $u\text{-}^{13}\text{C}$ -glucose quantities and incorporation rates of additional metabolites within the central carbon metabolism in BE(2)-C and SH-EP cells are summarized in the supplementary figure B.7.

In summary, the investigated *MYCN*-amplified neuroblastoma cell lines decreased proliferation in the absence of glutamine. However, only a subgroup of these cells went into apoptosis which was shown to be ATF4-mediated in BE(2)-C cells. The strong correlation of *MYCN* to PHGDH expression was disrupted by glutamine starvation as all investigated neuroblastoma cell lines upregulated PHGDH expression independent of their *MYCN* levels. Moreover, enhanced PHGDH expression did not increase *de novo* serine and glycine synthesis.

5 Discussion

Amplification of the *MYCN* oncogene is found in approximately 22% of all neuroblastoma cases. As a transcription factor, MYCN regulates the expression of a multitude of genes resulting in fundamental changes of cellular processes and making MYCN an attractive target for neuroblastoma therapy [Westermarck et al., 2011]. Direct targeting of the members in the MYC family still remains a key challenge due to their nuclear localization, the lack of a ligand binding site and the diverse physiological functions in the maintenance of normal tissues [Whitfield et al., 2017].

Tumor cells rely on an increased demand of building blocks (e.g. proteins, lipids and nucleotides) to generate cellular components, and they need to maintain their intracellular redox balance and their epigenetic status [Locasale, 2013]. All of these needs are directly or indirectly connected to the metabolic network. A deeper understanding of MYCN-dependent metabolism might enable us to exploit those pathways for therapeutic use. In the following sections, we discuss the MYCN-mediated regulation of neuroblastoma metabolism and its potential usage in the development of novel therapeutic interventions. Moreover, we discuss how neuroblastoma cells cope with nutrient limitation in form of serine and glycine or glutamine starvation.

5.1. PHGDH as a metabolic target of MYCN in neuroblastoma

The herein presented data reveals a high significance of the *de novo* serine synthesis pathway and the one-carbon metabolism in *MYCN*-amplified neuroblastoma and describes the identification of PHGDH as a metabolic target of MYCN.

We observed a significant correlation of high-level MYCN to the expression of proteins within *de novo* serine synthesis and one-carbon metabolism by performing shotgun proteomics on primary biopsies from patients with neuroblastoma and cell lines. The highest correlation factor was obtained for PHGDH, which catalyzes the rate-limiting step in *de novo* serine synthesis. PHGDH is strongly expressed in cancer as well as in normal tissue [The Human Protein Atlas - PHGDH¹]. We have shown that high-level PHGDH expression correlates with amplified *MYCN* on transcriptional and translational

¹<https://www.proteinatlas.org/ENSG00000092621-PHGDH>

level *in vitro*. We observed a recruitment of MYCN to two regions within the *PHGDH* promoter site by performing ChIP qRT-PCR. We further revealed an elevated routing of carbons through the *de novo* serine synthesis in *MYCN*-amplified cells compared to *MYCN* non-amplified cells by applying quantitative metabolomics analysis in combination with the application of u-¹³C-glucose. In line with our data, a *PHGDH* amplification on chromosome 1p12 in triple-negative breast cancer lacking the estrogen receptor [Possemato et al., 2011] and in melanoma [Locasale et al., 2011] has been demonstrated to increase PHGDH protein expression levels and subsequently glucose-derived serine and phosphoserine pools. Further, our analysis of *PHGDH* mRNA expression data of neuroblastoma tumors revealed a correlation of PHGDH overexpression to an unfavorable overall survival of patients suffering from neuroblastoma. Overexpression of PHGDH also correlates with higher tumor grade and unfavorable overall survival of patients with gliomas [Liu et al., 2013] and cervical cancer [Jing et al., 2013]. In line with our findings, Liu and colleagues describe a higher expression of serine-glycine pathway genes in correlation with advanced disease stages in neuroblastoma and with an unfavorable clinical outcome. Small hairpin RNA mediated knockdown of *PHGDH* expression inhibited cell growth and tumorigenicity in neuroblastoma sphere-forming cells [Liu et al., 2016]. Overall, our data argues for a role of MYCN in the transcriptional regulation of *PHGDH* in neuroblastoma cells. Enhanced PHGDH expression results in increased routing of glucose-derived carbons into the *de novo* serine synthesis pathway in *MYCN*-amplified cells and correlates with unfavorable overall survival of patients suffering from neuroblastoma.

ATF4-mediated PHGDH regulation

The recent study of Xia and colleagues highlights the requirement of ATF4 and MYCN in the transcriptional activation of proteins within the serine-glycine pathway and the one-carbon metabolism in neuroblastoma [Xia et al., 2019]. MYCN and ATF4 form a positive feedback loop in which MYCN activates *ATF4* mRNA expression and ATF4 stabilizes MYCN protein by antagonizing FBXW7-mediated MYCN ubiquitination [Xia et al., 2019]. We observed a significant decrease in PHGDH protein expression following an siRNA-mediated knockdown of *ATF4* in *MYCN*-amplified and *MYCN* non-amplified neuroblastoma cell lines. ATF4-mediated transcriptional regulation of *PHGDH* was also shown in mouse fibroblasts [Adams, 2007]. Further, nuclear factor erythroid 2-related factor 2 [DeNicola et al., 2015] and mTORC1 [Ben-Sahra et al., 2016] use ATF4 in downstream signaling to regulate PHGDH. Our data indicates that ATF4 alone is sufficient to regulate PHGDH protein expression.

5.1.1. Inhibition of PHGDH impairs cell growth and reduces *de novo* serine synthesis

As PHGDH is strongly expressed in *MYCN*-amplified neuroblastoma, its inhibition might be a valuable target for potential therapeutic drug developments (figure 5.1). Therefore we exposed neuroblastoma cells to two identified and validated PHGDH inhibitors (P2101 and NCT503) which suppress PHGDH activity [Pacold et al., 2016; Wang et al., 2017]. This suppression impaired proliferation in PHGDH-high and -low expressing cells, even under extracellular serine and glycine supply. Our finding is partly consistent with the study from Possemato and colleagues in triple-negative breast cancer. They report a decreased cell proliferation following shRNA-mediated suppression of *PHGDH* only in high-level PHGDH but not in low-level PHGDH expressing cells [Possemato et al., 2011]. This contradiction to our results might be due to the different approaches of PHGDH suppression. Possemato and colleagues used a genetic approach by targeting *PHGDH* through shRNAs, whereas we used a pharmacological approach by applying small molecule inhibitors that allosterically inhibit PHGDH activity. Small molecule inhibitors might also cause off-target effects which could further impair cell proliferation. However, the study of Wang and colleagues confirms the specific binding of P2101 to PHGDH whereas the specific binding site for NCT503 still remains unknown [Wang et al., 2017].

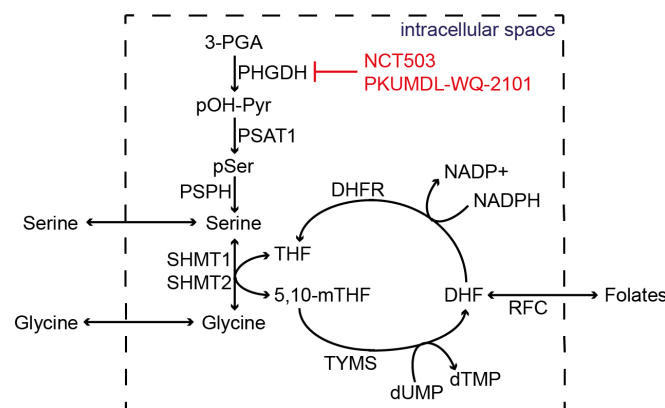


Figure 5.1.: Overview of *de novo* serine synthesis and serine-derived one-carbon unit utilization with applied small molecule inhibitors to target PHGDH. Figure adapted from [Newman and Maddocks, 2017].

Further, our data provides evidence that application of NCT503 reduced the conversion of glucose-derived carbons into *de novo* serine synthesis. Surprisingly, PHGDH suppression had no effect on the intracellular serine, glycine and nucleotide pools. Our finding is consistent with the result of Possemato and colleagues who show that suppression of *PHGDH* by shRNAs reduced *de novo* serine synthesis but did not decrease intracellular serine and glycine levels [Possemato et al., 2011]. We speculate that neuroblastoma cells acquire or activate alternative mechanisms to compensate for suppressed PHGDH activity. Possible strategies are discussed in section 5.1.2. Of note, the application of P2101 did not affect *de novo* serine synthesis. As the inhibitor is described to efficiently block PHGDH activity in various studies [Wang et al., 2017; Reid et al., 2018], we excluded the application of the inhibitor in further experiments.

5.1.2. Strategies to compensate for inhibited PHGDH activity

PHGDH suppression by NCT503 reduced *de novo* serine synthesis but did not affect intracellular serine and glycine levels. We therefore hypothesize that BE(2)-C cells can compensate for inhibited PHGDH activity and propose the following three mechanisms: (i) Conversion of glycine back into serine by SHMT enzymes, (ii) alterations in downstream pathways of serine metabolism to save serine pools, (iii) increased uptake of serine and glycine provided in the surrounding environment. The first mechanism is rather unlikely as intracellular glycine levels were not altered following PHGDH suppression. The second mechanism encompasses all pathways downstream of serine metabolism including biosynthetic reactions and metabolic signaling functions [Locasale et al., 2011]. Serine is associated with amino acid- and lipid metabolism and contributes to redox maintenance and the folate and nucleotide biosynthesis [Mattaini et al., 2016]. Additionally, serine can be catabolized directly into pyruvate or by transamination into 3-hydroxypyruvate and alanine. We observed a significant decrease in alanine production and stable nucleotide levels under NCT503 treatment in BE(2)-C cells, which are dependent on *de novo* serine synthesis. One could hypothesize that BE(2)-C cells downregulate subsequent conversion of serine into alanine to save capacities in order to constantly fuel critical pathways for cell maintenance including the folate cycle and nucleotide biosynthesis. The third mechanism implies the uptake of extracellular serine and glycine to compensate for suppressed *de novo* serine synthesis. Uptake of extracellular serine from the environment can be achieved by two different mechanisms such as upregulation of serine transporters or utilization of asparagine as an amino acid exchange factor [Mattaini et al., 2016; Krall et al., 2016]. As we did not measure the concentrations of serine, glycine or asparagine in the cell culture medium during our experiment, we here speculate about the following mechanisms.

Upregulation of serine transporters

Serine is a small neutral amino acid and is transferred into the cell by three different transporter systems. The first two systems are the alanine/serine/cysteine/threonine transporters (ASCT1 and ASCT2) and the system A transporters (SAT1 and SAT2), which are both sodium dependent. The third system is the alanine/serine/cysteine transporter (ASC), which belongs to a family of neutral amino acid antiporters. Antiporters are active in steady state enabling serine molecules to be constantly exchanged between the intra- and extracellular space [Mattaini et al., 2016]. This property of antiporters might lead to an underestimation of u-¹³C-labeled intracellular serine levels due to the rapid exchange with ¹²C-labeled serine in the medium [DeNicola et al., 2015].

Asparagine as an amino acid exchange factor

Intracellular asparagine levels play an important role in regulating the uptake of amino acids, especially serine, arginine and histidine [Krall et al., 2016]. Asparagine functions as an amino acid exchange factor such as intracellular asparagine exchanges with extracellular amino acids. Thus, high levels of asparagine can promote extensive uptake of extracellular serine [Krall et al., 2016].

5.1.3. Inhibition of PHGDH in mice carrying a patient-derived neuroblastoma xenograft

We performed a PDX experiment in order to analyze NCT503 and P2101 in an environment with physiological serine and glycine concentrations. As small molecule compounds would always be applied in combination with a chemotherapeutic drug in the clinic, the mice carrying subcutaneous PDX were treated with a combination therapy of PHGDH inhibitor and the chemotherapeutic drug cisplatin. Surprisingly, the combination therapy was counteractive to cisplatin monotherapy on tumor growth. Cisplatin is a chemotherapeutic which intercalates into the DNA and interferes with the DNA repair mechanisms subsequently leading to cell death [Trzaska, 2005]. Additional metabolomic changes by PHGDH inhibition, as discussed in section 5.1.4, might provide the tumor with advantageous properties to establish resistance to cisplatin. In order to further investigate this observation, additional experiments need to be performed. Those may include the treatment of neuroblastoma cell lines with the combination therapy in order to mimic the observed effect *in vitro*. Proliferation studies with our established *PHGDH* knockout clones may explain whether the antagonistic effect on tumor growth is due to an interaction of both compounds or due to metabolic changes upon PHGDH inhibition.

Single-treatment of the PDX-carrying mice with NCT503 or P2101 hindered initial tumor growth which relapsed in later stages. We hypothesize that other pathways might bypass the dependence on *de novo* serine synthesis in PHGDH-high expressing mice carrying subcutaneous PDX. One possible mechanism could be an increased uptake of serine and

glycine from the tumor environment as already observed in cell culture experiments. Our data is in line with work of Chen and colleagues who performed a *PHGDH* knockdown in estrogen receptor negative breast cancer xenograft models. They did not observe an effect on tumor maintenance and cell growth [Chen et al., 2013]. Contrary to our results is the work of Possemato and DeNicola. They performed an *in vivo* knockdown of *PHGDH* in breast and non-small cell lung cancer xenografts and observed reduced tumor growth [Possemato et al., 2011; DeNicola et al., 2015]. One could argue that knockdown of *PHGDH* is not comparable to suppression of PHGDH activity. However, treatment with the small molecule inhibitors NCT503 or P2101 also reduced glucose-derived serine pools *in vitro* and tumor growth *in vivo* [Pacold et al., 2016; Wang et al., 2017]. Xia and colleagues present data of reduced tumor volume and a prolonged event-free survival in mice carrying a BE(2)-C cell line xenograft. The mice were treated for ten days with NCT503 or vehicle control. Eventually all animals reached a tumor size of 1 cm in diameter and were euthanized [Xia et al., 2019]. In order to analyze the discrepancies in the study from Xia and colleagues to our performed experiment, differences in the experimental setups are discussed in greater detail below.

Patient-derived xenograft versus cell line-derived xenograft in mice

Discrepancies in NCT503 antitumoral efficacy may be due to the origin of the xenograft. In comparison to our patient-derived xenograft experiment, all other work published has been performed with cell line-derived xenografts. In cell culture, average serine concentrations in the standard DMEM cell culture medium are around $400 \mu\text{M}^2$. Physiological serine concentrations in the blood are around $77\text{--}178 \mu\text{M}$ in children with age of three months to six years³ and $173.2 \pm 51.3 \mu\text{M}$ in adults [Psychogios et al., 2011]. Consequently, cell lines are supplied with four-fold higher serine concentrations *in vitro* compared to their physiological supply. Transplantation of cell lines from cell culture into mice transfers them from a serine-rich to a serine-poor environment. We observed an upregulation of *de novo* serine synthesis and an induction of metabolic reprogramming upon serine and glycine depletion *in vitro* (section 5.2). Eventually, this metabolic reprogramming is also taking place when cell lines are transplanted into mice resulting in a higher vulnerability to metabolic interventions such as PHGDH inhibition. Thus, suppression of PHGDH activity or downregulation of *PHGDH* mRNA expression may be more effective in cell line-derived xenografts compared to patient-derived xenografts, which have not been exposed to an environment with high serine concentrations.

²<https://www.thermofisher.com/de/de/home/technical-resources/media-formulation.325.html>

³BC Children's Hospital Biochemical Genetics Lab

Tumor initiation versus tumor maintenance

The opposing effect of NCT503 treatment on tumor growth in mice carrying a neuroblastoma xenograft may be influenced by the size of the tumor at treatment initiation. In the recent study of Xia and colleagues, BE(2)-C and SK-N-AS cells were injected subcutaneously into both flanks of 6-week-old male and female NOD/SCID mice. Treatment with NCT503 was started at an average tumor volume of 100 mm³ [Xia et al., 2019]. In our study, treatment of mice carrying subcutaneous PDX was initiated at an average higher tumor volume of 140 mm³. Chen and colleagues, who also did not observe a growth inhibitory effect of *PHGDH* knockdown in mice carrying breast cancer cells, argued that smaller tumors may replicate more of a "tumor initiation" stage compared to larger tumors which represent more established tumors [Chen et al., 2013]. Thus, the stage of the tumor may be crucial in treating *PHGDH*-high expressing tumors. Treatment may be more efficient during the phase of tumor initiation, represented by smaller tumor volumes in the neuroblastoma xenograft study.

Differences in treatment duration and compound dosage

Application regimen and dosage of small molecule inhibitors is crucial to obtain a high drug efficacy with low side-effects. Treatment with NCT503 was performed for ten days in mice carrying neuroblastoma cell line xenografts by Xia and colleagues compared to 24 days of treatment in our study of mice carrying patient-derived neuroblastoma xenografts. Only the long-term treatment of *PHGDH* suppression revealed the overall minimal effect on tumor growth. NCT503 was injected intraperitoneal once a day in both studies, but treatment dosage was higher in BE(2)-C-derived xenografts (64 mg/kg bodyweight) compared to the patient-derived xenograft (40 mg/kg bodyweight). We can only speculate that an increase in treatment dosage might increase the inhibitory effect of NCT503 *in vivo* resulting in a prolonged event-free survival of mice carrying the cell line-derived xenograft.

5.1.4. Secondary effects induced by *PHGDH* inhibition

A recent study by Reid and colleagues on quantitative flux analysis following *PHGDH* inhibition by P2101 or siRNAs targeting *PHGDH* in HCT116 cells revealed large-scale metabolomic changes that resulted in alterations of the nucleotide metabolism, the pentose phosphate pathway and the TCA cycle [Reid et al., 2018]. Alterations in nucleotide metabolism were even independent of serine-derived nucleotide synthesis and redox maintenance. Of note, the majority of affected metabolic pathways were consistent between *PHGDH* inhibition by siRNAs targeting *PHGDH* or by application of P2101 [Reid et al., 2018]. Our data indicates that *PHGDH* inhibition in BE(2)-C cells decreased cell proliferation, but not, as expected, due to intracellular depleted serine, glycine or nucleotide pools. We hypothesize two scenarios how *PHGDH* suppression could then affect cell growth: (i)

PHGDH suppression has additional effects on central carbon metabolism perturbing other pathways or (ii) products of the *de novo* serine synthesis pathway are essential for cell growth.

Treatment with NCT503 deregulates routing of pyruvate into the TCA cycle

The here presented data demonstrates that NCT503 treated neuroblastoma cells increased lactate production and rerouted glucose-derived pyruvate into the TCA cycle. In the absence of NCT503, glucose-derived pyruvate was converted into acetyl-CoA which entered the TCA cycle and was further converted into citrate by the citrate synthase. However, pyruvate can also be carboxylated by the pyruvate carboxylase generating oxaloacetate and subsequently malate, thereby supporting TCA cycle anaplerosis. By applying u-¹³C-glucose to BE(2)-C and SH-EP cells, we observed an increased routing of pyruvate into malate and a significant decrease of pyruvate into citrate, suggesting a shift from the citrate synthase to increased usage of the pyruvate carboxylase under PHGDH suppression. This result was further supported by increased levels of acetyl-CoA that is required as an allosteric activator for pyruvate carboxylase activity [Jitrapakdee and Wallace, 1999]. Follow-up experiments are needed to analyze if this observation is an off-target effect of the NCT503 compound or triggered by suppressed PHGDH activity. Those may include the treatment of our CRISPR-Cas9 generated *PHGDH* knockout clones with NCT503 and the inactive compound with subsequent quantitative metabolomics analysis.

Products of *de novo* serine synthesis might be essential for cell proliferation

The second hypothesis encompasses the products of the serine synthesis pathway to be essential for cell proliferation. Twice as much cytosolic NADH per glucose molecule is generated within the *de novo* serine synthesis compared to glycolysis alone [Mullarky et al., 2011]. NADH is a reducing equivalent that can donate its electrons for ATP production to the electron transport chain. We have shown that ATP levels were not altered by NCT503 treatment *in vitro*. NADH is also used to maintain the redox balance within the cell. Thus, decreased NADH production within *de novo* serine synthesis by PHGDH suppression might induce redox stress due to an unbalanced NAD⁺/NADH ratio. However, the cellular redox status is not only determined by the NAD⁺/NADH ratio but also by the FAD⁺/FADH₂ ratio and glutathione levels. The here presented data does not allow any conclusion about deregulated NAD⁺/NADH ratio being responsible for the decreased cell proliferation.

Possemato and colleagues argue that the serine synthesis pathway is responsible for approximately 50% of the net conversion of glutamate to α -ketoglutarate [Possemato et al., 2011]. Thus, impaired *de novo* serine synthesis by suppressed PHGDH activity may result in a significant reduction of α -ketoglutarate fueling the TCA cycle. Contrary to the findings of Possemato and colleagues, literature suggests that *PHGDH* knockdown did not

affect α -ketoglutarate levels in breast cancer cell lines dependent on PHGDH expression [Locasale et al., 2011; Fan et al., 2015]. Locasale and colleagues argue that the amount of α -ketoglutarate produced within the *de novo* serine synthesis pathway is relatively small compared to other sources supplying α -ketoglutarate [Locasale et al., 2011]. Even though we could not detect α -ketoglutarate, the here presented data suggests that TCA cycle intermediates such as malate and succinate are reduced by NCT503 treatment, supporting the finding that perturbation of *de novo* serine synthesis has wide-ranging effects on other metabolic pathways.

5.1.5. PHGDH inhibition in PHGDH-low expressing SH-EP cells

We have shown that SH-EP cells express low-level PHGDH and convert only 1 - 2% of their glucose into serine. PHGDH suppression by NCT503 treatment did not alter *de novo* serine production in these cells. However, we observed a rerouting of glucose-derived carbons within the glycolysis as shown by enhanced routing of pyruvate into lactate and malate and decreased routing of pyruvate into citrate. The only difference observed in SH-EP cells compared to BE(2)-C cells after NCT503 treatment was the significant increase in alanine production. We speculate that PHGDH-dependent cell lines save the majority of serine to fuel the folate pool and nucleotide biosynthesis. SH-EP cells do not rely on PHGDH expression to fuel these reactions and therefore maintain downstream reactions of serine metabolism even under PHGDH suppression.

5.1.6. Summary

PHGDH is highly expressed in *MYCN*-amplified neuroblastoma cells by *MYCN*-mediated transcriptional activation of *PHGDH*. Pharmacological suppression of PHGDH activity by treatment with small molecule inhibitors arrested proliferation but did not affect intracellular serine, glycine or nucleotide levels in neuroblastoma cells. However, NCT503 treatment induced a metabolic rerouting of glucose-derived carbons within the central metabolic pathways which will be subject to further investigations. Treatment of mice carrying a patient-derived neuroblastoma xenograft with PHGDH inhibitors retarded initial tumor growth which resolved in later stages, indicating that PHGDH is dispensable for the cell growth of neuroblastoma tumors *in vivo*. The combination therapy of PHGDH inhibition with the chemotherapeutic drug cisplatin revealed an antagonizing effect on chemotherapy efficacy *in vivo* by induced resistance to cisplatin. We hypothesize, that PHGDH-high expressing neuroblastoma cells compensate for *de novo* serine inhibition by activation of alternative mechanisms or pathways to bypass PHGDH suppression. One possible mechanisms to bypass *de novo* serine inhibition is the increased uptake of serine and glycine from the surrounding environment. The potential role of external serine and glycine supply for neuroblastoma cell growth is discussed in the following section.

5.2. Cellular response to serine and glycine starvation

Tumor cells must constantly adapt to changes in nutrient and oxygen availability to sustain cell growth and survival as they invade new environments [Pavlova and Thompson, 2017]. Adaptation of cellular metabolism is crucial to adapt to stress conditions such as nutrient deprivation in form of serine and glycine starvation. The following sections describe the adaptation of neuroblastoma metabolism triggered by serine and glycine depletion and how cells combat with the consequences of those adaptations.

5.2.1. The role of extracellular serine and glycine on cell growth

Cells can either obtain serine from glucose through PHGDH or by uptake of serine from the environment (figure 5.2). Serine and glycine starvation in neuroblastoma cell lines induced a significant decrease in viable cell count only in the PHGDH-low expressing cell lines. These results are in line with findings of Locasale and colleagues who report that high PHGDH expression levels result in decreased dependency on exogenous serine for cell growth [Locasale et al., 2011].

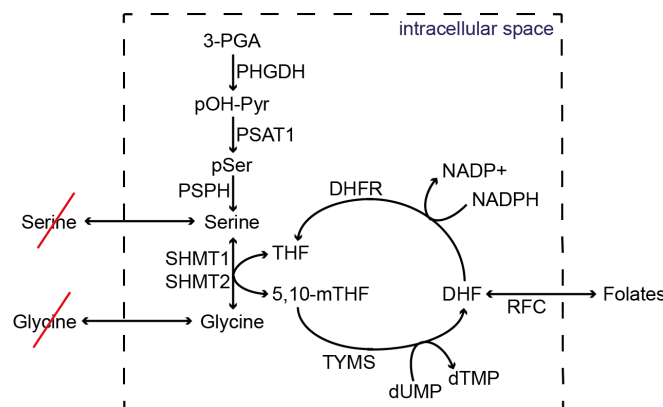


Figure 5.2.: Overview of *de novo* serine synthesis and serine-derived one-carbon unit utilization without extracellular serine and glycine supply. Figure adapted from [Newman and Maddocks, 2017].

5.2.2. Mechanisms to escape external serine and glycine dependency

We observed enhanced expression levels of *de novo* serine synthesis proteins in SH-EP cells. Higher protein expression levels resulted in increased pathway activity as shown by a 15-fold and 40-fold increase of ^{13}C -glucose incorporation into serine in SH-EP cells after 10 min and six hours of $u\text{-}^{13}\text{C}$ -glucose exposure, respectively. We here discuss two mechanisms of cells to increase *de novo* serine synthesis, either by (i) decreasing carbon routing through glycolysis by blockage of PKM2 activity or by (ii) sensing of amino acid deficiencies, such as serine and glycine, by mTORC1 or GCN2 kinase and subsequent ATF4 activation to promote serine synthesis.

Downregulation of PKM2 activity

One described mechanism to upregulate *de novo* serine synthesis in response to serine and glycine starvation is the downregulation of PKM2 activity, which controls glycolytic flux [Chaneton et al., 2012]. Decreased PKM2 activity causes an accumulation of upstream glycolytic intermediates for diversion to the serine synthesis pathway. In line with the work of Chaneton and colleagues, our data revealed evidence of low PKM2 activity in SH-EP cells by decreased routing of glucose-derived carbons into lactate and pyruvate and increased routing of glucose-derived carbons into serine upon serine and glycine starvation. Decreased routing through one of the ATP generating steps in glycolysis following PKM2 inhibition triggers energetic stress which is balanced by diverting more pyruvate to the mitochondria to support increased oxidative phosphorylation [Chaneton et al., 2012; Maddocks et al., 2013]. However elevated oxidative phosphorylation also enhances the production of ROS. Maddocks and colleagues report that the tumor suppressor protein p53 plays a critical role in cells to cope with extracellular serine depletion by enhancing glutathione biosynthesis as a mechanism to combat increased levels of ROS [Maddocks et al., 2013]. Their study illustrates that $p53^{+/+}$ HCT116 cells undergo a p21-dependent G1 arrest which allows the limited levels of *de novo* serine to be routed into glutathione biosynthesis enabling the cells to better combat with ROS [Maddocks et al., 2013]. We have shown that the removal of serine and glycine from the culture medium impaired proliferation in SH-EP and SK-N-AS cells but a significant loss in cell viability was only detected in SK-N-AS cells. Among other factors, the two cell lines differ in their p53 status. The SH-EP cells are p53 wildtype ($p53^{+/+}$) [Carr et al., 2006] whereas the SK-N-AS cell line harbors a homozygous deletion of exons 10-11 in *p53* ($p53^{-/-}$) [Maerken et al., 2011]. We hypothesize that $p53^{+/+}$ SH-EP cells better combat with oxidative stress by routing of *de novo* serine into glutathione synthesis. The $p53^{-/-}$ SK-N-AS cells fail to recover glutathione levels and thus accumulate increased intracellular ROS levels which reduced viability and proliferation. Additional studies, including the measurement of p53 and p21 expression, glutathione levels and cell cycle distribution are necessary to analyze whether a p53 activation in neuroblastoma cells induces higher metabolic flexibility under serine and glycine starvation.

Unexpectedly, we observed a significant increase of u-¹³C-glucose incorporation into serine in BE(2)-C cells. We hypothesize that BE(2)-C cells sense the absence of serine and glycine in the environment and consequently increase the routing of glucose-derived carbons into *de novo* serine synthesis. When serine and glycine were present in the culture medium, *de novo* serine production was 90-fold higher in BE(2)-C compared to SH-EP cells. Under serine and glycine starvation, this difference was reduced to a 4-fold higher serine production in BE(2)-C compared to SH-EP cells. Even though BE(2)-C cells synthesized around 9% of serine via the *de novo* pathway, they still need to obtain the remaining 91% of serine from external supply. Thus, BE(2)-C cells respond to deprivation of external serine and glycine but - due to generally higher PHGDH expression - reorganization of the metabolism is not required to meet the increase demand of *de novo* serine synthesis.

Amino acid sensing mechanisms

As reviewed by Gonzalez and colleagues, there are two main amino acid sensing mechanisms known in mammalian cells: mTOR and GCN2 [González and Hall, 2017]. mTOR is a conserved serine/threonine protein kinase and a master regulator of cell growth by balancing both anabolic and catabolic processes [Battu et al., 2017]. mTOR forms the catalytic subunit of two protein complexes, mTORC1 and mTORC2 [Jewell and Guan, 2013]. Both complexes respond to growth factors but only mTORC1 is sensitive to nutrient availability, such as amino acids and glucose, and regulates cell growth and metabolism. Moreover, mTORC1 regulates the translation of transcription factors including ATF4 and HIF1 α [Saxton and Sabatini, 2017]. GCN2 is a serine/threonine protein kinase and part of the integrated stress response pathways [Battu et al., 2017]. It promotes catabolic processes, such as autophagy, under amino acid deficiency. In case of an amino acid shortage, unloaded tRNAs accumulate in the cell and bind to the GCN2 kinase. Binding initiates autophosphorylation of GCN2 and simultaneous phosphorylation of eIF2 α at serine 51. Phosphorylated eIF2 α prevents the initiation of general protein translation and in parallel induces the translation of specific stress-responsive mRNAs such as ATF4 and CHOP [Battu et al., 2017]. Under amino acid deficiency, GCN2 also inhibits mTORC1 [Averous et al., 2016; Ye et al., 2015].

We have shown that the GCN2-eIF2 α -ATF4 stress response pathway is activated under serine and glycine starvation in SH-EP, but not in BE(2)-C cells. Moreover, ATF4 partly controlled PHGDH expression under serine and glycine starvation, as knockdown of *ATF4* resulted in PHGDH protein expression decline. *ATF4* can also be directly activated by the histone lysine demethylase KDM4C in response to serine starvation [Zhao et al., 2016]. KDM4C binds to the *ATF4* promoter and removes the repressive histone modification H3 lysine 9 trimethylation (H3K9m3) resulting in an epigenetically active state and subsequent increased ATF4 expression. Moreover, KDM4C directly activates serine pathway genes by removing the repressive H3K9m3 mark and thereby generating an epigenetically active

state [Zhao et al., 2016]. Under serine deprivation or low PKM2 activity, the mouse double minute 2 oncoprotein and major negative regulator of p53 is recruited to the chromatin in a p53 independent way and under involvement of the ATF3/4 transcription factors. Mouse double minute 2 protein together with ATF4 transcriptionally regulate serine-glycine and glutathione metabolism and are involved in redox maintenance under serine and glycine deprivation [Riscal et al., 2016]. Interestingly, mouse double minute 2 recruitment to serine synthesis genes correlates with increased H3K9 monomethylation marks [Riscal et al., 2016].

5.2.3. The importance of serine-glycine biosynthesis

We have shown that neuroblastoma cell lines restore their intracellular serine pools under suppressed *de novo* serine synthesis as well as under deprived serine and glycine condition, highlighting the importance of fueled serine pools for cell survival and maintenance. Besides functioning as a headgroup for phospholipids and being part of sphingolipid production, serine can be converted by SHMT to glycine and a one-carbon unit [Mattaini et al., 2016]. Serine-derived one-carbon units fuel into the folate cycle and support purine and thymidine biosynthesis. In mammals, serine can be converted to glycine in the cytosol via SHMT1 or in the mitochondria by SHMT2 [Mattaini et al., 2016]. We observed that serine and glycine starvation in SH-EP cells regulated PHGDH, PSAT1 and PSPH in *de novo* serine synthesis and SHMT1 and SHMT2 in serine-glycine synthesis, whereas protein expression in the one-carbon metabolism was not altered. Interestingly, SHMT1 and SHMT2 were inversely regulated under serine starvation with SHMT1 being downregulated and SHMT2 being upregulated in SH-EP cells. A recent study of Ducker and colleagues highlights the role of SHMT enzymes and the folate cycle as possible bottlenecks in tumor initiation and proliferation [Ducker et al., 2017]. Knockout of SHMT1&2 blocked tumor xenograft formation in HCT-116 colon cancer cells and SHMT1&2 inhibition reduced cell growth in diffuse large B-cell lymphoma [Ducker et al., 2017]. Inhibitor toxicity was even extended by adding the one-carbon donor formate to cells with impaired glycine uptake resulting in glycine depletion and subsequent apoptosis. Combination of formate with this inhibitor rescued cells from SHMT inhibition making formate and SHMT interesting targets for cancer therapy [Ducker et al., 2017].

5.2.4. Summary

The BE(2)-C cell line with high-level PHGDH expression is less dependent, contrary to the SH-EP cell line, on exogenous serine and glycine availability providing an advantage in tumor evasion and progression. The SH-EP cell line with low-level PHGDH expression highly depends on exogenous serine and glycine supply but is able to adapt to a serine and glycine deprived environment by upregulation of *de novo* serine synthesis and downregulation

of glycolysis. These adaptations in cellular metabolism might lead to higher ROS levels within the cell. Only $p53^{+/+}$ cells are known to combat with the consequences of adapted metabolism by shuffling more serine into glutathione synthesis. Follow-up experiments will exploit if the mechanism of $p53^{+/+}$ cells also approve for neuroblastoma cells and consequently if $p53$ -deficient neuroblastoma cells are more vulnerable to serine and glycine starvation. Recent literature highlighted the role of downstream reactions following serine metabolism as potential targets for cancer therapy, such as targeting SHMT enzymes or intermediates within the folate metabolism.

5.3. Disruption of the folate cycle by antifolates

Rapidly proliferating tumor cells meet the high demand for nucleotide pools by upregulation of the folate metabolism, which provides precursors of the pyrimidine and purine synthesis [Tedeschi et al., 2015]. As reviewed by Ducker and colleagues, folate-bound one-carbon units are interconverted between different oxidation states and thereby support nucleotide synthesis, amino acid homeostasis, epigenetic regulation and redox maintenance [Ducker and Rabinowitz, 2016]. We identified proteins of the one-carbon metabolism as highly correlating to amplified *MYCN* by applying shotgun proteomics of primary neuroblastoma biopsies and cell lines. In a next step, we directly targeted selective enzymes within the folate cycle, downstream of *de novo* serine synthesis, by applying the clinically approved antimetabolites 5-FU and MTX (figure 5.3).

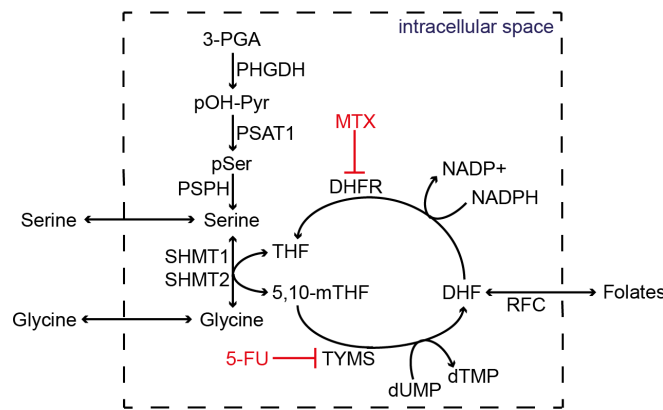


Figure 5.3.: Overview of serine-derived one-carbon unit utilization and applied therapeutics to target the folate-mediated one-carbon metabolism. Figure adapted from [Newman and Maddocks, 2017].

5.3.1. Antifolates disrupt nucleotide levels and impair proliferation

In line with our data, Lau and colleagues identified the folate-mediated one-carbon metabolism as highly upregulated in *MYCN*-amplified neuroblastoma tumors [Lau et al., 2015]. The pyrimidine analog 5-FU, structurally similar to uracile, exerts its cytotoxic effects through inhibition of TYMS and RNA misincorporation [Longley et al., 2003; Villa et al., 2019]. 5-FU is converted into three products: fluorodeoxyuridine monophosphate (FdUMP), fluorodeoxyuridine triphosphate (FdUTP) and fluorouridine triphosphate (FUTP). FdUMP blocks the nucleotide-binding site of TYMS by forming a stable tertiary complex with 5,10-mTHF. Thus, blocking of the TYMS binding site results in accumulation of dUMP and decreased synthesis of thymidine, as we observed in BE(2)-C cells. dTMP can be partly salvaged from thymidine through the thymidine kinase. Depletion of dTTP levels result in deoxynucleotide pool imbalances through various feedback mechanisms resulting in lethal overall DNA damage [Longley et al., 2003]. The folate antagonist MTX inhibits

the activity of DHFR and thus impairs the reduction of DHF to THF resulting in depleted folate-bound one-carbon units and a reduced conversion of dUMP to dTMP. Thus, we observed an accumulation of dUMP in BE(2)-C cells. However dTMP production might be partly rescued by the thymidine kinase [Abonyi et al., 1992]. Surprisingly, we observed that 5-FU and MTX overrun the proliferative pressure caused by MYCN in BE(2)-C cells as proliferation was significantly impaired but high PHGDH and MYCN levels were maintained.

We observed a significant downregulation in dUMP and dTMP levels in SH-EP cells in contrast to BE(2)-C cells. Combined with the increase in cell death, the decrease in proliferation and an overall stronger reduction in nucleotide levels, our data suggests a general destruction of SH-EP cells after 72 hours of 5-FU or MTX treatment. In contrast to our data, Lau and colleagues report a higher sensitivity of *MYCN*-amplified cell lines to MTX treatment compared to *MYCN* non-amplified cell lines [Lau et al., 2015]. The exact reason for this discrepancy remains unclear but may be due to the varying concentrations of MTX in the respective experiments. We treated BE(2)-C and SH-EP cells with 1 μ M MTX. Lau and colleagues report an IC_{50} of 0.59 μ M in BE(2)-C cells and did not even reach an IC_{50} with 1 mM MTX in SH-EP cells [Lau et al., 2015]. Thus, the strong decrease in proliferation in BE(2)-C cells may be due to an over dosage of MTX in our study. The discrepancy of increased sensitivity in SH-EP cells compared to BE(2)-C cells in response to MTX treatment still remains unclear and requires further investigation.

5.3.2. Bottlenecks of antifolate treatment

5-FU and MTX are used to treat a wide range of neoplastic diseases but are currently not applied in neuroblastoma treatment [Newman and Maddocks, 2017; Lau et al., 2015]. As the folate cycle is also essential for healthy proliferating cells, its inhibition goes along with high rates of toxicity if not applied appropriately [Newman and Maddocks, 2017]. Resistance of cancer cells to antifolate drugs may respond from changes in folate transporters, gene amplification of *DHFR* or *TYMS* resulting in increased enzyme expression, changes in drug affinity due to point mutations in *DHFR* or *TYMS* or general regulation in downstream pathways [Walling, 2006]. Purine and pyrimidine nucleobases may also be recycled through the activation of the nucleotide salvage pathways [Villa et al., 2019]. Uptake of MTX is mediated principally through the reduced folate carrier RFC which is encoded in the *SLC19A1* gene [Matherly et al., 2007]. Lau and colleagues report that the siRNA-mediated downregulation of *SLC19A1* decreases the uptake of MTX in the *MYCN*-amplified BE(2)-C cells [Lau et al., 2015]. Further, they identified *SLC19A1* as a direct transcriptional target of MYCN by quantitative ChIP applied to BE(2)-C and SH-EP-Tet21/N cells. This finding suggests that a subgroup of patients might be more eligible for MTX treatment. Besides DHFR and TYMS, enzyme expression within the mitochondrial one-carbon metabolism centered around MTHFD2 are highly increased in many cancers [Nilsson et al., 2014b;

Tedeschi et al., 2015]. A more targeted therapy of one-carbon metabolism proteins in cancer cells may inhibit tumor growth more selectively with less side-effects.

5.3.3. Summary

High-level MYCN expression strongly correlated to proteins within the one-carbon metabolism. Inhibition of the folate-mediated one-carbon metabolism in neuroblastoma cells by the antifolate drugs 5-FU and MTX was not affecting MYCN or PHGDH expression levels. However, nucleotide levels were significantly decreased and proliferation was strongly impaired. Levels of dTMP were partly rescued, most likely by the thymidine kinase. Sensitivity to the antifolate treatment was not correlated to the MYCN status of the cells in our study.

5.4. Cellular response to glutamine starvation

As reviewed by Altmann and colleagues, glutamine is a non-essential amino acid and its carbon and nitrogen groups are donated for TCA cycle anaplerosis, nucleotide, glutathione and amino acid biosynthesis and redox maintenance in mammalian cells [Altman et al., 2016]. Glucose and glutamine can serve as anaplerotic nutrients as both can be converted into oxaloacetate to enter the TCA cycle. In glioblastoma cells, glutamine is the major donor for anaplerotic reactions by contributing up to 90% to the oxaloacetate pool [DeBerardinis et al., 2007]. The oncogene *c-MYC* induces a metabolic reprogramming which enables cells to be addicted to glutamine catabolism to sustain their cellular viability and TCA cycle anaplerosis [Wise et al., 2008]. Although the role of c-MYC in glutaminolysis has been studied extensively, little is known about the role of MYCN in the regulation of glutamine metabolism. How glutamine starvation affects neuroblastoma cell growth, survival and metabolism including perturbations in the *de novo* serine synthesis pathway and TCA cycle anaplerosis is discussed in the following sections.

5.4.1. The role of extracellular glutamine on cell growth

It has been demonstrated that MYC protein expression is suppressed under external glutamine starvation in colon cancer cells [Dejure et al., 2017]. We have shown that neuroblastoma cell lines, which have been cultured without external glutamine, revealed a heterogeneous response on MYCN protein expression. NLF and BE(2)-C cells strongly- and IMR-32 moderately reduced MYCN expression, whereas no change was detectable in CHP-134 cells. MYCN expression was not detectable in the *MYCN* non-amplified cell lines SH-EP and SK-N-SH. Cell lines with only moderate to no decrease in MYCN protein expression also showed only minor decrease in viable cell count and increase of cell death upon glutamine starvation. BE(2)-C and NLF cell lines with a stronger decrease in MYCN protein levels showed a stronger decrease in viability. Recent data by Wang and colleagues show that MYCN is required in driving glutaminolysis in neuroblastoma [Wang et al., 2018]. Glutamine starvation in MYCN overexpressing cells resulted in a reduced proliferation and could be rescued by adding dimethyl α -ketoglutarate, a cell-permeable analog of α -ketoglutarate suggesting that glutaminolysis supports cell growth by providing α -ketoglutarate for TCA cycle anaplerosis [Wang et al., 2018]. In comparison to the work of Wang and colleagues, the here described data revealed only a minor decrease in cell proliferation under glutamine starvation for selected cell lines. One acquired mechanism of neuroblastoma cells to be independent of glutamine supply for TCA cycle anaplerosis is described in detail in section 5.4.4.

Glutamine is essential for *de novo* nucleotide synthesis

Despite the possibility of nucleotide uptake and salvage pathways, most proliferating cells synthesize nucleotides *de novo* [Lane and Fan, 2015]. Nucleotide biosynthesis requires NADPH, carbon and nitrogen from precursors such as aspartate, glutamine, serine, glycine and CO₂. Glutamine is essential for the pyrimidine ring synthesis and the transamination of UTP to CTP. In *de novo* purine synthesis, glutamine donates its nitrogen to produce IMP from PRPP and is essential for the biosynthesis of GMP [Lane and Fan, 2015]. Further, glutamate and oxaloacetate are converted into aspartate and α -ketoglutarate. Aspartate provides the nitrogen for the synthesis of AMP from IMP [Lane and Fan, 2015]. We observed an overall decrease in nucleotide levels, independent of MYCN expression in neuroblastoma cells upon glutamine starvation. Thus, we conclude, that glutamine is essential for *de novo* nucleotide biosynthesis in neuroblastoma.

5.4.2. Glutamine starvation triggers ATF4-dependent cell death

We observed that all analyzed *MYCN*-amplified neuroblastoma cell lines decreased their viable cell count and nucleotide levels following glutamine starvation. However, the response on cell death was heterogeneous. BE(2)-C, NLF and IMR-32 cells increased in cell death which was not seen in CHP-134 and Kelly. Further, we have shown that PUMA and cleaved PARP, two indicators for apoptosis, were upregulated on protein level only in BE(2)-C and NLF cells upon glutamine starvation. We conclude that the investigated *MYCN*-amplified cells decreased proliferation in the absence of glutamine but apoptosis is induced in only a subgroup of these cells.

In neuroblastoma, the transcription factor ATF4 is described to be stimulated by enhanced translation via the GCN2-eIF2 α cascade under glutamine starvation resulting in apoptosis [Qing et al., 2012]. Our data revealed a significant increase in ATF4 protein expression under glutamine starvation in BE(2)-C and NLF cells, which already showed an increase in apoptotic marker expression. We performed an siRNA-mediated knockdown of *ATF4* and observed reduced expression of PUMA and cleaved PARP in BE(2)-C cells under glutamine starvation. We conclude that glutamine starvation in BE(2)-C cells induces apoptosis through ATF4-dependent induction of PUMA and cleavage of PARP. Our data is partly overlapping with the work of Qing and colleagues who describe an increase of apoptosis through ATF4-dependent PUMA and NOXA induction in MYC-transformed neuroblastoma cells [Qing et al., 2012]. Qing and colleagues postulate that glutamine deprivation triggers cell death in a *MYC*-dependent manner as only a minor increase in cell death was observed in the MYCN and MYC-low expressing SH-EP cells. However, our data on glutamine-deprived SH-EP cells revealed an upregulation of the apoptotic markers PUMA and cleaved PARP as well as an increase in ATF4 protein expression (supplementary figure B.6) suggesting an increase in cell death also in MYCN and MYC low expressing cells. We conclude that cell death upon glutamine starvation is independent

of *MYCN*, as this response was observed in *MYCN*-amplified and *MYCN* non-amplified cells.

Additional molecular markers or pathways may be involved in the fate of neuroblastoma cells to either undergo apoptosis or cell cycle arrest under external glutamine deprivation. Dejure and colleagues identified the 3'UTR as a regulatory region to induce a MYC-dependent S-phase arrest under glutamine starvation [Dejure et al., 2017]. MYC expression is suppressed via the 3'UTR and mediated by adenosine-nucleotide levels to escape glutamine addiction and thus apoptosis. Ectopic MYC expression, by MYC transgene constructs missing the 3'UTR, undergo apoptosis under glutamine starvation [Dejure et al., 2017].

5.4.3. Glutamine starvation uncouples MYCN-mediated PHGDH regulation

It has been demonstrated that the *de novo* serine synthesis pathway can be stimulated in a c-MYC dependent manner under glutamine starvation [Sun et al., 2015]. In order to analyze the role of MYCN in *de novo* serine synthesis in the absence of glutamine, we starved *MYCN*-amplified and *MYCN* non-amplified neuroblastoma cells for glutamine, and analyzed MYCN and PHGDH expression by western blotting. Our data revealed a heterogeneous regulation of MYCN but also a general upregulation of PHGDH protein expression in all analyzed cell lines in the absence of glutamine. Interestingly, glutamine starvation triggered a cell response that uncouples the MYCN-mediated regulation of PHGDH by an so far unknown mechanism. We revealed reduced PHGDH protein expression upon siRNA-mediated knockdown of *ATF4*, suggesting that PHGDH expression is also regulated by ATF4 under glutamine starvation. However, increased expression of PHGDH did not result in activation of the *de novo* serine synthesis pathway. Incorporation of glucose-derived carbon-13 into serine and glycine was even significantly reduced in BE(2)-C cells. *De novo* serine synthesis requires glutamate for the conversion of phosphohydroxypyruvate into phosphoserine by the enzyme PSAT1 downstream of PHGDH. We hypothesize that glutamine starvation induces PHGDH expression by an ATF4-mediated mechanism but due to limited supply of glutamate, PSAT1 represents a bottleneck in *de novo* serine synthesis.

5.4.4. Glutamine starvation induces deregulation of central metabolic pathways

In the first step of glutaminolysis, glutamine is converted into glutamate either by mitochondrial glutaminases or by cytosolic glutamine amidotransferases. As reviewed by Cluntun and colleagues, glutamate is used for aspartate, phosphoserine and alanine production by supplying nitrogen for transamination reactions, is incorporated into the antioxidant glutathione, is secreted from the cell in exchange for other nutrients and can be converted

into α -ketoglutarate to support TCA cycle anaplerosis [Cluntun et al., 2017]. The role of glutamate in phosphoserine production is discussed in the section 5.4.3. Our further analysis of the u- ^{13}C -glucose incorporation data in the absence of external glutamine revealed a significant reduced utilization of glucose for alanine synthesis in BE(2)-C and SH-EP cells (supplementary figure B.7). The enzyme alanine transaminase transfers the amino group of glutamate to pyruvate, thus alanine production is highly glutamate-dependent [UniprotKB, P24298].

Glucose-derived pyruvate supports TCA cycle anaplerosis

Even though glutamine was removed from the cell culture medium, BE(2)-C and SH-EP cells did not completely abolish proliferation. We hypothesize that there might be an alternative mechanism to fuel TCA cycle anaplerosis upon glutamine starvation. We traced the routing of u- ^{13}C -glucose within the central carbon metabolism and calculated the ^{13}C -labeled quantities of central carbon metabolism intermediates (supplementary figure B.7). ^{13}C -labeled quantities of glycolytic intermediates were not affected by glutamine starvation with the exception of the described decrease in serine and alanine biosynthesis. However, replenishment of the TCA cycle was altered. We observed a decrease in glucose-derived citrate synthesis in BE(2)-C and SH-EP cells, as well as an increase in glucose-derived malate synthesis and acetyl-CoA levels in BE(2)-C cells. Enhanced acetyl-CoA levels point towards an allosteric regulation of increased pyruvate carboxylase activity [Jitrapakdee and Wallace, 1999]. Based on our data, we hypothesize that BE(2)-C cells induce the pyruvate carboxylase under glutamine deprived conditions to use glucose-derived pyruvate for TCA cycle anaplerosis. Activation of the pyruvate carboxylase in humans was shown for the first time in non-small cell lung cancer by [Fan et al., 2009]. A study of Cheng and colleagues reports the induction of the pyruvate carboxylase in glutaminase-silenced glioblastoma cells to use glucose-derived pyruvate rather than glutamine for TCA cycle anaplerosis [Cheng et al., 2011]. Further investigations are needed in order to validate our hypothesis of pyruvate carboxylase induction under glutamine starvation in neuroblastoma cells. Follow-up experiments might include the quantification of mRNA and protein expression of the pyruvate carboxylase and citrate synthase upon glutamine starvation.

5.4.5. Summary

In conclusion, the MYC-dependent response to external glutamine availability is not applicable for MYCN in neuroblastoma. The herein described data does not reveal a general pattern of MYCN protein expression in response to external glutamine starvation. However, a downregulation of MYCN protein expression in a subgroup of *MYCN*-amplified cells associates with an increase in cell death and on molecular level with an enhanced PUMA and cleaved PARP expression mediated via ATF4. The absence of external glutamine increases PHGDH expression levels but decreases *de novo* serine synthesis due

to the glutamate-consuming reaction catalyzed by PSAT1. Further, glutamine starvation uncouples MYCN-mediated regulation of PHGDH in neuroblastoma cells. Under glutamine starvation, BE(2)-C cells partly replace glutamine by glucose to fuel TCA cycle anaplerosis by increasing the routing of glucose-derived pyruvate into malate.

6 Outlook

The data presented here provides an enhanced understanding of metabolic vulnerabilities caused by amplified *MYCN* in neuroblastoma.

We revealed a high significance of *de novo* serine synthesis and one-carbon metabolism in *MYCN*-amplified neuroblastoma and identified *PHGDH* as a transcriptional target of *MYCN*. Enhanced *PHGDH* expression resulted in elevated levels of *de novo* serine synthesis in *MYCN*-amplified cells and in an independence of these cells to external serine and glycine supply. Treatment of *PHGDH*-high expressing cells with small molecules targeting *PHGDH* activity induced a proliferation arrest *in vitro* but was not affecting intracellular serine, glycine and nucleotide levels.

We further observed a rerouting of glucose-derived pyruvate entering the TCA cycle predominantly by conversion into oxaloacetate. We propose the validation of this finding with *PHGDH* knockout clones in order to decipher if the metabolic rerouting is due to suppressed *PHGDH* activity or an off-target effect of the applied inhibitor. Moreover, *PHGDH* inhibition revealed an antagonizing effect on chemotherapy efficacy in mice carrying subcutaneous a patient-derived neuroblastoma xenograft. We assume that *PHGDH* inhibition by small molecules diminishes proliferation but is not sufficient to induce lethality in neuroblastoma cells. These cells then establish resistance to classical chemotherapy. Further investigation is needed to understand the bypass mechanisms of cells to circumvent inhibited *de novo* serine synthesis. Possible mechanism include an enhanced expression of serine-glycine transporters in order to increase the uptake of serine and glycine from the environment or a decreased consumption of serine and glycine in downstream pathways.

PHGDH-low expressing cells were depended on external serine and glycine supply to maintain their nucleotide levels and proliferation *in vitro*. Serine and glycine starvation induced an upregulation of proteins within the *de novo* serine synthesis through GCN2-eIF2 α -ATF4 stress response signaling in line with an increased routing of glucose-derived carbons into the *de novo* serine synthesis pathway.

Our correlation analysis of cell lines and primary biopsies highlights the role of the one-carbon metabolism in *MYCN*-amplified neuroblastoma. Antifolate treatment impaired proliferation and diminished nucleotide levels *in vitro*. Our findings need to be validated by targeted siRNA-mediated knockdown of prominent genes within this pathway such as *TYMS* or *DHFR* *in vitro*. We further suggest the in-depth analysis of a potential

synergistic effect of antifolates to classical chemotherapy *in vivo* due to impaired nucleotide biosynthesis by antifolate treatment.

Glutamine starvation in *MYCN*-amplified neuroblastoma cells revealed a heterogeneous response on *MYCN* protein expression, proliferation and cell death. We propose that, in a subgroup of *MYCN*-amplified cells, cell death was induced by ATF4-mediated regulation of apoptotic proteins, including PUMA and cleavage of PARP. Further, we provided evidence for an uncoupled *MYCN*-mediated regulation of PHGDH in neuroblastoma cells upon glutamine starvation. We assume that PHGDH expression is regulated by additional mediators which might be identified by ChIP-Sequencing analysis upon glutamine starvation. Interestingly, an enhanced PHGDH protein expression did not result in elevated levels of *de novo* serine synthesis, most likely due to one glutamate consuming reaction within the pathway. Our preliminary data suggests that, independently of the *MYCN* expression level, BE(2)-C and SH-EP cells compensate for external glutamine depletion by enhanced usage of glucose to maintain TCA cycle anaplerosis. We suggest a quantitative pSIRM experiment and relative quantification of CCM enzymes upon glutamine starvation to elaborate this novel observation in neuroblastoma cells.

7 Bibliography

- M. Abonyi, N. Prajda, Y. Hata, H. Nakamura, and G. Weber. Methotrexate decreases thymidine kinase activity. *Biochemical and Biophysical Research Communications*, 187(1):522--528, 1992. doi: 10.1016/s0006-291x(05)81525-6.
- C. M. Adams. Role of the Transcription Factor ATF4 in the Anabolic Actions of Insulin and the Anti-anabolic Actions of Glucocorticoids. *The Journal of Biological Chemistry*, 282(23):16744--16753, 2007. doi: 10.1074/jbc.M610510200.
- B. Alberts, A. Johnson, J. Lewis, M. Raff, K. Roberts, and P. Walter. *Molekularbiologie der Zelle*. Wiley-VCH Verlag GmbH&Co, Weinheim, 4th edition, 2004. ISBN 3-527-30492-4.
- B. J. Altman, Z. E. Stine, and C. V. Dang. From Krebs to clinic: Glutamine metabolism to cancer therapy. *Nature Reviews Cancer*, 16(10):619--634, 2016. ISSN 14741768. doi: 10.1038/nrc.2016.71.
- I. Ambros, A. Zellner, B. Roald, G. Amann, R. Ladenstein, D. Printz, H. Gadner, and P. Ambros. Role of ploidy, chromosome 1p, and Schwann cells in the maturation of neuroblastoma. *New England Journal of Medicine*, 334(23):1505--1511, 1996. doi: 10.1056/NEJM199606063342304.
- I. M. Ambros, C. Brunner, R. Abbasi, C. Frech, and P. F. Ambros. Ultra-high density snparray in neuroblastoma molecular diagnostics. *Frontiers in Oncology*, 4(202):1--41, 2014. ISSN 2234943X. doi: 10.3389/fonc.2014.00202.
- P. F. Ambros, I. M. Ambros, G. M. Brodeur, M. Haber, J. Khan, A. Nakagawara, G. Schleiermacher, F. Speleman, R. Spitz, W. B. London, S. L. Cohn, A. D. Pearson, and J. M. Maris. International consensus for neuroblastoma molecular diagnostics: Report from the International Neuroblastoma Risk Group (INRG) Biology Committee. *British Journal of Cancer*, 100(9):1471--1482, 2009. ISSN 00070920. doi: 10.1038/sj.bjc.6605014.
- I. Amelio, F. Cutruzzolá, A. Antonov, M. Agostini, and G. Melino. Serine and glycine metabolism in cancer. *Trends in Biochemical Sciences*, 39(4):191--198, 2014. ISSN 09680004. doi: 10.1016/j.tibs.2014.02.004.

- N. D. Amoêdo, J. P. Valencia, M. F. Rodrigues, A. Galina, and F. D. Rumjanek. How does the metabolism of tumour cells differ from that of normal cells. *Bioscience Reports*, 33(6):865–873, 2013. ISSN 15734935. doi: 10.1042/BSR20130066.
- D. D. Anderson, C. M. Quintero, and P. J. Stover. Identification of a de novo thymidylate biosynthesis pathway in mammalian mitochondria. *Proceedings of the National Academy of Sciences*, 108(37):15163–15168, 2011. ISSN 0027-8424. doi: 10.1073/pnas.1103623108.
- M. Applebaum, T. Henderson, S. Lee, N. Pinto, S. Volchenboun, and S. Cohn. Second Malignancies in Patients With Neuroblastoma: The Effects of Risk-Based Therapy. *Pediatric Blood & Cancer*, 62:128–133, 2015. doi: 10.1002/pbc.
- E. Audet-Walsh, D. J. Papadopoli, G. Bourque, V. Gigue, J. St-pierre, D. J. Papadopoli, T. Yee, and S.-p. Gravel. The PGC-1 α /ERR α Axis Represses One-Carbon Metabolism and Promotes Sensitivity to Anti-folate Therapy in Breast Cancer. *Cell Reports*, 14: 920–931, 2016. doi: 10.1016/j.celrep.2015.12.086.
- J. Averous, S. Lambert-langlais, F. Mesclon, C. Valérie, L. Parry, C. Jousse, A. Bruhat, A.-c. Maurin, P. Pierre, C. G. Proud, and P. Fafournoux. GCN2 contributes to mTORC1 inhibition by leucine deprivation through an ATF4 independent mechanism. *Scientific Reports*, 6(27698):1–10, 2016. doi: 10.1038/srep27698.
- R. Bagatell, W. B. London, L. M. Wagner, S. D. Voss, C. F. Stewart, J. M. Maris, C. Kretschmar, and S. L. Cohn. Phase II study of irinotecan and temozolomide in children with relapsed or refractory neuroblastoma: A children’s oncology group study. *Journal of Clinical Oncology*, 29(2):208–213, 2011. ISSN 0732183X. doi: 10.1200/JCO.2010.31.7107.
- S. Battu, G. Minhas, A. Mishra, and N. Khan. Amino Acid Sensing via General Control Nonderepressible-2 Kinase and immunological Programming. *Frontiers in Immunology*, 8(1719):1–11, 2017. doi: 10.3389/fimmu.2017.01719.
- I. Ben-Sahra, G. Hoxhaj, S. Ricourt, J. Asara, and B. Manning. mTORC1 Induces Purine Synthesis Through Control of the Mitochondrial Tetrahydrofolate Cycle. *Science*, 351(6274):728–733, 2016. doi: 10.1126/science.aad0489.mTORC1.
- C. Bielow, G. Mastrobuoni, and S. Kempa. Proteomics Quality Control: Quality Control Software for MaxQuant Results. *Journal of Proteome Research*, 15(3):777–787, 2016. ISSN 15353907. doi: 10.1021/acs.jproteome.5b00780.
- A. Bollig-Fischer, T. G. Dewey, and S. P. Ethier. Oncogene Activation Induces Metabolic Transformation Resulting in Insulin-Independence in Human Breast Cancer Cells. *PLoS ONE*, 6(3):e17959, 2011. doi: 10.1371/journal.pone.0017959.

- N. Bown, S. Cotterill, M. Lastowska, S. O'Neill, A. Pearson, D. Plantaz, M. Meddeb, G. Danglot, C. Brinkschmidt, H. Christiansen, G. Laureys, and F. Speleman. Gain of chromosome arm 17q and adverse outcome in patients with neuroblastoma. *The New England Journal of Medicine*, 1999. doi: 10.1056/NEJM199906243402504.
- M. Brockmann, E. Poon, T. Berry, A. Carstensen, H. Deubzer, L. Rycak, Y. Jamin, K. Thway, S. Robinson, F. Roels, O. Witt, M. Fischer, L. Chesler, and M. Eilers. Small molecule inhibitors of aurora-a induce proteasomal degradation of N-myc in childhood neuroblastoma. *Cancer Cell*, 24(1):75--89, 2013. doi: 10.1016/j.ccr.2013.05.005.
- G. Brodeur, J. Pritchard, F. Berthold, N. Carlsen, V. Castel, R. Castelberry, B. De Bernardi, A. Evans, M. Favrot, and F. Hedborg. Revisions of the international criteria for neuroblastoma diagnosis, staging, and response to treatment. *Journal of Clinical Oncology*, 11(8):1466--1477, 1993.
- G. M. Brodeur. Neuroblastoma: Biological insights into a clinical enigma. *Nature Reviews Cancer*, 3(3):203--216, 2003. ISSN 1474175X. doi: 10.1038/nrc1014.
- J. M. Buescher and E. M. Driggers. Integration of omics: More than the sum of its parts. *Cancer and Metabolism*, 4(1):1--8, 2016. ISSN 20493002. doi: 10.1186/s40170-016-0143-y.
- J. Burchum and L. Rosenthal. *Pharmacology for Nursing Care*. Elsevier, 10th edition, 1990. ISBN 0323512275.
- E. L. Carpenter and Y. P. Mossé. Targeting ALK in neuroblastoma-preclinical and clinical advancements. *Nature Reviews Clinical Oncology*, 9(7):391--399, 2012. ISSN 17594774. doi: 10.1038/nrcclinonc.2012.72.
- J. Carr, E. Bell, A. D. J. Pearson, U. R. Kees, H. Beris, J. Lunec, and D. A. Tweddle. Increased Frequency of Aberrations in the p53 / MDM2 / p14 Pathway in Neuroblastoma Cell Lines Established at Relapse. *Cancer Research*, 66(4):2138--2146, 2006. doi: 10.1158/0008-5472.CAN-05-2623.
- B. Chaneton, P. Hillmann, L. Zheng, A. C. Martin, O. D. Maddocks, A. Chokkathukalam, J. E. Coyle, A. Jankevics, F. P. Holding, K. H. Vousden, C. Frezza, M. O'Reilly, and E. Gottlieb. Serine is a natural ligand and allosteric activator of pyruvate kinase M2. *Nature*, 491(7424):458--462, 2012. ISSN 00280836. doi: 10.1038/nature11540.
- J. Chen, F. Chung, G. Yang, M. Pu, H. Gao, W. Jiang, H. Yin, V. Capka, S. Kasibhatla, B. Laffitte, S. Jaeger, R. Pagliarini, Y. Chen, and W. Zhou. Phosphoglycerate dehydrogenase is dispensable for breast tumor maintenance and growth. *Oncotarget*, 4(12), 2013. doi: 10.18632/oncotarget.1540.

- T. Cheng, J. Sudderth, C. Yang, A. R. Mullen, E. S. Jin, and J. M. Matés. Pyruvate carboxylase is required for glutamine-independent growth of tumor cells. *PNAS*, 108(21):8674--8679, 2011. doi: 10.1073/pnas.1016627108.
- N. Cheung, J. Zhang, C. Lu, M. Parker, A. Bahrami, S. Tickoo, A. Heguy, A. Pappo, S. Federico, J. Dalton, I. Cheung, L. Ding, R. Fulton, J. Wang, X. Chen, J. Becksfort, J. Wu, C. Billups, D. Ellison, E. Mardis, R. Wilson, J. Downing, M. Dyer, and St Jude Children's Research Hospital-Washington University Pediatric Cancer Genome Project. Association of age at diagnosis and genetic mutations in patients with neuroblastoma. *JAMA*, 307(10):1062--1071, 2012. doi: 10.1001/jama.2012.228.
- Chi V. Dang. MYC on the Path to Cancer. *Cell*, 149(1):22--35., 2012. ISSN 00928674. doi: 10.1016/j.cell.2012.03.003.MYC.
- A. A. Cluntun, M. J. Lukey, R. A. Cerione, and J. W. Locasale. Glutamine Metabolism in Cancer: Understanding the Heterogeneity. *Trends in Cancer*, 3(3):169--180, 2017. ISSN 24058033. doi: 10.1016/j.trecan.2017.01.005.
- L. E. Cohen, J. H. Gordon, E. Y. Popovsky, S. Gunawardene, E. Duffey-Lind, L. E. Lehmann, and L. R. Diller. Late effects in children treated with intensive multimodal therapy for high-risk neuroblastoma: High incidence of endocrine and growth problems. *Bone Marrow Transplantation*, 49(4):502--508, 2014. ISSN 14765365. doi: 10.1038/bmt.2013.218.
- A. Copp, N. Adzick, L. Chitty, J. Fletcher, G. Holmbeck, and G. Shaw. Spina bifida. *Nature Reviews Disease Primers*, 1:15007, 2015. doi: 10.1038/nrdp.2015.7.
- C. Corbet and O. Feron. Cancer cell metabolism and mitochondria: Nutrient plasticity for TCA cycle fueling. *BBA-Reviews on Cancer*, 1868(1):7--15, 2017. doi: 10.1016/j.bbcan.2017.01.002.
- R. Corvi, L. C. Amler, L. Savelyeva, M. Gehring, and M. Schwab. MYCN is retained in single copy at chromosome 2 band p23-24 during amplification in human neuroblastoma cells. *PNAS*, 91(June):5523--5527, 1994. doi: 10.1073/pnas.91.12.5523.
- J. Cox and M. Mann. MaxQuant enables high peptide identification rates, individualized p.p.b.-range mass accuracies and proteome-wide protein quantification. *Nature Biotechnology*, 26:1367--1372, 2008. doi: 10.1038/nbt.1511.
- J. Cox and M. Mann. 1D and 2D annotation enrichment: A statistical method integrating quantitative proteomics with complementary high-throughput data. *BMC Bioinformatics*, 13, 2012. doi: 10.1186/1471-2105-13-S16-S12.

- J. Cox, M. Y. Hein, C. A. Lubner, I. Paron, N. Nagaraj, and M. Mann. Accurate proteome-wide label-free quantification by delayed normalization and maximal peptide ratio extraction, termed MaxLFQ. *Molecular and Cellular Proteomics*, 13(9):2513--2526, 2014. ISSN 15359484. doi: 10.1074/mcp.M113.031591.
- F. Crick. Central Dogma of Molecular Biology. *Nature*, 227:561--563, 1970.
- C. L. Cunsolo, M. P. Bicocchi, A. R. Petti, and G. P. Tonini. Numerical and structural aberrations in advanced neuroblastoma tumours by CGH analysis; survival correlates with chromosome 17 status. *British Journal of Cancer*, 83(10):1295--1300, 2000. ISSN 00070920. doi: 10.1054/bjoc.2000.1432.
- D. Daye and K. E. Wellen. Seminars in Cell & Developmental Biology Metabolic reprogramming in cancer : Unraveling the role of glutamine in tumorigenesis. *Seminars in Cell and Developmental Biology*, 23(4):362--369, 2012. ISSN 1084-9521. doi: 10.1016/j.semcdb.2012.02.002.
- R. J. DeBerardinis, A. Mancuso, E. Daikhin, I. Nissim, M. Yudkoff, S. Wehrli, and C. B. Thompson. Beyond aerobic glycolysis : Transformed cells can engage in glutamine metabolism that exceeds the requirement for protein and nucleotide synthesis. *PNAS*, 104(49):19345--19350, 2007. doi: 10.1073/pnas.0709747104.
- F. R. Dejure, N. Royla, S. Herold, J. Kalb, S. Walz, C. P. Ade, G. Mastrobuoni, J. T. Vanselow, A. Schlosser, E. Wolf, S. Kempa, and M. Eilers. The MYC mRNA 3-UTR couples RNA polymerase II function to glutamine and ribonucleotide levels. *The EMBO Journal*, 36(13):1854--1868, 2017. ISSN 0261-4189. doi: 10.15252/embj.201796662.
- G. M. DeNicola, P.-h. Chen, E. Mullarky, J. A. Sudderth, D. Wu, H. Tang, Y. Xie, J. M. Asara, K. E. Huffman, I. Ignacio, J. D. Minna, R. J. Deberardinis, and L. C. Cantley. NRF2 regulates serine biosynthesis in non-small cell lung cancer. *Nature Genetics*, 47(12):1475--1481, 2015. doi: 10.1038/ng.3421.NRF2.
- M. Deponter. Glutathione catalysis and the reaction mechanisms of glutathione-dependent enzymes. *Biochimica et biophysica acta*, 1830(5):3217--3266, 2013. ISSN 0304-4165. doi: 10.1016/j.bbagen.2012.09.018.
- A. Di Giannatale, N. Dias-Gastellier, A. Devos, K. Mc Hugh, A. Boubaker, F. Courbon, A. Verschuur, S. Ducassoul, K. Malekzadeh, M. Casanova, L. Amoroso, P. Chastagner, C. M. Zwaan, C. Munzer, I. Aerts, J. Landman-Parker, R. Riccardi, M. C. Le Deley, B. Geoerger, and H. Rubie. Phase II study of temozolomide in combination with topotecan (TOTEM) in relapsed or refractory neuroblastoma: A European Innovative Therapies for Children with Cancer-SIOP-European Neuroblastoma study. *European Journal of Cancer*, 50(1):170--177, 2014. ISSN 09598049. doi: 10.1016/j.ejca.2013.08.012.

- J. Ding, T. Li, X. Wang, E. Zhao, J. Choi, L. Yang, Y. Zha, Z. Dong, S. Huang, J. Asara, H. Cui, and H. Ding. The histone H3 methyltransferase G9A epigenetically activates the serine-glycine synthesis pathway to sustain cancer cell survival and proliferation. *Cell Metabolism*, 18(6):896--907, 2013. doi: 10.1016/j.cmet.2013.11.004.
- C. Dorneburg, M. Fischer, T. F. Barth, W. Mueller-Klieser, B. Hero, J. Gecht, D. R. Carter, K. de Preter, B. Mayer, L. Christner, F. Speleman, G. M. Marshall, K. M. Debatin, and C. Beltinger. LDHA in neuroblastoma is associated with poor outcome and its depletion decreases neuroblastoma growth independent of aerobic glycolysis. *Clinical Cancer Research*, 24(22):5772--5783, 2018. ISSN 15573265. doi: 10.1158/1078-0432.CCR-17-2578.
- G. Ducker, J. Ghergurovich, N. Mainolfi, V. Suri, S. Jeong, S. Hsin-Jung LI, A. Friedmann, M. Manfredi, Z. Gitai, H. Kim, and J. Rabinowitz. Human SHMT inhibitors reveal defective glycine import as a targetable metabolic vulnerability of diffuse large B-cell lymphoma. *PNAS*, 114(43):11404--11409, 2017. doi: 10.1073/pnas.1706617114.
- G. S. Ducker and J. D. Rabinowitz. One-Carbon Metabolism in Health and Disease. *Cell Metabolism*, 25(1):27--42, 2016. ISSN 1550-4131. doi: 10.1016/j.cmet.2016.08.009.
- S. Faber, L. Diamond, R. Mercer, R. Sylvester, and J. Wolff. Temporary remissions in acute leukemia in children produced by folic acid antagonist, 4-aminopteroyl-glutamic acid. *New England Journal of Medicine*, 238:787--793, 1948.
- J. Fan, X. Teng, L. Liu, K. R. Mattaini, and R. E. Looper. Human Phosphoglycerate Dehydrogenase Produces the Oncometabolite D-2-hydroxyglutarate. *ACS Chemical Biology*, 10:510--516, 2015. doi: 10.1021/cb500683c.
- T. W. M. Fan, A. N. Lane, R. M. Higashi, M. A. Farag, H. Gao, M. Bousamra, and D. M. Miller. Altered regulation of metabolic pathways in human lung cancer discerned by ^{13}C stable isotope-resolved metabolomics (SIRM). *Molecular Cancer*, 8(41):1--19, 2009. doi: 10.1186/1476-4598-8-41.
- S. S. Faria, C. F. M. Morris, A. R. Silva, and M. P. Fonseca. A Timely Shift from Shotgun to Targeted Proteomics and How it Can Be Groundbreaking for Cancer Research. *Frontiers in Oncology*, 7:1--28, 2017. doi: 10.3389/fonc.2017.00013.
- M. Favrot, V. Combaret, and C. Lasset. CD44 - A new prognostic marker for neuroblastoma. *New England Journal of Medicine*, 329(26):1965, 1993.
- M. Fischer, M. Skowron, and F. Berthold. Reliable transcript quantification by real-time reverse transcriptase-polymerase chain reaction in primary neuroblastoma using normalization to averaged expression levels of the control genes HPRT1 and SDHA.

- Journal of Molecular Diagnostics*, 7(1):89--96, 2005. ISSN 15251578. doi: 10.1016/S1525-1578(10)60013-X.
- A. González and M. N. Hall. Nutrient sensing and TOR signaling in yeast and mammals. *EMBO Journal*, 36(4):397--408, 2017. doi: 10.15252/embj.201696010.
- D. Hanahan and R. A. Weinberg. The Hallmarks of Cancer Review Douglas. *Cell*, 100(7): 57--70, 2000. ISSN 03407004. doi: 10.1007/s00262-010-0968-0.
- D. Hanahan and R. A. Weinberg. Hallmarks of cancer: The next generation. *Cell*, 144(5): 646--674, 2011. ISSN 00928674. doi: 10.1016/j.cell.2011.02.013.
- B. Hero, T. Simon, R. Spitz, K. Ernestus, A. Gnekow, H. Scheel-Walter, D. Schwabe, F. Schilling, G. Benz-Bohm, and F. Berthold. Localized infant neuroblastomas often show spontaneous regression: results of the prospective trials NB95-S and NB97. *J Clin Oncol*, 26:1504--1510, 2008. doi: 10.1200/JCO.2007.12.3349.
- D. Herranz. Glutaminolysis gets the spotlight in cancer. *Oncotarget*, 8(7):10761--10762, 2017. doi: 10.18632/oncotarget.12944.The.
- F. Hertwig, M. Peifer, and M. Fischer. Telomere maintenance is pivotal for high-risk neuroblastoma. *Cell Cycle*, 15(3):311--312, 2016. ISSN 15514005. doi: 10.1080/15384101.2015.1125243.
- W. Hobbie, T. Moshang, C. Carlson, E. Goldmuntz, N. Sacks, S. Goldfarb, S. Grupp, and J. Ginsberg. Late effects in survivors of tandem peripheral blood stem cell transplant for high-risk neuroblastoma. *Pediatric Blood & Cancer*, 51(5):679--683, 2008. doi: 10.1002/pbc.21683.
- A. M. Hosios, V. C. Hecht, L. V. Danai, M. L. Steinhauser, S. R. Manalis, and M. G. Vander Heiden. Amino Acids Rather than Glucose Account for the Majority of Cell Mass in Proliferating Mammalian Cells. *Developmental Cell*, 36:540--549, 2016. doi: 10.1016/j.devcel.2016.02.012.
- C. L. Hsu, H. Y. Chang, J. Y. Chang, W. M. Hsu, H. C. Huang, and H. F. Juan. Unveiling MYCN regulatory networks in neuroblastoma via integrative analysis of heterogeneous genomics data. *Oncotarget*, 7(24):36293--36310, 2016. ISSN 19492553. doi: 10.18632/oncotarget.9202.
- M. Jain, R. Nilsson, S. Sharma, N. Madhusudhan, T. Kitami, A. Souza, R. Kafri, M. Kirchner, C. Clish, and V. Mootha. Metabolite profiling identifies a key role for glycine in rapid cancer cell proliferation. *Science*, 336(6084):1040--1044, 2012. doi: 10.1126/science.1218595.

- J. Jewell and K.-L. Guan. Nutrient signaling to mTOR and cell growth. *Trends in Biochemical Sciences*, 38(5):233--242, 2013. doi: 10.1016/j.tibs.2013.01.004.
- Z. Jing, W. Heng, D. Aiping, Q. Yafei, and Z. Shulan. Expression and clinical significance of phosphoglycerate dehydrogenase and squamous cell carcinoma antigen in cervical cancer. *International Journal of Gynecologic Cancer*, 23(1465-1469), 2013. doi: 10.1097/IGC.0b013e3182a0c068.
- S. Jitrapakdee and J. C. Wallace. Structure, function and regulation of pyruvate carboxylase. *Biochemical Journal*, 340(1):1--16, 1999. ISSN 02646021. doi: 10.1042/0264-6021:3400001.
- D. Jun, H. Park, J. Lee, J. Baek, H. Park, K. Fukui, and Y. Kim. Positive regulation of promoter activity of human 3-phosphoglycerate dehydrogenase (PHGDH) gene is mediated by transcription factors Sp1 and NF-Y. *Gene*, 414(1-2):106--114, 2008. doi: 10.1016/j.gene.2008.02.018.
- S. Kempa, J. Hummel, T. Schwemmer, M. Pietzke, N. Strehmel, S. Wienkoop, J. Kopka, and W. Weckwerth. An automated GCxGC-TOF-MS protocol for batch-wise extraction and alignment of mass isotopomer matrixes from differential ^{13}C -labelling experiments: a case study for photoautotrophic-mixotrophic grown *Chlamydomonas reinhardtii* cells. *Journal of Basic Microbiology*, 49(1):82--91, 2009. doi: 10.1002/jobm.200800337.
- G. Kikuchi, Y. Motokawa, T. Yoshida, and K. Hiraga. Glycine cleavage system: reaction mechanism, physiological significance, and hyperglycinemia. *Proceedings of the National Academy of Sciences*, 84(10):246--263, 2008. doi: 10.2183/pjab/84.246.
- D. Kim, T. Huang, D. Schirch, and V. Schirch. Properties of Tetrahydropteroylpen-taglutamate Bound to 10-Formyltetrahydrofolate Dehydrogenase. *Biochemistry*, 35(49):15772--15783, 1996.
- E. Kováts. *Gas-chromatographische Charakterisierung organischer Verbindungen. Teil 1: Retentionsindices aliphatischer Halogenide, Alkohole, Aldehyde und Ketone*. Helvetica Chimica Acta, 41(7) edition, 1958. ISBN 01433334. doi: 0.1002/hlca.19580410703.
- A. S. Krall, S. Xu, T. G. Graeber, D. Braas, and H. R. Christofk. Asparagine promotes cancer cell proliferation through use as an amino acid exchange factor. *Nature Communications*, 7(11457), 2016. doi: 10.1038/ncomms11457.
- P. H. J. L. Kuich, N. Hoffmann, and S. Kempa. Maui-VIA: A User-Friendly Software for Visual Identification, Alignment, Correction, and Quantification of Gas Chromatography-Mass Spectrometry Data. *Frontiers in Bioengineering and Biotechnology*, 2(January):1--8, 2015. ISSN 2296-4185. doi: 10.3389/fbioe.2014.00084.

- B. Kushner, K. Kramer, S. Modak, and N. Cheung. Irinotecan plus temozolomide for relapsed or refractory neuroblastoma. *Journal of Clinical Oncology*, 24:5271--5276, 2006. doi: 10.1200/JCO.2006.06.7272.
- U. Laemmli. No TitleCleavage of structural proteins during the assembly of the head of bacteriophage T4. *Nature*, 227(5259):680--685, 1970.
- A. N. Lane and T. W. Fan. Regulation of mammalian nucleotide metabolism and biosynthesis. *Nucleic Acids Research*, 43(4):2466--2485, 2015. doi: 10.1093/nar/gkv047.
- D. T. Lau, C. L. Flemming, S. Gherardi, G. Perini, A. Oberthuer, M. Fischer, D. Juraeva, B. Brors, C. Xue, M. D. Norris, G. M. Marshall, M. Haber, J. I. Fletcher, and L. J. Ashton. MYCN amplification confers enhanced folate dependence and methotrexate sensitivity in neuroblastoma. *Oncotarget*, 6(17):15510--15523, 2015. ISSN 19492553. doi: 10.18632/oncotarget.3732.
- A. Lehninger, D. Nelson, and M. Cox. *Principles of Biochemistry*. New York, 2 edition, 1993.
- E. Liani, L. Rotheim, M. Bunni, C. Smith, G. Jansen, and Y. Assaraf. Loss of folypoly- γ -glutamate synthetase activity is a dominant mechanism of resistance to polyglutamylated novel antifolates in multiple human leukemia sublines. *International Journal of Cancer*, 103:587--599, 2003. doi: 10.1002/ijc.10829.
- J. Liu, S. Guo, Q. Li, L. Yang, Z. Xia, L. Zhang, Z. Huang, and N. Zhang. Phosphoglycerate dehydrogenase induces glioma cells proliferation and invasion by stabilizing forkhead box M1. *Journal of Neuro-Oncology*, 111(3):245--255, 2013. doi: 10.1007/s11060-012-1018-x.
- M. Liu, Y. Xia, J. Ding, B. Ye, E. Zhao, J. H. Choi, A. Alptekin, C. Yan, Z. Dong, S. Huang, L. Yang, H. Cui, Y. Zha, and H. F. Ding. Transcriptional Profiling Reveals a Common Metabolic Program in High-Risk Human Neuroblastoma and Mouse Neuroblastoma Sphere-Forming Cells. *Cell Reports*, 17(2):609--623, 2016. ISSN 22111247. doi: 10.1016/j.celrep.2016.09.021.
- K. Livak and T. Schmittgen. Analysis of relative gene expression data using real-time quantitative PCR and the 2(-Delta Delta C(T)) Method. *Methods*, 25(4):402--408, 2001. doi: 10.1006/meth.2001.1262.
- J. W. Locasale. Serine, glycine and one-carbon units: Cancer metabolism in full circle. *Nature Reviews Cancer*, 13(8):572--583, 2013. ISSN 1474175X. doi: 10.1038/nrc3557.
- J. W. Locasale, A. R. Grassian, T. Melman, C. A. Lyssiotis, K. R. Mattaini, A. J. Bass, G. Heffron, C. M. Metallo, T. Muranen, H. Sharfi, A. T. Sasaki, D. Anastasiou, E. Mullarky, N. I. Vokes, M. Sasaki, R. Beroukhim, G. Stephanopoulos, A. H. Ligon,

- M. Meyerson, A. L. Richardson, L. Chin, G. Wagner, J. M. Asara, J. S. Brugge, L. C. Cantley, and M. G. Vander Heiden. Phosphoglycerate dehydrogenase diverts glycolytic flux and contributes to oncogenesis. *Nature Genetics*, 43(9):869–874, 2011. ISSN 10614036. doi: 10.1038/ng.890.
- M. Lodrini, A. Sprüssel, K. Astrahantseff, D. Tiburtius, H. N. Lode, M. Fischer, U. Keilholz, and H. E. Deubzer. Using droplet digital PCR to analyze MYCN and ALK copy number in plasma from patients with neuroblastoma. *Oncotarget*, 8(49):85234–85251, 2017. doi: 10.18632/oncotarget.19076.
- W. London, R. Bagatell, B. Weigel, E. Fox, D. Guo, C. Ryn, A. Naranjo, and R. Julie. Historical time-to-progression (TTP) and progression-free survival (PFS) in relapsed/refractory neuroblastoma modern-era (2002-14) patients from Children’s Oncology Group (COG) early- phase trials. *Cancer*, 123(24):4914–4923, 2017. doi: 10.1002/cncr.30934.Historical.
- W. B. London, R. P. Castleberry, K. K. Matthay, A. T. Look, R. C. Seeger, H. Shimada, P. Thorner, G. Brodeur, J. M. Maris, C. P. Reynolds, and S. L. Cohn. Evidence for an age cutoff greater than 365 days for neuroblastoma risk group stratification in the Children’s Oncology Group. *Journal of Clinical Oncology*, 23(27):6459–6465, 2005. ISSN 0732183X. doi: 10.1200/JCO.2005.05.571.
- W. B. London, C. N. Frantz, L. A. Campbell, R. C. Seeger, B. A. Brumback, S. L. Cohn, K. K. Matthay, R. P. Castleberry, and L. Diller. Phase II randomized comparison of topotecan plus cyclophosphamide versus topotecan alone in children with recurrent or refractory neuroblastoma: A children’s oncology group study. *Journal of Clinical Oncology*, 28(24):3808–3815, 2010. ISSN 0732183X. doi: 10.1200/JCO.2009.27.5016.
- D. Longley, D. Harkin, and P. Johnston. 5-fluorouracil: mechanisms of action and clinical strategies. *Nature Reviews Cancer*, 3(5):330–338, 2003. doi: 10.1038/nrc1074.
- F. Lorenzin, U. Benary, A. Baluapuri, S. Walz, L. A. Jung, B. von Eyss, C. Kisker, J. Wolf, M. Eilers, and E. Wolf. Different promoter affinities account for specificity in MYC-dependent gene regulation. *eLife*, 5(e15161):1–35, 2016. ISSN 2050084X. doi: 10.7554/eLife.15161.
- P. Lorkiewicz, R. Higashi, A. Lane, and T. Fan. High information throughput analysis of nucleotides and their isotopically enriched isotopologues by direct-infusion FTICR-MS. *Metabolomics*, 8(5):930–939, 2012. doi: 10.1007/s11306-011-0388-y.
- W. Lutz, M. Stöhr, J. Schürmann, A. Wenzel, A. Löhr, and M. Schwab. Conditional expression of N-myc in human neuroblastoma cells increases expression of α -prothymosin

- and ornithine decarboxylase and accelerates progression into S-phase early after mitogenic stimulation of quiescent cells. *Oncogene*, 13:803–812, 1996.
- O. D. Maddocks, C. R. Berkers, S. M. Mason, L. Zheng, K. Blyth, E. Gottlieb, and K. H. Vousden. Serine starvation induces stress and p53-dependent metabolic remodelling in cancer cells. *Nature*, 493(7433):542–546, 2013. ISSN 00280836. doi: 10.1038/nature11743.
- T. V. Maerken, A. Rihani, D. Dreidax, S. D. Clercq, N. Yigit, J.-c. Marine, F. Westermann, A. D. Paepe, J. Vandesompele, and F. Speleman. Functional Analysis of the p53 Pathway in Neuroblastoma Cells Using the Small-Molecule MDM2 Antagonist Nutlin-3. *Molecular Cancer Therapeutics*, 10(6):983–994, 2011. doi: 10.1158/1535-7163.MCT-10-1090.
- B. A. Malynn, I. M. De Alboran, R. C. O’Hagan, R. Bronson, L. Davidson, R. A. DePinho, and F. W. Alt. N-myc can functionally replace c-myc in murine development, cellular growth, and differentiation. *Genes and Development*, 14(11):1390–1399, 2000. ISSN 08909369. doi: 10.1101/gad.14.11.1390.
- J. M. Maris. Recent advances in neuroblastoma. Suppl. *The New England Journal of Medicine*, 362(23):2202–11, 2010. ISSN 1533-4406. doi: 10.1056/NEJMra0804577.Recent.
- J. M. Maris, M. J. Weiss, Y. Mosse, G. Hii, C. Guo, P. S. White, M. D. Hogarty, T. Mirensky, G. M. Brodeur, T. R. Rebbeck, M. Urbanek, and S. Shusterman. Evidence for a hereditary neuroblastoma predisposition locus at chromosome 16p12-13. *Cancer Research*, 62(22):6651–6658, 2002. ISSN 00085472.
- L. Matherly, Z. Hou, and Y. Deng. Human reduced folate carrier: translation of basic biology to cancer etiology and therapy. *Cancer Metastasis Rev*, 26(1):111–128, 2007. doi: 10.1007/s10555-007-9046-2.
- K. R. Mattaini, M. R. Sullivan, and M. G. Vander Heiden. The importance of serine metabolism in cancer. *Journal of Cell Biology*, 214(3):249–257, 2016. ISSN 15408140. doi: 10.1083/jcb.201604085.
- K. Matthay, J. Maris, G. Schleiermacher, A. Nakagawara, C. Mackall, L. Diller, and W. Weiss. Neuroblastoma. *Nature Reviews, Disease Primers*, 2:1–21, 2016. ISSN 14653621. doi: 10.4324/9781315113968.
- K. K. Matthay, R. E. George, and A. L. Yu. Promising therapeutic targets in neuroblastoma. *Clinical Cancer Research*, 18(10):2740–2753, 2012. ISSN 10780432. doi: 10.1158/1078-0432.CCR-11-1939.
- A. Meister. Selective modification of glutathione metabolism. *Science*, 220:472–477, 1983.
- S. J. Mentch, M. Mehrmohamadi, L. Huang, A. E. Thalacker-mercer, S. N. Nichenametla, J. W. Locasale, S. J. Mentch, M. Mehrmohamadi, L. Huang, X. Liu, D. Gupta, and

- D. Mattocks. Histone Methylation Dynamics and Gene Regulation Occur through the Sensing of One-Carbon Metabolism. *Cell Metabolism*, 22:861–873, 2015. doi: 10.1016/j.cmet.2015.08.024.
- J. J. Molenaar, J. Koster, D. A. Zwiijnenburg, P. Van Sluis, L. J. Valentijn, I. Van Der Ploeg, M. Hamdi, J. Van Nes, B. A. Westerman, J. Van Arkel, M. E. Ebus, F. Haneveld, A. Lakeman, L. Schild, P. Molenaar, P. Stroeken, M. M. Van Noesel, I. Øra, E. E. Santo, H. N. Caron, E. M. Westerhout, and R. Versteeg. Sequencing of neuroblastoma identifies chromothripsis and defects in neuritogenesis genes. *Nature*, 483(7391):589–593, 2012. ISSN 00280836. doi: 10.1038/nature10910.
- T. Monclair, G. M. Brodeur, P. F. Ambros, H. J. Brisse, G. Cecchetto, K. Holmes, M. Kaneko, W. B. London, K. K. Matthay, J. G. Nuchtern, D. Von Schweinitz, T. Simon, S. L. Cohn, and A. D. Pearson. The International Neuroblastoma Risk Group (INRG) staging system: An INRG Task Force report. *Journal of Clinical Oncology*, 27(2): 298–303, 2009. ISSN 0732183X. doi: 10.1200/JCO.2008.16.6876.
- D. M. Moran, P. B. Trusk, K. Pry, K. Paz, D. Sidransky, and S. S. Bacus. KRAS Mutation Status Is Associated with Enhanced Dependency on Folate Metabolism Pathways in Non – Small Cell Lung Cancer Cells. *Molecular Cancer Therapeutics*, pages 1611–1625, 2014. doi: 10.1158/1535-7163.MCT-13-0649.
- Y. P. Mossé, M. Laudenslager, L. Longo, K. A. Cole, A. Wood, E. F. Attiyeh, M. J. Laquaglia, R. Sennett, J. E. Lynch, P. Perri, G. Laureys, F. Speleman, C. Kim, C. Hou, H. Hakonarson, A. Torkamani, N. J. Schork, G. M. Brodeur, G. P. Tonini, E. Rappaport, M. Devoto, and J. M. Maris. Identification of ALK as a major familial neuroblastoma predisposition gene. *Nature*, 455(7215):930–935, 2008. ISSN 00280836. doi: 10.1038/nature07261.
- Y. P. Mosse, E. Fox, D. T. Teachey, J. M. Reid, S. L. Safgren, H. Carol, R. B. Lock, P. J. Houghton, M. A. Smith, D. Hall, D. A. Barkauskas, M. Krailo, S. D. Voss, S. L. Berg, S. M. Blaney, and B. J. Weigel. A phase II study of alisertib in children with recurrent/refractory solid tumors or leukemia: Children’s Oncology Group Phase I and pilot Consortium (ADVL0921). *Clinical Cancer Research*, 25(11):3229–3238, 2019. ISSN 15573265. doi: 10.1158/1078-0432.CCR-18-2675.
- S. Mudd, J. Brosnan, M. Brosnan, R. Jacobs, S. Stabler, R. Allen, D. Vance, and C. Wagner. Methyl balance and transmethylation fluxes in humans. *The American Journal of Clinical Nutrition*, 85(1):19–25, 2007. doi: 10.1093/ajcn/85.1.19.
- E. Mullarky, K. R. Mattaini, M. G. Vander Heiden, L. C. Cantley, and J. W. Locasale. PHGDH amplification and altered glucose metabolism in human melanoma. *Pigment Cell & Melanoma*, 24(6):1112–1115, 2011. doi: 10.1111/j.1755-148X.2011.00919.x.

- E. Mullarky, N. C. Lucki, R. Beheshti Zavareh, J. L. Anglin, A. P. Gomes, B. N. Nicolay, J. C. Y. Wong, S. Christen, H. Takahashi, P. K. Singh, J. Blenis, J. D. Warren, S.-M. Fendt, J. M. Asara, G. M. DeNicola, C. A. Lyssiotis, L. L. Lairson, and L. C. Cantley. Identification of a small molecule inhibitor of 3-phosphoglycerate dehydrogenase to target serine biosynthesis in cancers. *Proceedings of the National Academy of Sciences*, 113(7):1778--1783, 2016. ISSN 0027-8424. doi: 10.1073/pnas.1521548113.
- A. C. Newman and O. D. Maddocks. One-carbon metabolism in cancer. *British Journal of Cancer*, 116(12):1499--1504, 2017. ISSN 15321827. doi: 10.1038/bjc.2017.118.
- M. A. Nikiforov, S. Chandriani, B. O’Connell, O. Petrenko, I. Kotenko, A. Beavis, J. M. Sedivy, and M. D. Cole. A Functional Screen for Myc-Responsive Genes Reveals Serine Hydroxymethyltransferase, a Major Source of the One-Carbon Unit for Cell Metabolism. *Molecular and Cellular Biology*, 22(16):5793--5800, 2002. ISSN 0270-7306. doi: 10.1128/mcb.22.16.5793-5800.2002.
- R. Nilsson, M. Jain, N. Madhusudhan, N. Sheppard, L. Strittmatter, C. Kampf, J. Huang, A. Asplund, and V. Mootha. Metabolic enzyme expression highlights a key role for MTHFD2 and the mitochondrial folate pathway in cancer. *Nature Communications*, 5(3128), 2014a. doi: 10.1038/ncomms4128.
- R. Nilsson, M. Jain, N. Madhusudhan, N. G. Sheppard, L. Strittmatter, C. Kampf, J. Huang, A. Asplund, and V. K. Mootha. Metabolic enzyme expression highlights a key role for MTHFD2 and the mitochondrial folate pathway in cancer. *Nature Communications*, 5(3128), 2014b. doi: 10.1038/ncomms4128.
- G. Oliynyk, M. V. Ruiz-Pérez, L. Sainero-Alcolado, J. Dzieran, H. Zirath, H. Gallart-Ayala, C. Wheelock, H. J. Johansson, R. Nilsson, J. Lehtiö, and M. Arsenian-Henriksson. MYCN-enhanced Oxidative and Glycolytic Metabolism Reveals Vulnerabilities for Targeting Neuroblastoma. *iScience*, 21:188--204, 2019. ISSN 25890042. doi: 10.1016/j.isci.2019.10.020.
- M. E. Pacold, K. R. Brimacombe, S. H. Chan, J. M. Rohde, C. A. Lewis, L. J. Swier, R. Possemato, W. W. Chen, L. B. Sullivan, B. P. Fiske, S. Cho, E. Freinkman, K. Birsoy, M. Abu-Remaileh, Y. D. Shaul, C. M. Liu, M. Zhou, M. J. Koh, H. Chung, S. M. Davidson, A. Luengo, A. Q. Wang, X. Xu, A. Yasgar, L. Liu, G. Rai, K. D. Westover, M. G. Vander Heiden, M. Shen, N. S. Gray, M. B. Boxer, and D. M. Sabatini. A PHGDH inhibitor reveals coordination of serine synthesis and one-carbon unit fate. *Nature Chemical Biology*, 12(6):452--458, 2016. ISSN 15524469. doi: 10.1038/nchembio.2070.
- J. Park, R. Bagatell, W. London, J. Maris, S. Cohn, K. Mattay, M. Hogarty, and C. N. Committee. Children’s Oncology Group’s 2013 blueprint for research: neuroblastoma. *Pediatric Blood & Cancer*, 60(6):985--993, 2013. doi: 10.1002/pbc.24433.

- N. Pavlova and C. Thompson. The emerging hallmarks of cancer metabolism. *Cell Metabolism*, 23(1):27--47, 2017. doi: 10.1016/j.cmet.2015.12.006.
- M. Peifer, F. Hertwig, F. Roels, D. Dreidax, M. Gartlgruber, R. Menon, A. Krämer, J. L. Roncaioli, F. Sand, J. M. Heuckmann, F. Ikram, R. Schmidt, S. Ackermann, A. Engesser, Y. Kahlert, W. Vogel, J. Altmüller, P. Nürnberg, J. Thierry-Mieg, D. Thierry-Mieg, A. Mariappan, S. Heynck, E. Mariotti, K. O. Henrich, C. Gloeckner, G. Bosco, I. Leuschner, M. R. Schweiger, L. Savelyeva, S. C. Watkins, C. Shao, E. Bell, T. Höfer, V. Achter, U. Lang, J. Theissen, R. Volland, M. Saadati, A. Eggert, B. De Wilde, F. Berthold, Z. Peng, C. Zhao, L. Shi, M. Ortmann, R. Büttner, S. Perner, B. Hero, A. Schramm, J. H. Schulte, C. Herrmann, R. J. O'Sullivan, F. Westermann, R. K. Thomas, and M. Fischer. Telomerase activation by genomic rearrangements in high-risk neuroblastoma. *Nature*, 526(7575):700--704, 2015. ISSN 14764687. doi: 10.1038/nature14980.
- M. Pietzke, C. Zasada, S. Mudrich, and S. Kempa. Decoding the dynamics of cellular metabolism and the action of 3-bromopyruvate and 2-deoxyglucose using pulsed stable isotope-resolved metabolomics. *Cancer & Metabolism*, 2(1):9, 2014. ISSN 2049-3002. doi: 10.1186/2049-3002-2-9.
- R. Possemato, K. M. Marks, Y. D. Shaul, M. E. Pacold, D. Kim, K. Birsoy, S. Sethumadhavan, H. K. Woo, H. G. Jang, A. K. Jha, W. W. Chen, F. G. Barrett, N. Stransky, Z. Y. Tsun, G. S. Cowley, J. Barretina, N. Y. Kalaany, P. P. Hsu, K. Ottina, A. M. Chan, B. Yuan, L. A. Garraway, D. E. Root, M. Mino-Kenudson, E. F. Brachtel, E. M. Driggers, and D. M. Sabatini. Functional genomics reveal that the serine synthesis pathway is essential in breast cancer. *Nature*, 476(7360):346--350, 2011. ISSN 00280836. doi: 10.1038/nature10350.
- N. Psychogios, D. D. Hau, J. Peng, A. C. Guo, R. Mandal, S. Bouatra, R. Krishnamurthy, R. Eisner, B. Gautam, N. Young, C. Knox, E. Dong, P. Huang, Z. Hollander, T. L. Pedersen, R. Steven, F. Bamforth, R. Greiner, B. Mcmanus, J. W. Newman, T. Goodfriend, and D. S. Wishart. The Human Serum Metabolome. *PloS one*, 6(2), 2011. doi: 10.1371/journal.pone.0016957.
- T. J. Pugh, O. Morozova, E. F. Attiyeh, S. Asgharzadeh, J. S. Wei, D. Auclair, S. L. Carter, K. Cibulskis, M. Hanna, A. Kiezun, J. Kim, M. S. Lawrence, L. Lichtenstein, A. McKenna, C. S. Peadarallu, A. H. Ramos, E. Shefler, A. Sivachenko, C. Sougnez, C. Stewart, A. Ally, I. Birol, R. Chiu, R. D. Corbett, M. Hirst, S. D. Jackman, B. Kamoh, A. H. Khodabakshi, M. Krzywinski, A. Lo, R. A. Moore, K. L. Mungall, J. Qian, A. Tam, N. Thiessen, Y. Zhao, K. A. Cole, M. Diamond, S. J. Diskin, Y. P. Mosse, A. C. Wood, L. Ji, R. Sposto, T. Badgett, W. B. London, Y. Moyer, J. M. Gastier-Foster, M. A. Smith, J. M. Auvil, D. S. Gerhard, M. D. Hogarty, S. J. Jones, E. S. Lander, S. B.

- Gabriel, G. Getz, R. C. Seeger, J. Khan, M. A. Marra, M. Meyerson, and J. M. Maris. The genetic landscape of high-risk neuroblastoma. *Nature Genetics*, 45(3):279–284, 2013. ISSN 10614036. doi: 10.1038/ng.2529.
- G. Qing, N. Skuli, P. A. Mayes, B. Pawel, D. Martinez, J. M. Maris, and M. C. Simon. Combinatorial regulation of neuroblastoma tumor progression by N-Myc and hypoxia inducible factor HIF-1 α . *Cancer Research*, 70(24):10351–10361, 2010. ISSN 00085472. doi: 10.1158/0008-5472.CAN-10-0740.
- G. Qing, B. Li, A. Vu, N. Skuli, Z. E. Walton, X. Liu, P. A. Mayes, D. R. Wise, C. B. Thompson, J. M. Maris, M. D. Hogarty, and M. C. Simon. ATF4 Regulates MYC-Mediated Neuroblastoma Cell Death upon Glutamine Deprivation. *Cancer Cell*, 22(5): 631–644, 2012. ISSN 15356108. doi: 10.1016/j.ccr.2012.09.021.
- R Core Team. *R: A Language and Environment for Statistical Computing*. R Foundation for Statistical Computing, Vienna, Austria, 2018. URL <https://www.R-project.org/>.
- E. H. Raabe, M. Laudenslager, C. Winter, N. Wasserman, K. Cole, M. Laquaglia, D. J. Maris, Y. P. Mosse, and J. M. Maris. Prevalence and functional consequence of PHOX2B mutations in neuroblastoma. *Oncogene*, 27(4):469–476, 2008. ISSN 09509232. doi: 10.1038/sj.onc.1210659.
- J. Rappsilber, M. Mann, and Y. Ishihama. Protocol for micro-purification, enrichment, pre-fractionation and storage of peptides for proteomics using StageTips. *Nature Protocols*, 2(8):1896–1906, 2007. doi: 10.1038/nprot.2007.261.
- M. A. Reid, A. E. Allen, S. Liu, M. V. Liberti, P. Liu, X. Liu, Z. Dai, X. Gao, Q. Wang, Y. Liu, L. Lai, and J. W. Locasale. Serine synthesis through PHGDH coordinates nucleotide levels by maintaining central carbon metabolism. *Nature Communications*, 9(1):1–11, 2018. ISSN 20411723. doi: 10.1038/s41467-018-07868-6.
- M. Reina-Campos, M. T. Diaz-meco, and J. Moscat. The complexity of the serine glycine one-carbon pathway in cancer. *Journal of Cell Biology*, 219(1):1–17, 2019. doi: 10.1083/jcb.201907022.
- P. Ren, M. Yue, D. Xiao, R. Xiu, L. Gan, H. Liu, and G. Qing. ATF4 and N-Myc coordinate glutamine metabolism in MYCN-amplified neuroblastoma cells through ASCT2 activation. *Journal of Pathology*, 235(1):90–100, 2015. ISSN 10969896. doi: 10.1002/path.4429.
- M. W. Richards, S. G. Burgess, E. Poon, A. Carstensen, M. Eilers, L. Chesler, and R. Bayliss. Structural basis of N-Myc binding by Aurora-A and its destabilization by kinase inhibitors. *PNAS*, 113(48):13726–13731, 2016. ISSN 10916490. doi: 10.1073/pnas.1610626113.

- R. Richards, E. Sotillo, and R. Majzner. CAR T Cell Therapy for Neuroblastoma. *Frontiers in Immunology*, 9(2380), 2018. doi: 10.3389/fimmu.2018.02380.
- R. Riscal, E. Schrepfer, G. Arena, J.-e. Sarry, L. L. Cam, and L. K. Linares. Chromatin-Bound MDM2 Regulates Serine Metabolism and Redox Homeostasis Independently of p53 Article Chromatin-Bound MDM2 Regulates Serine Metabolism and Redox Homeostasis Independently of p53. *Molecular Cell*, 62:890--902, 2016. doi: 10.1016/j.molcel.2016.04.033.
- I. Rizzuto, E. Ghazaly, and G. Peters. Pharmacological factors affecting accumulation of gemcitabine's active metabolite, gemcitabine triphosphate. *Pharmacogenomics*, 18(9), 2017. doi: 10.2217/pgs-2017-0034.
- RStudio Team. *RStudio: Integrated Development Environment for R*. RStudio, PBC., Boston, MA, 2020. URL <http://www.rstudio.com/>.
- S. M. Sanderson, X. Gao, Z. Dai, and J. W. Locasale. Methionine metabolism in health and cancer: a nexus of diet and precision medicine. *Nature Reviews Cancer*, 19(November): 625--637, 2019. ISSN 1474-175X. doi: 10.1038/s41568-019-0187-8.
- R. A. Saxton and D. M. Sabatini. mTOR Signaling in Growth, Metabolism, and Disease. *Cell*, 168(6):960--976, 2017. ISSN 0092-8674. doi: 10.1016/j.cell.2017.02.004.
- F. Schilling, C. Spix, F. Berthold, R. Erttmann, N. Fehse, B. Hero, G. Klein, J. Sander, K. Schwarz, J. Treuner, U. Zorn, and J. Michaelis. Neuroblastoma screening at one year of age. *New England Journal of Medicine*, 346(14):1047--1053, 2002.
- C. Schneider, W. Rasband, and K. Eliceiri. NIH Image to ImageJ: 25 years of image analysis. *Nature Methods*, 9(7):671--675, 2012. doi: 10.1038/nmeth.2089.
- A. Schramm, J. Köster, T. Marschall, M. Martin, M. Schwermer, K. Fielitz, G. Büchel, M. Barann, D. Esser, P. Rosenstiel, S. Rahmann, A. Eggert, and J. H. Schulte. Next-generation RNA sequencing reveals differential expression of MYCN target genes and suggests the mTOR pathway as a promising therapy target in MYCN-amplified neuroblastoma. *International Journal of Cancer*, 132(3), 2013. ISSN 00207136. doi: 10.1002/ijc.27787.
- M. Schwab, K. Alitalo, K. Klemptner, H. Varmus, J. Bishop, F. Gilbert, G. Brodeur, M. Goldstein, and J. Trent. Amplified DNA with limited homology to myc cellular oncogene is shared by human neuroblastoma cell lines and a neuroblastoma tumour. *Nature*, 305:245--248, 1983. doi: 10.1038/305245a0.
- M. Schwab, H. Varmus, J. Bishop, K. Grzeschik, S. Naylor, A. Sakaguchi, G. Brodeur, and J. Trent. Chromosome localization in normal human cells and neuroblastomas of a gene related to c-myc. *Nature*, 308:288--291, 1984. doi: 10.1038/308288a0.

- R. Seeger, G. Brodeur, H. Sather, A. Dalton, S. Siegel, K. Wong, and D. Hammond. Association of multiple copies of the N-myc oncogene with rapid progression of neuroblastomas. *New England Journal of Medicine*, 313(18):1111--1116, 1985.
- M. Shamir, Y. Bar-On, R. Phillips, and R. Milo. SnapShot: Timescales in Cell Biology. *Cell*, 164, 2016. doi: 10.1016/j.cell.2016.02.058.
- H. Shimada, I. Ambros, L. Dehner, J. Hata, V. Joshi, B. Roald, D. Stram, R. Gerbing, J. Lukens, K. Matthay, and R. Castleberry. The International Neuroblastoma Pathology Classification (the Shimada system). *Cancer*, 86:364--372, 2000.
- H. Shimada, S. Umehara, Y. Monobe, Y. Hachitanda, A. Nakagawa, S. Goto, R. Gerbing, D. Stram, J. Lukens, and K. Matthay. International neuroblastoma pathology classification for prognostic evaluation of patients with peripheral neuroblastic tumors: a report from the Children's Cancer Group. *Cancer*, 92(9):2451--2461, 2001. doi: 10.1002/1097-0142(20011101)92:9<2451::aid-cnrc1595>3.0.co;2-s.
- O. Shuvalov, A. Petukhov, A. Daks, O. Fedorova, E. Vasileva, and N. A. Barlev. One-carbon metabolism and nucleotide biosynthesis as attractive targets for anticancer therapy. *Oncotarget*, 2017. ISSN 1949-2553. doi: 10.18632/oncotarget.15053.
- T. Simon, B. Hero, J. Schulte, H. Deubzer, P. Hundsdoerfer, D. Von Schweinitz, J. Fuchs, M. Schmidt, V. Prasad, B. Krug, B. Timmermann, I. Leuschner, M. Fischer, T. Langer, K. Astrahantseff, F. Berthold, H. Lode, and A. Eggert. 2017 GPOH Guidelines for Diagnosis and Treatment of Patients with Neuroblastic Tumors. In *Klin Padiatr*, volume 229, pages 147--167. Georg Thieme Verlag KG Stuttgart, New York, 2017. doi: 10.1055/s-0043-103086.
- Z. E. Stine, Z. E. Walton, B. J. Altman, A. L. Hsieh, and C. V. Dang. MYC, Metabolism, and Cancer. *Cancer Discovery*, 5(10):1024--1039, 2015. ISSN 2159-8274. doi: 10.1158/2159-8290.CD-15-0507.
- M. Stovroff, F. Dykes, and W. G. Teague. The complete spectrum of neurocristopathy in an infant with congenital hypoventilation, Hirschsprung's disease, and neuroblastoma. *Journal of Pediatric Surgery*, 30(8):1218--1221, 1995. ISSN 00223468. doi: 10.1016/0022-3468(95)90027-6.
- V. Strenger, R. Kerbl, H. Dornbusch, R. Ladenstein, P. Ambros, I. Ambros, and C. Urban. Diagnostic and Prognostic Impact of Urinary Catecholamines in Neuroblastoma Patients. *Pediatric Blood & Cancer*, 48:504--509, 2007. doi: 10.1002/pbc.
- W. Strober. Trypan blue exclusion test of cell viability. *Current Protocols in Immunology*, page Appendix3:Appendix3B, 2001. doi: 10.1002/0471142735.ima03bs21.

- L. Sun, L. Song, Q. Wan, G. Wu, X. Li, Y. Wang, J. Wang, Z. Liu, X. Zhong, X. He, S. Shen, X. Pan, A. Li, Y. Wang, P. Gao, H. Tang, and H. Zhang. CMyc-mediated activation of serine biosynthesis pathway is critical for cancer progression under nutrient deprivation conditions. *Cell Research*, 25(4):429--444, 2015. ISSN 17487838. doi: 10.1038/cr.2015.33.
- P. M. Tedeschi, A. Vazquez, J. E. Kerrigan, and J. R. Bertino. Mitochondrial Methylenetetrahydrofolate Dehydrogenase (MTHFD2) Overexpression Is Associated with Tumor Cell Proliferation and Is a Novel Target for Drug Development. *Molecular Cancer Research*, (7):1361--1367, 2015. doi: 10.1158/1541-7786.MCR-15-0117.
- C. Thiele, C. Reynolds, and M. Israel. Decreased expression of N-myc precedes retinoic acid-induced morphological differentiation of human neuroblastoma. *Nature*, 313:404--406, 1985. doi: 10.1038/313404a0.
- G. P. Tonini, A. Nakagawara, and F. Berthold. Towards a turning point of neuroblastoma therapy. *Cancer Letters*, 326(2):128--134, 2012. ISSN 03043835. doi: 10.1016/j.canlet.2012.08.017.
- R. M. Trigg and S. D. Turner. ALK in neuroblastoma: Biological and therapeutic implications. *Cancers*, 10(4), 2018. ISSN 20726694. doi: 10.3390/cancers10040113.
- D. Trochet, S. J. Hong, J. K. Lim, J. F. Brunet, A. Munnich, K. S. Kim, S. Lyonnet, C. Goridis, and J. Amiel. Molecular consequences of PHOX2B missense, frameshift and alanine expansion mutations leading to autonomic dysfunction. *Human Molecular Genetics*, 14(23):3697--3708, 2005. ISSN 09646906. doi: 10.1093/hmg/ddi401.
- S. Trzaska. Cisplatin. *Chemical & Engineering News*, 83(25), 2005. doi: 10.1021/cen-v083n025.p052.
- S. Tyanova, T. Temu, P. Sinitcyn, A. Carlson, M. Y. Hein, T. Geiger, M. Mann, and J. Cox. The Perseus computational platform for comprehensive analysis of (prote)omics data. *Nature Methods*, 13(9):731--740, 2016. ISSN 15487105. doi: 10.1038/nmeth.3901.
- L. J. Valentijn, J. Koster, F. Haneveld, R. A. Aissa, P. Van Sluis, M. E. Broekmans, J. J. Molenaar, J. Van Nes, and R. Versteeg. Functional MYCN signature predicts outcome of neuroblastoma irrespective of MYCN amplification. *PNAS*, 109(47):19190--19195, 2012. ISSN 00278424. doi: 10.1073/pnas.1208215109.
- M. Vander Heiden and R. DeBerardinis. Understanding the Intersections between Metabolism and Cancer Biology. *Cell*, 168:657--669, 2017. doi: 10.1016/j.cell.2016.12.039.
- M. G. Vander Heiden, L. C. Cantley, and C. B. Thompson. Understanding the Warburg Effect: The Metabolic Requirements of Cell Proliferation. *Science*, 324:1029--1033, 2009. doi: 10.1126/science.1160809.

- J. Vandesompele, M. Baudis, K. De Preter, N. Van Roy, P. Ambras, N. Bown, C. Brinkschmidt, H. Christiansen, V. Combaret, M. Lastowska, J. Nicholson, A. O'Meara, D. Plantaz, R. Stallings, B. Brichard, C. Van Den Broecke, S. De Bie, A. De Paepe, G. Laureys, and F. Speleman. Unequivocal delineation of clinicogenetic subgroups and development of a new model for improved outcome prediction in neuroblastoma. *Journal of Clinical Oncology*, 23(10):2280--2299, 2005. ISSN 0732183X. doi: 10.1200/JCO.2005.06.104.
- E. Villa, E. S. Ali, U. Sahu, and I. Ben-sahra. Cancer Cells Tune the Signaling Pathways to Empower de Novo Synthesis of Nucleotides. *Cancers*, 11(688):1--20, 2019. doi: 10.3390/cancers11050688.
- J. Walling. From methotrexate to pemetrexed and beyond . A review of the pharmacodynamic and clinical properties of antifolates. *Investigational New Drugs*, 24:37--77, 2006. doi: 10.1007/s10637-005-4541-1.
- Q. Wang, M. V. Liberti, P. Liu, X. Deng, Y. Liu, J. W. Locasale, and L. Lai. Rational Design of Selective Allosteric Inhibitors of PHGDH and Serine Synthesis with Antitumor Activity. *Cell Chemical Biology*, 24(1):55--65, 2017. ISSN 24519448. doi: 10.1016/j.chembiol.2016.11.013.
- T. Wang, L. Liu, X. Chen, Y. Shen, G. Lian, N. Shah, A. M. Davidoff, J. Yang, and R. Wang. MYCN drives glutaminolysis in neuroblastoma and confers sensitivity to an ROS augmenting agent article. *Cell Death and Disease*, 9(2), 2018. ISSN 20414889. doi: 10.1038/s41419-018-0295-5.
- O. Warburg. Über den Stoffwechsel der Carcinomzelle. *Naturwissenschaften*, 12:1131--1137, 1924. doi: 10.1007/BF01504608.
- O. Warburg, F. Wind, and E. Negelein. Killing-Off of Tumor Cells in Vitro. *The journal of General Physiology*, 8(6):519--530, 1927.
- F. Westermann, D. Muth, A. Benner, T. Bauer, K. O. Henrich, A. Oberthuer, B. Brors, T. Beissbarth, J. Vandesompele, F. Pattyn, B. Hero, R. König, M. Fischer, and M. Schwab. Distinct transcriptional MYCN/c-MYC activities are associated with spontaneous regression or malignant progression in neuroblastomas. *Genome Biology*, 9(10), 2008. ISSN 14747596. doi: 10.1186/gb-2008-9-10-r150.
- U. K. Westermarck, M. Wilhelm, A. Frenzel, and M. A. Henriksson. The MYCN oncogene and differentiation in neuroblastoma. *Seminars in Cancer Biology*, 21(4):256--266, 2011. ISSN 1044579X. doi: 10.1016/j.semcancer.2011.08.001.

- J. R. Whitfield, M. E. Beaulieu, and L. Soucek. Strategies to inhibit Myc and their clinical applicability. *Frontiers in Cell and Developmental Biology*, 5:1--13, 2017. ISSN 2296634X. doi: 10.3389/fcell.2017.00010.
- D. R. Wise and C. B. Thompson. Glutamine Addiction: A New Therapeutic Target in Cancer. *Trends in Biochemical Science*, 35(8):427--433, 2011. doi: 10.1016/j.tibs.2010.05.003.Glutamine.
- D. R. Wise, R. J. DeBerardinis, A. Mancuso, N. Sayed, X.-Y. Zhang, H. K. Pfeiffer, I. Nissim, E. Daikhin, M. Yudkoff, S. B. McMahon, and C. B. Thompson. Myc regulates a transcriptional program that stimulates mitochondrial glutaminolysis and leads to glutamine addiction. *Proceedings of the National Academy of Sciences*, 105(48):18782--18787, 2008. ISSN 10715754. doi: 10.1097/00152192-198605000-00048.
- Z. L. Wu, E. Schwartz, S. Ladisch, and R. Seeger. Expression of gd2 ganglioside by untreated primary human neuroblastomas. *Cancer Research*, 46(1):440--443, 1986. ISSN 15387445.
- Y. Xia, B. Ye, J. Ding, Y. Yu, A. Alptekin, M. Thangaraju, P. D. Prasad, Z. C. Ding, E. J. Park, J. H. Choi, B. Gao, O. Fiehn, C. Yan, Z. Dong, Y. Zha, and H. F. Ding. Metabolic reprogramming by MYCN confers dependence on the serine-glycine-one-carbon biosynthetic pathway. *Cancer Research*, 79(15):3837--3850, 2019. ISSN 15387445. doi: 10.1158/0008-5472.CAN-18-3541.
- D. Xiao, P. Ren, H. Su, M. Yue, R. Xiu, Y. Hu, H. Liu, and G. Qing. Myc promotes glutaminolysis in human neuroblastoma through direct activation of glutaminase 2. *Oncotarget*, 6(38):40655--40666, 2015. ISSN 1949-2553. doi: 10.18632/oncotarget.5821.
- M. Yang and K. Vousden. Serine and one-carbon metabolism in cancer. *Nature Reviews Cancer*, 16:650--662, 2016. doi: 10.1038/nrc.2016.81.
- J. R. Yates. The revolution and evolution of shotgun proteomics for large-scale proteome analysis. *Journal of the American Chemical Society*, 135(5):1629--1640, 2013. ISSN 00027863. doi: 10.1021/ja3094313.
- J. Ye, A. Mancuso, X. Tong, P. S. Ward, J. Fan, J. D. Rabinowitz, and C. B. Thompson. Pyruvate kinase M2 promotes de novo serine synthesis to sustain mTORC1 activity and cell proliferation. *PNAS*, 109(18):6904--6909, 2012. ISSN 00278424. doi: 10.1073/pnas.1204176109.
- J. Ye, W. Palm, M. Peng, B. King, T. Lindsten, M. O. Li, C. Koumenis, and C. B. Thompson. GCN2 sustains mTORC1 suppression upon amino acid deprivation by inducing Sestrin2. *Genes and Development*, 29:2331--2336, 2015. doi: 10.1101/gad.269324.115.

- C. Zasada. *Experimental and mathematical analysis of the central carbon metabolism in cancer and stem cells*. PhD thesis, Humboldt-Universität zu Berlin, 2017.
- C. Zasada and S. Kempa. Quantitative Analysis of Cancer Metabolism: From pSIRM to MFA. In T. Cramer and C. Schmitt, editors, *Metabolism in Cancer*, pages 207--220. Springer International Publishing, 2016a. ISBN 978-3-319-42118-6. doi: 10.1007/978-3-319-42118-69.
- C. Zasada and S. Kempa. Quantitative Analysis of Cancer Metabolism: From pSIRM to MFA. In *Metabolism in Cancer, Recent Results in Cancer Research*, volume 207, pages 135--156. Springer International Publishing, 2016b. ISBN 978-3-319-42116-2. doi: 10.1007/978-3-319-42118-6.
- R. Zeid, M. A. Lawlor, E. Poon, J. M. Reyes, M. Fulciniti, M. A. Lopez, T. G. Scott, B. Nabet, M. A. Erb, G. E. Winter, Z. Jacobson, D. R. Polaski, K. L. Karlin, R. A. Hirsch, N. P. Munshi, T. F. Westbrook, L. Chesler, C. Y. Lin, and J. E. Bradner. Enhancer invasion shapes MYCN-dependent transcriptional amplification in neuroblastoma. *Nature Genetics*, 50(4):515--523, 2018. ISSN 15461718. doi: 10.1038/s41588-018-0044-9.
- M. Zeineldin, S. Federico, X. Chen, B. Xu, E. Stewart, A. Naranjo, M. Hogarty, and M. Dyer. Abstract IA18: MYCN amplification and ATRX mutations are incompatible in neuroblastoma. In *AACR Special Conference: Pediatric Cancer Research: From Basic Science to the Clinic; December 3-6, 2017; Atlanta, Georgia*, volume 78, 2018.
- J. Zhang, N. N. Pavlova, and C. B. Thompson. Cancer cell metabolism: the essential role of the nonessential amino acid, glutamine. *The EMBO Journal*, 36(10):1302--1315, 2017. ISSN 0261-4189. doi: 10.15252/embj.201696151.
- J. M. Zhang, T. Yadav, J. Ouyang, L. Lan, and L. Zou. Alternative Lengthening of Telomeres through Two Distinct Break-Induced Replication Pathways. *Cell Reports*, 26(4):955--968.e3, 2019. ISSN 22111247. doi: 10.1016/j.celrep.2018.12.102.
- E. Zhao, J. Ding, Y. Xia, M. Liu, B. Ye, J. H. Choi, C. Yan, Z. Dong, S. Huang, Y. Zha, L. Yang, H. Cui, and H. F. Ding. KDM4C and ATF4 Cooperate in Transcriptional Control of Amino Acid Metabolism. *Cell Reports*, 14(3):506--519, 2016. ISSN 22111247. doi: 10.1016/j.celrep.2015.12.053.
- R. Zhao and I. D. Goldman. Resistance to antifolates. *Oncogene*, 22(47 REV. ISS. 6): 7431--7457, 2003. ISSN 09509232. doi: 10.1038/sj.onc.1206946.
- M. J. Zhou, M. Y. Doral, S. G. DuBois, J. G. Villablanca, G. A. Yanik, and K. K. Matthay. Different outcomes for relapsed versus refractory neuroblastoma after therapy with 131I-metaiodobenzylguanidine (131I-MIBG). *European Journal of Cancer*, 51(16):2465--2472, 2015. ISSN 18790852. doi: 10.1016/j.ejca.2015.07.023.

A Supplementary: Materials and Methods

Table A.1.: Cell culture reagents and chemicals.

Name	Supplier
Blasticidin	Merck, Darmstadt, Germany
FCS Superior	Merck (Biochrom), Darmstadt, Germany
Dimethylsulfoxid (DMSO)	Carl Roth, Karlsruhe, Germany
DMEM (high glucose, gltaMAX supplement, pyruvate)	Thermo Fisher Scientific (Gibco), Waltham, USA
DMEM (no glucose, glutamine, sodium pyruvate, phenol red)	Thermo Fisher Scientific (Gibco), Waltham, USA
DMEM (no glucose, glutamine, serine, glycine, sodium pyruvate, phenol red)	US Biological, Salem, USA
G418 sulfate	Merck, Darmstadt, Germany
Glucose	Merck (Sigma-Aldrich), Darmstadt, Germany
Glutamine	Thermo Fisher Scientific (Gibco), Waltham, USA
HiPerFect	Qiagen, Hilden, Germany
Hygromycin B	Merck (Sigma-Aldrich), Darmstadt, Germany
MEM non-essential amino acid solution	Lonza, Basel, Switzerland
Opti-MEM	Thermo Fisher Scientific (Gibco), Waltham, USA
Phosphate-buffered saline (PBS)	Thermo Fisher Scientific (Gibco), Waltham, USA
Puromycin dihydrochloride	Merck (Sigma-Aldrich), Darmstadt, Germany
Tetracycline	Merck (Sigma-Aldrich), Darmstadt, Germany
Trypan Blue Solution	Thermo Fisher Scientific (Gibco), Waltham, USA
Trypsine (0.05% EDTA, Phenol red)	Thermo Fisher Scientific (Gibco), Waltham, USA
u- ¹³ C-Glucose	Campro-Scientific, Berlin, Germany
u- ¹³ C-Glutamine	Campro-Scientific, Berlin, Germany
Versene	Thermo Fisher Scientific (Gibco), Waltham, USA

Table A.2.: Chemicals.

Name	Supplier
Mercaptoethanol	Merck (Sigma-Aldrich), Darmstadt, Germany
Acetic acid	Carl Roth, Karlsruhe, Germany
Acetonitrile	VWR, Radnor, USA
Agarose	Biozym, Hessisch Oldendorf, Germany
Albumin from bovine serum (BSA) Fraction V	Carl Roth, Karlsruhe, Germany
Albumin from bovine serum (BSA)	SERVA, Heidelberg, Germany
Ammonium acetate (NH ₄ Ac)	Carl Roth, Karlsruhe, Germany
Ammonium bicarbonate	Merck (Fluka) Darmstadt, Germany

Continued on next page

Table A.2.: Continued from previous page

Name	Supplier
Ammonium hydroxide (NH ₄ OH)	Merck (Sigma-Aldrich), Darmstadt, Germany
Ammonium persulfate	Carl Roth, Karlsruhe, Germany
Ampicillin	Carl Roth, Karlsruhe, Germany
Bromphenol blue	Carl Roth, Karlsruhe, Germany
BSA	SERVA, Heidelberg, Germany
Chloroform	Merck (Sigma-Aldrich), Darmstadt, Germany
Chloramphenicol	Merck (Sigma-Aldrich), Darmstadt, Germany
Cinnamic acid	Merck (Sigma-Aldrich), Darmstadt, Germany
cOmplete protease inhibitor	Roche, Basel, Switzerland
Crystal violet	Merck (Sigma-Aldrich), Darmstadt, Germany
Cy3 dye	Thermo Fisher Scientific, Waltham, USA
Diaminobenzidine	Agilent, Santa Clara, USA
Dithiothreitol (DTT)	Merck (Sigma-Aldrich), Darmstadt, Germany
DNA Loading Dye (6x Orange, #R0631)	Thermo Fisher Scientific (Invitrogen), Waltham, USA
Ethylenediaminetetraacetic acid (EDTA)	Carl Roth, Karlsruhe, Germany
Ethanol	Carl Roth, Karlsruhe, Germany
Ethidium bromide solution(0.5%)	Carl Roth, Karlsruhe, Germany
Formic acid	Fluka, Darmstadt, Germany
Glycerol gelatine	Merck (Sigma-Aldrich), Darmstadt, Germany
H ₂ O, nuclease-free	Thermo Fisher Scientific (Invitrogen), Waltham, USA
Hematoxylin	Merck (Millipore), Darmstadt, Germany
HEPES	Merck (Sigma-Aldrich), Darmstadt, Germany
Hexylamine	Merck (Sigma-Aldrich), Darmstadt, Germany
HiPerFect	Qiagen, Hilden, Germany
Hydrochloric acid fuming 37%	Carl Roth, Karlsruhe, Germany
Iodoacetamide (IAA)	Merck (Sigma-Aldrich), Darmstadt, Germany
Isopropanol	Carl Roth, Karlsruhe, Germany
LB-Agar	Carl Roth, Karlsruhe, Germany
LB-Medium	Carl Roth, Karlsruhe, Germany
Magnesiumchloride (MgCl ₂)	Carl Roth, Karlsruhe, Germany
Magnesium sulfate (MgSO ₄)	Merck (Sigma-Aldrich), Darmstadt, Germany
Milk powder	Carl Roth, Karlsruhe, Germany
Methanol	Merck (Sigma-Aldrich), Darmstadt, Germany
Methanol	Carl Roth, Karlsruhe, Germany
Methoxyamine (MeOx)	Merck (Sigma-Aldrich), Darmstadt, Germany
N-Methyl-N-(trimethylsilyl) trifluoroacetamide (MSTFA)	VWR, Radnor, USA
PageRuler Prestained Protein ladder	Thermo Fisher Scientific (Invitrogen), Waltham, USA
Polyethyleneglycol (PEG) 3300	Merck (Sigma-Aldrich), Darmstadt, Germany
Propidium iodide	Thermo Fisher Scientific (Invitrogen), Waltham, USA
Pyridine	Merck (Sigma-Aldrich), Darmstadt, Germany
Rotiphorese Gel 30	Carl Roth, Karlsruhe, Germany
Roti Quant (Bradford)	Carl Roth, Karlsruhe, Germany
Sodiumchloride (NaCl)	Merck (Sigma-Aldrich), Darmstadt, Germany
Sodium dodecyl sulfate (SDS) Pellets	Carl Roth, Karlsruhe, Germany
Sodium hydroxide solution (NaOH)	Carl Roth, Karlsruhe, Germany

Continued on next page

Table A.2.: *Continued from previous page*

Name	Supplier
Tetramethylethylenediamin (TEMED)	Carl Roth, Karlsruhe, Germany
Trifluoroacetic acid (TFA)	Merck (Sigma-Aldrich), Darmstadt, Germany
Tris-HCl	Carl Roth, Karlsruhe, Germany
Triton X-100	Carl Roth, Karlsruhe, Germany
Trizma base (Tris(hydroxymethyl)aminomethan base)	Carl Roth, Karlsruhe, Germany
Trypsin Beads	Applied Biosystems, Waltham, USA
Tween-20	Carl Roth, Karlsruhe, Germany
Urea	Carl Roth, Karlsruhe, Germany
Western Lightning Plus-ECL	PerkinElmer, Waltham, USA

Table A.3.: Consumables.

Name	Supplier
0.5 mL microtube	Sarstedt, Nmbrecht, Germany
1.5 mL microtube	Sarstedt, Nmbrecht, Germany
2 mL microtube	Sarstedt, Nmbrecht, Germany
2 mL cryogenic vial, sterile	Sarstedt, Nmbrecht, Germany
5 mL round bottom polystyrene test tube	Corning, New York, USA
8 well PCR tube strip	4titude, Wotton, UK
15 mL tube, conical bottom, steile	Corning, New York, USA
50 mL tube, conical bottom, sterile	Corning, New York, USA
Cell culture dish (100mm), sterile	Corning, New York, USA
Cell culture flask (T25), sterile	Corning, New York, USA
Cell culture flask (T75), sterile	Corning, New York, USA
Cell culture flask (T175), sterile	Corning, New York, USA
Cell lifter	Merck (Sigma-Aldrich), Darmstadt, Germany
epT.I.P.S Standard (0.1-5 mL)	Eppendorf, Hamburg, Germany
Filter tips, sterile (10 μ l)	Biozym, Hessisch Oldendorf, Germany
Filter tips, sterile (100 μ l)	Biozym, Hessisch Oldendorf, Germany
Filter tips, sterile (1250 μ l)	Biozym, Hessisch Oldendorf, Germany
FrameStar 96-well plates ABi FAST PCR	4titude, Wotton, UK
Gas liner, CI34	Gerstel, Mühlheim an der Ruhr, Germany
Glas vials	Th.Geyer, Berlin, Germany
MonoCap C18 HighResolution 2000 column	GL Science, Tokyo, Japan
Multiwell (6-well), sterile	Corning, New York, USA
Multiwell (12-well), sterile	Corning, New York, USA
Multiwell (24-well), sterile	Corning, New York, USA
Multiwell (96-well), sterile	Corning, New York, USA
Pasteur pipette, glas, 230mm	Brand, Wertheim, Germany
Pasteur pipette, glas, 150mm	Brand, Wertheim, Germany
PVDF western blotting membrane	Roche, Basel, Switzerland
qPCR seal	4titude, Wotton, UK
Serological pipette (5 mL), sterile	Corning, New York, USA
Serological pipette (10 mL), sterile	Corning, New York, USA
Serological pipette (25 mL), sterile	Corning, New York, USA
Serological pipette (50 mL), sterile	Corning, New York, USA
Solid phase extraction disk (C18)	Thermo Fisher Scientific, Waltham, USA
Stericup-GP (0.22 μ m)	Merck (Millipore), Darmstadt, Germany
Surphob Reload tips (10 μ L)	Biozym, Hessisch Oldendorf, Germany
Surphob Reload tips (200 μ L)	Biozym, Hessisch Oldendorf, Germany
Surphob Reload tips (1250 μ L)	Biozym, Hessisch Oldendorf, Germany
Syringe (50 mL)	Braun, Melsungen, Germany
Syringe filter (0.2 μ M)	Carl Roth, Karlsruhe, Germany
Vi-Cell sample vials (4 mL)	BeckmanCoulter, Brea, USA
Whatman blotting paper	Carl Roth, Karlsruhe, Germany
ZipTips (C18, #ZTC18S096)	Merck (Millipore), Darmstadt, Germany

Table A.4.: Equipment.

Name	Manufacturer
Axiomager Z1 microscope	Carl Zeiss, Jena, Germany
Axio Vert.A1 microscope	Carl Zeiss, Jena, Germany
Analytical balance ABS-N	Kern, Balingen, Germany
Balance EW-N	Kern, Balingen, Germany
Biophotometer No 6131 01964	Eppendorf, Hamburg, Germany
Bioruptor	Diagenode, Liège, Belgium
C1000 Touch Thermal Cycler	BioRad, Hercules, USA
Cell counter TC20	BioRad, Hercules, USA
Cell counter Vi-Cell XR	BeckmanCoulter, Brea, USA
Centrifuge 5424R	Eppendorf, Hamburg, Germany
Centrifuge 5810 R	Eppendorf, Hamburg, Germany
EnVision+ System	Agilent, Santa Clara, USA
Freezing container 5100 Cryo 1°C (Mr. Frosty)	Thermo Fisher Scientific, Waltham, USA
Fusion-FX	Vilber Lourmat, Eberhardzell, Germany
HeraCell 240i CO2 Incubator	Thermo Fisher Scientific, Waltham, USA
LSR Fortessa X-20	Beckton Dickinson, Franklin Lakes, USA
Mass Spectrometer - Q Exactive HF	Thermo Fisher Scientific, Waltham, USA
Mass Spectrometer-GC-ToF - Pegasus IV	LECO, St. Joseph, USA
Mass Spectrometer-TSQ Quantiva	Thermo Fisher Scientific, Waltham, USA
Microplate reader, Infinite M200	Tecan, Männedorf, Switzerland
Mini-PROTEAN tetra system	BioRad, Hercules, USA
MiniStar silverline Microcentrifuge	VWR, Darmstadt
MultiPurpose Sampler 2 XL	Gerstel, Mühlheim an der Ruhr, Germany
Nanodrop	Thermo Fisher Scientific, Waltham, USA
Nano Liquid Chromatograph 400	Eksigent, Darmstadt, Germany
Olympus BX43	Olympus, Shinjuku, Japan
pH Meter, five easy	Mettler-Toledo, Gien, Germany
pH meter - VMS C7	VWR, Radnor, USA
Phoenix RS-TR 5 tube roller	Phoenix Instrument, Garbsen, Germany
PowerPac Basic Power supply	BioRad, Hercules, USA
Precellys 24 homogeniser	Bertin Technologies, Montigny-le-Bretonneux, France
Reax top Vortexer	Heidolph Instruments, Schwabach, Germany
RH basic magnetic stirrer	IKA, Stauffen, Germany
Sonicator - Sonorex Digitech DT 100	Bandelin, Berlin, Germany
Spectrophotometer, Epoch	BioTek Instruments, Winooski, USA
StepOnePlus Real-Time PCR System	Thermo Fisher Scientific (Applied Biosystems), Waltham, USA
Trans-Blot Turbo Transfer system	BioRad, Hercules, USA
Thermomixer comfort	Eppendorf, Hamburg, Germany
Vacuum concentrator - 2-33 CD plus	Eppendorf, Hamburg, Germany
Waterbath GFL 1086	GFL, Burgwedel, Germany

Table A.5.: Kits.

Name	Supplier
Fast Start Essential Mastermix SYBR green	Roche, Basel, Switzerland
First Strand cDNA Synthesis Kit	Thermo Fisher Scientific, Waltham, USA
NucleoBond Xtra Maxi Kit	Macherey und Nagel, Dren, Germany
Pierce BCA Protein Assay Kit	Thermo Fisher Scientific (Invitrogen), Waltham, USA
PlasmoTest Mycoplasma detection kit	InVivogen, Toulouse, France
QIAamp DNA Mini Kit	Qiagen, Hilden, Germany
QIAprep Spin Miniprep Kit	Qiagen, Hilden, Germany
QIAquick Gel Extraction Kit	Qiagen, Hilden, Germany
RNeasy Mini Kit	Qiagen, Hilden, Germany

Table A.6.: Overview of compounds added to neuroblastoma cells for proliferation assays, metabolome and proteome studies.

Inhibitor	Concentration		Company
	in cell culture	in mice	
5-Fluorouracile	10 μ M	--	Merck (Sigma-Aldrich), Darmstadt, Germany
Cisplatin	--	2 & 1 mg/kg	Merck (Sigma-Aldrich), Darmstadt, Germany
Methotrexate	1 μ M	--	Pfizer, New-York, USA
NCT503	10 μ M	40 mg/kg	Merck (Sigma-Aldrich), Darmstadt, Germany
P2101	10 μ M	20 mg/kg	Merck (Sigma-Aldrich), Darmstadt, Germany
inactive NCT503	10 μ M	--	Merck (Sigma-Aldrich), Darmstadt, Germany

Table A.7.: Enzymes.

Enzyme	Supplier
BbsI, R0539 S	New England Biolabs, Ipswich, USA
DNase	Thermo Fisher Scientific (Invitrogen), Waltham, USA
Lys-C	Thermo Fisher Scientific (Wako), Waltham, USA
Pure Link RNase A	Thermo Fisher Scientific (Invitrogen), Waltham, USA
T4-Ligase	New England Biolabs, Ipswich, USA

Table A.8.: Antibodies.

Target	Catalog No	Supplier	Application
ACTB (AC-15)	A5441	Merck (Sigma-Aldrich), Darmstadt, Germany	WB
ATF4 (D4B8)	11815	Cell Signaling, Danvers, USA	WB
eIF2a	9722	Cell Signaling, Danvers, USA	WB
GCN2	3302S	Cell Signaling, Danvers, USA	WB
Mouse, horseradish peroxidase-linked	115-035-003	Dianova, Hamburg, Germany	WB
MYCN (B8.4.B)	sc53993	Santa Cruz, Dallas, USA	WB
PARP	9542	Cell Signaling, Danvers, USA	WB
PHGDH	HPA021241	Atlas Antibodies, Bromma, Sweden	IHC
PHGDH	13428	Cell Signaling, Danvers, USA	WB
Phospho-eIF2a	9721S	Cell Signaling, Danvers, USA	WB
PUMA (D30C10)	12450	Cell Signaling, Danvers, USA	WB
Rabbit, horseradish peroxidase-linked	111-035-003	Dianova, Hamburg, Germany	WB
Rabbit, horseradish peroxidase-linked	K400311-2	Agilent, Santa Clara, USA	IHC
TRB3 (B-2)	sc-390242	Santa Cruz, Dallas, USA	WB

Table A.9.: Primer sequences for qPCR.

Name	Sequence (5'-3')	Supplier
HPRT forward	TGACACTGGCAAAACAATGCA	Eurofins, Luxemburg
HPRT reverse	GGTCCTTTTCACGCAAGCT	Eurofins, Luxemburg
SDHA forward	TGGGAACAAGAGGGCATCTG	Eurofins, Luxemburg
SDHA reverse	CCACCACTGCATCAAATTCATG	Eurofins, Luxemburg
MYCN forward	CCACGTCCGCTCAAGAGTGT	Metabion, Planegg, Germany
MYCN reverse	CCCTGAGCGTGAGAAAGCTG	Metabion, Planegg, Germany
PHGDH forward	TTTGGGATGAAGACTATAGGGTATGA	Metabion, Planegg, Germany
PHGDH reverse	CAGCTGCTGAACACCAAGG	Metabion, Planegg, Germany

Table A.10.: Primer sequences for ChIP-qPCR.

Name	Sequence (5'-3')	Supplier
PHGDH Peak3783 forward	GGTGACTTTAATCCCAAATTGAA	Metabion, Planegg, Germany
PHGDH Peak3783 reverse	GACCAAGGAGGCACTTCTCA	Metabion, Planegg, Germany
PHGDH Peak3784 forward	CAGGTTACCTCTCAAAGCCTCT	Metabion, Planegg, Germany
PHGDH Peak3784 reverse	TTATTCTCTTCACTCAAGG	Metabion, Planegg, Germany

Table A.11.: GuideRNA sequences for CRISPR-Cas9 *PHGDH* knockout.

Guide RNA	Sequence (5'-3')	Supplier
PH_ex4_83f	caccg TGCAAGATCTTCCGGCAGCA	Eurofins, Luxemburg
PH_ex4_83r	aaac TGCTGCCGGAAGATCTTGCAc	Eurofins, Luxemburg
PH_ex4_80f	caccg TGCCGGAAGATCTTGCAAGA	Eurofins, Luxemburg
PH_ex4_80r	aaac TCTTGCAAGATCTTCCGGCAc	Eurofins, Luxemburg
PH_ex5_86f	caccg TGGATCTGGAGGCCGCAACA	Eurofins, Luxemburg
PH_ex5_86r	aaac TGTGCGGCCCTCCAGATCCAc	Eurofins, Luxemburg
PH_ex6_83f	caccg AGTGCCGCAGAACTCACTTG	Eurofins, Luxemburg
PH_ex6_83r	aaac CAAGTGAGTTCTGCGGCACTc	Eurofins, Luxemburg
PH_ex7_96f	caccg CTTTCATCGAAGCCGTCGCCT	Eurofins, Luxemburg
PH_ex7_96r	aaac AGGCGACGGCTTCGATGAAGc	Eurofins, Luxemburg
PH_ex7_93f	caccg CTTTCGATGAAGGACGGCAA	Eurofins, Luxemburg
PH_ex7_93r	aaac TTTGCCGTCCTTCATCGAAGc	Eurofins, Luxemburg

Table A.12.: small interfering RNAs.

Name	Supplier
siPOOL-5 ATF4	siTOOLS Biotech GmbH, Planegg, Germany
siPOOL-5 PHGDH	siTOOLS Biotech GmbH, Planegg, Germany
siPOOL-negative control	siTOOLS Biotech GmbH, Planegg, Germany
siGENOME RISC-free	Thermo Fisher Scientific, Waltham, USA

Table A.13.: Plasmid.

Name	Supplier
px459	Addgene, Watertown, USA

Table A.14.: GC-MS masses used for absolute quantification.

Metabolite	Derivate	Quantification masses [m/z]
Alanine	2TMS	86+117+116+100+103+118
Alanine	3TMS	110+133+114+100+188+190
Citrate	4TMS	149+273+183+133+211+275+277+278
Fumarate	2TMS	143+246+133+115+245+247+249
Glyceric acid-3-phosphate	4TMS	211+227+299+101+133+357+359
Glycine	2TMS	86+176+103+104+102+276+277
Glycine	3TMS	86+133+175+100+174
Lactate	2TMS	118+190+191+117+133+119+193+219+222
Malate	3TMS	101+133+117+149+233+245+247+249
Pyruvate	1MeOx, 1TMS	100+99+89+174+115+177
Serine	2TMS	103+116+132+117+144+118
Serine	3TMS	116+218+133+204+100+206
Serine	4TMS	290+115+100+276+114+293
Succinate	2TMS	149+247+129+133+172+249+251

Table A.15.: GC-MS fragments used for determination of stable isotope incorporation.

Metabolite	Derivate	Mass fragments [m/z]		
		Unlabeled	u- ¹³ C-glucose	u- ¹³ C-glutamine
Alanine	2TMS	116	118	--
Alanine	3TMS	188	190	--
Citrate	4TMS	273	275	--
Citrate	4TMS	273	276	--
Citrate	4TMS	273	277	--
Fumarate	2TMS	245	247	--
Glyceric acid-3-phosphate	4TMS	357	359	--
Glycine	3TMS	276	278	--
Lactate	2TMS	219	222	--
Malate	3TMS	245	247	249
Malate	3TMS	245	248	--
Pyruvate	1MeOx, 1TMS	174	177	--
Serine	3TMS	204	206	--
Succinate	2TMS	247	249	251

Table A.16.: Direct-infusion MS transitions.

Compound	Precursor [m/z]	Product [m/z]
Acetyl-CoA	808.10	408.00
Acetyl-CoA	808.10	461.11
ADP	426.02	134.06
ADP	426.02	158.92
AMP	346.06	107.08
AMP	346.06	134.06
ATP	505.99	158.96
ATP	505.99	408.04
CDP	402.01	159.03
CDP	402.01	272.94
CMP	322.04	79.03
CMP	322.04	97.01
CTP	481.98	159.05
CTP	481.98	383.93
dADP	410.09	158.94
dADP	410.09	256.96
dAMP	330.09	134.12
dAMP	330.09	194.94
dATP	490.05	158.94
dATP	490.05	256.96
dCDP	86.05	158.96
dCDP	86.05	177.01
dCMP	306.08	97.00
dCMP	306.08	110.11
dCTP	66.01	158.94
dCTP	66.01	256.80
dGDP	426.05	158.96
dGDP	426.05	176.94
dGMP	346.09	79.00
dGMP	346.09	150.07
dGTP	506.11	159.03
dGTP	506.11	238.97
dTDP	401.05	158.94
dTDP	401.05	256.96
dTMP	321.11	125.05
dTMP	321.11	194.95
dTTP	480.98	158.94
dTTP	480.98	256.84
dUDP	387.02	159.00
dUDP	387.02	177.01
dUMP	307.03	111.07
dUMP	307.03	195.01
GDP	442.00	158.93
GDP	442.00	343.96
GMP	362.05	133.05
GMP	362.05	150.06
GTP	522.03	240.96
GTP	522.03	320.90
UDP	402.99	158.91
UDP	402.99	272.89
UMP	323.03	79.04
UMP	323.03	97.02
UTP	482.98	158.93
UTP	482.98	403.01

Table A.17.: Software.

Name	Reference
ChromaToF (version 4.51.6.0)	LECO, St.Joseph, USA
FACS Diva Software (version 8.0.2)	BD Biosciences
FlowJo-X (version 10.0.7r2)	BD Biosciences
GraphPad Prism (version 7)	Graphpad Software, San Diego, USA
Illustrator (version 21.1.0)	Adobe, San Jose, USA
ImageJ (version 1.48)	[Schneider et al., 2012]
MAUI-VIA (version 1.0.5)	[Kuich et al., 2015]
MaxQuant (version 1.5.3.30)	[Cox and Mann, 2008]
MetMax (version 1.0.1.12)	MPIMP Golm
MTXQC (version X)	[Zasada, 2017]
Perseus (version 1.6.0.2)	[Tyanova et al., 2016]
PTXQC (version 0.92.0)	[Bielow et al., 2016]
R (version 3.5.1)	[R Core Team, 2018]
R Studio Desktop (version 1.1.463)	[RStudio Team, 2020]
StepOnePlus (version 2.3)	Applied Biosystems, Waltham, USA
Vision-Capt (version 16.11a)	Vilber Lourmat
Xcalibur (version 4.0.27.13)	Thermo Fisher Scientific, Waltham, USA

B Supplementary: Results

Identification of MYCN-dependent metabolic targets

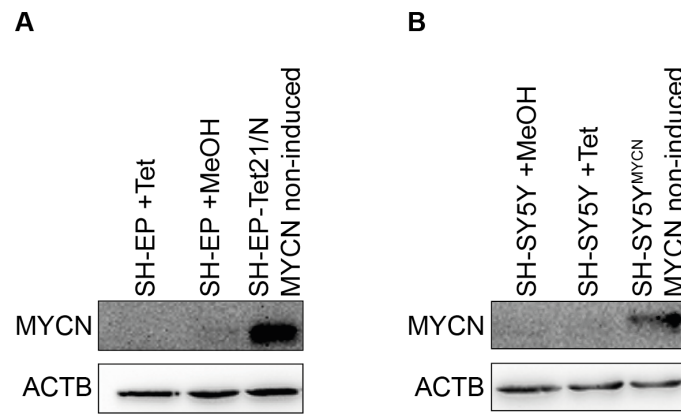


Figure B.1.: MYCN expression in SH-EP-Tet21/N and SH-SY5Y^{MYCN} cells. Immunoblotting showing non-induced and induced MYCN expression in the tetracycline-inducible cell lines SH-EP-Tet21/N (A) and SH-SY5Y^{MYCN} (B). Abbreviations: MeOH - Methanol, Tet - Tetracycline.

Table B.1.: MYCN target genes.

Target gene	Regulation
<i>CD44</i>	downregulated [Schramm et al., 2013]
<i>HK2</i>	upregulated [Schramm et al., 2013]
<i>LIG3</i>	upregulated [Valentijn et al., 2012]
<i>MCM3</i>	upregulated [Valentijn et al., 2012]
<i>MCM5</i>	upregulated [Valentijn et al., 2012]
<i>MSH6</i>	upregulated [Valentijn et al., 2012]
<i>MTAP</i>	upregulated [Valentijn et al., 2012]
<i>NCAPH</i>	upregulated [Valentijn et al., 2012]
<i>Npm1</i>	upregulated [Zeid et al., 2018]
<i>PHGDH</i>	upregulated [Valentijn et al., 2012]
<i>POLA2</i>	upregulated [Valentijn et al., 2012]
<i>PRMT1</i>	upregulated [Valentijn et al., 2012]
<i>RRM2</i>	upregulated [Valentijn et al., 2012]
<i>TMSB4X</i>	downregulated [Schramm et al., 2013]

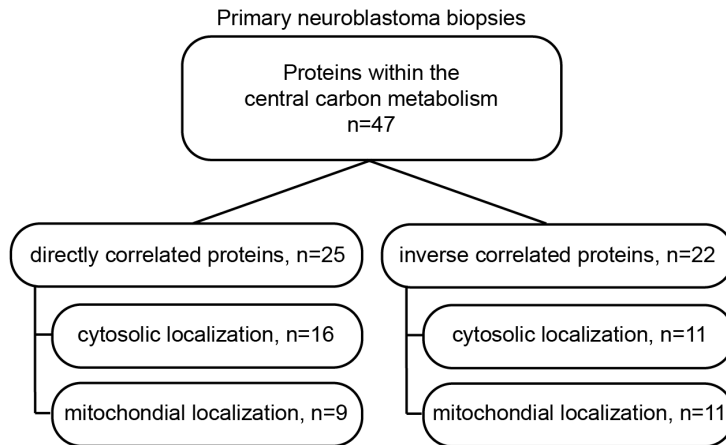
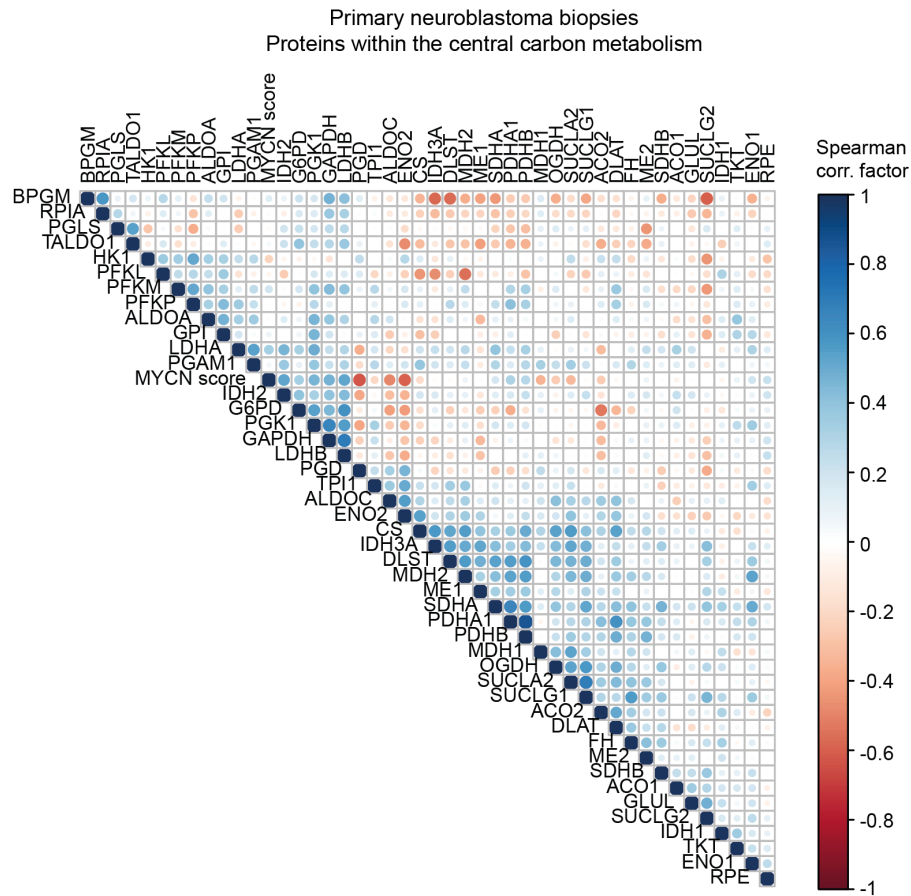
A**B**

Figure B.2.: Spearman correlation analysis with hierarchical clustering after shotgun proteomics displaying proteins within the CCM. Proteins identified with LC-MS with a least one unique peptide were correlated to the MYCN levels of the primary biopsies. Hierarchical clustering of Spearman correlation factor of proteins within the CCM to the MYCN score.

Influence of serine and glycine starvation on PHGDH regulation

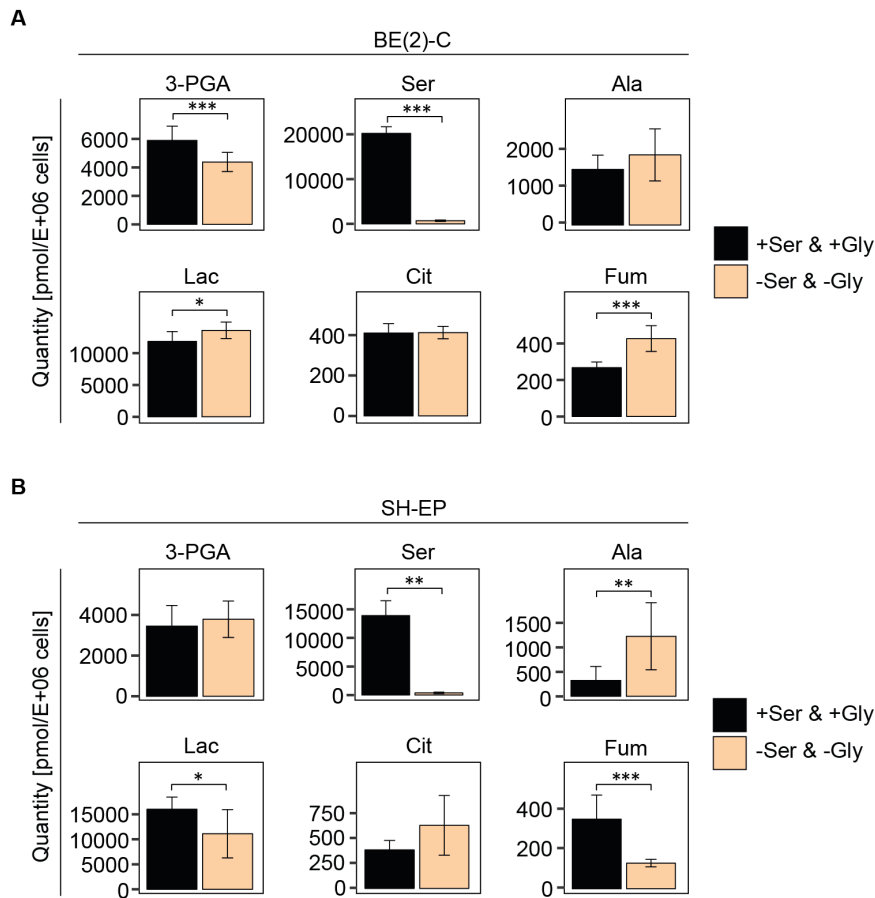


Figure B.3.: Effects of serine and glycine starvation on CCM intermediates. BE(2)-C and SH-EP cells were cultivated in the presence (+Ser & +Gly) and absence (-Ser & -Gly) of serine and glycine for 48 hours. Samples were subjected to GC-MS for metabolite measurement of BE(2)-C (A) and SH-EP (B). Total pool sizes of serine decrease significantly in BE(2)-C and SH-EP. Results represent mean \pm SD, $n=3$. P-values were calculated using an unpaired Student's t-test (* $0.01 < p \leq 0.05$; ** $0.001 < p \leq 0.01$; *** $p \leq 0.001$). Abbreviations: 3-PGA - 3-Phosphoglycerate, Ala - Alanine, Cit - Citrate, Lac - Lactate, Ser - Serine, Fum - Fumarate.

Pharmacological inhibition of PHGDH activity

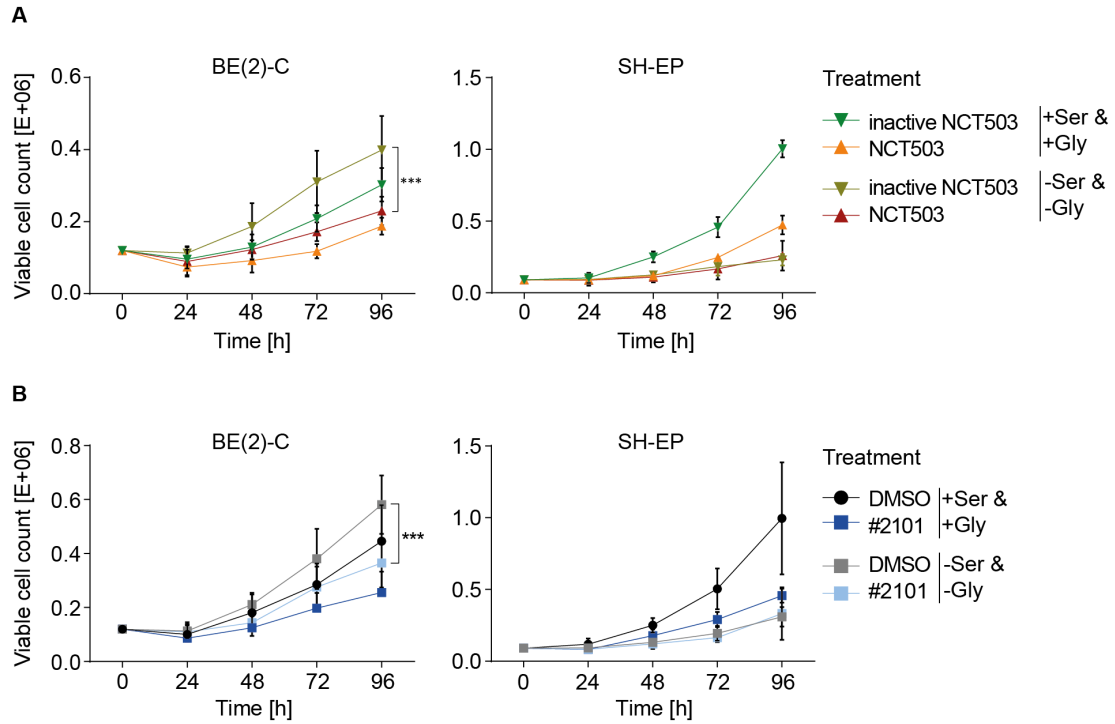


Figure B.4.: Effect on proliferation of PHGDH inhibitor application in combination with serine and glycine starvation. Proliferation measurement of BE(2)-C and SH-EP cells in control (+Ser & +Gly) and serine and glycine depleted condition (-Ser & -Gly) with the application of NCT503 (A) or P2101 (B) and respective controls. Results represent mean \pm SD, $n=3$, each in three technical replicates. P-values were calculated using an unpaired Student's t-test (* $0.01 < p \leq 0.05$; ** $0.001 < p \leq 0.01$; *** $p \leq 0.001$).

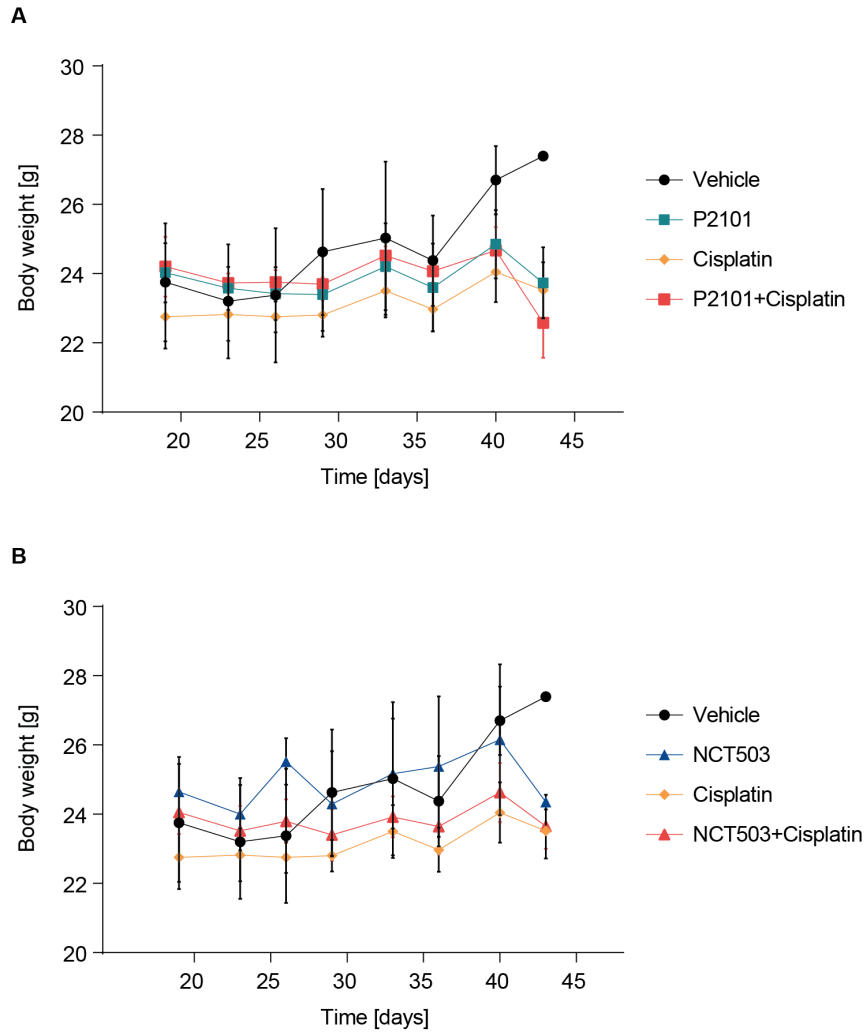


Figure B.5.: Effects of PHGDH inhibitors on bodyweight of NOG mice transplanted with patient-derived neuroblastoma xenograft and treated in mono- or combination therapy with PHGDH inhibitors or cisplatin. Treatment was started three weeks post transplantation. NCT503 and P2101 were injected intraperitoneally daily with a concentration of 40 mg/kg and 20 mg/kg, respectively. Cisplatin was applied intravenously once a week with 2 mg/kg in the first week and 1 mg/kg in weeks 2-4.

Response of neuroblastoma cell lines to glutamine starvation

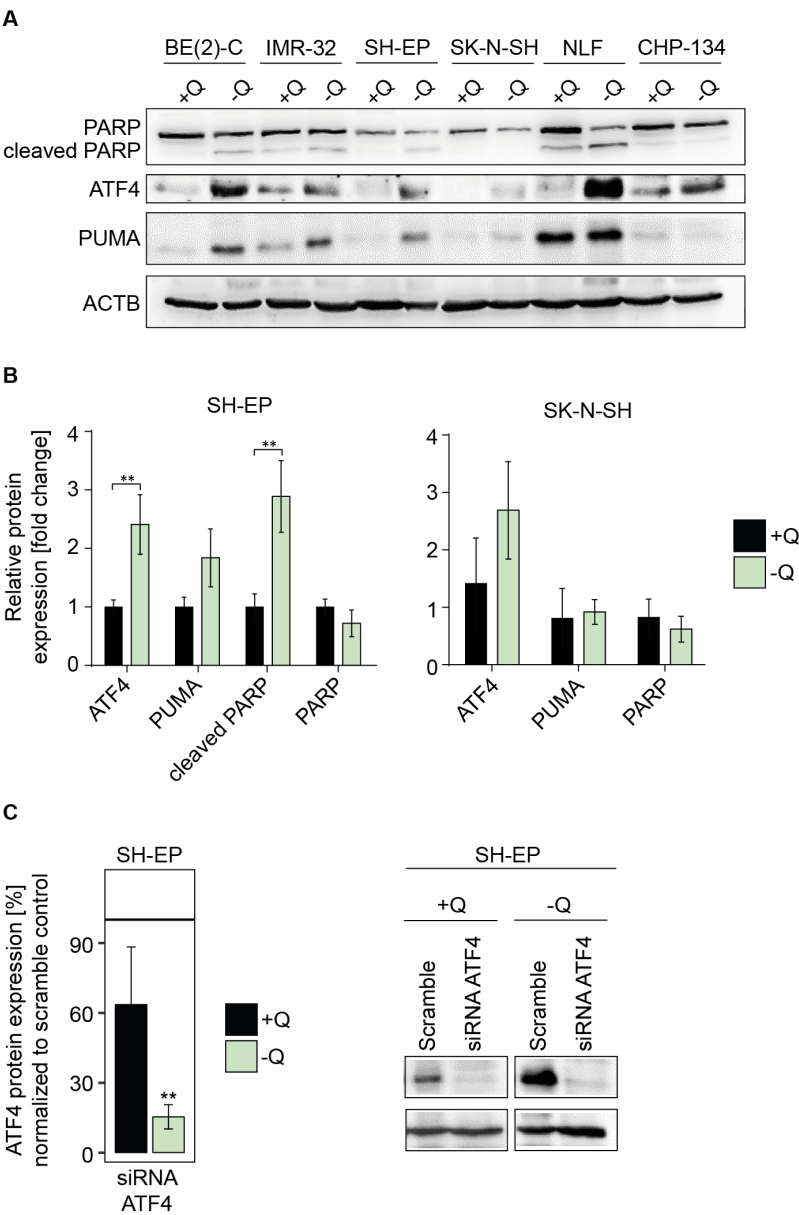


Figure B.6.: Effects of glutamine starvation on the expression of apoptotic marker proteins. *Continued on next page.*

D

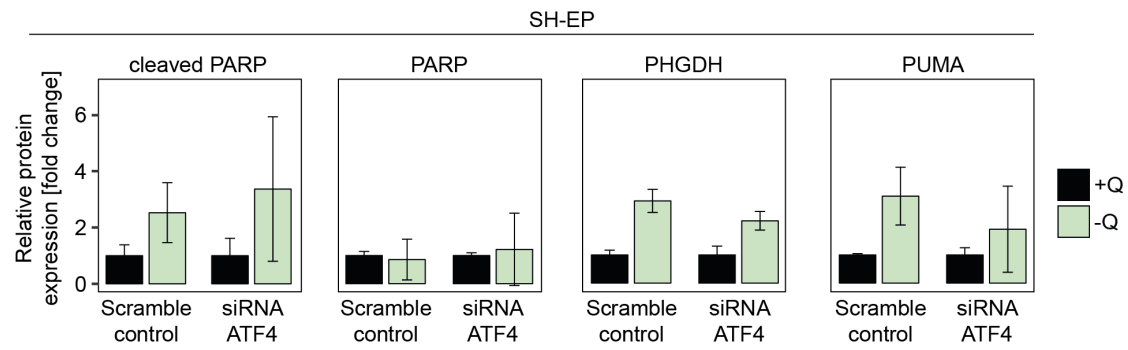


Figure B.6.: Effects of glutamine starvation on the expression of apoptotic marker proteins. A: Representative immunoblotting showing PARP, cleaved PARP, ATF4 and PUMA expression in neuroblastoma cell lines after 48 hours of glutamine starvation. B: SH-EP and SK-N-SH cells were cultured in the presence (+Q) or absence (-Q) of glutamine for 48 hours and relative protein expression is shown for the apoptotic marker proteins PARP, cleaved PARP and PUMA, as well as ATF4. C-D: SH-EP cells were transfected with siRNA Pool targeting *ATF4* with subsequent starvation for glutamine (-Q) for 96 hours. Representative immunoblot and relative quantification revealed the downregulation of ATF4 expression and no change in the expression of apoptotic marker proteins. Results represent mean \pm SD, n=3. P-values were calculated using an unpaired Student's t-test (* $0.01 < p \leq 0.05$; ** $0.001 < p \leq 0.01$; *** $p \leq 0.001$), n=3.

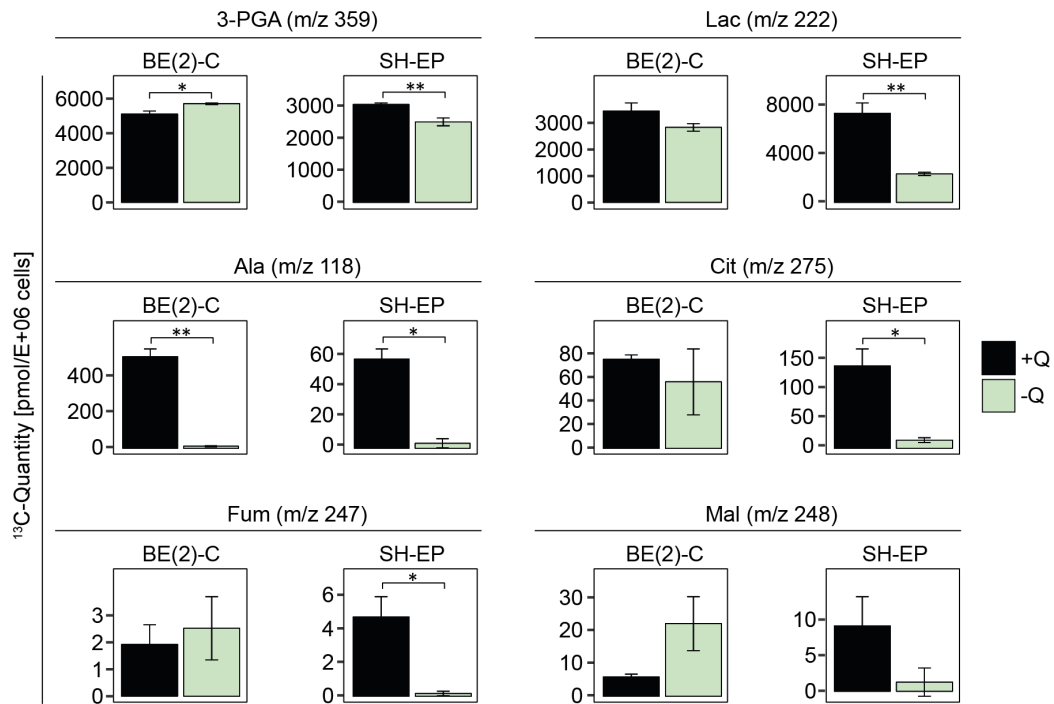
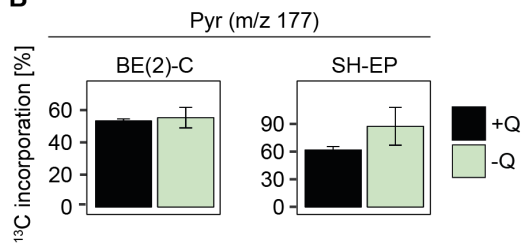
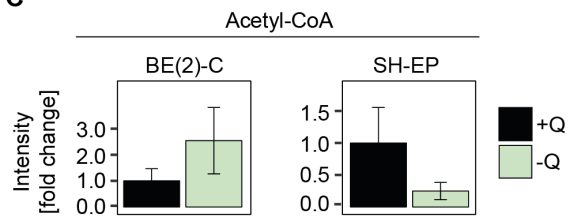
A**B****C**

Figure B.7.: Effects of glutamine starvation on CCM intermediates. BE(2)-C and SH-EP cells were cultivated in the presence (+Q) and absence (-Q) of glutamine for 48 hours with subsequent incubation in medium containing fully labeled ^{13}C -glucose for 20 min before harvest. ^{13}C -labeled quantities (A) of CCM intermediates, ^{13}C -glucose incorporation into pyruvate (B) and relative concentration of acetyl-CoA (C). Results represent mean \pm SD, $n=3$. P-values were calculated using an unpaired Student's t-test (* $0.01 < p \leq 0.05$; ** $0.001 < p \leq 0.01$; *** $p \leq 0.001$). Abbreviations: 3-PGA - 3-Phosphoglycerate, Acetyl-CoA - Acetyl coenzyme A, Ala - Alanine, Cit - Citrate, Fum - Fumarate, Gly - Glycine, Lac - Lactate, Mal - Malate, Pyr - Pyruvate, Ser - Serine.